Development of an Improved Parametrisation of the ATLAS Detector Performance for Tau Leptons and their Application in Studies of Supersymmetric Models within the pMSSM

Master Thesis

Faculty of Physics

Ludwig-Maximilians-Universität München

submitted by

Daniel Buchin

born in Munich

Munich, 9th June 2021

Entwicklung einer verbesserten Detektorparametrisierung für Tau-Leptonen im ATLAS-Detektor und deren Anwendung in Studien zu supersymmetrischen Modellen innerhalb des pMSSM

Masterarbeit der Fakultät für Physik
der
Ludwig-Maximilians-Universität München

vorgelegt von
Daniel Buchin
geboren in München

München, den 09.06.2021

Abstract

Monte Carlo simulations needed to model signal and background in searches for physics beyond the Standard Model (SM) consist of two steps: simulation of the physics process itself (truth-level) and of the detector response (reconstruction-level). For certain large-scale studies of physics beyond the SM, i.e. where large amounts of simulated data are required, running both steps of the simulation is computationally not feasible. An example for such a study is a scan of the parameter space of the phenomenological Minimal Supersymmetric SM (pMSSM) which involves the simulation of multiple supersymmetric processes for a large number of model points. To substitute the resource-hungry reconstruction-level simulation, smearing functions are used to make truth-level objects resemble reconstruction-level objects as much as possible. This method is known as 'truth smearing'.

This thesis investigates ways to improve the performance of the truth smearing of tau leptons at the ATLAS detector for a range of supersymmetric and SM processes. To achieve this, the efficiency of the tau reconstruction and identification algorithms is measured in Monte Carlo simulated data and then predicted using a Boosted Decision Tree (BDT) based on truth-level variables. The set of truth-level variables was chosen such that the predicted efficiencies would match the actual efficiencies for multiple signal points of different processes. Compared to the previous implementation, this method improves the agreement between smeared truth-level and reconstruction-level tau leptons.

An implementation of this newly developed method is then demonstrated for a scan of the pMSSM parameter space. This scan targets models with relatively light supersymmetric partners of the tau lepton using the direct stau analysis.

Contents

Chapter 1

Introduction

For over 50 years, the Standard Model of particle physics has lead the path to the discovery of new elementary particles. Its predictions about the physics on the smallest reachable scales were confirmed in multiple experiments over this period of time with each experiment getting more precise and reaching smaller scales. The last missing piece in this puzzle of particles, the Higgs Boson, was discovered in 2012 [1, 2] at the Large Hadron Collider at CERN. However, our understanding of the fundamental particles and their interactions is still far from complete. The Standard Model leaves some fundamental questions open: Is it possible to unify the strong and the electroweak interactions at high energies? Is there a way to implement gravity in a quantum field theory? Furthermore, the mentioned discovery of the Higgs Boson was accompanied by a new problem: Its measured mass [3] can only be explained within the Standard Model if the parameters which govern the dependence of the Higgs mass on the masses of the other particles are tuned in a very specific way. This fine-tuning without any deeper explanation is deemed unnatural. Finally, a problem originating from astrophysical measurements has also become a problem of particle physics: What is dark matter made of, which governs the rotational behaviour of galaxies and is even more abundant in our universe than normal matter? None of the particles described by the Standard Model can answer this question.
There is however a possible solution to these problems by extending the Standard Model in a quite elegant manner. It is called Supersymmetry.

Supersymmetry is a concept used in a whole framework of theories. Its main purpose is to introduce a new symmetry between particles of different spin. Therefore, a supersymmetric extension of the Standard Model mainly adds partner particles which only differ in spin from their respective Standard Model counterparts. As a consequence, these partner particles should have been found alongside the original particles which is not the case. Due to this, Supersymmetry is expected to be a broken symmetry which makes the masses of the hypothetical supersymmetric particles free parameters. To be able to explain the Higgs mass and to be in agreement with constraints from astrophysical measurements on dark matter, the masses of supersymmetric particles should be within a certain range. The already mentioned Large Hadron Collider is sensitive to this range since the proton-proton collisions at this collider happen at energies high enough to be able to produce heavy supersymmetric particles. Until now, however, no evidence of Supersymmetry was found.

The majority of searches for Supersymmtery at the detectors of the Large Hadron Collider focus on specific decays of certain supersymmetric particles while neglecting the influence of other possible interactions and particles of the rest of the supersymmetric spectrum. Therefore, an approach taking into account a larger part of the supersymmetric parameter space, in a range already thought to be excluded, might be able to find evidence of Supersymmtery. One such approach is the 'pMSSM scan' which searches for Supersymmetry using a 19 dimensional subspace of supersymmetric models, called the pMSSM. In order to spot the excess caused by supersymmetric particles in the data taken by the detector, one has to first simulate how this excess would look like and where to find it. In the pMSSM scan, this has to be done for a large amount of models. Hence a method called truth smearing is employed to reduce the amount of time and resources needed to run these simulations. To achieve this, truth smearing replaces a part of the simulation by simple, so-called smearing functions.

In this thesis, the performance of this method will be investigated for simulated data of the ATLAS detector situated at the Large Hadron Collider. The focus will be on tau leptons which are the heaviest leptons and are being produced in a number of decays of supersymmetric particles. They themselves decay promptly, which results in a quite challenging signature in the detector and makes their truth smearing particularly interesting. For the truth smearing of tau leptons, this thesis will present how the currently used smearing functions can be improved for individual supersymmetric processes and how an improved truth smearing can be employed in searches for such processes. Additionally, this thesis reveals how the performance of the tau lepton truth smearing depends on the process the tau lepton is part of as well as the assumed supersymmetric model. In order to find a realisation of the tau lepton truth smearing which is not subject to this dependence, an improved parametrisation of the reconstruction and identification efficiency of tau leptons at the ATLAS detector will be developed using machine learning methods. Finally, this parametrisation will be implemented in a demonstrative pMSSM scan. This scan will investigate the sensitivity of the search for the direct production of staus, i.e. the supersymmetric partners of the tau lepton, in the context of the pMSSM.

Chapter 2

Theory

In this chapter, the theoretical basis for this thesis is presented. First, the particles and interactions within the Standard Model of particle physics are described. Then, by showing some of the Standard Model's shortcomings, Supersymmetry is presented as a possible solution. Finally, the phenomenological Minimal Supersymmetric Standard Model, a special theoretical model within Supersymmetry is introduced and the supersymmetric processes which were used in this work are presented. In this thesis, natural units are used, i.e. $\hbar = c = 1$ and e is the elementary charge. The Einstein summation convention for greek indices running over the four spacetime dimensions is implied.

2.1 Standard Model of particle physics

The Standard Model (SM) of particle physics is a theory summing up all known elementary particles and their interactions[1] in the language of quantum field theories. Elementary particles are particles which do not have any constituents according to our current understanding. The interactions described by the SM are: first, the electromagnetic interaction which can be experienced in everyday phenomena like light, electricity or friction. Secondly, the weak interaction, best known as the interaction responsible for radioactive beta decays. Thirdly, the strong interaction, known for keeping together the constituents of atomic nuclei.

2.1.1 Particle Spectrum

There are different kinds of elementary particles. The most general distinction would be between fermions, which have a half-integer spin, and bosons, which have a integer spin. These particles are named after the statistical behaviour which an ensemble of these particles would obey: fermions obey Fermi-Dirac statistics, bosons obey Bose-Einstein statistics.
Fermions are the particles which are the fundamental components of normal matter. The fermions described by the SM all have a spin of 1/2. They can be further separated into three generations, each generation containing two leptons and two quarks. Quarks are particles which can interact via all three fundamental interactions while leptons can only interact via weak and the charged ones also via electromagnetic interactions. The different types of leptons and quarks are also called flavours.
In table 2.1, the SM fermions with their mass and electric charge are listed[2]. Precision mea-

[1] Except for gravitation since there is no known way to express it in terms of a quantum field theory.
[2] In the SM, neutrinos are expected to be massless. However, recent experiments have established that neutrinos ought to have a mass, even if there are only upper limits known right now.

surements have been able to determine the charged lepton masses more accurately than shown here while the quark masses are shown with their current precision [4, 5].

Bosons are separated into the gauge bosons and the higgs boson. The gauge bosons have spin 1 and can be seen as the messenger particles of the fundamental interactions, more on them will follow in 2.1.2. The higgs boson on the other hand has a spin 0 and is the excitation of the higgs field. This field is responsible for the higgs mechanism which explains how the massive elementary particles of the SM acquired their mass. The higgs boson has the mass [3]:

$$m_{h^0} = 125.10 \pm 0.14 \text{ GeV} \tag{2.1}$$

Every particle in the SM which is charged w.r.t. one of the three interactions has an anti-particle with the same properties except that every charge-like quantum number has a different sign.

	Generation	Name	Symbol	Mass in MeV	Q in e
	1	electron	e	0.5110	-1
		electron neutrino	ν_e	0	0
leptons	2	muon	μ	105.7	-1
		muon neutrino	ν_μ	0	0
	3	tau	τ	1777	-1
		tau neutrino	ν_τ	0	0
	1	up	u	2.2	$+2/3$
		down	d	4.7	$-1/3$
quarks	2	charm	c	$1.27 \cdot 10^3$	$+2/3$
		strange	s	93	$-1/3$
	3	top	t	$172.8 \cdot 10^3$	$+2/3$
		bottom	b	$4.18 \cdot 10^3$	$-1/3$

Table 2.1: List of all fermions with their mass and electric charge. The lepton masses are shown up to 4 digits, the quark masses with the precision specified by the Particle Data Group [4, 5].

2.1.2 Interactions

Quantum Field Theory

The SM is based on Quantum Field Theories (QFT), so a few basic characteristics of QFTs shall be explained here (based on [6, 7]).

In QFT, particles are not seen as point-like objects in space which might be the intuitive assumption. They are rather seen as excitations of underlying quantum fields which, in vacuum, can be thought of as a superposition of quantum harmonic oscillators[3]. Particles with different quantum numbers are therefore described by different quantum fields. The dynamics and interactions of these fields are encoded in Lagrangian densities $\mathcal{L}$. To acquire equations of motion for the quantum fields from the Lagrangian, the principle of least action is needed. It states that the action S, defined as the integral over space and time of the Lagrangian density,

$$S = \int d^4x \, \mathcal{L} \tag{2.2}$$

[3]In quantum mechanics, creation and annihilation operators $a^\dagger$ and a are used to increase/decrease the energy level of a particle in a harmonic oscillator potential. Operators with a very similar algebra $a_p^\dagger/a_p$ are used in QFT to create/annihilate particles with momentum p from the vacuum. A quantum field is now the superposition of these operators for every possible momentum p.

should be stationary under infinitesimal changes, $\delta S = 0$. This principle directly translates to the Euler-Lagrange equations:

$$\frac{\partial \mathcal{L}}{\partial \phi} - \partial_\mu \frac{\partial \mathcal{L}}{\partial(\partial_\mu \phi)} = 0 \tag{2.3}$$

However, in QFT one is even more interested in scattering amplitudes $\langle f|S|i\rangle$. These give us a measure of the probability that an initial state of particles $|i\rangle$ ends up in another state of particles, the final state $\langle f|$. The Operator S indicates the interactions (the *scattering*) that are needed to get from $|i\rangle$ to $\langle f|$. The calculation of these amplitudes is quite sophisticated though. Due to the Heisenberg Uncertainty Principle $\Delta E \Delta t \simeq \hbar$ which states that in a sufficiently small time interval Δt, a certain amount of energy ΔE can be 'created' from the vacuum, loops of particles will appear during the scattering. Therefore, these calculations are normally done using perturbation theory, only calculating the amplitudes to a certain loop order since each additional loop has an exponentially decreasing contribution to the amplitude.
Fortunately, there is a visualisation of these perturbation theoretical calculations called Feynman diagrams. They show possible realisations of the scattering from initial to final state for a certain loop order (see e.g. figure 2.1), so in general one has to add up multiple of these diagrams (self-made feynman diagrams in this work are created using [8]).

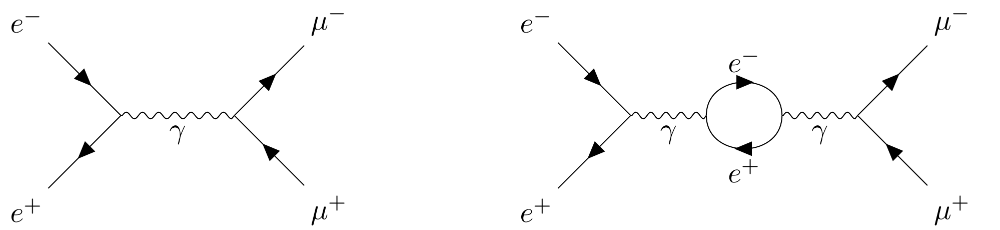

(a) Leading Order (LO) diagram (b) Next-to-Leading Order (NLO) diagram

Figure 2.1: LO and NLO diagrams of the scattering from the initial state consisting of electron e^- and positron e^+ to the final state consisting of muon μ^- and anti-muon μ^+ via interactions with a photon γ.

In the following, LO (also called 'tree-level') diagrams will be used to visualise the different processes that are studied in this thesis.

Symmetries

A very important part of the SM are symmetries. Symmetries manifest themselves as invariances of the Lagrangian, so if a certain transformation of the fields does not change the Lagrangian of the QFT, it is a symmetry of this QFT. A key consequence of symmetries of a theory are conserved charges and currents, as stated by Noether's theorem [9]. This is the reason why symmetries are integral to the SM.
The most fundamental symmetry of the SM is under transformations of the Poincaré group. This group includes translations in space and time as well as Lorentz transformations[4], resulting in the conservation of energy, momentum and angular momentum. These conserved quantities are of utmost importance to the analysis of interactions of elementary particles.
Another crucial class of symmetries in the SM are gauge symmetries. Theories with a gauge symmetry are invariant under gauge transformations, e.g. a local phase shift for a spin $\frac{1}{2}$ field ψ like the electron:

$$\psi \to e^{-i\alpha(x)}\,\psi \tag{2.4}$$

[4]These consist of boosts to different inertial systems and rotations.

The gauge transformations involving a phase shift by a real phase $\alpha(x)$ make up the unitary group $U(1)$. This classification of symmetries in terms of mathematical groups is very useful from a mathematical point of view. Gauge symmetries also imply a global symmetry from which again the existence of a conserved quantity and current follows by Noether's theorem. In the $U(1)$ case, this is achieved with a global phase α:

$$\psi \to e^{-i\alpha}\,\psi \tag{2.5}$$

The importance of gauge transformations can be made clear in the context of Quantum Electrodynamics (QED), the QFT for electromagnetic interactions. Let's consider the Lagrangian for free electrons ψ:

$$\mathcal{L} \;=\; \overline{\psi}(i\gamma^\mu\partial_\mu - m)\psi \tag{2.6}$$

Here, γ^μ are the Dirac matrices and m the electron mass. It is clear, that this Lagrangian is invariant under (2.5). Hence the free Lagrangian already gives a conserved quantity and electron current. However, to understand what this quantity refers to, one needs the gauge symmetry. Since (2.6) is not invariant under the gauge transformation (2.4), an additional massless gauge field A_μ is needed which has the following $U(1)$ gauge transformation (the factor $\frac{1}{e}$ is due to convention):

$$A_\mu \to A_\mu + \frac{1}{e}\partial_\mu\alpha(x) \tag{2.7}$$

By adding this gauge field to the theory, one gets the QED Lagrangian which is gauge invariant:

$$\mathcal{L} \;=\; \overline{\psi}(i\gamma^\mu\partial_\mu - e\gamma^\mu A_\mu - m)\psi - \frac{1}{4}F_{\mu\nu}^2 \tag{2.8}$$

Here, one gets an additional term for the interaction between the electron and this gauge field as well as a term involving the electromagnetic field tensor $F_{\mu\nu} = \partial_\mu A_\nu - \partial_\nu A_\mu$ for the dynamics of the free gauge field. It can be shown by further calculations that this gauge field couples to the conserved electron current with the coupling strength e, thus one can identify A_μ as the photon, the mediator of electromagnetic interactions. Also, the conserved quantity turns out to be the electric charge of the electron. Gauge symmetries are therefore integral to the formulation of the interactions in the SM, here it was shown as an example that the electromagnetic interaction is related to a $U(1)$ gauge symmetry[5].
(based on [6])

The electroweak theory

While the electromagnetic and weak interactions seem quite different at low energy scales – the electromagnetic being far stronger than the weak –, at high energies they appear to be aspects of the same unified electroweak interaction. This unification was first theorised in the 1960s [10, 11] and is based on a gauge symmetry characterised by the group $SU(2) \otimes U(1)$. For $SU(2)$ one gets three conserved quantities according to Noether's theorem and three associated gauge fields W^1_μ, W^2_μ and W^3_μ. The conserved charges are called the three components of the weak isospin I_{W_i} $(i = 1, 2, 3)$ and the W^i_μ gauge fields make up an isospin triplet. For the $U(1)$ symmetry one gets the weak hypercharge Y_W and the gauge field B_μ. Therefore, the W_μ-fields couple to particles with non-zero weak isospin with a coupling strength of g and the B_μ-fields to particles with non-zero weak hypercharge with a coupling strength g'. The observed gauge bosons of weak ($W^\pm_\mu$ and Z_μ) and electromagnetic (A_μ) interactions are

[5] Additionally, gauge symmetries are important in QFTs to ensure the correct degrees of freedom of the gauge bosons and renormalisability.

actually linear combinations of those gauge fields:

$$W_\mu^\pm = \frac{1}{\sqrt{2}} \left(W_\mu^1 \mp i W_\mu^2\right) \tag{2.9a}$$

$$Z_\mu = \cos(\theta_W)\, W_\mu^3 - \sin(\theta_W)\, B_\mu \tag{2.9b}$$

$$A_\mu = \sin(\theta_W)\, W_\mu^3 + \cos(\theta_W)\, B_\mu \tag{2.9c}$$

Where the Weinberg angle θ_W is defined as:

$$\tan(\theta_W) = \frac{g'}{g} \tag{2.10}$$

As a consequence of these mixtures, the observed gauge bosons couple to combinations of the electroweak charges: the Z boson Z_μ couples to the vertex factor c_Z (2.11b) and the photon A_μ to the electric charge Q (2.11a) while the W bosons $W_\mu^\pm$ still couple to the weak isospin.

$$Q = I_{W_3} + \frac{Y_W}{2} \tag{2.11a}$$

$$c_Z = I_{W_3} - Q\, \sin^2(\theta_W) \tag{2.11b}$$

The main reason why the electromagnetic interaction is stronger and also seen in macroscopic phenomena in contrast to the weak interactions is the mass of the Z and the W bosons [3]:

$$m_{W^\pm} = 80.379 \pm 0.012 \text{ GeV} \; ; \; m_Z = 91.1876 \pm 0.0021 \text{ GeV} \tag{2.12}$$

Since the Wu experiment [12] it has been clear that the charged/neutral weak gauge bosons only/preferably couple to fermions of left-handed chirality[6]. Therefore, left-handed leptons/quarks of the same generation are merged into weak isospin doublets (e.g. u- and d'-quarks or the electron and its neutrino) while the right-handed fermions are treated as isospin singlets:

$$\begin{pmatrix} I_{W_3} = +1/2 \\ I_{W_3} = -1/2 \end{pmatrix} = \begin{pmatrix} \nu_{e,L} \\ e_L \end{pmatrix}, \begin{pmatrix} \nu_{\mu,L} \\ \mu_L \end{pmatrix}, \begin{pmatrix} \nu_{\tau,L} \\ \tau_L \end{pmatrix}, \begin{pmatrix} u_L \\ d'_L \end{pmatrix}, \begin{pmatrix} c_L \\ s'_L \end{pmatrix}, \begin{pmatrix} t_L \\ b'_L \end{pmatrix} \tag{2.13a}$$

$$(I_{W_3} = 0) = (e_R), (\mu_R), (\tau_R), (u_R), (d'_R), (c_R), (s'_R), (t_R), (b'_R) \tag{2.13b}$$

At this point, it is important to note that the isospin (or *flavour*) eigenstates of the fermions are not necessarily the same as their observable mass eigenstates. Therefore, the mass eigenstates are linear combinations of the flavour eigenstates, similar to (2.9). That is why the down-type quarks in the isospin doublets are denoted as primed[7].

One last aspect of the electroweak theory which is worth mentioning is the Higgs mechanism. It is responsible for the masses of the weak gauge bosons and the fermions and therefore for the mixing of electroweak fields (see (2.9) and the mixing of down-type quarks). This is also called the breaking of the electroweak $SU(2) \otimes U(1)$ symmetry. The mechanism introduces a complex scalar isospin doublet field Φ (2.14a), the Higgs field, which interacts with itself according to a Mexican hat shaped potential $V(\Phi)$ (2.14b).

$$\Phi = \begin{pmatrix} \phi^+ \\ \phi^0 \end{pmatrix} \tag{2.14a}$$

$$V(\Phi) = \mu^2 \Phi^\dagger \Phi + \lambda (\Phi^\dagger \Phi)^2 \tag{2.14b}$$

[6]Chirality is a rather abstract property of spinor representations of the Lorentz group. For massless particles, it is equivalent to the helicity, the projection of the spin on the direction of motion. For massive particles, a chiral state is a linear combination of the two possible helicity states.

[7]The mixing angles for the down-type quarks are described by the Cabibbo-Kobayashi-Maskawa (CKM) matrix. The distinction between the two types of eigenstates is only made for down-type quarks since up-type quarks are part of the same respective doublet and the eigenstates can be chosen in a way that only one of the isospin components is affected. For the leptons, mixing is not possible since neutrinos are assumed to be massless (which is not the case in our modern understanding and neutrino mixing has already been observed).

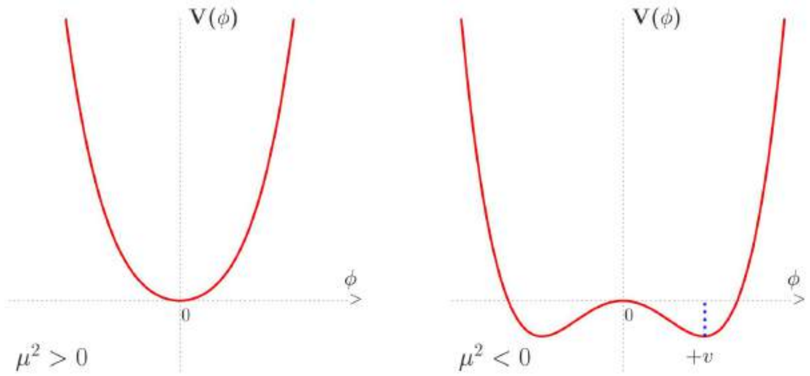

Figure 2.2: The Higgs potential for $\mu^2 > 0$ (left) and $\mu^2 < 0$ (right) [14].

As can be seen in figure 2.2 for $\mu^2 < 0$, the field has non-zero vacuum expectation values v. Since this field interacts with every massive field of the SM, $v \neq 0$ has direct consequences for the whole theory. At high energies, all fields of the SM are assumed to be massless and the electroweak symmetry holds. When approaching the vacuum however, the non-zero v of the Higgs field makes for the masses of the SM fields and the observed mixing of fields. Three of the four degrees of freedom[8] of the Higgs field go into the new degree of freedom of the now massive weak gauge bosons, while one remains as an excitation of the field around the minimum at v which can be identified as the already mentioned Higgs boson h.
(based on [6, 13, 14])

Strong Interactions
Apart from the electroweak interactions, the SM also includes strong interactions. This type of interaction is described by a QFT called quantum chromodynamics (QCD). It is based on a $SU(3)$ gauge symmetry from which one gets so-called colour charges as conserved quantities. Each quark can be seen as a colour triplet, having the colour charge red (R), green (G) or blue (B). The anti-quarks make up anti-colour triplets with the corresponding anti-colours ($\overline{R}$, $\overline{G}$, $\overline{B}$). The leptons and the gauge bosons of the electroweak theory are colour singlets however. From the $SU(3)$ symmetry of QCD it also follows that there are eight gauge fields coupling to the colour charge, called the gluon octet. These gluons each carry a combination of colour and anti-colour charges, thus they can interact among themselves. Since gluons only couple to colour charge, they will not couple to leptons and electroweak gauge bosons.
On the currently observable energy scales, quarks can only be detected as constituents of colourless states of matter. These states are either baryons or mesons. Baryons are made up of three quarks with different colours, so the combination of all three colour charges results in a colour neutral state. Mesons consist of a quark and an anti-quark which ought to have opposite colour charges also assuring colour neutrality. The fact that only colourless states are observed at low energies (or equivalently, big distances), is called confinement. In the opposite scenario, at high enough energies or small enough distances, asymptotic freedom is expected, meaning that quarks and gluons can exist outside colour neutral states. The reason for confinement and asymptotic freedom is the dependence of the energy density of the gluon field on the distance between two quarks. While e.g. the energy density of the electromagnetic field decreases with increasing distance, the opposite can be observed for gluon fields[9]. This effect has some important implications. Consider the production of a quark anti-quark pair in a particle collision. The two particles will now move in different directions and the distance

[8]From the two complex components of the doublet.
[9]The reason for this are running coupling constants which depend on the observed energy scale due to the renormalisation procedure in QFTs. In QCD, the coupling constant increases for lower energies/bigger distances.

will increase. Therefore the energy density of the gluon field between them increases, up to the point where the energy is sufficiently large in order to create a new quark anti-quark pair from the field. Together with the original pair they will build two mesons. This so-called hadronisation process will go on, resulting in the production of a shower of hadrons. These showers and possible decays of the produced hadrons are called jets. They are an important class of objects observed in particle detectors.
(based on [13])

2.1.3 Shortcomings of the Standard Model

The SM has been very successful in describing the observations of experiments probing the smallest reachable scales in the last decades. However, it is not a complete theory of the microcosmos since it leaves some ambiguities and fundamental problems to be solved. A few of them shall be specified in the following.

The Hierarchy Problem
While the SM describes physics up to the electroweak scale M_W which is of the order of a few hundred GeV, one would expect that there are currently unknown phenomena hidden at higher energy scales. At the very least, a suspected QFT description of gravity would have effects on the microcosmos on energy scales around the reduced Planck scale $M_P \simeq 10^{18}$ GeV. This gap of 16 orders of magnitude between these two scales lies at the core of the Hierarchy problem. This problem has a measurable (or rather not measurable) effect on the mass of the Higgs boson m_H. Namely, its mass gets corrections from loops of the particles directly (or even indirectly) coupling to the Higgs boson (see figure 2.3). To be exact, the loop terms are written as corrections $\Delta\mu^2$ of the mass parameter in the Higgs potential (2.14b), but this parameter is directly related to the Higgs mass by $m_H^2 = -2\mu^2$. The corrections coming from fermions coupling to the Higgs field can be written as:

$$\Delta\mu^2 = -\frac{|\lambda_f|^2}{8\pi^2}\Lambda_{UV}^2 + ... \tag{2.15}$$

Here, λ_f is the coupling strength of the fermion to the Higgs field, which is proportional to the fermion mass, and Λ_{UV} is the ultraviolet energy cutoff scale. This cutoff is understood as the energy scale at which new physics will become important. This is how the Hierarchy problem has an impact on the Higgs boson mass: the higher order loop corrections to the mass are extremely sensitive to phenomena at larger energy scales. Therefore, the corrections to m_H will be multiple orders of magnitude larger than the measured value itself (see (2.1)). A way around this might be the assumption that the Higgs field will not couple to any new phenomena outside the SM. This is however a rather unsatisfying assumption. Another solution can be motivated by looking at the corrections $\Delta\mu^2$ for a hypothetical complex scalar field S:

$$\Delta\mu^2 = \frac{\lambda_S}{16\pi^2}\Lambda_{UV}^2 + ... \tag{2.16}$$

Here, λ_S is the coupling strength of S to the Higgs boson which is proportional to m_S^2. From (2.15) and (2.16), one can immediately see that the existence of two complex scalars with $\lambda_S = |\lambda_f|^2$ would lead to a cancellation of the corrections from the respective fermion and scalars. Therefore, a symmetry of fermions and bosons, ensuring that to every fermion/boson there will be a boson/fermion to cancel the loop corrections, would solve the Hierarchy problem for the Higgs boson. This is exactly what Supersymmetry introduces, as will be explained in the next section.
(based on [15, 16])

Figure 2.3: One-loop order corrections to the Higgs mass due to fermion (a) and scalar (b) loops [15].

Unification of interactions

The fact that the electromagnetic and weak interactions could be unified under one symmetry group suggests that all of the interactions described by the SM are aspects of just one fundamental interaction. Since the gauge couplings are dependent on the energy scale, an indicator of this would be that the coupling constants meet at some high energy scale. When extrapolating the coupling constants' behaviour to high energies within the SM, one does not get a single scale where all couplings have the same value. As can be seen in figure 2.4, a supersymmetric theory might be able to assure the unification at an energy scale $M_U \sim 1.5 \times 10^{16}$ GeV.
(based on [15])

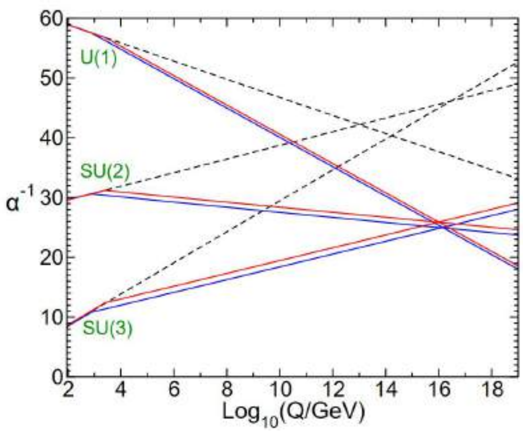

Figure 2.4: Extrapolation to high energies of the different inverse gauge coupling constants for the SM (dashed) and a supersymmetric theory (coloured). From [15].

Dark Matter

In 1933, the Swiss astronomer Fritz Zwicky found a large velocity dispersion of the galaxies in the Coma cluster which lies about 322 million lightyears from earth [17]. From the velocity dispersion, he was able to estimate the total mass of the cluster which turned out to be 50 times the value calculated from observations of luminous matter[10]. This led him to believe that the cluster contained some kind of dark matter (DM) which is not detectable by radiation. Since then, astrophysical observations using gravitational microlensing or the cosmic microwave background have established the existence of DM as a non-baryonic (not made up of quarks like baryons) type of matter. Recent measurements of the cosmic microwave background by the Planck mission show that over 80 percent of the matter in the universe is DM [18]. Since DM seems to interact predominantly through gravitation, its composition is

[10] It is worth mentioning that the mass estimated from observations of luminous matter at the time did not include intracluster gas. Still, the majority of the cluster's mass comes from an unknown type of matter.

quite unclear. One approach to identify the nature of DM is the search for weakly interacting massive particles (WIMPs). These are massive particles with a very weak coupling to normal matter which is why they have not been found yet.
Apart from the constraint that WIMP DM candidates should only interact weakly and be massive, the universe gives a more quantitative requirement as well. In the early stages of the universe, the temperature and density was high enough that processes converting heavier into lighter particles would happen at the same rate as the opposite conversion (they are in 'thermal equilibrium'). As the temperature of the universe was decreasing, lighter particles were no longer energetic enough to produce certain heavy particles and the universe's expansion made interactions less likely. Therefore, at a certain temperature, a 'freeze-out' occurs after which the comoving[11] number density of this certain heavy particle remains constant to the present day. To put this more quantitatively, the freeze-out happens when the reaction rate Γ of the WIMP drops below the Hubble constant H ('reactions are slower than the expansion'). The density of the particle after freeze-out is known as the relic density. The relic density of a theorised DM candidate can be calculated by considering its coannihilation with either itself or other theorised particles to SM particles, its possible decay modes and its scattering off of the thermal background. The present measurement of the DM relic density in the universe given by the Planck mission is [18]:

$$\Omega_c h^2 = 0.1198 \pm 0.0012 \tag{2.17}$$

A viable DM WIMP must have a relic density equal to this value — or below it if there are more kinds of DM particles. Fortunately, some supersymmetric theories predict particles that meet those requirements.
(based on [19])

2.2 Supersymmetry

The main idea behind Supersymmetry (SUSY) is to introduce a symmetry between fermions and bosons. This symmetry can be introduced mathematically using an operator Q:

$$Q|\text{Boson}\rangle = |\text{Fermion}\rangle;\ Q|\text{Fermion}\rangle = |\text{Boson}\rangle \tag{2.18}$$

The fermions and bosons related by such a transformation are called superpartners. They form supermultiplets which are the irreducible representations of this symmetry[12]. It can be shown that Q does commute with the spacetime momentum operator and the squared mass operator, ensuring that the SUSY transformations are independent of the position in spacetime and that the masses of superpartners are equal. Additional commutation relations with the generators of the gauge symmetries prove that superpartners also share the same charges with respect to the SM interactions.
This however would imply that the selectron, the superpartner of the electron, should have been found long ago since they only differ in spin and have the same mass. No SUSY particles have been discovered at this point so they clearly cannot have the same masses as their SM counterparts. Hence, SUSY has to be a broken symmetry at low energies similar to the electroweak symmetry. If SUSY is broken, the masses of the superpartners of SM particles will be free parameters which allows the supersymmetric masses to be arbitrarily heavier than

[11] A certain cosmological parameter is called comoving if the effects of the universe's expansion are removed by choosing the corresponding coordinate system 'moving' with the expansion.

[12] Irreducible representations can be understood as the smallest subset of states (of a certain vector space the symmetry group is acting on) which are closed w.r.t. the symmetry operation. E.g., the isospin doublets and singlets of the electroweak theory were irreducible representations of the $SU(2)$ symmetry.

the SM masses. However, one has to remember that to solve the hierarchy problem (see subsection 2.1.3), the masses of superpartners should be as close as possible. Therefore, present SUSY theories only introduce a *soft* SUSY breaking with supersymmetric masses postulated well within the reach of current particle physics experiments like the Large Hadron Collider. (based on [15])

2.2.1 Minimal Supersymmetric Standard Model

Particle Spectrum
The minimal supersymmetric SM (MSSM) extends the SM with a minimal set of new particles. It postulates that every SM particle acquires a superpartner and it adds a second complex, scalar Higgs doublet[13]. The superpartners form two types of supermultiplets: chiral supermultiplets, containing a Weyl fermion of spin $\frac{1}{2}$ (two degrees of freedom) and a complex scalar boson of spin 0 (two degrees of freedom) as well as gauge supermultiplets, containing a gauge boson of spin 1 (two degrees of freedom in the massless case) and a Weyl fermion of spin $\frac{1}{2}$. It should be mentioned that the SM fermions are treated as Dirac fermions while their left- and right-handed components can be seen as Weyl fermions. This distinction in chirality has already been made in the electroweak theory. Superpartners of SM fermions are given the same name as the SM particle with a s- prepended (electron $\rightarrow$ selectron) while the superparners of SM bosons get the ending -ino (W $\rightarrow$ wino). The symbols of superpartners are the same, but with a tilde ($e_L \rightarrow \tilde{e}_L$).

Mass eigenstates of the MSSM
An overview of the gauge and mass eigenstates of the MSSM can be seen in table 2.2.
From the two complex Higgs field doublets (H_u^+, H_u^0) and (H_d^-, H_d^0), one now gets 5 real Higgs bosons since both doublets have 4 degrees of freedom and three of these again turn into the third polarisation of the three heavy gauge bosons ($W^\pm$, Z^0) during electroweak symmetry breaking. Through the symmetry breaking, the remaining Higgs gauge eigenstates mix to the two CP-even[14], neutral mass eigenstates h^0 and H^0, the CP-odd, neutral A^0 and the charged $H^\pm$ where h^0 has the lowest mass and is identified as the SM Higgs boson.
Since both the supersymmetric counterparts of the electroweak gauge bosons and the higgs bosons have spin $\frac{1}{2}$, they can mix among each other to form the mass eigenstates after electroweak symmetry breaking. Respecting electric charge, one gets the four neutralinos ($\tilde{\chi}_1^0$, $\tilde{\chi}_2^0$, $\tilde{\chi}_3^0$, $\tilde{\chi}_4^0$) from the neutral bino, wino and higgsino gauge eigenstates ($\tilde{B}^0$, $\tilde{W}^0$, $\tilde{H}_u^0$, $\tilde{H}_d^0$) and the four charginos ($\tilde{\chi}_1^\pm$, $\tilde{\chi}_2^\pm$) from the charged wino and higgsino gauge eigenstates ($\tilde{W}^\pm$, $\tilde{H}_u^+$, $\tilde{H}_d^-$). A lower index of the neutralinos and charginos implies a lower mass. The exact composition of the mass eigenstates from the gaugino/higgsino eigenstates determine the coupling strengths of the neutralinos and charginos to the different interactions.
In the MSSM, the superpartners of left- and right-handed fermions can mix since chirality has no impact on sfermions of spin 0. It is expected that especially sfermions of the third generation will be subject to mixing. E.g., from the two stau gauge eigenstates $\tilde{\tau}_L$ and $\tilde{\tau}_R$ one would get the mass eigenstates $\tilde{\tau}_1$ and $\tilde{\tau}_2$ where a lower index implies a lower mass again. And again, the mixing determines the coupling strength of the sfermion mass eigenstates to the interactions.
The gluino will not mix with any of the electroweak gauginos and higgsinos because $SU(3)$ is not involved in the electroweak symmetry breaking. Nevertheless, gluinos will acquire mass

[13] A second Higgs doublet is necessary to avoid anomalies and to give every fermion a mass through Yukawa couplings in a supersymmteric structure. For up-type quarks, a Higgs field with $Y_W = 1$ is needed, for down-type quarks and charged leptons a Higgs field with $Y_W = -1$.
[14] CP refers to the charge conjugation and parity symmetry transformations [13].

due to SUSY breaking.
For some SUSY breaking scenarios, the MSSM includes an additional spin $\frac{3}{2}$ gravitino which in these scenarios would be the superpartner of the graviton[15].

Names	Spin	P_R	Gauge Eigenstates	Mass Eigenstates
Higgs bosons	0	+1	$H_u^0\ H_d^0\ H_u^+\ H_d^-$	$h^0\ H^0\ A^0\ H^\pm$
squarks	0	−1	$\widetilde{u}_L\ \widetilde{u}_R\ \widetilde{d}_L\ \widetilde{d}_R$	(same)
			$\widetilde{s}_L\ \widetilde{s}_R\ \widetilde{c}_L\ \widetilde{c}_R$	(same)
			$\widetilde{t}_L\ \widetilde{t}_R\ \widetilde{b}_L\ \widetilde{b}_R$	$\widetilde{t}_1\ \widetilde{t}_2\ \widetilde{b}_1\ \widetilde{b}_2$
sleptons	0	−1	$\widetilde{e}_L\ \widetilde{e}_R\ \widetilde{\nu}_e$	(same)
			$\widetilde{\mu}_L\ \widetilde{\mu}_R\ \widetilde{\nu}_\mu$	(same)
			$\widetilde{\tau}_L\ \widetilde{\tau}_R\ \widetilde{\nu}_\tau$	$\widetilde{\tau}_1\ \widetilde{\tau}_2\ \widetilde{\nu}_\tau$
neutralinos	1/2	−1	$\widetilde{B}^0\ \widetilde{W}^0\ \widetilde{H}_u^0\ \widetilde{H}_d^0$	$\widetilde{N}_1\ \widetilde{N}_2\ \widetilde{N}_3\ \widetilde{N}_4$
charginos	1/2	−1	$\widetilde{W}^\pm\ \widetilde{H}_u^+\ \widetilde{H}_d^-$	$\widetilde{C}_1^\pm\ \widetilde{C}_2^\pm$
gluino	1/2	−1	$\widetilde{g}$	(same)
goldstino (gravitino)	1/2 (3/2)	−1	$\widetilde{G}$	(same)

Table 2.2: Gauge and mass eigenstates of the additional fields introduced in the MSSM. Here, mixing of sfermions in the first two generations is neglected, the neutralinos $\tilde{\chi}_i^0$ are denoted as $\tilde{N}_i$ and the charginos $\tilde{\chi}_i^\pm$ as $\tilde{C}_i$. From [15].

R-Parity

General supersymmetric extensions of the SM Lagrangian introduce terms which would imply baryon number B and lepton number L[16] violating interactions. This is problematic since there is no experimental evidence for such processes. For example, the decay of the proton would be allowed, even though the proton has a measured lifetime of $\sim 10^{31} - 10^{33}$ years [20]. To avoid these phenomena, in the MSSM, an additional symmetry is introduced called R-parity. It is a multiplicative quantum number defined as:

$$P_R = (-1)^{3(B-L)+2s} \tag{2.19}$$

Where s is the spin of the respective particle. When calculating the value of this quantum number for the particles of the MSSM, it becomes clear that the SM particles and Higgs bosons get $P_R = 1$ while the other, supersymmetric particles get $P_R = -1$. Therefore, this symmetry has further consequences: to conserve P_R, each interaction vertex has to include an even number of SUSY particles when having SM particles in the initial state. Thus, the lightest supersymmetric particle (LSP) is stable and will not decay.
The LSP is usually assumed to be the lightest neutralino $\tilde{\chi}_1^0$ (or, if the model includes gravitinos, sometimes the gravitino $\tilde{G}$). Due to its stability and coupling to only the weak gauge bosons, it is a prime DM candidate. However, if its relic density meets the requirements of astrophysical measurements depends on its composition of binos, winos and higgsinos. This will be important later on.
(subsection based on [15, 19])

[15] That is, if gravity is included in the model.
[16] The baryon number is defined as (-)$\frac{1}{3}$ for supermultiplets containing (anti-)quarks and 0 in all other cases. The lepton number is defined as (-)1 for supermultiplets containing leptons and 0 in all other cases.

2.2.2 phenomenological MSSM

The MSSM contains a vast range of models due to its 124 free parameters, of which 105 come from soft SUSY breaking and 19 from the SM [21]. This makes any analysis of the MSSM parameter space, which attempts to be exhaustive, very challenging if not impossible. Experimental data however justifies a number of assumptions which help constrain the number of parameters. One such constrained version of the MSSM is the phenomenological MSSM (pMSSM). The pMSSM makes the following assumptions [22]:

(1) No new source of CP-violation: this sets any additional complex phases outside the SM to zero. The assumption is motivated by observations of the neutron and electron electric moments.

(2) No Flavour Changing neutral currents (FCNCs): this eliminates any non-diagonal terms in sfermion mass matrices and trilinear couplings. It is motivated by the non-observation of any FCNCs.

(3) First and Second Generation Universality: this sets the first and second generation sfermion masses to equal values and neglects the trilinear couplings of these generations. It is motivated by experimental data of e.g. $K^0 - \bar{K}^0$ meson mixing.

Through these assumptions, the pMSSM ends up with just 19 parameters:

$\tan\beta$: the ratio of vacuum expectation values of the two Higgs doublets, $\tan\beta = \frac{v_u}{v_d}$ [21]

M_A: the mass of the CP-odd neutral Higgs boson A^0

μ: the Higgs-higgsino mass parameter

M_1, M_2, M_3: the mass parameters of bino, wino and gluino, respectively

$m_{\tilde{q}}, m_{\tilde{u}_R}, m_{\tilde{d}_R}, m_{\tilde{l}}, m_{\tilde{e}_R}$: first/second generation sfermion mass parameters

$m_{\tilde{Q}}, m_{\tilde{t}_R}, m_{\tilde{b}_R}, m_{\tilde{L}}, m_{\tilde{\tau}_R}$: third generation sfermion mass parameters

A_t, A_b, A_τ: third generation trilinear couplings

In the mentioned models which include a gravitino, the gravitino mass $m_{\tilde{G}}$ becomes an additional parameter.

2.3 Processes in this study

In this work, six processes — one SM and five MSSM — are used to look into the truth smearing of tau leptons. While the SM process will incorporate multiple decay possibilities of the W boson, the SUSY processes will focus on just one (in some cases two) specific decay chain. Also, while the particle masses in the SM process are well known, some of the masses in the SUSY processes are treated as free parameters and therefore multiple mass configurations will be studied for them. Usually, only two of the participating particle masses are varied. Any other MSSM parameter is fixed at some value so that the considered process can be studied free of any disturbance by other SUSY processes. This practice will be further discussed in section 4.4.2. Therefore, each of the following SUSY processes assumes different values for the MSSM parameters.
In the following sections and also in the discussion of the SUSY processes shown here, antiparticles will be mainly called particles as well since the distinction between the two is not of concern in this work (e.g. anti-squarks will just be called squarks, too).

Top quark pair production

The SM process used in this study is the top quark pair production (ttbar). As can be seen from figure 2.5, a top quark and the corresponding antiquark are produced from gluon fusion[17]. The top quark has a decay width of $\Gamma_t = 1.42^{+0.19}_{-0.15}$ GeV [5] from which it can be inferred[18] that it has a lifetime of $\sim 10^{-25}$ s. Therefore, it will almost immediately decay into a bottom quark and a W boson. While the bottom is stable, the W boson will also decay in $\tau_W \sim 10^{-25}$ s. The W boson decays either into *(a)* a quark and an antiquark of different type (hadronic decay) or *(b)* into a charged lepton and the corresponding antineutrino (leptonic decay). The hadronic decay dominates with a branching ratio (BR)[19] of BR($W \to had$)= $(66.5 \pm 1.4)\%$. The BRs to the individual lepton flavours account for $\sim 11\%$ each [5]. Therefore, at least one tau lepton will appear in the final state with a probability of $\sim 21\%$.

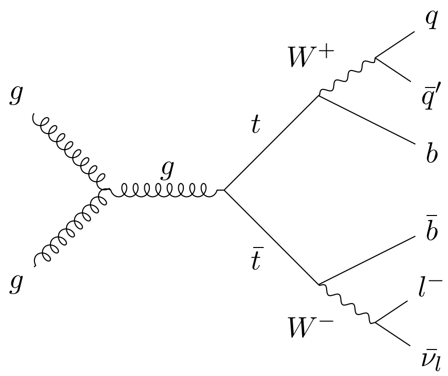

Figure 2.5: Tree-level feynman diagram of the $t\bar{t}$ production. Here, one W boson decays hadronically while the other one decays leptonically.

Squark and Gluino pair production

The squark (SqSq) and gluino (GoGo) pair production processes are quite similar. The feynman diagrams in figure 2.6 show the production[20] of the squark (figure 2.6a) and the gluino (figure 2.6b) pair and the subsequent two-step cascade decay of these particles. In the SqSq process, only the four first generation squarks ($\tilde{u}_L$, $\tilde{u}_R$, $\tilde{d}_L$ and $\tilde{d}_R$) are considered and they are assumed to be mass degenerate.

In the SqSq case, the squark decays into either $\tilde{\chi}_1^{\pm} q$ or $\tilde{\chi}_2^0 q$ with a 50% BR each, where q stands for a generic first or second generation quark. The lightest chargino $\tilde{\chi}_1^{\pm}$ is then expected to decay into $\tilde{\tau}_1 \nu_\tau$ or $\tilde{\nu}_\tau \tau$ at the same rate, while the second lightest neutralino $\tilde{\chi}_2^0$ is expected to decay into $\tilde{\tau}_1 \tau$ or $\tilde{\nu}_\tau \nu_\tau$ at the same rate. The lightest tau slepton would then decay into $\tilde{\chi}_1^0 \tau$ and the tau sneutrino into $\tilde{\chi}_1^0 \nu_\tau$.

In the GoGo case, the only difference is that the gluino is assumed to decay into $\tilde{\chi}_1^{\pm} q\bar{q}'$ or $\tilde{\chi}_2^0 q\bar{q}$ with the same probability. The subsequent decay chain is the same as for the SqSq case. Later on, the tau leptons in versions of these processes with different SUSY masses will be studied. However, only the masses of the squark/gluino and the lightest neutralino - which is assumed to be the LSP - are varied. The masses of the other SUSY particles are determined

[17]This is the most common strong production mechanism at the Large Hadron Collider. Of course, other production mechanisms contribute as well, but the exact production mode is not of interest here.

[18]The formula $\tau = \frac{\hbar}{\Gamma}$ gives the mean lifetime for a given decay width/rate Γ. This relation can be motivated by the uncertainty principle for time and energy.

[19]The BR is calculated by taking the ratio of the decay mode i's decay width Γ_i and the full decay width Γ, $\text{BR}_i = \frac{\Gamma_i}{\Gamma}$. It corresponds to the probability that some particle will decay in the mode i.

[20]For the SUSY diagrams, the exact production mode is not shown, instead the collision of two protons is shown which should indicate any possible production mode.

in the following way [23]:

$$m_{\tilde{\chi}_1^\pm} = m_{\tilde{\chi}_2^0} = \tfrac{1}{2}(m_i + m_{\tilde{\chi}_1^0}),\ m_{\tilde{\tau}_1} = m_{\tilde{\nu}_\tau} = \tfrac{1}{2}(m_{\tilde{\chi}_1^\pm} + m_{\tilde{\chi}_1^0})\ ;\ i = \tilde{g}, \tilde{q} \tag{2.20}$$

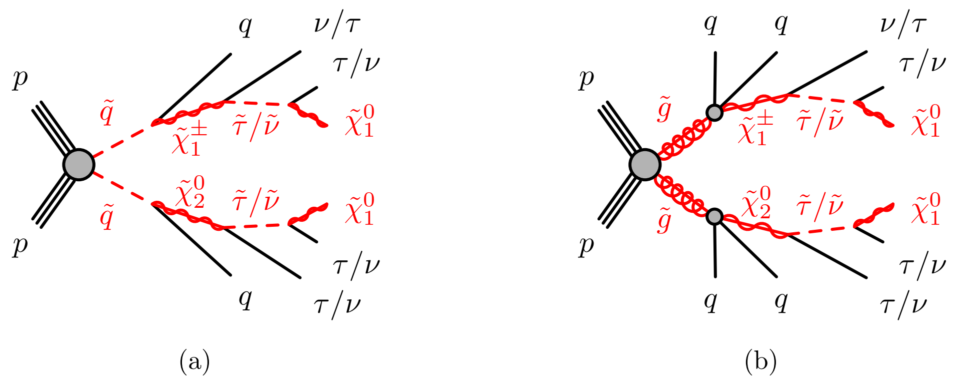

Figure 2.6: Tree-level feynman diagrams of the (a) $\tilde{q}\tilde{q}$ and (b) $\tilde{g}\tilde{g}$ production.

Direct tau slepton production
In the direct tau slepton production process (direct stau), each tau slepton of the produced pair is assumed to decay into $\tilde{\chi}_1^0\tau$. Different mass configurations for this process will be studied with varied tau slepton and lightest neutralino masses.
For this process, the two tau slepton mass eigenstates $\tilde{\tau}_1$ and $\tilde{\tau}_2$ are assumed to be mass degenerate and the neutralino is assumed to be purely made up of the bino and to be the LSP [24].

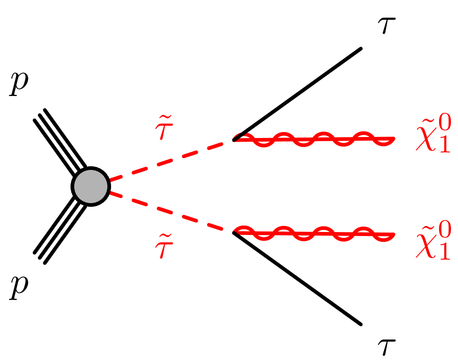

Figure 2.7: Tree-level feynman diagram of the direct stau process.

Direct chargino production
In the direct chargino production process (C1C1), the produced lightest charginos are assumed to be pure winos and decay into $\tilde{\tau}_1\nu_\tau$ or $\tilde{\nu}_\tau\tau$ at the same rate. The lightest tau slepton then decays into $\tilde{\chi}_1^0\tau$ and the tau sneutrino into $\tilde{\chi}_1^0\nu_\tau$.
Furthermore, the lightest tau slepton $\tilde{\tau}_1$ is assumed to be purely made up of the superpartner of the left-handed tau lepton $\tilde{\tau}_L$ and the lightest neutralino $\tilde{\chi}_1^0$ is assumed to be the LSP and a pure bino [25].
The masses of the chargino and the neutralino are varied, while the mass of the tau slepton is assumed to be:

$$m_{\tilde{\tau}_1} = \tfrac{1}{2}(m_{\tilde{\chi}_1^\pm} + m_{\tilde{\chi}_1^0}) \tag{2.21}$$

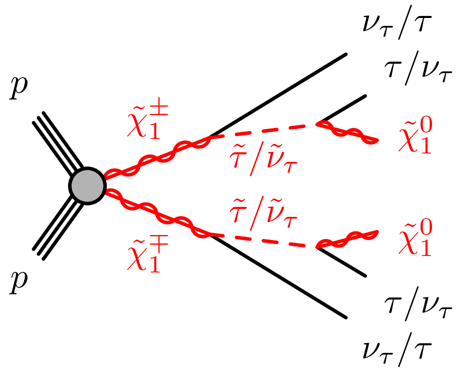

Figure 2.8: Tree-level feynman diagram of the C1C1 process.

Top squark pair production
In the top squark pair production process (ttStau), the produced lightest top squarks $\tilde{t}_1$ decay into $\tilde{\tau}_1\nu_\tau b$ and the subsequently produced lightest tau slepton then decays into $\tilde{G}\tau$. Therefore, this process assumes the existence of the gravitino $\tilde{G}$ and that it is the LSP. The $\tilde{t}_1$ is assumed to be the lightest squark.
The masses of the lightest top squark and the lightest tau slepton are varied while the gravitino mass is assumed to be negligible [26, 27].

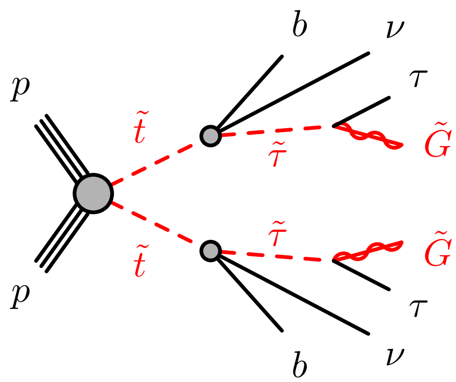

Figure 2.9: Tree-level feynman diagram of the ttStau process.

Chapter 3

Experiment

This work is based on simulated data from the ATLAS detector at the Large Hadron Collider (LHC). The experiment is run by CERN (Conseil Européen pour la Recherche Nucléaire) and located near Geneva at the french-swiss border.

3.1 The Large Hadron Collider

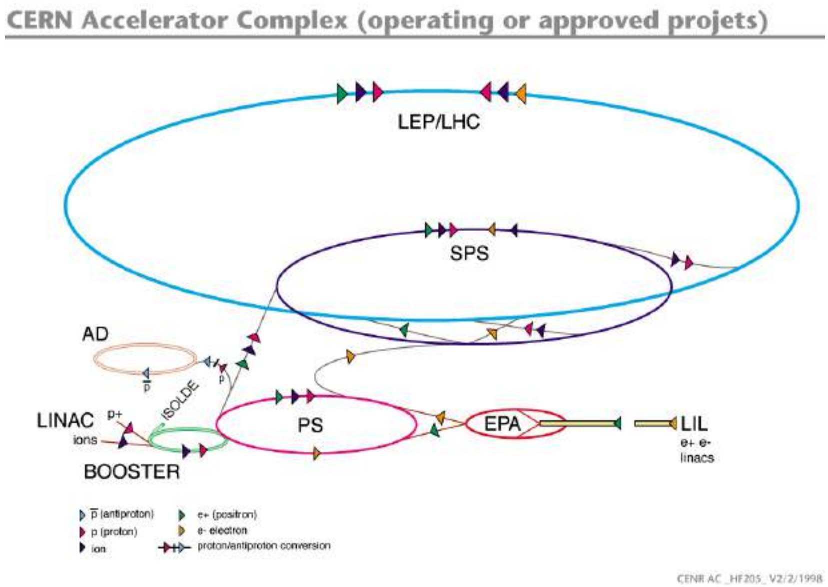

Figure 3.1: The accelerator complex of the LHC [28].

The LHC is an underground, circular particle accelerator with a circumference of 27 km. It accelerates beams of proton bunches up to energies of 7 TeV. A beam consists of about 2808 bunches which in turn contain about 10^{11} protons. However, the LHC is just the last link in a chain of accelerators. Before the proton beam is injected into the LHC, it is accelerated to 450 GeV by a complex of multiple accelerators (see figure 3.1) [29]. Actually, two of those proton beams are injected into the LHC which circulate in opposite directions. At 4 points along the accelerator ring, the two beams are forced to collide which happens at a frequency of up to 40 MHz and with the protons travelling at 99.999999% of the speed of light [29, 30]. During the most recent run of the LHC, Run 2, the proton beams had energies of 6.5 TeV, resulting in a centre-of-mass energy of $\sqrt{s} = 13$ TeV. This corresponds to the maximum energy that is available for creating new particles in each collision.

Another important parameter of the LHC is its *luminosity* $\mathcal{L}$. It is a measure of how many collisions happen per unit area and time. Therefore, using $\mathcal{L}$, one can estimate the number of collision events N_{events} in a certain period of time Δt in which a particular physical process p happens [31]:

$$N_{events} = \sigma_p \cdot \underbrace{\int_0^{\Delta t} \mathcal{L} dt'}_{L} \tag{3.1}$$

Here σ_p is the cross-section of the considered process and L the time integrated luminosity. The cross-section σ_p is a measure of the probability that the process p will take place, described in the form of a 'collision area'[1]. Cross-sections are commonly given in units of b (barn)[2], thus the luminosity is given in units of b^{-1}.

3.2 The ATLAS Detector

At each of the 4 collision points along the LHC beam pipe, a detector is located. These are ATLAS, ALICE, CMS and LHCb. While ALICE is specialised on the observation of lead-ion collisions to study the quark-gluon plasma and LHCb is specialised in observing B-particles to study the matter-antimatter asymmetry, ATLAS and CMS are general-purpose particle detectors. The goals of ATLAS and CMS are SM precision measurements as well as searches for physics beyond the SM like SUSY, but they use different technical solutions to do so [29]. As mentioned, this work will focus on the ATLAS experiment.
The ATLAS detector has a cylindrical shape, is 44 m long and 25 m high [32]. This makes it the largest-volume collider-detector ever built. Figure 3.2 shows the detector and its components.

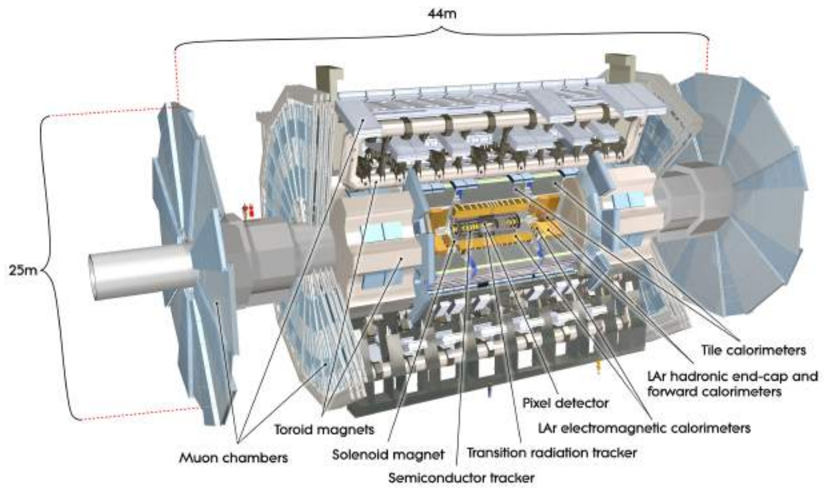

Figure 3.2: Cut-away view of the ATLAS detector. [32].

[1]The cross-section is usually calculated via the scattering amplitude of the particular process which has already been mentioned in section 2.1.2

[2]$1\ \mathrm{b} = 10^{-24}\ \mathrm{cm}^2$

3.2.1 Coordinate System

The ATLAS detector has a well-defined coordinate system. The cartesian coordinates are defined as follows: the x-axis points to the middle of the LHC ring, the y-axis to the surface and the z-axis along the beam pipe. The origin is placed at the collision point.
Since the detector has a cylindrical symmetry, it is useful to define two angles: the azimuthal angle ϕ, measured around the beam axis in the x-y-plane and the polar angle θ, measured from the beam axis in the y-z-plane. As the produced particles will be boosted in z-direction, one should use the lorentz-invariant *pseudorapidity* η instead of the polar angle for (nearly) massless particles [32]:

$$\eta = -\ln\left(\tan\left(\frac{\theta}{2}\right)\right) \tag{3.2}$$

For very massive particles like the top quark, one uses the *rapidity* y [32]

$$y = \frac{1}{2}\ln\left(\frac{E+p_z}{E-p_z}\right) \tag{3.3}$$

Here, E describes the energy of the particle in question and p_z the momentum in z-direction. The distance ΔR in the pseudorapidity-azimuthal angle space, also referred to as the *angular distance*, is thus defined as $\Delta R = \sqrt{\Delta\eta^2 + \Delta\phi^2}$.
Since in the collisions, not the protons as a whole but instead their partons[3] will interact, it is not possible to assess the initial kinetic state in z-direction. This is because the partons will carry only a fraction of the known proton momentum and the exact fraction is not accessible. Therefore, calculations using variables defined in the transverse plane (i.e. the x-y-plane) are very important as momentum conservation can be used then. The transverse momentum vector $\mathbf{p}_\mathrm{T}$ and its magnitude p_T are defined as:

$$\mathbf{p}_\mathrm{T} = \begin{pmatrix} p_x \\ p_y \end{pmatrix} \; ; p_\mathrm{T} = \sqrt{p_x^2 + p_y^2} \tag{3.4}$$

The missing transverse energy $\mathbf{E}_\mathrm{T}^\mathrm{miss}$ (or MET) is defined as the negative sum over the transverse momenta $\mathbf{p}_\mathrm{T}$ of every detected object in one event:

$$\mathbf{E}_\mathrm{T}^\mathrm{miss} = -\sum \mathbf{p}_\mathrm{T} \tag{3.5}$$

Therefore, this variable describes the particles which were not recorded by the detector since the overall transverse momentum should be zero due to momentum conservation. The magnitude of the missing transverse energy is denoted as $E_\mathrm{T}^\mathrm{miss}$.

3.2.2 Components

The main goal of the ATLAS detector is to identify particles that were created in the processes following collision events in its core. To be able to measure a wide range of particles and their properties, the ATLAS experiment consists of three sub-systems: the inner detector, the calorimeters and the muon spectrometer.

The Inner Detector
The inner detector has again three sub-systems which are all contained in a solenoidal magnet with a central magnetic field of 2 T [34]. Each of the sub-systems are divided into a barrel part for low $|\eta|$ and end-caps in forward and backward z-direction for a higher $|\eta|$ range.

[3] Partons of the proton are its three valence quarks (two up and one down quark) as well as constituents of the gluon field between them, i.e. gluons and quark-antiquark pairs (sea quarks).

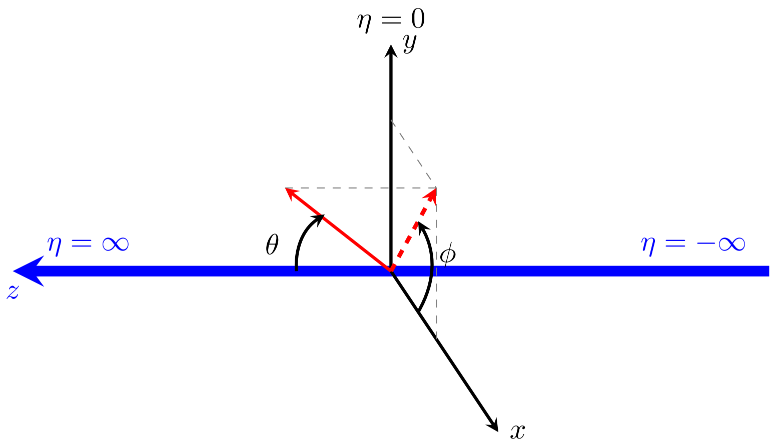

Figure 3.3: Coordinate system of the ATLAS detector, seen from the centre of the LHC ring. Inspired by [33].

The innermost component is a semiconductor pixel detector. It provides high spatial resolution for the measurement of electrically charged particles in three layers as close as possible to the collision point. This enables the identification of short-lived particles like hadrons from b-quarks or τ-leptons [34].
At intermediate radii, the semiconductor tracker (SCT) system contributes to the measurement of impact parameters and interaction vertex positions of charged particles. Both the SCT and the pixel detector cover a pseudorapidity range of $|\eta| < 2.5$ [34].
Finally, the transition radiation tracker (TRT) covers outermost inner detector region. By the use of straw tubes, it provides a large number of tracking points (typically 36) and therefore enables track-following for charged particles up to a pseudorapidity of $|\eta| = 2$ [32].
Since the inner detector is penetrated by a magnetic field, charged particles will leave curved tracks due to the Lorentz force. This allows for the measurement of even more particle properties: by calculating the radius of the curved tracks and the sign of the curvature, momentum and electric charge can be deduced.

The Calorimeters

The calorimeter system which surrounds the inner detector, consists of the inner electromagnetic calorimeter (ECAL) and the outer hadronic calorimeter (HCAL). In the calorimeters, incoming particles deposit their energy through the creation of particle showers as they interact with the calorimeter medium. ECAL and HCAL are sampling calorimeters, hence they consist of alternating layers of absorbing and active material, where the absorbing material should promote the production of showers while the active material is used for measuring the shower's energy. Unlike the inner detector components, the calorimeters are not only divided into barrels and end-caps. Instead, additional forward calorimeter components result in sensitivity in an overall pseudorapidity range of $|\eta| < 4.9$ [32].
In the ECAL, the absorbing material is lead (copper for the forward calorimeter), which promotes the production of electromagnetic cascades through bremsstrahlung and pair production. The material used for measuring the shower is liquid-argon. The ECAL is therefore predominantly used for measuring the energy of electromagnetically interacting particles like electrons or photons [7, 32].
In the HCAL, the absorbing material is steel (copper in the end-caps, tungsten in the forward calorimeter), which promotes interaction between hadrons and the nuclei of the medium. Scintillator (liquid-argon in the end-caps and the forward calorimeter) is used as the active medium. The HCAL is therefore used to measure the energy of hadronic particles [7, 32].

The Muon Spectrometer
The muon spectrometer (MS) forms the outermost part of the ATLAS detector. Since only muons and non-detectable weakly interacting particles like neutrinos are expected to traverse the calorimeters without being stopped, this component of ATLAS is specifically designed to detect muons. Using the toroid magnets surrounding the calorimeter system and additional tracking chambers, namely Monitored Drift Tubes (MDTs) and Cathode-Strip Chambers (CSCs), muons and their properties can be measured. Through the combination of barrel and end-cap components, the MS is sensitive up to pseudorapidities $|\eta|$ of 2.7 [32].

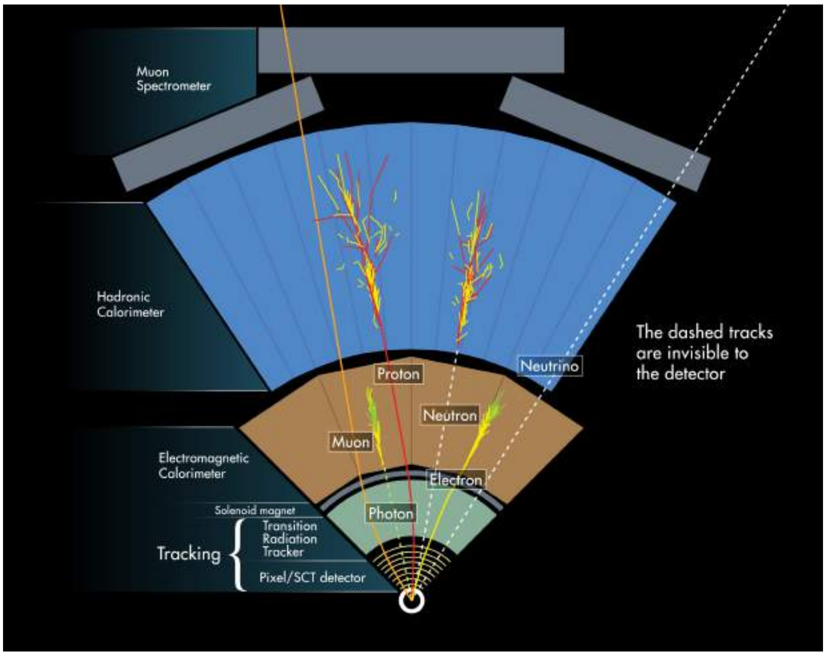

Figure 3.4: Cross-section of the ATLAS detector perpendicular to the z-axis. The white circle in the bottom of the picture marks the beam pipe and one can see how different particles interact with the main components of the detector [35].

3.2.3 Trigger System

Due to limits in present technology, it is not possible to record the data of every collision event. Hence, to reduce the event rate by focusing on 'interesting' events, a trigger system is used. The upgraded trigger system in Run 2 consisted two levels.
The first level trigger (Level-1) uses hardware information, namely from parts of the calorimeter and muon detector, to determine Regions-of-Interest (RoI). This happens with a decision time of 2.5 μs and reduces the event rate from about 30 MHz to 100 kHZ [36].
The high level trigger (HLT) is purely software-based. It runs selection algorithms taking either the RoI or the full event as input. This reduces the event rate from 100 kHz to about 1 kHz with a processing time of 200 ms [36].

Chapter 4

Probing Supersymmetry at the ATLAS Detector

So far, the theoretical background of the SM and SUSY has been established as well as the experiment used to put these theories under scrutiny. In the following, some tools and strategies needed to find evidence of SUSY in the ATLAS detector data will be discussed.
First, the importance and basics of Monte Carlo simulations are explained. Then, definitions used for the reconstruction of physical objects from detector-level data are stated. As a method to save resources in the simulation, truth smearing is introduced which is crucial for large-scale studies like the pMSSM scan. This kind of study will be presented as a broader approach to SUSY searches than traditional simplified models. Finally, the simulated samples of the SM and SUSY processes studied in this work are shown.

4.1 Monte Carlo Simulations

The data recorded by the ATLAS detector contains information about the final states of processes induced by the LHC collisions. In general, this final state information cannot be used to unambiguously determine the underlying physical process. Therefore, virtual simulations of particular physical processes and the ensuing detector response are used to get more insight. With these simulations, it is possible to better understand how one arrives at detector-level data from the original physical interactions. Furthermore, when one is looking for a specific process (e.g. a SUSY process), the so-called signal process, simulations model the expected kinematics of the signal which can then be used to separate it from background processes with a similar signature [37].

Usually, these simulations are done using the Monte Carlo (MC) method. The MC method is based on the generation of pseudo-random numbers according to a given probability distribution. In particle physics, theoretically calculated probabilities for the involved processes are used while the pseudo-random numbers assure the stochastic nature of quantum physics. This enables the virtual generation of multiple events of a given process.

4.1.1 The Simulation Chain

The simulation of a collision event at the LHC should begin with the colliding protons and end with detector-level information about the event, analogous to the real ATLAS data. This process can be divided into two parts: the event generation and the detector simulation.

Event Generation
The first step in the event generation is the simulation of the *hard process* of interest, i.e. the process of highest momentum transfer in the collision event. This is done by calculating the matrix element (ME)[1] of the process in perturbation theory using the parton distribution functions (PDFs) of the incoming protons. The PDFs $pdf(x, Q)$ respect the non-elementary nature of the proton, describing the probability density of the different partons. They depend on the momentum fraction x the parton carries of the overall proton momentum and the energy scale Q of the interaction. The decays of 'resonances', i.e. heavy particles created in the hard process, are viewed as a part of this hard process as well to incorporate e.g. spin correlations in the decays.
The next step is called the *parton shower* (PS) phase. As the partons involved in the process are accelerated, they radiate off gluons. If this happens before the hard process, it is called initial state radiation (ISR) and if the outgoing partons emit gluons, it is called final state radiation (FSR). Since these ISR and FSR gluons possess colour charge themselves, they will radiate off further gluons, triggering a shower of partons. The showers can be simulated as an evolution down from the hard process energy scale to an infrared scale at which confinement has to be respected.
Confinement leads to the *hadronisation* process which cannot be described from first principles thus far, as the strong coupling reaches values where perturbation theory breaks down. Instead, modelling procedures like string fragmentation [38] or cluster fragmentation [39] are used. Some of the hadrons produced in the hadronisation step are unstable and might decay before reaching the final state which is accessible by the detector.
In addition to the already described simulation steps, it is important to consider the remaining partons of the collided protons, which did not result in the hard process, as well. These partons will also trigger a PS and hadronisation, contaminating the products of the hard process. This is also called the *underlying event*.
This completes the event generation part of the simulation. The generated event information at this point is called *truth-level*, *generator-level* or *particle-level* information [40].

Detector Simulation
The generator-level information from the first part of the simulation is then taken as input for the detector simulation. The Geant4 particle simulation toolkit [42] is used to simulate the interaction of the generated particles with the ATLAS detector geometry. Since at the LHC, whole proton bunches are crossed to obtain collisions, one expects to have more proton collisions than the one containing the hard process. These additional interactions are called *pile-up*. Pile-up as well as detector responses from previous collisions and interactions of the protons with the beam gas or upstream accelerator elements can contaminate the signature of the hard process. Therefore, these need to be taken into account in the simulation of the detector response as well [40].
(based on [37, 43, 44])

[1]The ME is directly related to the scattering amplitude mentioned in chapter 2 and gives a measure of the probability that the considered process takes place.

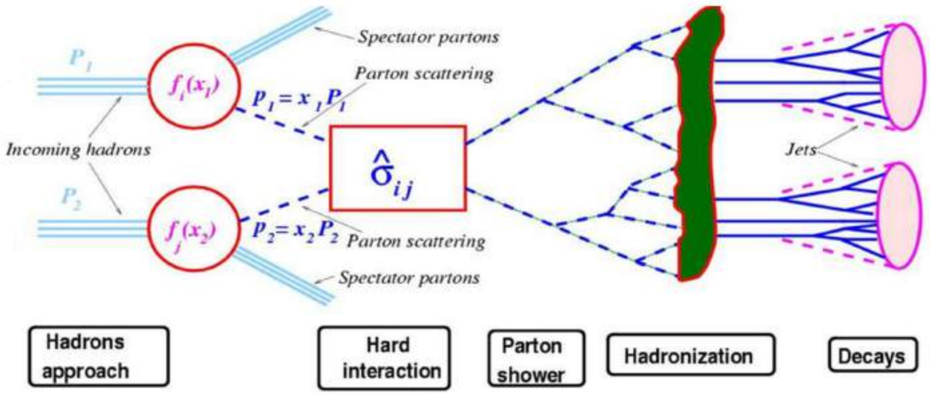

Figure 4.1: Visualisation of a hadron collision and the subsequent processes (from [41]).

4.1.2 Simulation Software

Event Generators

The event generation for the processes studied in this work is divided between two different generators. The generators used to simulate the hard process are MadGraph5_aMC@NLO [45] for the SUSY processes and Powheg (POsitive Weight Hard Event Generator) [46–49] for the $t\bar{t}$ process. Both are then interfaced to Pythia8 [50] for the simulation of PS, hadronisation and underlying event. It should be mentioned that to avoid the double-counting of events, MadGraph5_aMC@NLO uses negative weights which can lead to unphysical negative event yields in some cases [51]. Powheg uses exclusively positive weights and is not affected by this problem. A brief description of the event generation for the SUSY and SM processes follows, the event generator versions used can be found in table 4.1.

For the SUSY processes, the ME is calculated at tree-level in MadGraph5_aMC@NLO with up to two additional partons. PS, hadronisation and underlying event was simulated using Pythia8 with the A14 [52] tune. For the PDFs, the NNPDF23LO set [53] was used and the ME-PS matching[2] was done using the CKKW-L [54, 55] prescription. The matching scale was set to a quarter of the pair produced SUSY particle mass. In the case of ttStau, MadSpin [56] is employed for the decays of the SUSY particles to preserve spin correlations and finite-width effects [27].

The $t\bar{t}$ hard process is simulated with Powheg-Box and the NNPDF3.0NLO [57] set of PDFs. The events are then interfaced to Pythia8 for the modelling of PS, hadronisation and underlying event with the NNPDF23LO set of PDFs and A14 tune [27].

process	ME Generator	PS generator
$t\bar{t}$	Powheg-Box v2	Pythia 8.230
SqSq	MadGraph5_aMC@NLO 2.6.2	Pythia 8.235
GoGo	MadGraph5_aMC@NLO 2.6.2	Pythia 8.212
direct stau	MadGraph5_aMC@NLO 2.6.1 - 2.6.2	Pythia 8.230
C1C1	MadGraph5_aMC@NLO 2.6.2	Pythia 8.230
ttStau	MadGraph5_aMC@NLO 2.6.2	Pythia 8.212

Table 4.1: Event generator versions of the different processes.

[2]This matching is needed to consistently combine tree-level ME calculations and parton showering.

Decays of heavy flavour hadrons, i.e. b- and c-hadrons, are modelled in EvtGen v.1.6.0 in every process.

Detector Simulation
The ATLAS detector simulation for every process was done in Geant4. However, while for the SM process the full detector modelling was used, for the SUSY processes a fast simulation was employed which relies on a parametrised response of the calorimeters[3] called Atlfast-II or AF-II [58].
Pileup is modelled through the overlay of simulated inelastic collision events generated with Pythia8.186 and the NNPDF23LO set of PDFs.

4.2 Object definitions

After the detector simulation, the simulated data contains the same kind of information as the real detector does. Therefore, as for the real data, it is now necessary to reconstruct physical objects — like leptons or jets — from this detector-level information. In the following, the definitions needed for these reconstructed objects will be presented. These objects are then called *reconstruction-level* objects.
Furthermore, it is necessary to point out how physical objects can be defined from the generator-level information. These are then called *truth-level* objects.

4.2.1 Reconstruction-Level Objects

Primary Vertex
First, it is important to define the primary vertex, as it is the expected location of the hard process in the detector and only events having one shall be considered. A primary vertex is required to have at least two associated tracks with $p_T > 500$ MeV, $|\eta| < 2.5$ and a clean interaction with the inner detector. If multiple vertices pass these criteria, the vertex with the highest sum of squared associated track momenta $\sum {p_T}^2$ is considered the primary vertex [59].

Electrons
Basically, electrons are reconstructed by matching clusters of energy deposits in the ECAL and HCAL to tracks in the inner detector. The reconstruction algorithm also involves intermediate steps for corrections and energy calibrations. This reconstruction is not perfect however, so depending on the needed purity of the electrons, one can apply further quality criteria [60] which will be explained in the following.
Electron identification (ID) is based on multiple variables which should discriminate the desired signal, i.e. prompt[4] isolated electrons, from background objects, i.e. hadronic jets, converted photons[5] and electrons from heavy-flavour hadron decays. These discriminating variables are then combined to a single likelihood discriminant which is then used to define the electron ID working points (WP): the loose WP introduces a requirement on the likelihood discriminant so that the signal efficiency, i.e. what percentage of the signal is left after the requirement, is at about 93%. The medium/tight WPs have a background rejection approximately 2.0/3.5 times higher, but at the cost of lower signal efficiencies at about 88% and 80%, respectively. Signal efficiency and background rejection might vary for different values

[3] The calorimeter simulation is responsible for nearly 80% of the full simulation time [40].
[4] A prompt electron is not the product of a B-hadron decay.
[5] A converted photon decayed into an electron positron pair through interaction with the detector medium.

of the electron transverse energy, however [60]. In this work, electrons are required to have the *medium* WP.
In addition to the electron identification, cuts on the impact parameters are applied to assure that the electron originates from the primary vertex. The requirements are $|\frac{d_0}{\sigma(d_0)}| < 5$ where d_0 is the transverse distance to the beam axis and $\sigma(d_0)$ its resolution and $|\Delta z_0 \sin\theta| < 0.5$ mm where Δz_0 is the z-distance to the primary vertex and θ is defined as in figure 3.3.
Another criterion is the electron isolation. Two variables can be defined which indicate the activity either near the electron track in the inner detector or near the electron's energy cluster in the calorimeters. The momentum of background tracks in a $\Delta R < \frac{\mathrm{XX}}{100}$ cone around the electron track, $p_{\mathrm{T}}^{\mathrm{coneXX}}$, is used for the track isolation. For the energy cluster isolation, a similar variable, $\mathrm{E}_{\mathrm{T}}^{\mathrm{coneXX}}$, is defined for the transverse energy around the cluster. Again, WPs are defined for different requirements on these two variables. Often, the variable $p_{\mathrm{T}}^{\mathrm{varconeXX}}$ is used instead of $p_{\mathrm{T}}^{\mathrm{coneXX}}$, where the cone is taken to be shrinking with increasing electron p_{T} [60]. In this work, electrons have the *FCTight* WP and the *FCHighPtCaloOnly* WP for high p_{T}.
Finally, the reconstructed electrons are required to have p_{T}> 17 GeV and $|\eta| < 2.47$ (as this is the $|\eta|$-range of the inner detector).

Muons

Muon reconstruction depends mainly on the inner detector and the MS. First, tracks are reconstructed independently in the two detector components. Depending on how the muons interacted with the different subdetectors, muons are then classified by the technique that was used for the reconstruction. The corresponding classes are: combined muons (tracks from inner detector and MS are matched), segment-tagged muons (track from the inner detector only matched to one MS segment), calorimeter-tagged muons ($|\eta| < 0.1$) and extrapolated muons ($2.5 < |\eta| < 2.7$). Overlaps between these different types have to be resolved afterwards [61]. Similar quality criteria as for the electrons are applied to assure adequate purity. As in the case of electrons, muons also have ID WPs. These are however based on different discriminating variables. For muons the focus of the ID discrimination is on variables that ensure a good compatibility between the momentum measured in the inner detector and the MS to suppress background from hadron decays. Hence, combined muons are preferred in the ID selection. Again, loose, medium and tight WPs are available. For muons, an additional High-p_{T} WP exists to maximise momentum resolution for p_{T}> 100 GeV as well as a very loose WP for even higher signal efficiencies [61]. For this work, the muons are required to satisfy the *loose* WP.
As for the electrons, cuts are applied to the muons impact parameters. The requirements are $|\frac{d_0}{\sigma(d_0)}| < 3$ and $|\Delta z_0 \sin\theta| < 0.5$.
The isolation WPs for muons use the same variables as the electron WPs — even if the requirements differ slightly to achieve the same signal efficiencies. Muons studied in this thesis are required to satisfy the *FCTight* WP.
Further, cuts on p_{T}> 14 GeV and $|\eta| < 2.7$ (as this is the $|\eta|$-range of the MS) of the reconstructed muons are applied.

Jets

Jets are showers of hadrons originating from quarks, gluons or hadronically decaying tau leptons. They usually extend in a conic shape through the detector geometry.
Jets considered in this work are reconstructed from the detector information in two ways. Traditionally, they are built from three-dimensional topologically connected calorimeter cell clusters (*topo-clusters*) in which energy has been deposited [62]. These topo-clusters are cal-

ibrated at the electromagnetic (EM) energy scale[6] and then used as input to the anti-k_t jet algorithm [63] with a distance parameter $R = 0.4$ to reconstruct the jets. The anti-k_t algorithm targets hard particles, i.e. constituents of the hadron shower with high momentum, and clusters softer particles within a cone with distance parameter R around this hard particle to a jet. A cone with distance parameter R will include any soft particle that has an angular distance $\Delta R < R$ to the hard particle in the centre of the cone. If the cones around two hard particles i and j share an overlapping region, i.e. if their angular distance Δ_{ij} is $\Delta_{ij} < 2R$, the soft particles within the overlapping region will be preferably assigned to the hard particle with higher momentum [63]. The resulting, so-called *EMTopo* jets are then subject to the jet energy scale (JES) calibration which improves η-resolution by correcting the jet so that it points back to the primary vertex, calibrates the reconstructed JES to the energy scale of truth-level jets and includes corrections against pileup effects [64]. Further suppression of pileup is achieved using the jet vertex tagging (JVT) algorithm [65] which uses a likelihood discriminant to tag jets coming from the primary vertex [66]. EMTopo jets in this study are required to have the *medium* JVT WP.
While the EMTopo jets are built from calorimeter topo-clusters only and track information is only used in the calibration, the second jet class, *PFlow* jets, combine measurements from the inner detector and calorimeter for the whole reconstruction. The PFlow algorithm [67] subtracts energy deposits associated with charged tracks from the jets' topo-clusters in the calorimeter to get topo-clusters originating from neutral particles only. The charged particles then enter through their tracks. The jet reconstruction is then performed on these *particle flow objects*, i.e. the neutral particle topo-clusters and the charged particle tracks, using the anti-k_t algorithm with a distance parameter $R = 0.4$ [66]. As for the EMTopo jets, the JES calibration procedure is applied, but a *tight* JVT WP is normally required.
Both types of jets are also required to fulfil p_{T}> 20 GeV and $|\eta| < 2.8$. If not stated otherwise, EMTopo jets will be used in the following.

Tau Leptons
With a mean life time of $\tau_\tau = (290.3 \pm 0.5)$ fs [4], the tau lepton will not be directly detected in the ATLAS detector. Instead, it will decay either leptonically, i.e. $(\tau \to l\nu_l\nu_\tau, l = e, \mu)$ with a BR of about 35%, or hadronically, i.e. ($\tau \to$ hadrons ν_τ) with a BR of about 65%, therefore, only these decay products will be recorded by the detector. Leptonically decaying tau leptons will be reconstructed as either electrons or muons. However, a the decay products of a hadronically decaying tau lepton can actually be reconstructed as a tau lepton — at least the visible part, i.e. the hadrons without the tau neutrino. Hence, when tau leptons are mentioned in the following, hadronic ones are implied unless stated otherwise. These tau leptons are then categorized depending on the number of charged hadrons, i.e. pions $\pi^\pm$ and kaons $K^\pm$, they decay into: about 77.2% decay into one charged pion/kaon, labelled as *one-prong*, 22.5% decay into three charged hadrons, labelled *three-prong* and 0.15% decay into five charged hadrons, labelled *five-prong*[7] [4]. Additionally, tau decays contain a varying number of neutral hadrons (mainly π^0). The BR for one- and three-prong taus with a different number of accompanying neutral hadrons is shown in table 4.2.

The reconstruction of taus uses anti-k_t jets with $R = 0.4$ which were built from topo-clusters in the calorimeter. To actually seed a tau candidate, the jet needs to fulfil the requirements $p_{\mathrm{T}} > 10$ GeV and $|\eta| < 2.5$ [69]. The tau vertex is defined as the vertex with the largest fraction of momentum from tracks associated ($\Delta R < 0.2$) to the jet [70]. With this vertex as

[6]This ensures a correct energy reconstruction for electrons and photons, but does not include corrections for signal loss in the HCAL.
[7]Higher prongness is possible as well — as can be seen from adding up the fractions —, but very unlikely and not relevant in the further discussion.

hadronic tau decay mode	BR w.r.t. hadronic taus [%]
$h^{\pm}$	17.7
$h^{\pm}1\pi^0$	40.0
$h^{\pm} \geq 2\pi^0$	16.7
$3h^{\pm}$	14.6
$3h^{\pm}1\pi^0$	7.1
$3h^{\pm} \geq 2\pi^0$	0.8

Table 4.2: BRs (with respect to the hadronic decay width) of the dominant hadronic decay modes. $h^{\pm}$ denotes either charged pions or kaons. As neutrinos are not part of the reconstructible visible component of the tau decay, they are omitted. Inspired by [68], based on the values from [4].

origin, the tau direction (η, ϕ) is calculated using the topo-clusters within $\Delta R < 0.2$ of the jet barycentre. The number of charged tracks associated to the jet corresponds to the tau's prongness. The mass is defined as zero. To get the energy of the tau candidate, an energy calibration is applied to correct the measured deposited energy to the predicted truth-level energy of the decay products. The individual charged hadrons and π^0 are reconstructed using the Tau Particle Flow (TPF) method[8] [71] which improves the energy and directional resolution at low p_{T} and allows for the identification of the decay mode.
For tau leptons, the ID algorithm is designed to reject background from quark- and gluon-initiated jets. Traditionally, the tau ID is based on boosted decision trees (BDTs), trained separately for one- and three-track taus. These BDTs use properties of the calorimeter clusters, tracks and individual reconstructed hadrons to discriminate between tau jets and background jets. Loose, medium and tight ID WPs are defined. The target signal efficiencies are defined differently for one- and three-track taus and can be found in table 4.3 [70]. Recently, an alternative identification algorithm using recurrent neural networks (RNN) has been introduced. This algorithm uses similar input variables as the BDT-based approach, but achieves higher background rejection by a factor of 1.4 to 3.6 [72] for the same signal efficiency (see figure 4.2). Here, the defined WPs are very loose, loose, medium and tight. The target signal efficiencies can be found in table 4.3 as well. In this work, the *medium RNN* WP is used if not explicitly stated otherwise.

ID WP	BDT/RNN signal efficiency [%]	
	1-track	3-track
Tight	60	45
Medium	75	60
Loose	85	75
Very Loose	95	95

Table 4.3: Target signal efficiencies of the different WPs for the BDT-based and RNN-based ID algorithms. Based on the values from [72].

In addition to the discrimination against non-tau jets through the ID algorithms, a BDT-based discrimination against electrons misidentified as tau candidates is used. This BDT uses variables targeting e.g. transition radiation or energy deposited in the ECAL versus energy deposited in the HCAL, which yield good discrimination between taus and electrons. Three WPs are defined: loose, medium and tight, chosen to have signal efficiencies of 0.95, 0.85 and

[8]This method is based on a method similar to the one described for the reconstruction of PFlow jets.

0.75, respectively [69]. In this thesis, the *medium* WP is chosen.
As the ID algorithms are only defined for one- and three-prong taus, only these are used in this thesis and they are required to have $p_{\mathrm{T}}>$ 20 GeV and $|\eta| < 2.5$.

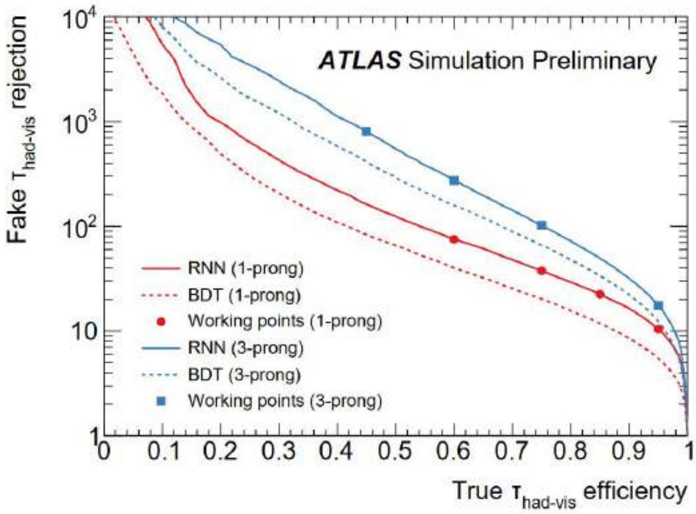

Figure 4.2: The rejection strength of the BDT and RNN algorithms for one and three prong depending on the target signal efficiency [72].

Overlap Removal
In most analyses, overlap removal is used to resolve ambiguities in the reconstruction of different physical objects. This is done by removing one of the objects if two different objects have a small angular distance. In this study, overlap removal is not required since the focus lies on the reconstruction procedure itself.

Trigger
In a usual analysis, simulated events on reconstruction-level need to fulfil a trigger selection since the events at the ATLAS detector need to fulfil at least one trigger condition to be recorded as well. There are multiple HLT trigger selections to choose from depending on the process one is trying to study. In this work however, no trigger selection is applied as the focus lies on the detector simulation and the reconstruction of truth-level objects in general. Therefore, an analysis specific trigger selection is not of interest here.

4.2.2 Truth-Level Objects

Truth Electrons/Muons
In the truth record, i.e. the generator-level information, electrons/muons are required to be stable to be labelled electrons/muons. This study looks at dressed electrons/muons, i.e. photons radiated off these charged particles are considered by adding the photons in a cone with $R = 0.1$ around the lepton using the anti-k_t algorithm [73]. Therefore, the visible[9] dressed 4-momentum of these particles will be used. Requirements on p_{T} and η are the same as for the respective reconstruction-level leptons while ID, isolation and impact parameter criteria

[9]The visible 4-momentum does not include the momentum of eventual non-interacting decay products. For the electron/muon, this is of course redundant as they are required to be stable, but for the later described truth tau lepton, this distinction is important.

are not available on truth-level.

Truth Taus
In this thesis, truth taus are required to be hadronically decaying taus from the generator-level data and as for electrons and muons, the visible dressed 4-momentum is used (hence, tau neutrinos from the decay are neglected). The dressing for tau leptons is done with a distance parameter $R = 0.2$, though. The number of charged and neutral decay products is accessible. Truth-level taus are required to fulfil the same p_{T} and η cuts as the reconstruction-level taus, ID and electron discrimination is however not available.

Truth Jets
In this study, so-called *TruthDressedWZJets* are used. These are defined by clustering all stable particles — except electrons and muons from W, Z, higgs or τ decays (including their dressing photons) and photons from higgs decays — using the anti-k_t algorithm with $R = 0.4$ and $p_{\mathrm{T}}>$ 20 GeV [74]. Truth jets also include jets resulting from the hadronic tau decays. However, while the truth tau properties are defined from the tau's true decay products, the truth tau-jet is defined using the anti-k_t algorithm, allowing for potential differences between truth tau and truth tau-jet. Labels which classify the truth jets according to their origin by geometrically matching[10] the jet to truth-level particles like taus or b-quarks are available. As for reconstruction-level jets, a cut on $|\eta| < 2.8$ is required.

Truth $E_{\mathrm{T}}^{\mathrm{miss}}$
The truth-level $E_{\mathrm{T}}^{\mathrm{miss}}$ includes the transverse momenta of every non-interacting particle like e.g. neutrinos, neutralinos, etc.

4.3 Truth Smearing

The full detector simulation and reconstruction of events is very demanding with respect to CPU resources. Consequently, there are multiple methods which aim to speed up the process, e.g. the AF-II simulation which has already been mentioned as it has been used for the simulation of the SUSY processes in this study. In some large-scale studies which require a huge amount of events to be generated, one even goes further than just speeding up the simulation: the detector simulation is skipped entirely, therefore basically relying on only truth-level objects. In order to still maintain a good agreement to the reconstruction-level objects, a method called *truth smearing* is used. Truth smearing applies functions on the truth-level objects which make them resemble the reconstruction-level objects without actually doing the detector simulation and reconstruction. These functions implement e.g. parametrisations of reconstruction and ID efficiencies and energy resolution effects. As an example for the realisation of a truth smearing, the main functions of the UpgradePerformanceFunctions (for the release 21.2.100, [75]) are presented in the following. This framework currently includes smearing functions for electrons, muons, taus, jets, photons and missing transverse energy.

Energy Smearing
A function that has to be applied on nearly every truth-level object is the energy smearing. This function considers the finite energy resolution of the detector by adding an energy correction to the truth-level energy. The energy correction is usually generated according to a gaussian distribution around 0 with a standard deviation equalling the detector resolution. The detector resolution, in turn, depends on the p_{T} and η of the object as these properties

[10] The matching implies that these labels can be subject to misidentification.

would influence the detector response. For example, the detector resolution might be worse in regions of η corresponding to a transition between barrel and end-cap of a detector component.

Reconstruction and ID efficiency
The efficiency function is also needed for most objects. It incorporates the inefficiencies in the reconstruction algorithms and the signal efficiency of the ID WP selection, referred to as the ID efficiency in the following, of the respective reconstruction-level object. The efficiency function is usually parametrised in p_{T} and η.

Fake Rate
Some objects have a non-zero probability to be misidentified in the reconstruction. The fake rate function is responsible for adding objects of, say, type A to the objects of type B at a certain rate if type A objects have been observed to be misidentified as type B at this rate. The fake rate is generally dependent on p_{T} and η.

4.4 Simplified Models and the pMSSM Scan

Now that the basics of the simulation and reconstruction procedure at the ATLAS detector have been introduced, one can look into strategies employed to search for evidence of SUSY. First, the procedure of the statistical data analysis will be outlined. This involves the description of the conditions which need to be met for either a discovery of SUSY particles or the exclusion of a part of the SUSY parameter space. Then, an example will be given how this plays out with a simplified model. Finally, the pMSSM scan is shown as a complementary approach to the simplified models.

4.4.1 Discovery and Exclusion

In a search for SUSY, one deals with two kinds of processes: the *signal* processes, i.e. SUSY processes which one wishes to observe and the *background* processes, i.e. SM processes which have a similar or even the same signature in the detector. It is the goal of an analysis to find kinematic observables with the help of the simulated data which can be used to discriminate between signal and background.

Regions
Such discriminating variables can be used to define a signal region (SR) in which a statistical analysis would be sensitive to the signal, i.e. a kinematic region which is expected to contain a significant number of events of the desired process. This region is hence used to look for potential SUSY processes.
In addition to SRs, background-dominated, disjoint control regions (CRs) are defined in a usual SUSY search. These can be used to compare the event predictions of the MC simulation to real data, normally by employing a certain fitting procedure. From this comparison, a scaling of the simulated event count is derived to calculate the expected number of events from background processes in the real data.
Before employing this scaling in the SR, it first needs to be validated. This happens in dedicated, disjoint validation regions (VRs) which typically lie kinematically between CRs and SRs. Finally, the simulated event counts in the SRs are normalised using the scaling factors from the CRs, hence making a meaningful comparison of signal and background expectation from the MC simulation and the actual data in the SR possible.

Significance
To conduct the statistical analysis in the SR, the notion of statistical significance is crucial. The statistical significance gives a measure from which to decide if a certain hypothesis H_0 - or null hypothesis - should be rejected in favour of another hypothesis H_1. To achieve this, it is based on the p-value p, i.e. the probability of observing data of equal or greater incompatibility with the hypothesis H_0 one is trying to reject. Therefore, the lower the p-value, the stronger the argument for rejecting the null hypothesis and favouring the alternative hypothesis H_1. The statistical significance Z is now the number of standard deviations of a gaussian distribution one needs to get an upper tail probability of p. Hence:

$$Z = \Phi^{-1}(1 - p) \tag{4.1}$$

Where Φ^{-1} is the inverse cumulative distribution of the standard gaussian distribution. A higher significance thus represents a lower p-value and a stronger argument for rejecting the null hypothesis. The relationship between the significance Z and the p-value p is illustrated in figure 4.3.

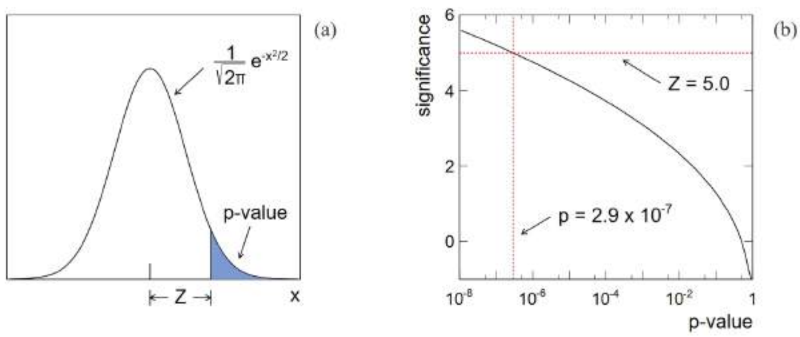

Figure 4.3: (a) Illustration of the definition of the statistical significance Z and the p-value p, (b) the functional relation between significance and p-value (from [76]).

Discovery
When a statistical analysis is conducted in the SR in order to discover new physics which is represented by signal events, one defines the hypothesises as follows: the null hypothesis H_0 is the background-only hypothesis, i.e. that the events observed in the SR are due to background processes only (b) and the alternative hypothesis H_1 represents the hypothesis that the observed events come from background as well as the sought after signal ($s + b$). In order to proclaim the discovery of this desired signal and reject H_0 in favour of H_1, at least a significance of $Z = 5$ is required. This corresponds to a p-value of $p = 2.87 \times 10^{-7}$.
However, if this requirement is not met, the background-only hypothesis cannot be rejected and instead, exclusion limits are drawn.

Exclusion Limits
To draw exclusion limits, one needs to aim to reject a different null hypothesis. In this case H_0 is instead the hypothesis that the signal region contains background and a signal predicted by a certain SUSY model while H_1 is the background-only hypothesis. The exclusion limits are then usually set at 95% confidence level (CL), i.e. H_0 is rejected for p-values $p_{s+b} < 5\%$ corresponding to a significance above $Z \simeq 1.64$. This way, parts of the investigated SUSY parameter space can be excluded for future searches.
Especially in cases where the sensitivity is low, i.e. where the expected signal is very faint

compared to the background, the CL is usually based on the CL_s prescription. Instead of the p-value p_{s+b}, this method uses the ratio [77]

$$CL_s = \frac{p_{s+b}}{1 - p_b} \tag{4.2}$$

to set the limit, where the meaning of $(1 - p_b)$ and the advantages in using the CL_s prescription will become clear in the following discussion of test statistics.

Apart from a model-dependent exclusion as described above, it is also possible to derive a model-independent exclusion limit. This limit is often given as the maximum number of signal events N^{95}_{max} for which the signal plus background hypothesis cannot be rejected at 95% CL.

Test Statistics

In order to actually calculate the p-value p for a certain hypothesis, one has to define a test statistic q which measures the compatibility of the observation with the hypothesis. In a search for physics beyond the SM, the test statistic depends on the signal strength μ and a set of nuisance parameters $\boldsymbol{\theta}$. μ is defined with respect to a certain reference model that predicts s_i signal events in the bin i (e.g. a SR or CR). Hence, for an unspecified signal model, one expects to find μs_i signal events in the bin i and the signal strength can be seen as a measure of the total SUSY cross section of the considered model relative to the reference signal model. The nuisance parameters $\boldsymbol{\theta}$ include parameters not fixed by the SUSY model, e.g. the expected number of background events b_i in the bin i (therefore, one expects $\mu s_i + b_i$ events in the bin i) and statistical and systematic uncertainties of the expected number of events in the different bins. Usually, M auxiliary measurements help constrain these nuisance parameters.

A common choice of the test statistic q_μ (the index μ indicates its dependence on the hypothesis with a signal strength μ) involves the *profile likelihood ratio*. It can be constructed using the likelihood $L(\mu, \boldsymbol{\theta})$, which is defined as the product of the probability distributions of both the measured events n_i in the considered bins $i = 1, ..., N$ and the auxiliary measurements m_k with $k = 1, ..., M$:

$$L(\mu, \boldsymbol{\theta}) = \prod_{i=1}^{N} \frac{(\mu s_i(\boldsymbol{\theta}) + b_i(\boldsymbol{\theta}))^{n_i}}{n_i!} e^{-(\mu s_i(\boldsymbol{\theta}) + b_i(\boldsymbol{\theta}))} \prod_{k=1}^{M} c_k(m_k, \boldsymbol{\theta}) \tag{4.3}$$

The probability distributions of the n_i are of the form of a poisson distribution as in the bins, counting experiments are performed, while the distributions corresponding to the auxiliary measurements are usually either of poissonian or gaussian shape. The profile likelihood ratio $\lambda(\mu)$ is defined as

$$\lambda(\mu) = \frac{L(\mu, \hat{\hat{\boldsymbol{\theta}}})}{L(\hat{\mu}, \hat{\boldsymbol{\theta}})}, \tag{4.4}$$

where $\hat{\hat{\boldsymbol{\theta}}}$ describes the values of the nuisance parameters that maximise the likelihood L for the signal strength μ of the specified SUSY model and $\hat{\mu}$ and $\hat{\boldsymbol{\theta}}$ are the values that maximise the given likelihood in general. Hence, the nuisance parameters are essentially fixed and $\lambda(\mu)$ only depends on the signal strength. This ratio will get closer to 1 the more the measurement and the expectation from the hypothesis are in agreement in the bins. From the profile likelihood ratio $\lambda(\mu)$, one can finally define the test statistic for a SUSY model with signal strength $\mu > 0$ being the null hypothesis $(s + b)$ as:

$$q_\mu = \begin{cases} -2 \ln \lambda(\mu) & \hat{\mu} \leq \mu \\ 0 & \hat{\mu} > \mu \end{cases} \tag{4.5}$$

This test statistic will be 0 for maximum compatibility between measurement and expectation and increase in value for less compatible observations. As in the $s + b$ case the goal is to find exclusion limits in the SUSY model space which correspond to upper limits on the signal strength, observations with an event number exceeding the expected value should yield the best possible agreement. Therefore, the discrimination into two cases in equation (4.5) is necessary.
For the background-only null hypothesis, the test statistic q_0 is defined slightly different:

$$q_0 = \begin{cases} -2\ln\lambda(0) & \hat{\mu} \geq 0 \\ 0 & \hat{\mu} < 0 \end{cases} \tag{4.6}$$

Here, the discrimination into two cases is necessary as measurements yielding a smaller number of events than expected with the background-only hypothesis should yield maximum compatibility[11].

The test statistics can now be used to obtain p-values for an observation with respect to a certain hypothesis. When one is trying to reject the background-only hypothesis (discovery), the p-value p_0 is defined as:

$$p_0 = \int_{q_{0,\mathrm{obs}}}^{\infty} f(q_0|0)dq_0 \tag{4.7}$$

Here, $q_{0,\mathrm{obs}}$ denotes the test statistic q_0 corresponding to the observed event counts and $f(q_0|0)$ denotes the probability density function (pdf) of q_0 when the background-only hypothesis is assumed to be true. $f(q_0|0)$ can be derived either by conducting background-only MC pseudo-experiments and calculating q_0 for each experiment or through asymptotic formulae described in detail in [76].
The p-value p_{s+b}, relevant for rejecting the hypothesis of having a signal strength μ and therefore deriving exclusion limits in the SUSY parameter space, is defined as:

$$p_{s+b} = p_\mu = \int_{q_{\mu,\mathrm{obs}}}^{\infty} f(q_\mu|\mu)dq_\mu \tag{4.8}$$

Here, $q_{\mu,\mathrm{obs}}$ denotes the test statistic q_μ corresponding to the observed event counts and $f(q_\mu|\mu)$ denotes the pdf of q_μ when the hypothesis of having a signal strength μ is assumed to be true. The pdf in this case could be derived with MC pseudo-experiments assuming a signal strength μ and calculating q_μ or again through asymptotic formulae which are described in [76].
However, in cases of low sensitivity, the rejection of hypotheses with p_{s+b} can be misleading. If one is not sensitive to a certain $s+b$ hypothesis, i.e. if the signal yield is very small relative to the background yield, the hypothesis should not be rejected as the experiment can't deliver the necessary evidence. But in such a case, p_{s+b} would give very small values, indicating the rejection of the hypothesis. In order to avoid this problem and consider the sensitivity, the already mentioned CL_s prescription is used. It takes the quotient of p_{s+b} and $1 - p_b$ (see equation (4.2)), where $1 - p_b$ is defined as:

$$1 - p_b = \int_{q_{\mu,\mathrm{obs}}}^{\infty} f(q_\mu|0)dq_\mu = 1 - \int_{-\infty}^{q_{\mu,\mathrm{obs}}} f(q_\mu|0)dq_\mu \tag{4.9}$$

Here, $f(q_\mu|0)$ is again the pdf of q_μ, but this time it is derived under the assumption that the background-only hypothesis is true. $f(q_\mu|0)$ can also be calculated using MC pseudo-experiments or the asymptotic formulae in [76]. If the signal yield is very faint in comparison

[11] One has to keep in mind that less compatibility would indicate the alternative hypothesis, i.e. the existence of signal events. This is obviously not the case if the number of measured events lies below the expected number of background events.

to the background yield, $f(q_\mu|0)$ and $f(q_\mu|\mu)$ should be nearly identical and the CL_s should hence be close to one, i.e. far from indicating rejection.
(based on [76, 78–80])

4.4.2 Simplified Models

The majority of SUSY searches are based on simplified models. These models fix the SUSY parameters and make assumptions so that only one SUSY process will have an observable cross section and only a limited amount of parameters can be varied in the search. BRs and decay modes are normally fixed as well to ensure a specific signature from which to craft a suitable signal region. Examples for this can be found in section 2.3, where a certain simplified model was assumed in each case in order to investigate solely the respective process with two free parameters. In particular, the search for the direct stau process [24] shall be presented here in more detail.
The direct stau process is shown at tree level in figure 2.7 and in section 2.3, the main assumptions of the simplified model used in this search were presented. The model was chosen so that tau slepons will be the only sparticles to be produced at a meaningful rate and that the decay to tau leptons and neutralinos has a 100% BR. In the current direct stau analysis [24], two signal regions were developed for the case that both tau leptons decay hadronically (HadHad). In figure 4.4, the exclusion limits derived from the statistical analysis of the combination of these signal regions is shown. As only the mass of the stau and the neutralino were left as free parameters, the model dependent exclusion limit takes the form of a 2-dimensional contour. Additionally, the analysis placed a model-independent upper limit on the visible cross section of a hypothetical signal process for each signal region.

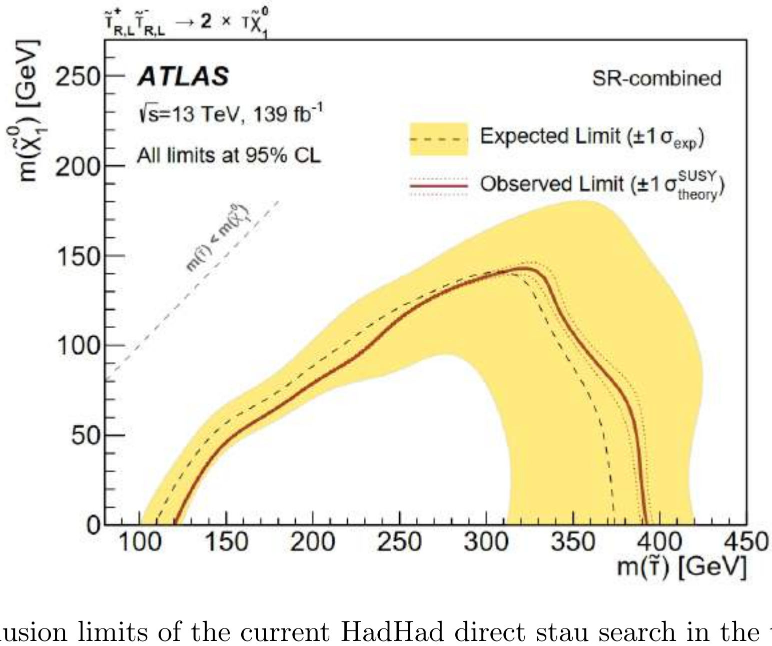

Figure 4.4: Exclusion limits of the current HadHad direct stau search in the two free parameters of the simplified model for the combination of the two signal regions (from [24]).

Simplified models are very useful. They provide the possibility to investigate slices of a complex parameter space by simply analysing the signature of a small set of processes. Therefore, they help identify approximate boundaries of sensitivity for specific process topologies [81]. Also, the model-independent exclusion limits can be used to constrain more generalised models as well.

However, while it may seem from figure 4.4 that stau masses up to ~ 400 GeV can be excluded for neutralinos with low masses, it is important to keep in mind that these exclusion limits are only drawn assuming specific simplified models. A more complex choice of SUSY parameters might lead to non-trivial BRs and interferences with other SUSY processes. This, in turn, might have an impact on the model-dependent exclusion limits.

4.4.3 The pMSSM Scan

A more comprehensive approach to the analysis of SUSY models compared to simplified models is the pMSSM scan. As the name suggests, its goal is a thorough investigation of the 19 dimensional parameter space of the pMSSM. In contrast, most simplified models were only able to investigate a 2 dimensional SUSY parameter space. Still, the sensitivity achieved with the signal regions of simplified model analyses and the resulting model independent exclusion limits are elementary to the pMSSM scan in order to achieve exclusion limits in the pMSSM parameter space. Such a scan has already been conducted for the ATLAS run 1 data [82], for the run 2 data, the procedure behind the scan has been streamlined and consists of the following steps [83]:

1. **Model Generation**: In the first step, pMSSM models have to be generated. These models are based on a random set of values for each parameter where each value was generated according to a flat prior in a pre-defined range. Then, from these parameter values, the SUSY particle spectrum and their individual decay widths are calculated.
2. **Model Removal**: In the next step, models containing unphysical particles like tachyons as well as models which do not satisfy experimental constraints on certain observables like the DM relic density are removed and not further studied.
3. **Cross Section Calculation**: Then, cross sections for the different possible SUSY processes are calculated. Models which contain only processes with a too small cross section are not further processed as it is assumed they can't be excluded with the current sensitivity anyway.
4. **Event Generation**: With the cross sections calculated, events of the different SUSY processes are generated in an amount corresponding to the individual cross section. For the run 2 pMSSM scan, a luminosity of $L = 139$ fb^{-1} is assumed usually.
5. **(Smeared) Truth Evaluation**: Then, signal regions derived from previous simplified model analyses are used to evaluate if the generated models can be excluded at 95% CL or not. In order to estimate the CL, the CL_s value is calculated with the number of events from the pMSSM model as signal, the background estimate and its error from the respective analysis and the observed number of data events in the signal region. It is important to note that the signal event count in the signal regions is evaluated at (smeared) truth-level since a full detector simulation would not be feasible in a large-scale study like this.
6. **Pick uncertain Models**: The (smeared) truth-level number of expected signal events in the signal regions is only a rough estimate as no detector level simulation is involved. Therefore, models which are very close to the 95% CL threshold are picked for a further AF-II detector level simulation to ensure a correct decision on the exclusion.
7. **Fast Detector Simulation**: The generator-level events of the models picked in the previous step are then subject to the AF-II simulation and subsequent reconstruction of physical objects.

8. **Reconstruction-level Evaluation**: For these unclear models, the exclusion is finally evaluated on reconstruction-level.

In figure 4.5, a resulting plot from the run 1 pMSSM scan is shown as an example. The exclusion rate of pMSSM models in bins of the 2 dimensional parameter space of gluino and neutralino mass is indicated by the colour scale on the z-axis. This plot additionally shows the exclusion limit at 95% CL derived by the analysis at the time of the simplified model focusing on the pair production of gluinos with a subsequent $\tilde{g} \to qq\tilde{\chi}_1^0$ decay [84]. The plot shows a good agreement between the simplified model exclusion limit and the exclusion rate of pMSSM models from the run 1 scan which means that in this case, the simplified model was able to capture the main pMSSM phenomenology [82]. However, it also highlights regions where the simplified model analysis under- or overestimated the sensitivity.

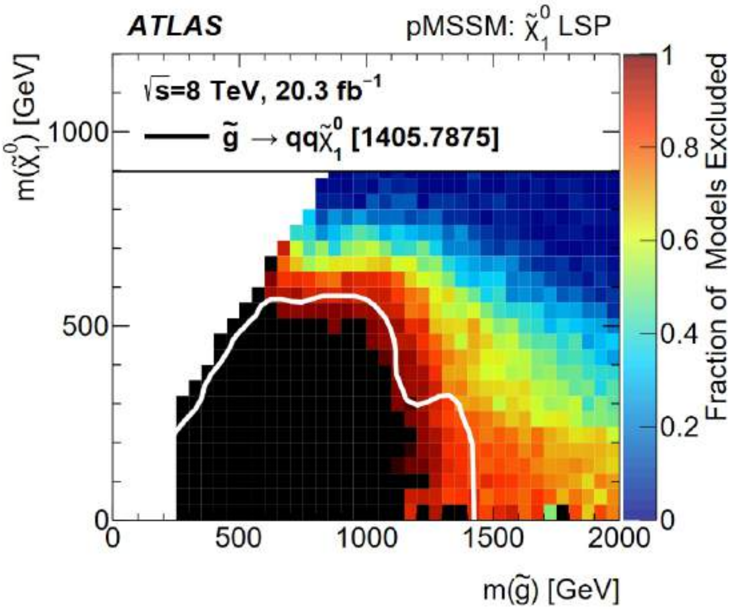

Figure 4.5: Fraction of excluded pMSSM models in the gluino-neutralino mass plane and the exclusion limit derived in the simplified model analysis in [84] (from [82]).

As can be deduced from the scanning procedure, the truth smearing should deliver results as similar to the reconstruction-level simulation as possible. This would minimise the number of models which have to be processed in the last three steps and ensure CPU efficiency.
The demand for a well performing truth smearing in the pMSSM is a key motivation for the study of the truth smearing of tau leptons in this thesis. In chapter 7, an example pMSSM scan will be conducted to test the implementation of an updated truth smearing for tau leptons.

4.4.4 Truth Smearing for Simplified Models

The improvement of the truth smearing of tau leptons for SUSY processes in general in order to increase the CPU efficiency of the pMSSM scan is the main goal of this thesis. However, some examples of implementations of truth smearing which are beneficial for simplified model analyses will be presented as well. Namely, these examples will be a sensitivity study for the

SqSq process and providing high statistics samples for the direct stau analysis which focuses on event topologies with one leptonically and one hadronically decaying tau lepton (LepHad channel).

Sensitivity in the SqSq Signal Grid
Out of the processes described in section 2.3, each has a dedicated recent analysis drawing exclusion limits in the respective two dimensional parameter space except for one. The SqSq process has, at this time, no recent dedicated analysis. However, since the GoGo process is very similar to the SqSq process, the signal regions derived in the GoGo analysis [23] might be sensitive to the signature of the SqSq process as well. In this thesis, the SqSq process will be simulated for multiple model points in the $m_{\tilde{q}}$-$m_{\tilde{\chi}_1^0}$-parameter space (called the SqSq grid in the following). Only the event generation will be run and an improved tau truth smearing will be used to evaluate the expected significance for each of the model points with the GoGo signal regions and corresponding background estimates. This way, it will be possible to estimate the sensitive region in which model points can probably be excluded at 95% CL. This is in turn helpful for future SqSq analyses as this sensitivity estimate in the parameter space narrows down the region of interesting model points to simulate at detector level, thus reducing the amount of computational resources needed.

Direct Stau LepHad Analysis
The direct stau analysis in the HadHad channel has previously been mentioned as an example for simplified models. The analysis of the LepHad channel uses the same simplified model, but focuses on the more challenging signature of one leptonically and one hadronically decaying tau lepton. In a recent analysis of this channel [85], a BDT was used to discriminate between the signal and background processes. The BDT needs to be trained using simulated events from signal and background processes to figure out discriminating properties. To ensure the reliability of the BDT, high statistics, i.e. a large amount of events, are needed in the training. As the amount of reconstruction-level simulated events of the direct stau process is limited, generator-level simulated events might provide a computationally cheap way to get high statistics. Again, a well performing truth smearing is needed to compensate for the skipped detector-level simulation and reconstruction. For this purpose, an improved truth smearing for tau leptons as well as electrons and muons (since the LepHad channel includes leptonically decaying taus) will be developed in the next chapter for the direct stau process.

4.5 Samples

In order to test the truth smearing of tau leptons, the six processes mentioned in section 2.3 were studied. For each of these processes, a number of simulated datasets, called samples, were used. While only one sample was used for the SM process as the participating particles' masses are already known, samples with different mass configurations were considered for the SUSY processes. Some of the samples were processed in two different ways:

SimpleAnalysis
The software framework SimpleAnalysis [86] was used to acquire the smeared truth-level objects from TRUTH3[12] datasets of some of the samples. Normally, SimpleAnalysis uses the UpgradePerformanceFunctions to implement truth smearing. Hence this data format will mainly be used to test the current and improved truth smearing functions in the following chapters.

[12] TRUTH3 datasets contain only generator-level information.

XAMPPstau

The software framework XAMPPstau [87] was used to acquire reconstruction-level as well as truth-level objects from SUSY3[13] datasets of every sample. These XAMPPstau-processed samples are — in addition to the requirements on the truth- and reconstruction-level objects themselves — subject to an event cleaning procedure. This removes events which contain muons or jets from a non-collision source like from cosmic ray interactions. Also, at least one reconstructed vertex is required.

In table 4.4 and table 4.5, the different samples for each process will be presented with their ID, their SUSY mass configuration and the event numbers processed by SimpleAnalysis and XAMPPstau from TRUTH3 and SUSY3 data sets, respectively. TRUTH3 datasets are only used for the SqSq, GoGo and direct stau processes because these are the main focus for the tasks of estimating sensitivity in the SqSq grid and producing a high statistics sample for the direct stau analysis.

ttbar		
Sample ID (DSID)	$N_{\text{events}}^{\text{SUSY3}}$	$N_{\text{events}}^{\text{TRUTH3}}$
410470	30000	-

Table 4.4: Sample ID and number of events for the ttbar sample.

SqSq				
Sample ID (DSID)	$m_{\tilde{q}}$ [GeV]	$m_{\tilde{\chi}_1^0}$ [GeV]	$N_{\text{events}}^{\text{SUSY3}}$	$N_{\text{events}}^{\text{TRUTH3}}$
378445	1600	45	10000	30000
378446	1200	845	10000	30000
378447	600	570	30000	90000
GoGo				
Sample ID (DSID)	$m_{\tilde{g}}$ [GeV]	$m_{\tilde{\chi}_1^0}$ [GeV]	$N_{\text{events}}^{\text{SUSY3}}$	$N_{\text{events}}^{\text{TRUTH3}}$
378448	1100	835	50000	80000
378449	1700	1135	10000	30000
378450	2200	85	10000	30000
Direct Stau				
Sample ID (DSID)	$m_{\tilde{\tau}}$ [GeV]	$m_{\tilde{\chi}_1^0}$ [GeV]	$N_{\text{events}}^{\text{SUSY3}}$	$N_{\text{events}}^{\text{TRUTH3}}$
396104	200	1	60000	20000
397011	200	120	40000	20000
397017	320	1	6000	16000
397030	440	1	2000	6000
397049	100	1	50000	20000
398349	120	80	40000	20000
398350	160	100	40000	-

[13] SUSY3 datasets contain generator-level as well as reconstruction-level information.

C1C1				
Sample ID (DSID)	$m_{\tilde{\chi}_1^\pm}$ [GeV]	$m_{\tilde{\chi}_1^0}$ [GeV]	$N_{\text{events}}^{\text{SUSY3}}$	$N_{\text{events}}^{\text{TRUTH3}}$
396367	700	0	10000	-
396368	700	100	10000	-
396369	700	200	10000	-
396370	700	300	10000	-
396371	700	400	10000	-
396372	700	500	10000	-
396373	700	600	10000	-
ttStau				
Sample ID (DSID)	$m_{\tilde{t}}$ [GeV]	$m_{\tilde{\tau}}$ [GeV]	$N_{\text{events}}^{\text{SUSY3}}$	$N_{\text{events}}^{\text{TRUTH3}}$
437366	700	90	10000	-
437368	700	690	10000	-
437392	950	90	10000	-
437398	950	690	10000	-
437454	1350	90	10000	-
437460	1350	690	10000	-

Table 4.5: Sample ID, SUSY mass configuration and number of events for the samples of the different SUSY processes.

For the majority of the studies presented in the following chapters, only these samples were used for an in-depth analysis of the truth smearing of tau leptons (and electrons/muons in the case of the direct stau process). However, in the later stages of this work, it became clear that a tighter coverage of the signal grids of the studied processes as well as higher statistics is needed to achieve an improvement in the tau truth smearing consistent with multiple mass configurations of the SUSY processes.
Therefore, the whole available signal grid of reconstruction-level simulated data for the considered SUSY processes as well as a larger amount of ttbar events was used in some parts of the following studies. These sample will be called the PHYS samples because the PHYS data format was taken as input to produce these samples with XAMPPstau. Similar to SUSY3, the PHYS format also contains reconstruction-level and truth-level objects[14]. In table 4.6, the number of samples which were available in the signal grids of the SUSY processes, the mass ranges and the number of taus in all samples are presented. The number of taus gives a sense of the available statistics of each process. Unfortunately, no additional samples in the SqSq and GoGo grid were available. However, the samples' statistics was increased by including multiple MC simulation campaigns. For the ttbar process, the PHYS sample contains 44152 taus.

[14]The PHYS data format is more storage efficient than the SUSY3 format, though.

SqSq			
N_{samples}	$m_{\tilde{q}}$ range [GeV]	$m_{\tilde{\chi}_1^0}$ range [GeV]	$\sum_{\mathrm{samples}} N_\tau$
3	600 - 1600	45 - 845	74426
GoGo			
N_{samples}	$m_{\tilde{g}}$ range [GeV]	$m_{\tilde{\chi}_1^0}$ range [GeV]	$\sum_{\mathrm{samples}} N_\tau$
3	1100 - 2200	85 - 1135	217547
Direct Stau			
N_{samples}	$m_{\tilde{\tau}}$ range [GeV]	$m_{\tilde{\chi}_1^0}$ range [GeV]	$\sum_{\mathrm{samples}} N_\tau$
59	80 - 440	1 - 200	4548275
C1C1			
N_{samples}	$m_{\tilde{\chi}_1^\pm}$ range [GeV]	$m_{\tilde{\chi}_1^0}$ range [GeV]	$\sum_{\mathrm{samples}} N_\tau$
119	100 - 1200	0 - 600	10367360
ttStau			
N_{samples}	$m_{\tilde{t}}$ range [GeV]	$m_{\tilde{\tau}}$ range [GeV]	$\sum_{\mathrm{samples}} N_\tau$
38	500 - 1850	90 - 1690	579498

Table 4.6: Number of samples, SUSY mass ranges and number of taus for the SUSY processes produced from the PHYS data format.

Chapter 5

Lepton Truth Smearing

A good performance of the truth smearing is integral to the previously introduced pMSSM scanning procedure. In this chapter, the smearing functions of the UpgradePerformanceFunctions will be presented. Then a comparison between the smeared truth-level and reconstruction-level objects will show the present performance of the smearing functions. As will become clear, a recalculation of the Reconstruction and ID efficiencies entering the efficiency functions in the smearing is needed to achieve adequate performance. Finally, an unexpectedly observed sample dependence in this recalculated efficiency will be scrutinised.
The main focus in this study are tau leptons. Therefore, this chapter will primarily deal with their truth smearing functions. However, as the analysis of the LepHad channel for the direct stau process depends on electrons and muons as well, their smearing functions will be put under scrutiny here, too.

5.1 Smearing Functions

The main types of smearing functions have already been discussed in section 4.3. Here, the functions used on taus, electrons and muons in the UpgradePerformanceFunctions shall be presented in more detail.

5.1.1 Tau Leptons

The UpgradePerformanceFunctions for tau leptons include an efficiency, an energy smearing and a fake rate function. Tau leptons are required to fulfil $p_{\mathrm{T}} > 20$ GeV and $|\eta| < 4$ before the smearing.

Tau Efficiency
A parametrisation in p_{T}, $|\eta|$ and prongness of the tau lepton is used for the efficiency function. In practice, this means that the Reconstruction and ID efficiency ε is calculated as

$$\varepsilon = a + b|\eta|, \tag{5.1}$$

where a and b are parameters which are fixed at different values for different regions with respect to p_{T}, $|\eta|$ and prongness. Furthermore, there are three different parametrisations for the different ID WPs loose, medium and tight. This efficiency function intends to parametrise both the reconstruction and the ID efficiency, therefore these ε will be called *reconstruction* *and ID efficiency* in the following.

Tau Energy Smearing
The tau energy smearing is achieved by adding an energy correction, which is randomly chosen from a gaussian distribution, to the tau energy. The gaussian distribution of the correction is centred at 0 and has a standard deviation equal to the energy resolution σ_E of the calorimeters which consists of three terms with different energy dependence

$$\frac{\sigma_E}{E} = \sqrt{\left(\frac{c}{E/\mathrm{GeV}}\right)^2 + \left(\frac{b}{\sqrt{E/\mathrm{GeV}}}\right)^2 + a^2}, \tag{5.2}$$

where a, b and c are parametrised in $|\eta|$ and prongness of the tau. The a-term respects effects of leakage and calibration, the b-term effects of shower fluctuations and the c-term electronic noise in the calorimeters [88].

Tau Fake Rate
Finally, a tau fake rate function is implemented. This function determines the fraction of jets which will be counted as smeared truth-level tau leptons to account for misidentifications in the reconstruction. It is, similar to the efficiency function, parametrised in p_T, η and prongness. There are also different parametrisations for different tau ID WPs. The jets need to fulfil $p_\mathrm{T} > 20$ GeV and $|\eta| < 4$.

5.1.2 Electrons

The smearing functions for electrons include an efficiency, an energy smearing, two fake rate and a charge flip function. Electrons are required to fulfil $|\eta| < 4.9$ before the smearing.

Electron Efficiency
The electron efficiency function is parametrised in p_T and $|\eta|$. To get the efficiency for a p_T-value in a certain p_T-bin, an interpolation between the respective bin boundaries is used. Different binnings are used for different ID WPs.

Electron Energy Smearing
The energy smearing functions of electrons is similar to the corresponding tau smearing function. Again, the correction term is governed by a gaussian distribution for the energy resolution. The energy resolution has again a parameter for each of the three terms relevant to the calorimeter resolution. These parameters are only binned in $|\eta|$, however.

Electron Fake Rate
The electron fake rate function gives the rate at which jets are misidentified as electrons. It determines the number of jets which will be counted as smeared truth-level electrons. The rate is parametrised in p_T, $|\eta|$ and a different parameter map is used for the loose, medium and tight ID WPs. Similar to the electron efficiency function, an interpolation in the p_T bins is used to calculate the fake rate.

Electron-to-Photon Fake Rate
Another detector effect which needs to be considered is the misidentification of electrons as photons. The electron to photon fake rate determines which electrons will be added to the smeared truth photons instead of the electrons. Two fixed values are used for the barrel and end-cap $|\eta|$-regions of the calorimeters and electrons need to fulfil $p_\mathrm{T} > 20$ GeV.

Electron Charge Flip
There is a chance that the electron charge is measured incorrectly. The charge flip probability function makes up for that. Parameters are taken from bins in p_{T} and $|\eta|$.

5.1.3 Muons

For muons, only an efficiency and a charge over p_{T} resolution function are used.

Muon Efficiency
The efficiency function for muons uses a different $|\eta|$ parametrisation for the WPs loose, tight and highPt. Muons have to satisfy a $p_{\mathrm{T}} > 4$ GeV requirement.

Muon Charge-over-Momentum Resolution
The muon charge over momentum resolution function accounts for inaccuracies in the p_{T} and charge measurements of the detector at the same time. This resolution is calculated by dividing the p_{T} resolution by the ${p_{\mathrm{T}}}^2$. The p_{T} resolution, in turn, is acquired by combining the p_{T} resolutions of both the inner detector and the MS. Each have a different parametrisation in $|\eta|$ and ϕ for the p_{T}-dependent terms entering the respective resolutions[1] [89].
The actual smearing of the muon charge over momentum is not calculated in the UpgradePerformanceFunctions themselves. Here, it is calculated in SimpleAnalysis through a gaussian distributed correction term with a standard deviation equal to the resolution.

5.2 Comparison of smeared truth-level and reconstruction-level leptons

Now, the performance of the current truth smearing, i.e. the UpgradePerformanceFunctions as they are implemented in SimpleAnalysis, will be tested. This is done by comparing the distributions of smeared truth-level leptons and reconstruction-level leptons in different variables like p_{T} or $|\eta|$. The efficiency and fake rate functions are defined for different ID WPs, so the ID WP used for the corresponding reconstruction-level object is used to ensure comparability. While the tau leptons will be compared for both SqSq and direct stau samples, electron and muon comparisons will only be carried out for direct stau samples. As the smeared truth-level objects are acquired from TRUTH3 and reconstruction-level from SUSY3 datasets, the number of events of each dataset has to be normalised to the same luminosity to ensure a meaningful comparison. Therefore, the following weighting factor is used on the events:

$$w_i = \frac{k \cdot F \cdot \sigma \cdot L}{N^i_{\text{events}}} \cdot w_{gen} \ , \ i = \text{TRUTH3, SUSY3} \tag{5.3}$$

Where k is the k-factor which comes from higher order corrections, F is the filter efficiency and σ the cross section for the model point[2]. L is the integrated luminosity (see 3.1), here taken to be $L = 140\ \mathrm{fb}^{-1}$, i.e. the luminosity integrated over the run-2 period of the ATLAS

[1]The momentum resolution of the MS is a combination of terms resulting from energy leakage in the calorimeter, multiple scattering and the intrinsic resolution in the tracking detectors. They each have a different dependence on the momentum, similar to the terms in the calorimeter resolution. The inner detector is only subject to inaccuracies due to multiple scattering and the intrinsic resolution.

[2]The cross sections of the SqSq process samples were calculated at NNLO and at NLO for the direct stau process sanmples [90].

detector.

5.2.1 Tau Leptons

A comparison between smeared truth-level and reconstruction-level taus in terms of their p_{T} and η can be found in figure 5.1 for a SqSq sample and in figure 5.2 for a direct stau sample. It can be seen immediately that the smearing improves the agreement between truth- and reconstruction-level taus. However, it can also be seen that in both cases — especially for the SqSq sample — there are too many smeared truth taus as compared to the reconstruction-level taus.
A general remark concerning the comparison plots in this work: the number of objects, weighted according to equation (5.3), is generally shown in the legend. One might note that the number of taus in the p_{T} distribution plots is generally lower than in the η distribution plots for the same sample. This is due to the fact that the leptons in this study all have an upper limit on η while their p_{T} distribution is not restricted to high p_{T}. The histograms of the p_{T} distributions will therefore almost always cut off some taus at high p_{T}, resulting in a lower yield.

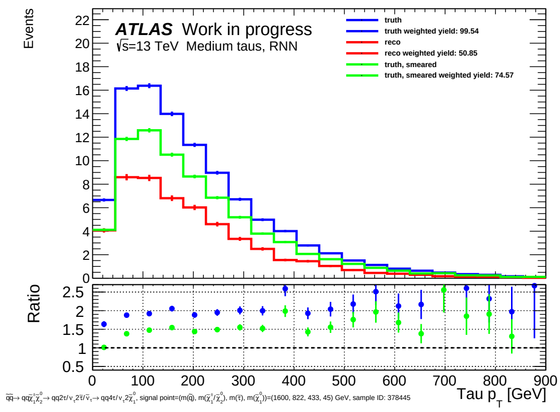

(a) p_{T}

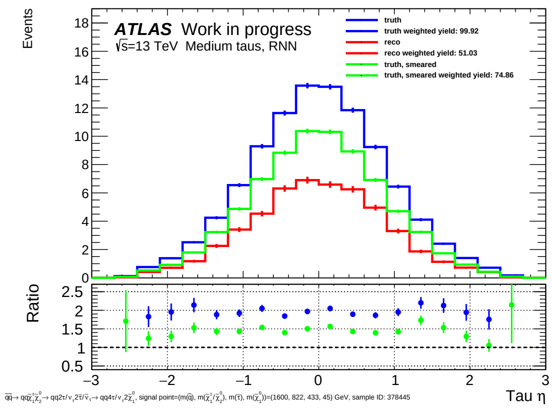

(b) η

Figure 5.1: Distribution of tau p_{T} (a) and η (b) for the SqSq sample with ID 378445. The red line indicates reconstruction-level, the green line smeared truth-level and the blue line truth-level taus. The ratio of each of the truth-level distributions to reconstruction-level is shown in the bottom part.

Before actually changing the smearing functions to tackle this problem, the BDT-based ID WPs for the reconstruction-level taus were used instead of the RNN-based ones. This might resolve the differences, as the smearing functions in the UpgardePerformanceFunctions were designed at a time where the BDT-based algorithm was the default. In figure 5.3, the tau p_{T} distributions for the SqSq and the direct stau samples is again shown, this time the reconstruction-level taus fulfil the BDT-based medium WP. As can be seen, the disagreement through an excess in smeared truth taus remains. Hence, the usage of the RNN ID algorithm is not the reason for the bad performance of the smearing.

As the difference in abundance seems to be the key difference between smeared truth- and reconstruction-level, one can deduce that the tau efficiency function is overestimating the reconstruction and ID efficiency of the taus. The energy smearing or the fake rate function do not seem to be at fault at the moment. Therefore, if one sets out to improve the smearing of

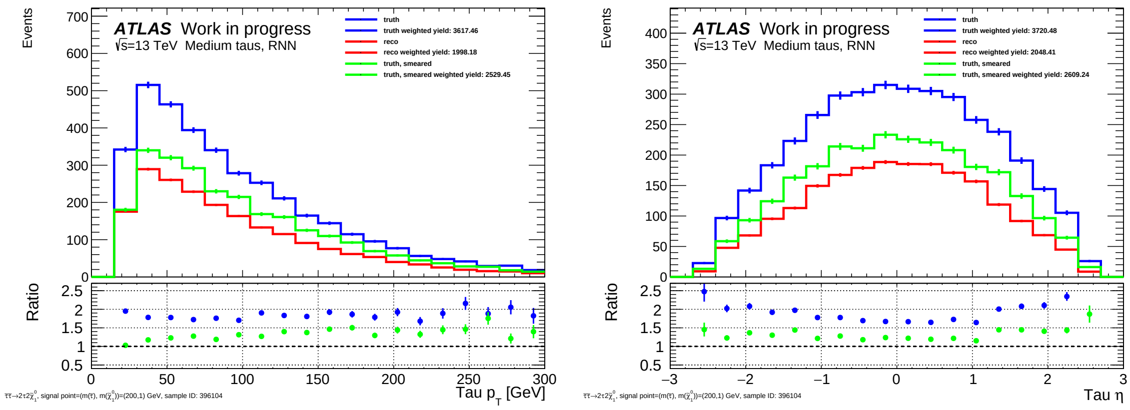

(a) p_{T} (b) η

Figure 5.2: Distribution of tau p_{T} (a) and η (b) for the direct stau sample with ID 396104. The red line indicates reconstruction-level, the green line smeared truth-level and the blue line truth-level taus. The ratio of each of the truth-level distributions to reconstruction-level is shown in the bottom part.

tau leptons, the efficiency function seems to be the place to start.
Something that might catch the eye here as well is the fact that the disagreement in the SqSq sample is significantly higher than for the direct stau sample. This will become important later in the context of sample dependence.

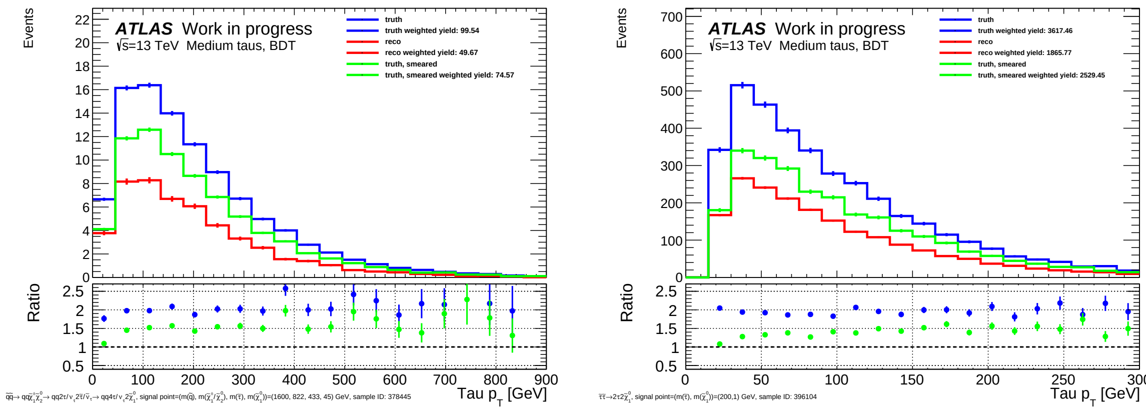

(a) 378445 (b) 396104

Figure 5.3: Distribution of tau p_{T} for the SqSq (a) and the direct stau (b) sample. As opposed to figures 5.1 and 5.2, the reconstruction-level taus here are subject to a BDT-based ID WP.

5.2.2 Electrons and Muons

For the electrons and muons, the comparison of (smeared) truth-level and reconstruction-level in the direct stau sample is shown in figure 5.4a and 5.4b, respectively. While for electrons, an improvement in the agreement of reconstruction- and truth-level is again achieved through the smearing, the muon smearing is not really changing anything due to the loose WP. In both cases however, the smearing falls short of delivering a good agreement.
One reason for this might be that the impact parameter cuts can not be implemented on truth-

level leptons[3] and are not respected in any smearing functions [91]. This is demonstrated in figure 5.4c and 5.4d, where the electron and muon p_T distributions are shown without impact parameter cuts on the reconstruction-level objects. As can be seen, the agreement is slightly better for the electrons and significantly better for the muons. At low p_T, the efficiency functions also seem to overestimate the reconstruction and ID efficiency, like in the case of the tau leptons.

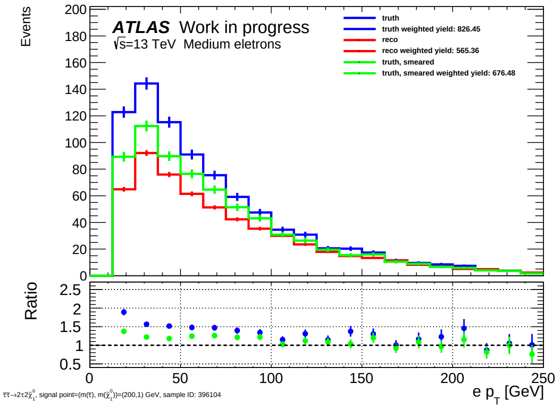

(a) electron p_T, cut

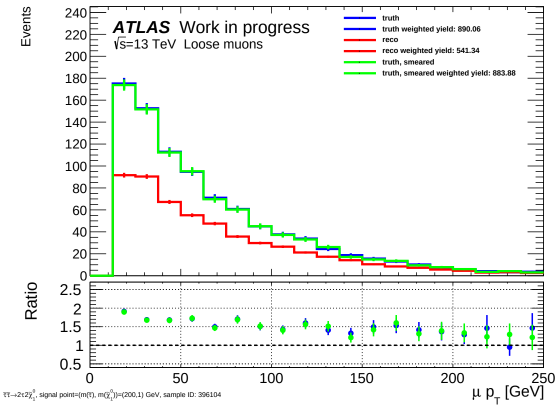

(b) muon p_T, cut

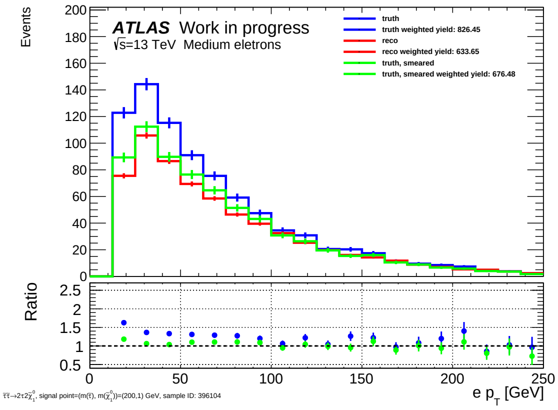

(c) electron p_T, uncut

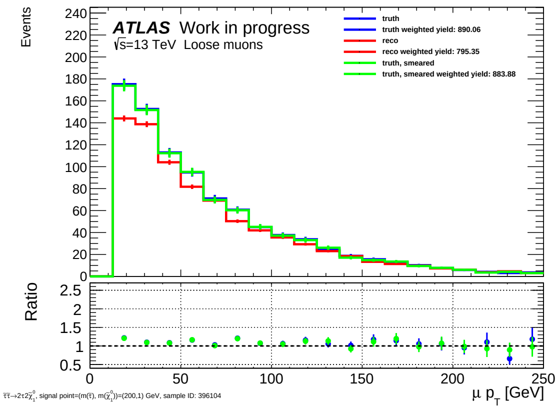

(d) muon p_T, uncut

Figure 5.4: Distribution of the electron p_T (a) and muon p_T (b) with implemented impact parameter cuts for the reconstruction-level electrons/muons. Below are the electron p_T (c) and muon p_T (d) distributions with no impact parameter cuts applied.

5.2.3 Jets and E_T^{miss}

For the truth smearing of leptons, there appears to be quite some potential for improvement. Apart from the leptons, however, jets and E_T^{miss} are also important objects in the analyses that will later be used on the truth smeared samples. Even if an in-depth investigation is outside of the scope of this thesis, some comparison plots regarding jets and E_T^{miss} will be shown here as well. This will help determine if one has to expect further inaccuracies in the truth smearing from these objects.
Figure 5.5 shows a comparison between truth, smeared truth-level and reconstruction-level jets/E_T^{miss} for both the SqSq and the direct stau sample. The agreement of smeared truth-level and reconstruction-level seems to be fine for the E_T^{miss} distribution and for high jet p_T.

[3] As impact parameters are properties of reconstruction-level objects.

At low jet p_{T}, an excess of reconstruction-level jets over smeared truth jets can be observed, however. This discrepancy can probably be explained by the fact that the run 2 version of the SimpleAnalysis truth smearing does not include pile-up jets[4].

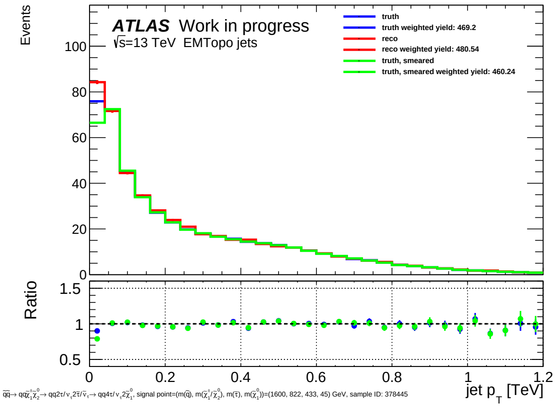

(a) DSID 378445, jet p_{T}

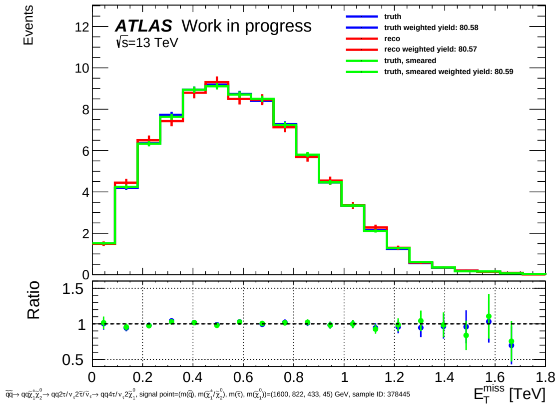

(b) DSID 378445, $E_{\mathrm{T}}^{\mathrm{miss}}$

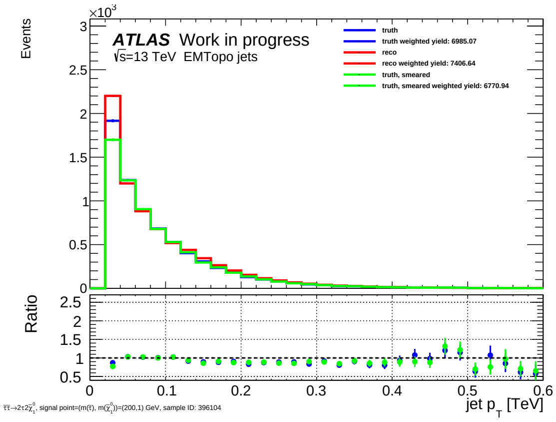

(c) DSID 396104, jet p_{T}

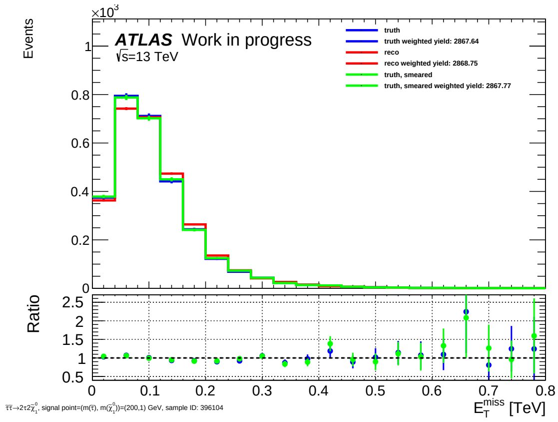

(d) DSID 396104, $E_{\mathrm{T}}^{\mathrm{miss}}$

Figure 5.5: On the left: Distribution of the jet p_{T} for the SqSq (a) and the direct stau sample (c). On the right: Distribution of the missing transverse energy $E_{\mathrm{T}}^{\mathrm{miss}}$ for the SqSq (b) and the direct stau (d) sample.

5.3 Implementation of calculated Reconstruction and ID efficiencies

The main issue with the smearing of leptons appears to be that the reconstruction and ID efficiencies implemented in the lepton efficiency functions are overestimated. To improve the performance of the smearing and tackle this problem, the reconstruction and ID efficiencies will be recalculated. This will be done for the SqSq and direct stau samples since an accurate smearing is needed for the sensitivity estimate in the SqSq signal grid and for the high statistics direct stau sample (see section 4.4.4). First, it will be shown how this calculation was carried out. Then, the recalculated efficiencies will be implemented in new tau efficiency functions for the SqSq and the direct stau process, and finally, the same will be done for the

[4]The UpgradePerformanceFunctions do include a pile-up overlay to account for pile-up jets, it is just not used in the SimpleAnalysis truth smearing for run 2.

electron and muon efficiency functions in the direct stau case.
At the end of this section, an improved tau lepton truth smearing will be developed for both the SqSq process and the direct stau process. For the direct stau process, an improved electron and muon truth smearing will be presented as well. The results of the actual application of these new truth smearing functions in the use cases described in section 4.4.4 will be shown in chapter 8.

5.3.1 Efficiency Calculation

The calculation of the reconstruction and ID efficiency can be done using the truth- and reconstruction-level objects from the samples based on the SUSY3 data format. In this general description of the calculation, 'object' refers to either electrons, muons or taus. The idea is to divide the number of truth-level objects which will be reconstructed into a reconstruction-level object after the detector simulation[5] by all of the truth objects. This fraction would give the reconstruction and ID efficiency $\varepsilon_{\text{reco+ID}}$, i.e.:

$$\varepsilon_{\text{reco+ID}} = \frac{N_{\text{truth}}^{\text{matched}}}{N_{\text{truth}}} \tag{5.4}$$

Where $N_{\text{truth}}^{\text{matched}}$ is the number of matched truth objects and N_{truth} the number of all truth objects. Matched truth objects are those objects which will be reconstructed after the detector simulation and can therefore be matched to a reconstruction-level object. Since the simulated datasets do not contain the links between a truth- and its corresponding reconstruction-level object, the matching has to be done geometrically. In this study, a truth-level object is matched to a reconstruction-level object, if their distance parameter fulfils $\Delta R < 0.2$. This condition is commonly used for tau leptons [69] and it is possible to motivate the cut at 0.2 by looking at the distribution of $\Delta R(\text{truth } \tau, \text{ reco } \tau)$. This variable calculates the distance parameter for any pairing of a truth-level and a reconstruction-level tau in the same event. In figure 5.6, this variable is shown logarithmically for the available direct stau samples and one can clearly see a rapid decline in the distribution at around 0.2. One now assumes that the peak at $\Delta R < 0.2$ corresponds to those truth-level and reconstruction-level taus where the truth-level tau was reconstructed into the reconstruction-level tau. Higher ΔR would then correspond to unrelated truth-level and reconstruction-level taus in the same event.
For electrons and muons, the same condition $\Delta R < 0.2$ for the matching is chosen. As can be seen in figure 5.7, a stricter cut would have been possible here as well, however. The peak at low ΔR appears to be far narrower than in the tau lepton case.

5.3.2 Tau Leptons

First Implementation
As mentioned in section 5.1, the tau efficiency function uses a parametrisation in p_{T}, $|\eta|$ and prongness. It applies a different efficiency for three p_{T} (20 GeV $\leq p_{\text{T}} <$ 50 GeV, 50 GeV $\leq p_{\text{T}} <$ 100 GeV, $p_{\text{T}} \geq$ 100 GeV) and two $|\eta|$ ($0 \leq |\eta| < 1.2$, $0 < |\eta| < 1.2$)[6] regions as well as the 1-prong and 3-prong taus, thus 12 bins in total.

[5] The number of reconstruction-level objects is specifically not used, the reason being that among the reconstruction-level objects, there might be some misidentified objects of another type which do not fall into the definition of the reconstruction and ID efficiency. Also, the energy calibration of truth-level and reconstruction-level objects is quite different (an energy smearing function is needed, after all) and thus a direct comparison would be problematic.

[6] To be exact, 3 regions are defined, the $2.5 \leq |\eta| < 4$ bin is not relevant for this study, however.

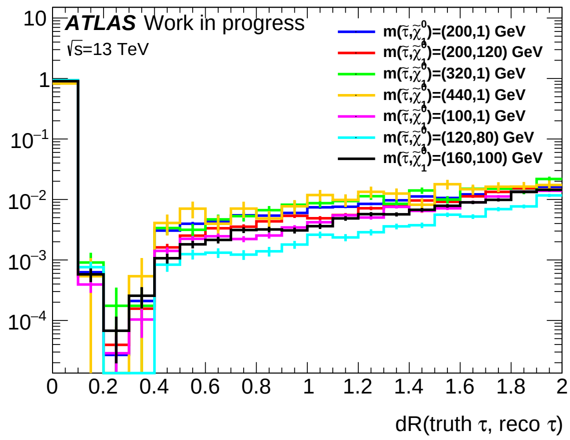

Figure 5.6: Normalised distribution of ΔR(truth τ, reco τ) for the available direct stau samples (labelled by their SUSY mass configuration).

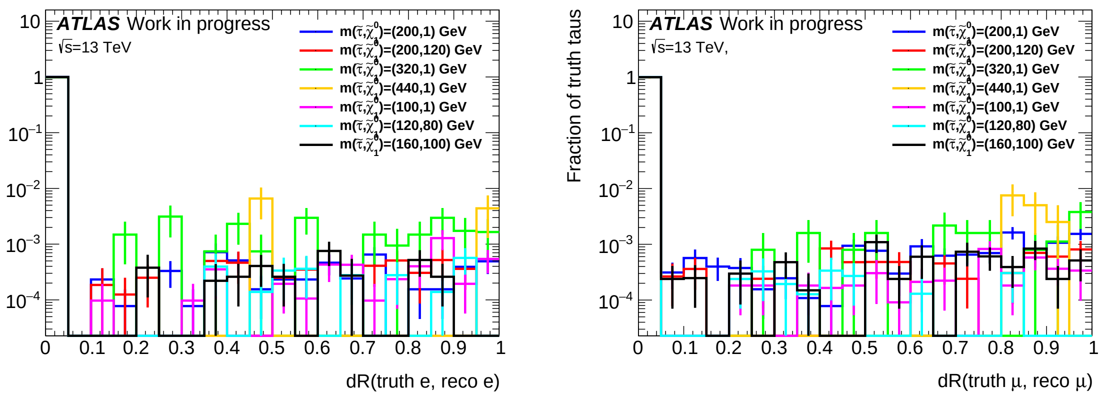

(a) electrons (b) muons

Figure 5.7: Normalised distribution of ΔR(truth e, reco e) (a) and ΔR(truth μ, reco μ) (b) for the available direct stau samples (labelled by their SUSY mass configuration).

The observation that the original smearing performs quite differently in the SqSq and the direct stau case (see figure 5.1 and 5.2) brings up the question if the new tau efficiency functions should be calculated separately. In figure 5.8, the reconstruction and ID efficiency is calculated in different regions of p_{T}, $|\eta|$ and prongness for both the SqSq sample with DSID 378445 and the direct stau sample with DSID 396104. The histograms show that even in the same p_{T}, $|\eta|$ and prongness bin, the two processes have very different efficiencies in many cases. Therefore, two different tau efficiency functions were constructed for the SqSq and the direct stau samples.

The improved efficiency functions for the SqSq and the direct stau samples will keep the parametrisation in p_{T} and $|\eta|$ as the efficiency maps in figure 5.8 show that the efficiency depends on these variables with the efficiency dropping when going to high p_{T} or $|\eta|$. However, slightly different p_{T} and $|\eta|$ bins will be employed to optimise the agreement between smeared truth-level and reconstruction-level taus for the respective samples. Discrimination in prongness remains part of the parametrisation, as prong-3 taus generally show a lower efficiency than prong-1 taus. In each of these bins, the reconstruction and ID efficiency is then calculated, the scaling with $|\eta|$ as in equation (5.1) is not used, however. These are the two new binnings:

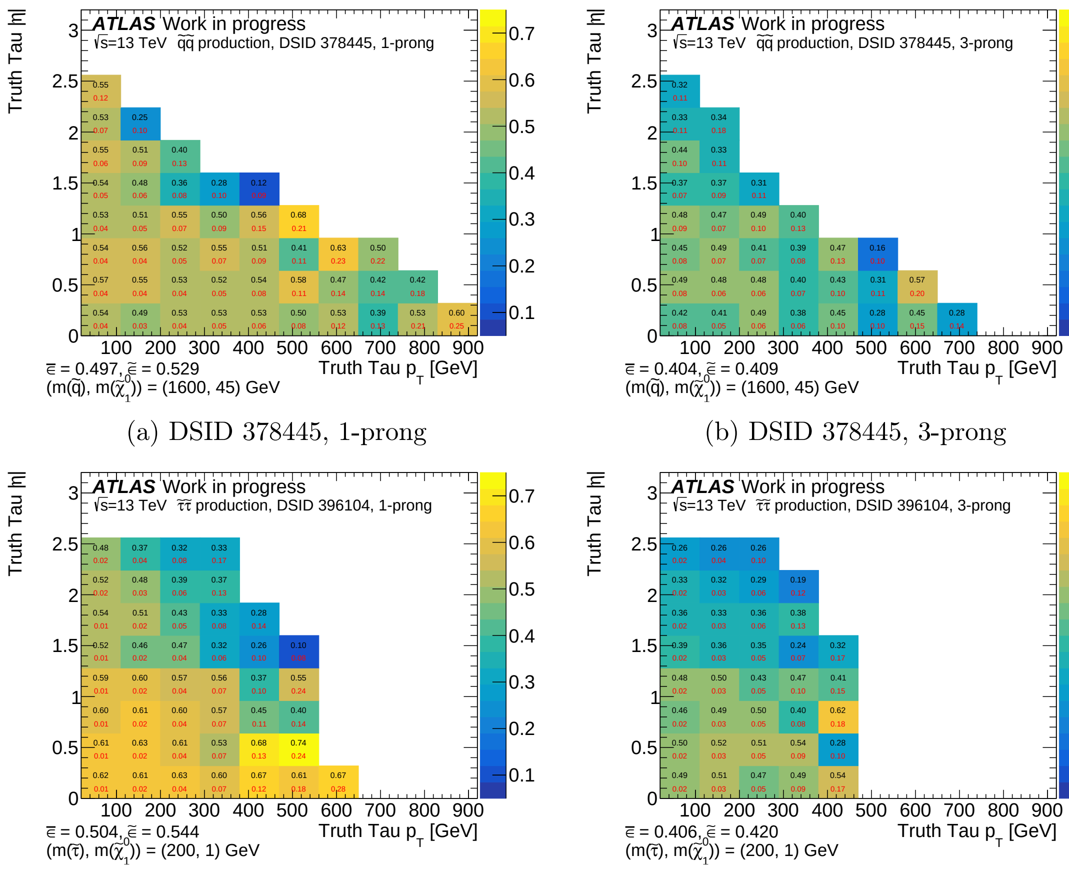

(a) DSID 378445, 1-prong

(b) DSID 378445, 3-prong

(c) DSID 396104, 1-prong

(d) DSID 396104, 3-prong

Figure 5.8: Tau reconstruction and ID efficiency maps in tau p_{T} and $|\eta|$ for 1-prong and 3-prong tau leptons of the SqSq sample with DSID 378445 ((a) and (b)) and of the direct stau sample with DSID 396104 ((c) and (d)). The colour indicates the value of the efficiency. Black numbers denote the calculated efficiency in the bin, red numbers the corresponding statistical uncertainty. $\bar{\epsilon}$ gives the unweighted mean and $\tilde{\epsilon}$ gives the unweighted median of the efficiency.

- In the SqSq case, an extra p_{T} bin was introduced for $p_{\mathrm{T}} \geq 350$ GeV as from that momentum onward, the efficiencies start to fluctuate (see figure 5.1a). The second bin boundary was increased from 100 to 110 GeV as it improved the performance. In the variable $|\eta|$, an additional bin was employed in the so-called *crack region*, i.e. the transition from barrel to end-cap calorimeter $1.37 \leq |\eta| < 1.52$. Hence, the first bin boundary had to be raised from 1.2 to 1.37. In figure 5.9, the calculated reconstruction and ID efficiencies are shown in the new binning for the 1-prong and the 3-prong taus. The SqSq sample with ID 378445 was used for the calculation.

- In the direct stau case, the extra high p_{T} bin and the new bin boundary at 110 GeV was used as well. Additionally, for the direct stau sample it turned out that a finer binning for low p_{T} yielded better results, thus a new bin boundary at 30 GeV was introduced and the bin boundary at 50 GeV was decreased to 40 GeV. The new $|\eta|$-bin in the crack region was employed as well. In figure 5.10, the calculated reconstruction and ID efficiencies are shown in the new direct stau binning. For the calculation, the sample with DSID 396104 was used.

With the new tau efficiency functions in place, the SqSq and direct stau smeared truth samples

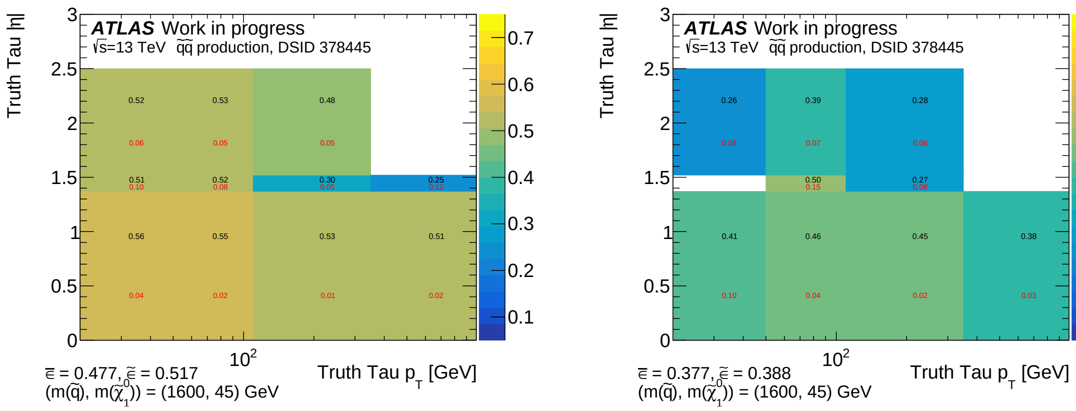

(a) 1-prong taus (b) 3-prong taus

Figure 5.9: Tau reconstruction and ID efficiency maps in tau p_{T} and $|\eta|$ for 1-prong and 3-prong tau leptons of the SqSq sample with ID 378445. The shown parametrisation is implemented in the tau efficiency function of the new SqSq smearing.

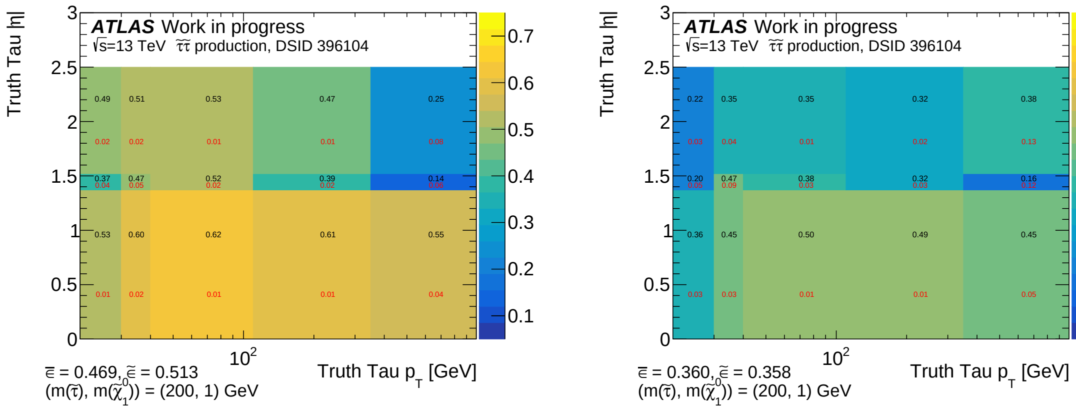

(a) 1-prong taus (b) 3-prong taus

Figure 5.10: Tau reconstruction and ID efficiency maps in tau p_{T} and $|\eta|$ for 1-prong and 3-prong tau leptons direct stau sample with ID 396104. The shown parametrisation is implemented in the tau efficiency function of the new direct stau smearing.

were produced again. In the following, when talking about SqSq samples, 'new smearing' refers to the SqSq smearing and when talking about direct stau samples, 'new smearing' refers to the direct stau smearing. A comparison of the p_{T} and η distributions of the truth taus which are subject to the new smearing, truth taus which are subject to the original[7] smearing and reconstruction-level taus is shown in figure 5.11a and 5.11b for the SqSq sample and in figure 5.12a and 5.12b for the direct stau sample.
In both cases, the new smearing results are in a far better agreement with the reconstruction-level data than the original smearing, both in the p_{T} and in the η distribution. Especially in the direct stau sample, however, one can still see some discrepancies in the first p_{T} bins.

Pre-Smear Cuts

One reason for this worse performance at low p_{T} are the pre-smear cuts. The pre-smear cuts are applied on the pure truth-level taus even before they are subject to the smearing functions. In the SimpleAnalysis implementation of the UpgradePerformanceFunctions, i.e.

[7] I.e. the smearing with the tau efficiency function of the UpgradePerformanceFunctions.

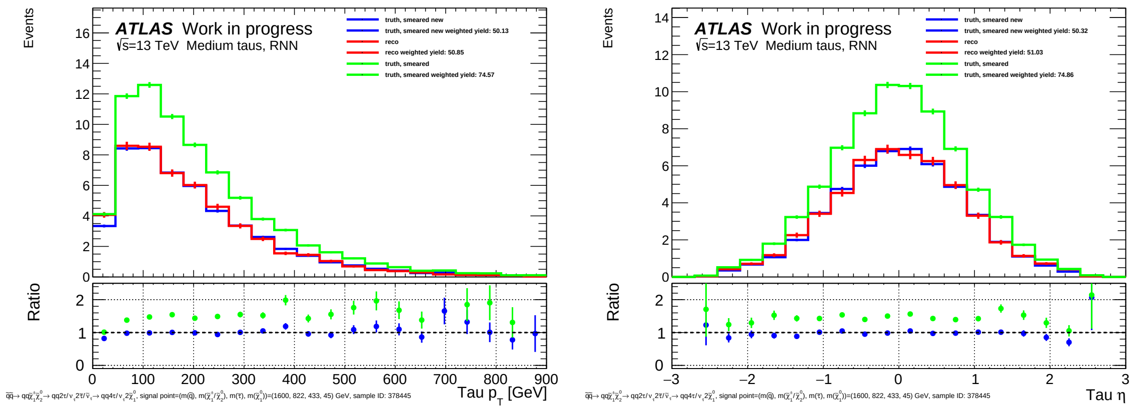

(a) p_{T}, pre-smear cut (b) η, pre-smear cut

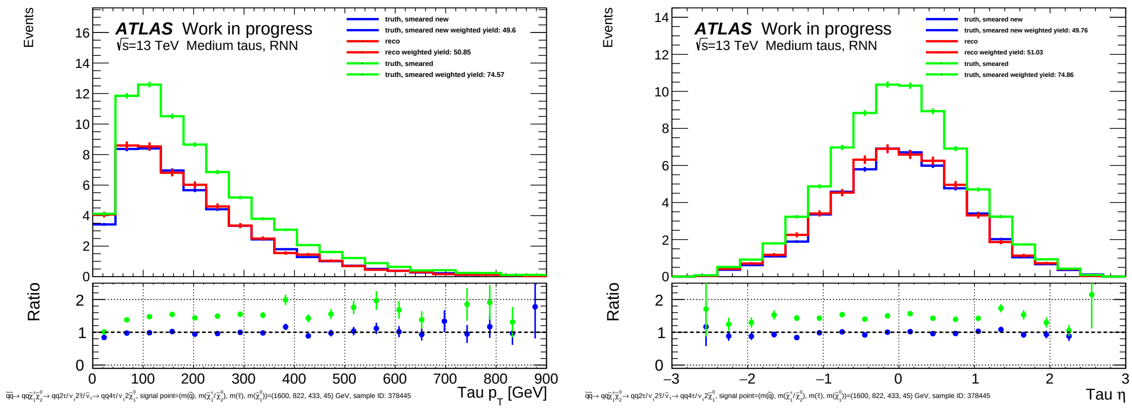

(c) p_{T}, loosened pre-smear cut (d) η, loosened pre-smear cut

Figure 5.11: The tau p_{T} (a) and η (b) distribution with pre-smear cuts in place and the tau p_{T} (c) and η (d) distribution with loosened pre-smear cuts for the SqSq sample with ID 378445. The red line indicates reconstruction-level, the green line smeared truth-level and the blue line smeared truth-level taus with the new tau efficiency function.

in the original smearing, these cuts are $p_{\mathrm{T}}> 20$ GeV and $|\eta| < 4$. The $|\eta|$ condition is not of concern here, but the p_{T} cut has consequences on the smearing.
Consider a truth-level tau lepton with a p_{T} just below 20 GeV. Through the finite resolution of the detector components, it is possible that it might be reconstructed with a momentum above 20 GeV. This would allow a tau which had a truth-level p_{T} below 20 GeV to pass the selection criterion $p_{\mathrm{T}}> 20$ GeV (see section 4.2) for the reconstruction-level taus. To incorporate this effect into the smearing and allow truth taus from below 20 GeV to migrate above this momentum and pass the selection requirement, the pre-smear cuts have to be loosened. Therefore, the pre-smear cuts of the new smearing were lowered to 10 GeV and the efficiency of the first bin above 20 GeV was also used in this additional region. The effect of this change on the p_{T} distribution of the new smeared taus can be seen in figure 5.11c for the SqSq sample and in figure 5.12c for the direct stau sample. In the SqSq sample, the effect is hardly visible, but in the direct stau sample, a better performance through an increased number of smeared truth taus for low p_{T} can be observed.

Fake Taus

Although loosening the pre-smear cuts brought better agreement in the direct stau case at low p_{T}, one can still observe some discrepancy in that region. It turns out that this is due to missing fake taus as the fake rate function is currently not implemented in the run-2 smearing in SimpleAnalysis. In figure 5.13, one can see that the fake taus are responsible for the gap at

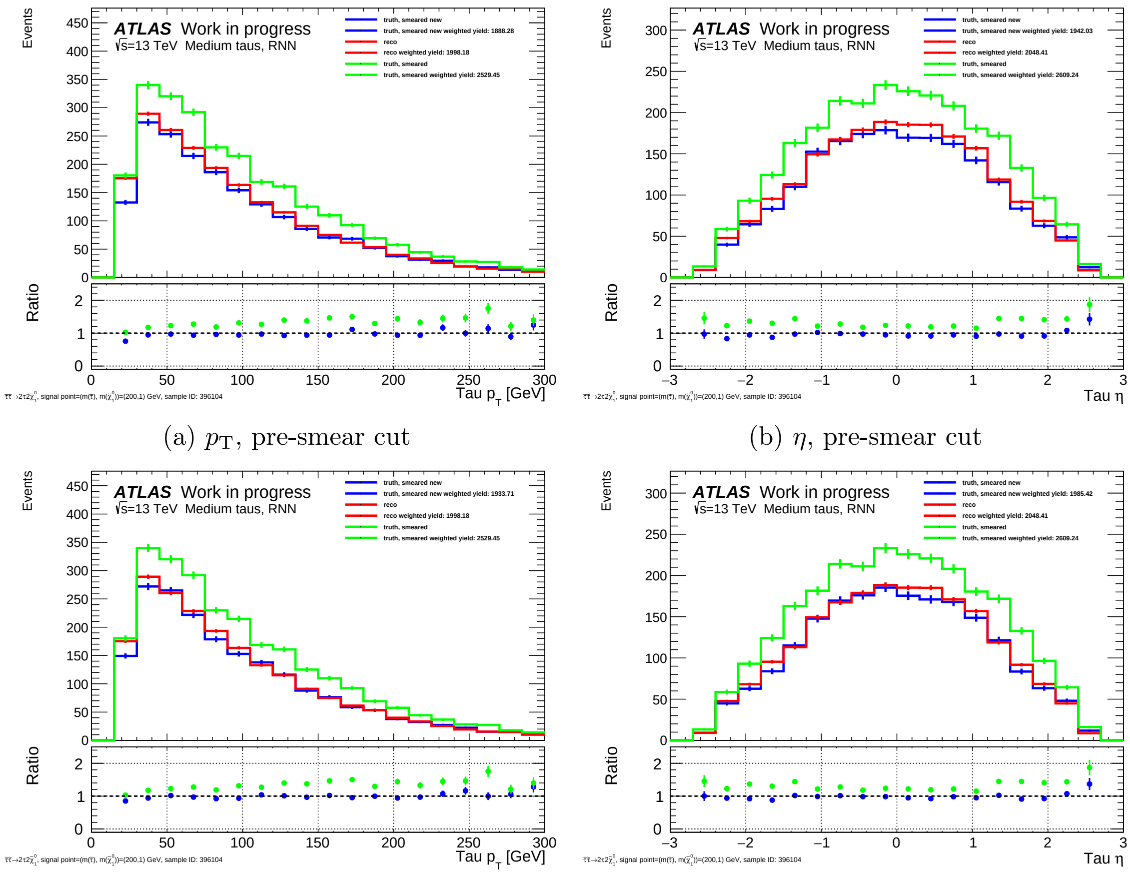

(a) p_T, pre-smear cut

(b) η, pre-smear cut

(c) p_T, loosened pre-smear cut

(d) η, loosened pre-smear cut

Figure 5.12: The tau p_T (a) and η (b) distribution with pre-smear cuts in place and the tau p_T (c) and η (d) distribution with loosened pre-smear cuts for the direct stau sample with ID 396104. The red line indicates reconstruction-level, the green line smeared truth-level and the blue line smeared truth-level taus with the new tau efficiency function.

low p_T in both the SqSq and the direct stau sample. In these histograms, the p_T distribution of matched reconstruction-level taus is shown, i.e. those reconstruction-level taus that have a truth-level counterpart which obviously excludes fake taus. Since the matched reconstruction-level and the new smearing distribution are in good agreement at low p_T, one can conclude that the remaining discrepancy is due to missing fake taus.

Different Mass Configurations

New tau smearing implementations for the SqSq and the direct stau process have been developed using one specific sample in each case with a certain mass configuration. Now, it has to be confirmed that the performance of the new smearing is sufficient for other mass configurations of the same process as well.
In figure 5.14a and 5.14b, the new SqSq and the original smeared truth tau p_T are shown in comparison to the reconstruction-level tau p_T for the SqSq samples of DSID 378446 and 378447, i.e. the two SqSq samples with a more compressed mass configuration (see table 4.5), respectively. It can be seen that the performance of the new smearing for 378446 is still good. However, the performance in the most compressed SqSq sample 378447 is even worse than that of the original smearing. This is due to the loosening of the pre-smear cuts, since the performance of the new smearing with the pre-smear cut $p_\mathrm{T} > 20$ GeV (see figure 5.14c) excels the original smearing's performance again. The efficiency which was assumed for $p_\mathrm{T} <$

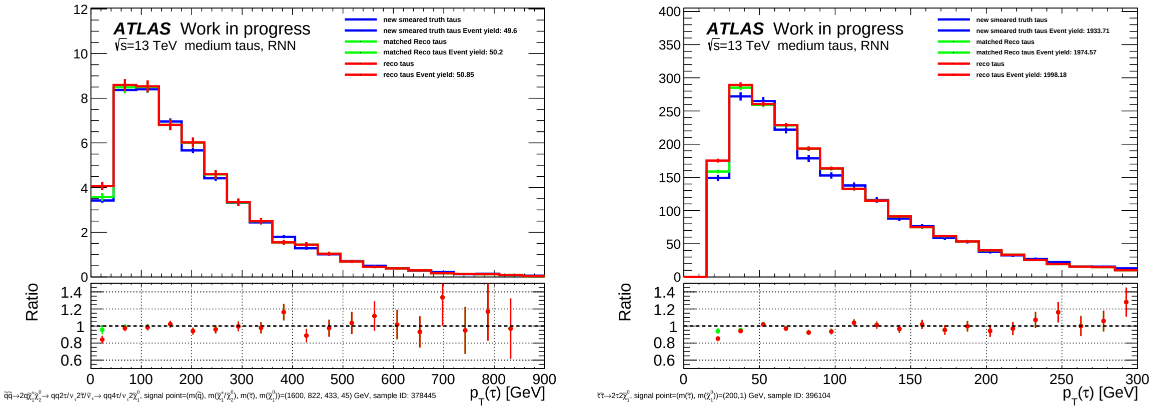

(a) 378445 (b) 396104

Figure 5.13: The p_{T} distribution for the SqSq (a) and the direct stau (b) sample. In these histograms, the red curve again shows reconstruction-level taus and the blue curve shows the truth-level taus subject to the new smearing while the green curve shows the reconstruction-level taus which were matched to a truth-level tau. The ratio plot shows the ratio of the blue distribution to the red and the green one (in the respective colours).

20 GeV (since it could not be calculated as the reconstruction-level taus fulfil $p_{\mathrm{T}} > 20$ GeV) was obviously greatly overestimated. Even with the pre-smear cut reinstated, it seems that at higher p_{T}, the number of smeared taus exceeds the number of reconstruction-level taus significantly. Hence, for this compressed sample, the calculated efficiencies from 378445 do not yield good results.
In figure 5.14d and 5.14e, the same comparison is shown for the direct stau samples with DSID 398349 and 397017, respectively. 398349 is a sample with a more compressed configuration of smaller masses, while 397017 describes a less compressed mass configuration with a high stau mass (see table 4.5). The agreement between the new smeared truth-level taus and reconstruction-level taus is quite good.
The corresponding plots for the remaining direct stau samples can be found in appendix A.1.1.

5.3.3 Electrons and Muons

As has previously been established, the main problem with the original electron and muon smearing was its neglect of the cuts on the impact parameters. Therefore, the new efficiencies

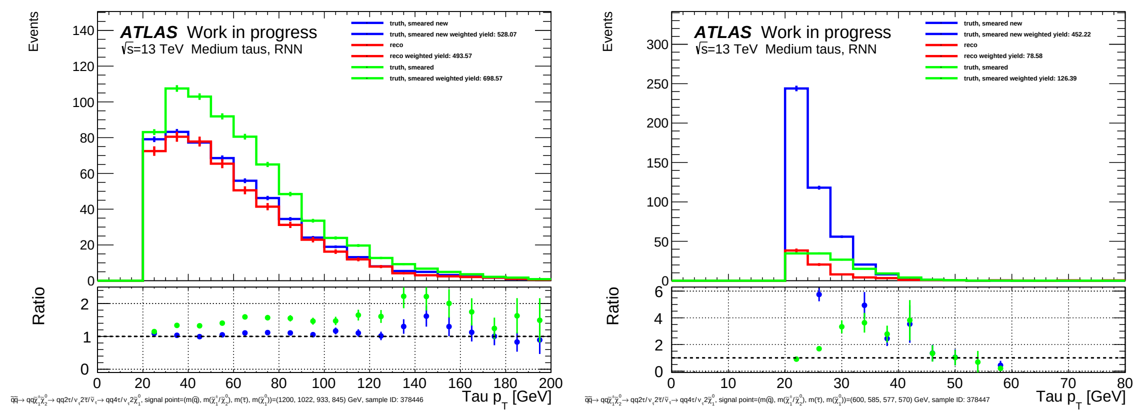

(a) 378446 (b) 378447

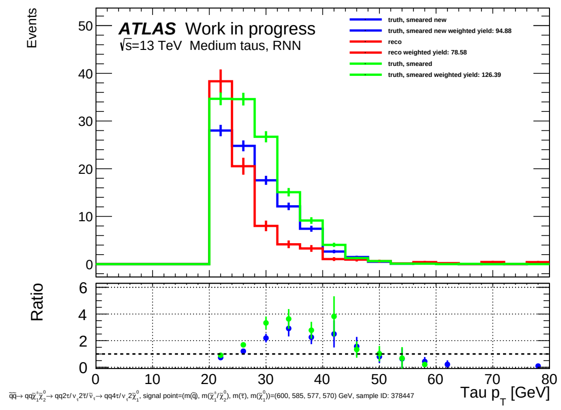

(c) 378447, pre-smear cut

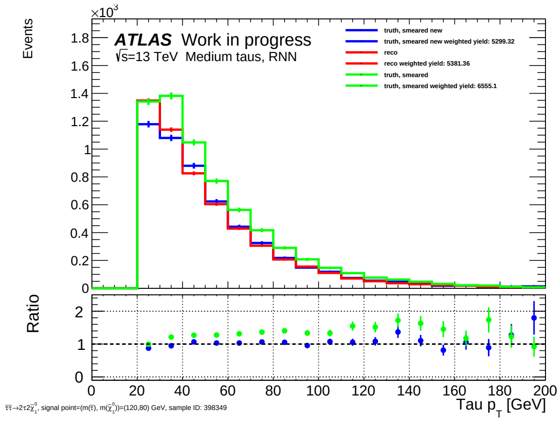

(d) 398349

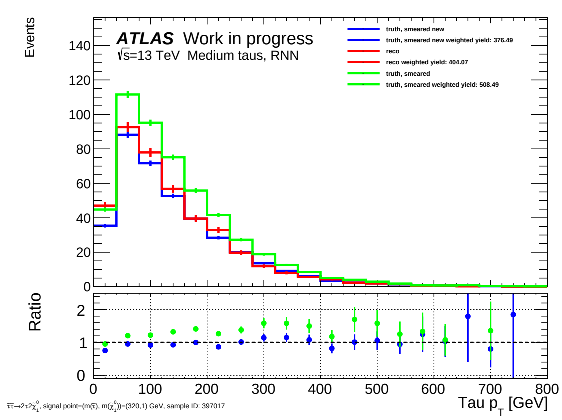

(e) 397017

Figure 5.14: The tau p_T distribution of the SqSq samples with DSID 378446 (a) and 378447 ((b) and (c)) and the direct stau samples with DSID 398349 (d) and 397017 (e) for the new smeared, original smeared truth-level and reconstruction-level taus.

which will be calculated in the following from the DSID 396104 sample are rather reconstruction, ID and impact parameter efficiencies, depending not only on the chosen ID WP but also on the employed impact parameter cuts. The impact parameter cuts and ID WPs used for leptons in this study have been presented in section 4.2.

Parametrisation

The original electron efficiency function had a very fine binning in p_T and $|\eta|$. Since very little variation with respect to the statistical error can be seen in the $|\eta|$ dependence of the calculated electron reconstruction and ID efficiencies (see figure 5.15a), a pure p_T binning is used here for the improved electron efficiency function. The binning and the calculated efficiencies can be seen in figure 5.15b.

The original muon efficiency function was parametrised in the $|\eta|$ variable only for the tight and high p_T WPs and was employing generally very high efficiencies as has become clear from figure 5.4b. The new smearing will use the $|\eta|$ bins from the original smearing, i.e. one bin below 0.1 and one above. Furthermore, a binning in p_T will be introduced as a dependence of the efficiency in this variable can be observed (see figure 5.15c). The binning and the calculated efficiencies used in the new muon efficiency function can be seen in figure 5.15d.

New Smearing Performance

The performance of this new smearing with an improved electron/muon efficiency function is shown in figure 5.16. There, both the electron and the muon p_T distribution of the direct stau sample with DSID 396104 is shown for the new smeared and the original smeared truth-level taus and the reconstruction-level taus. The agreement is good for both electrons and muons, hence the implementation of the impact parameter cuts into the efficiency function has been successful.

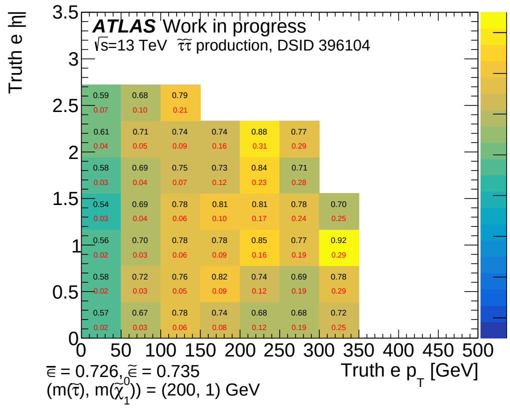

(a) electrons, uniform binning

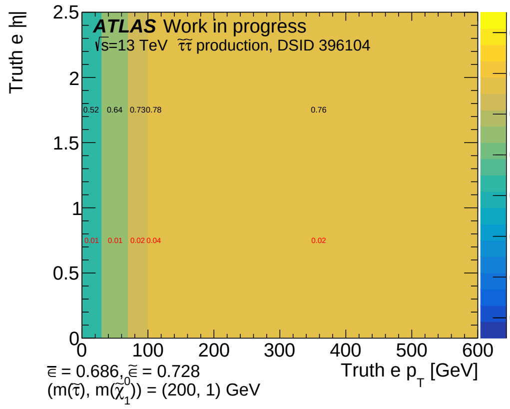

(b) electrons, binning for smearing

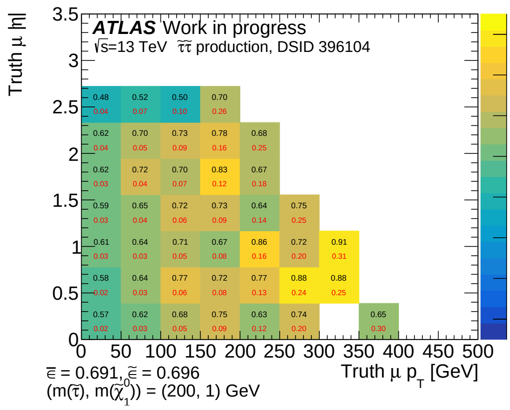

(c) muons, uniform binning

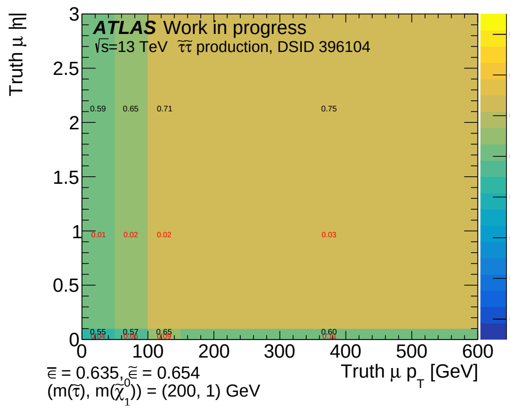

(d) muons, binning for smearing

Figure 5.15: Electron reconstruction and ID efficiency maps in electron p_T and $|\eta|$ in a uniform binning (a) and the binning used for the new electron smearing (b). Below, the muon reconstruction and ID efficiency maps in muon p_T and $|\eta|$ in a uniform binning (c) and the binning used for the new muon smearing (d).

Different Mass Configurations

For the lighter leptons, it should be checked as well that the newly implemented efficiency function perform sufficiently well for direct stau samples other than DSID 396104. In figure 5.17, the electron and muon p_T distributions of the direct stau samples with DSID 398349 and 397017 are shown. For both samples, the agreement between the new smeared truth and reconstruction-level taus is sufficient and outperforms the agreement of the original smearing. However, for the more compressed sample with DSID 398349, the new smearing seems to slightly underestimate the electron reconstruction and ID efficiency.

The corresponding plots for the remaining direct stau process samples can be found in appendix A.1.2.

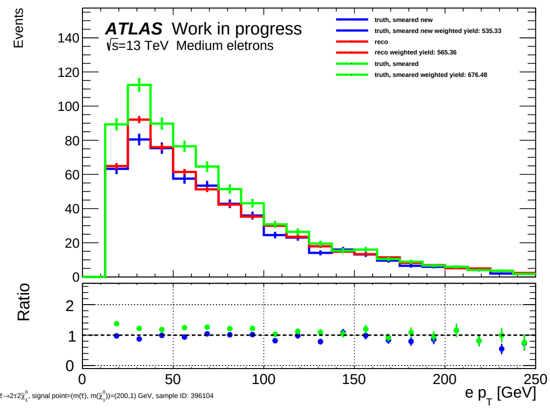

(a) electron p_{T}

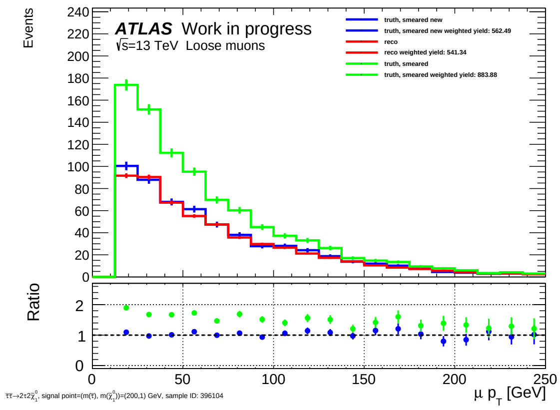

(b) muon p_{T}

Figure 5.16: Electron (a) and muon (b) p_{T} distribution for the new smeared and original smeared truth-level as well as the reconstruction-level electrons/muons for the direct stau sample with DSID 396104.

5.4 The Problem of Sample Dependence

The new SqSq and direct stau efficiency functions improve the performance of the truth smearing in most cases to an almost perfect agreement between smeared truth-level and reconstruction-level leptons. However, two aspects appeared to be quite problematic: first, due to a difference in the tau efficiency maps of the SqSq sample with DSID 378445 and the direct stau sample with DSID 396104, two separate tau efficiency functions had to be constructed, and secondly, for a more compressed SqSq sample, with DSID 378447, the new SqSq smearing showed an unsatisfactory performance. Both of these issues are actually results of a single problem: that of sample dependence in the tau reconstruction and ID efficiencies, i.e. the calculated efficiencies vary depending on the process and mass configuration of the sample used.
This sample dependence is a problem from a physical perspective: whether a tau lepton is reconstructed or not should not depend on the tau's history, i.e. the kind of process or the mass of the particle which decayed into the tau. One would expect that it only depends on properties of the tau itself or its relation with other final state particles which might influence the detector response or reconstruction.
From a pragmatic point of view, the sample dependence is an issue as well: one would wish to have a coherent tau efficiency function in the smearing so that the smearing has roughly the same performance for any sample, independently of the mass configuration or process. Especially for the pMSSM scan this is an important aspect, as a lot of different SUSY models with different mass configurations and processes have to be evaluated using truth smearing.
Therefore, the sample dependence of the tau lepton reconstruction and ID efficiency will be further scrutinised in this section and a possible way of resolving the dependence will be introduced.

5.4.1 Sample Dependence in Efficiency Maps

The difference in the efficiency maps for the SqSq and the direct stau sample in figure 5.8 gave a first hint about the existence of the sample dependence. To get a more comprehensive overview of the sample dependence in SqSq and direct stau samples, figures 5.18 and 5.19 show p_{T}-$|\eta|$-prongness efficiency maps for the remaining SqSq samples and the direct stau samples

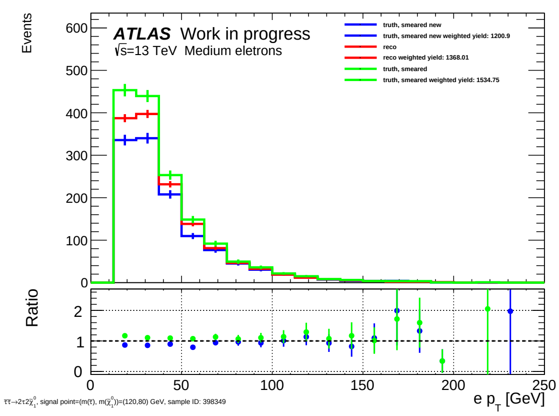

(a) electron p_{T}, DSID 398349

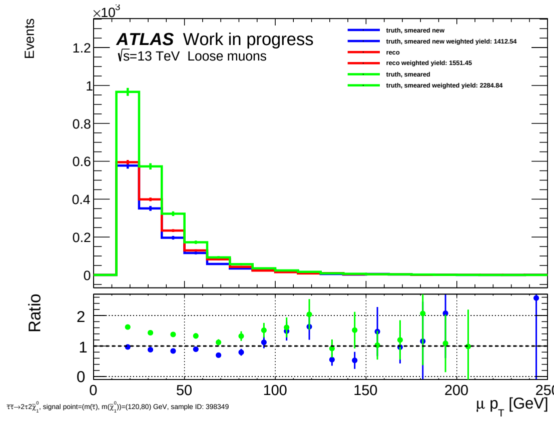

(b) muon p_{T}, DSID 398349

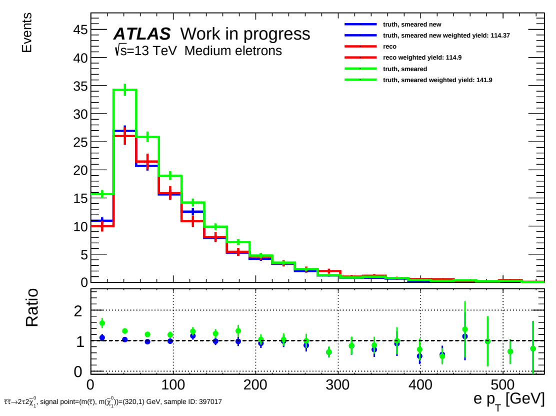

(c) electron p_{T}, DSID 397017

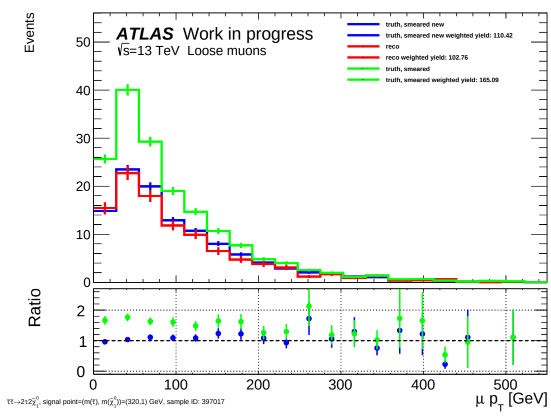

(d) muon p_{T}, DSID 397017

Figure 5.17: Electron (a) and muon (b) p_{T} distribution for the new smeared and original smeared truth-level as well as the reconstruction-level electrons/muons for the direct stau sample with DSID 398349. Below, the electron (c) and muon (d) p_{T} distributions for the direct stau sample with DSID 397017 can be found.

with DSID 398349 and 397017. These are the same samples that were used to test the performance of the new smearings on different mass configurations. The different histograms in the figure show very clearly how the efficiencies vary between samples of different processes and even between sample of the same process but with different mass configurations. As in figure 5.8, taus produced in the direct stau process achieve higher efficiencies than in the SqSq case. Additionally, one can already spot a pattern in the efficiency differences between samples with the same process: it seems that in samples with more compressed mass configurations, the efficiencies are generally lower.

It is important to note that one efficiency map extending to higher p_{T} than another is not a symptom of sample dependence. This is just the effect of a different p_{T} distribution. Only efficiency differences in the same p_{T}-$|\eta|$-prongness bin are implying this dependence. Also, in these kinds of histograms, it is generally best to compare bins with low statistical error as these contain the most meaningful efficiencies. It is therefore harder to compare the efficiency maps of samples with very different p_{T} or $|\eta|$ distributions, as in these cases discrepancies in the efficiency might just be the result of statistical fluctuations. However, as the mentioned pattern can be seen across all the efficiency maps, one has to assume its significance.

To see if the pattern persists in further processes, similar efficiency maps have been calculated for every SUSY sample in table 4.5 and the ttbar sample. As an example, figure 5.20 shows two C1C1 process samples with different mass configurations. Again, lower reconstruction and ID efficiencies can be observed in the sample with a more compressed mass spectrum

when comparing bins of the same p_{T}, $|\eta|$ and prongness.
The tau efficiency maps for the rest of the available samples can be found in appendix A.2.1. Furthermore, a rather short discussion of the sample dependence of the electron/muon reconstruction and ID efficiency alongside the electron/muon efficiency maps of the remaining direct stau samples are given in appendix A.2.2.

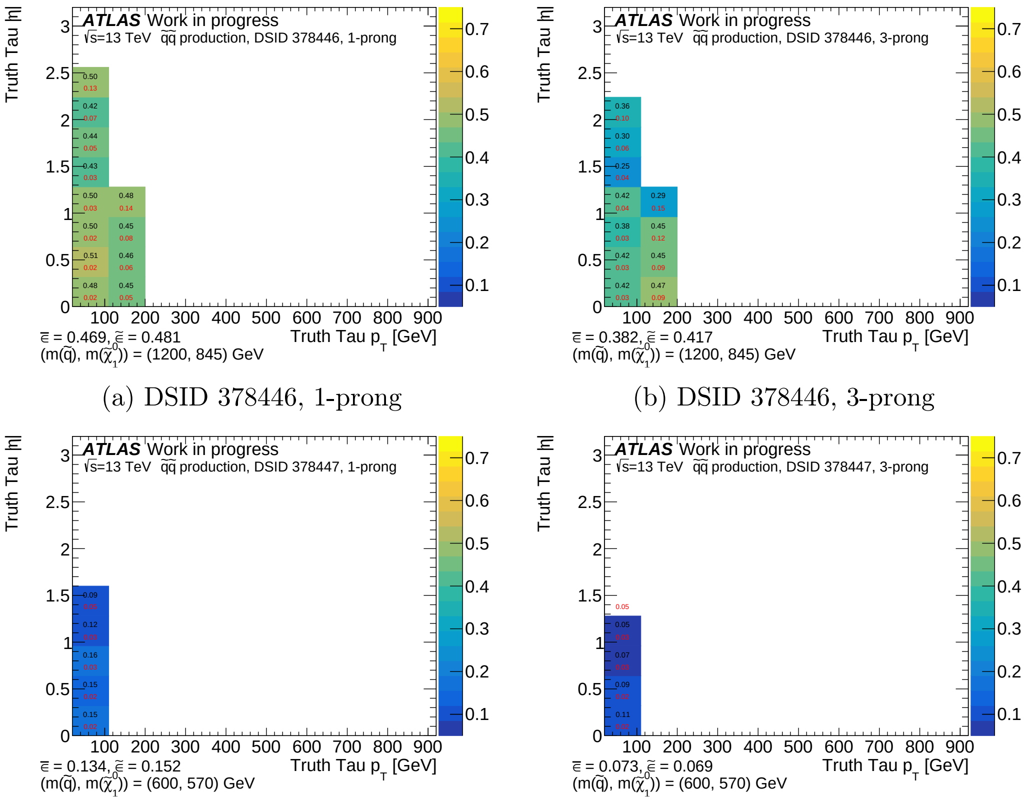

(a) DSID 378446, 1-prong

(b) DSID 378446, 3-prong

(c) DSID 378447, 1-prong

(d) DSID 378447, 3-prong

Figure 5.18: Tau reconstruction and ID efficiency maps in tau p_{T} and $|\eta|$ for 1-prong and 3-prong tau leptons of the remaining SqSq samples with DSID 378446 ((a) and (b)) and 378447 ((c) and (d)).

5.4.2 Properties of the Sample Dependence

The Mass Difference

To get a more comprehensive overview of the reconstruction and ID efficiency and its sample dependence, one might want to look at all available samples at the same time. In order to achieve this in a well arranged manner, p_{T}, $|\eta|$ and prongness dependencies will be neglected and instead the overall reconstruction and ID efficiency of a sample will be used. In figure 5.21, these overall efficiencies are plotted for the available samples in dependency of a sample's mass difference $\Delta m(\mathrm{X}, \mathrm{Y})$. $\Delta m(\mathrm{X}, \mathrm{Y})$ is the mass difference of the particles X and Y where X$\rightarrow \tau$Y, i.e. X decays into the tau and Y. This mass difference is a measure of how compressed a sample is. It is useful to formulate the previously observed pattern in a more quantitative way.

Figure 5.21 shows that for each studied process, the reconstruction and ID efficiency increases with higher mass difference up to a certain point. This would confirm the observed pattern

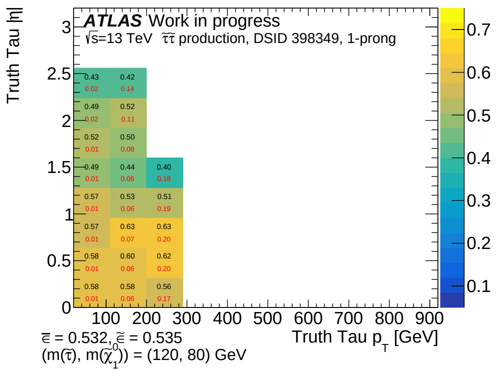

(a) DSID 398349, 1-prong

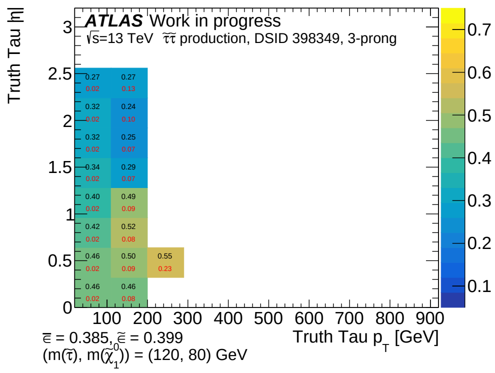

(b) DSID 398349, 3-prong

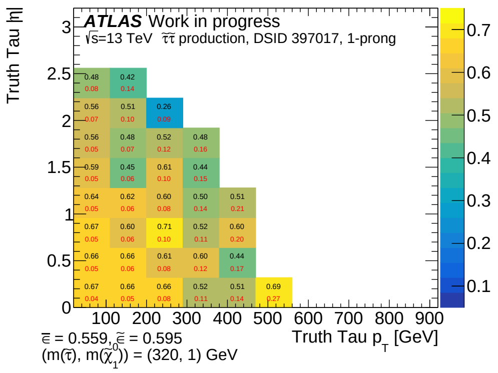

(c) DSID 397017, 1-prong

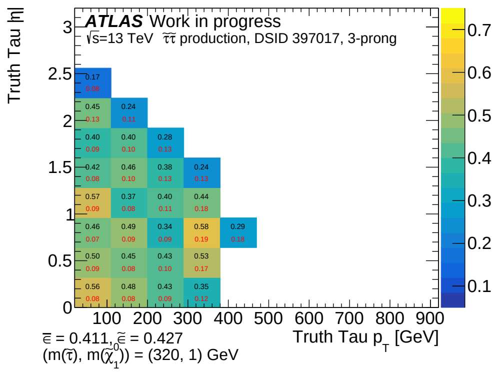

(d) DSID 397017, 3-prong

Figure 5.19: Tau reconstruction and ID efficiency maps in tau p_{T} and $|\eta|$ for 1-prong and 3-prong tau leptons of the direct stau samples with DSID 398349 ((a) and (b)) and 397017 ((c) and (d)).

in the efficiency maps. The ttbar process, where only one sample is available, seems to be in agreement with the behaviour of the GoGo process. Studying the sample dependence in this plot even more precisely, it seems that the efficiency increases rapidly in the compressed region while at intermediate $\Delta m(\mathrm{X, Y})$, the efficiency reaches some kind of maximum. For even higher mass differences, the efficiencies appear to be slightly decreasing, at least for the GoGo process and the ttStau process.

The Influence of Jets

Another interesting aspect in this plot is the sample dependence of the ttStau samples. Three of the samples have a rather low mass difference while the other three possess the highest shown in this plot. The pattern persists as the sample with a higher mass splitting also have higher efficiencies. However, in the case of the three high-$\Delta m(\mathrm{X, Y})$ samples, one can see that one of the model points has an efficiency significantly higher than the rest. This sample has the DSID 437368. When consulting table 4.5, the outstanding property of this sample seems to be a very small difference in the masses of the top squark and the tau slepton. This mass difference will be called the jet mass difference $\Delta m_{jet} = m_{\tilde{t}} - m_{\tilde{\tau}}$ as it dictates the amount of energy available to the decay products of the stop apart from the stau, namely the b quark and the tau neutrino, and only the b quark will leave a signal in the detector as a jet. This observation hints that a softer jet from the SUSY decay might be beneficial to the tau lepton reconstruction. Another effect to be aware of; however, it is not adequate to call it a pattern yet, as it has only been observed for one process.

This effect of the softness of jets from the SUSY jets is probably not as overt in the other

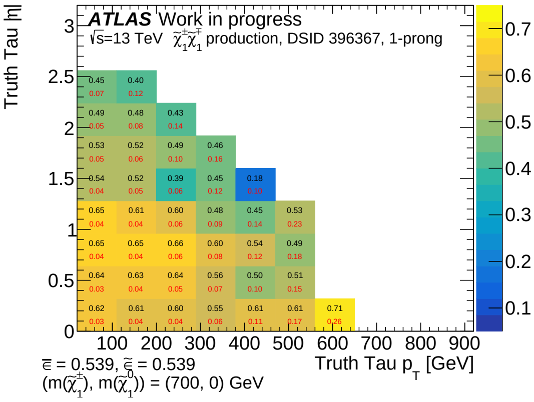

(a) DSID 396367, 1-prong

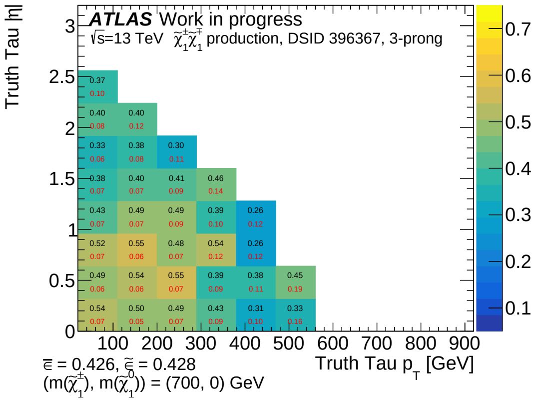

(b) DSID 396367, 3-prong

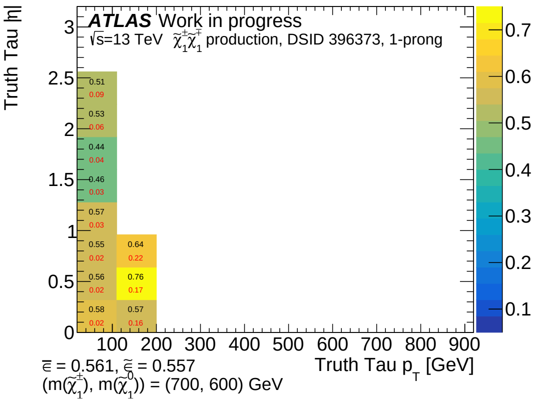

(c) DSID 396373, 1-prong

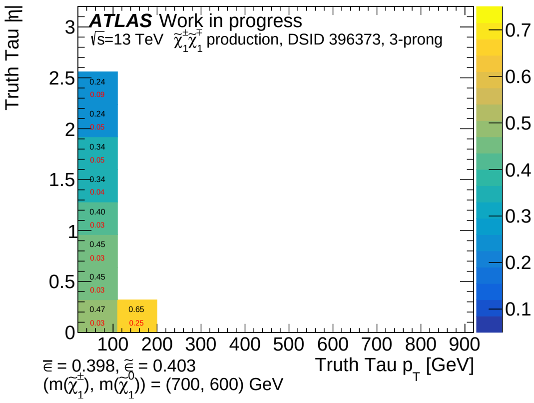

(d) DSID 396373, 3-prong

Figure 5.20: Tau reconstruction and ID efficiency maps in tau p_{T} and $|\eta|$ for 1-prong and 3-prong tau leptons of the C1C1 samples with DSID 396367 ((a) and (b)) and 396373 ((c) and (d)).

processes since on the one hand, in the direct stau and C1C1 case, the SUSY decay does not involve any jets. On the other hand, in the SqSq, GoGo and ttbar case, samples with the same Δm(X, Y), but different Δm_{jet} are not available as ttbar is a SM process with fixed masses and for the SqSq and GoGo simplified models, the relationship $\Delta m_{jet} = 2 \times \Delta m$(X, Y) always holds (see equation (2.20)).
One can, however, use this observation to propose an explanation of the efficiency differences between different processes. If the softness of SUSY decay jets has indeed an influence on the reconstruction and ID efficiency of the tau leptons, one would expect that the mere existence and number of jets in the process play a part as well. Then one would conclude that the direct stau and C1C1 process achieve the highest efficiencies for the same Δm(X, Y) in the absence of jets in their decay chain while the taus in the GoGo process have the lowest efficiencies due to the four jets in the decay chain (see section 2.3). This is indeed the behaviour observable in figure 5.21.

PHYS samples

Fortunately, a further investigation of the previously mentioned observations is possible with the available PHYS samples mentioned in section 4.5. With these samples, a more comprehensive study of the patterns in the direct stau, C1C1 and ttStau processes is possible as a lot more samples are available containing these processes. Figure 5.22 shows the efficiencies of the PHYS samples against the Δm(X, Y) of the respective model point.

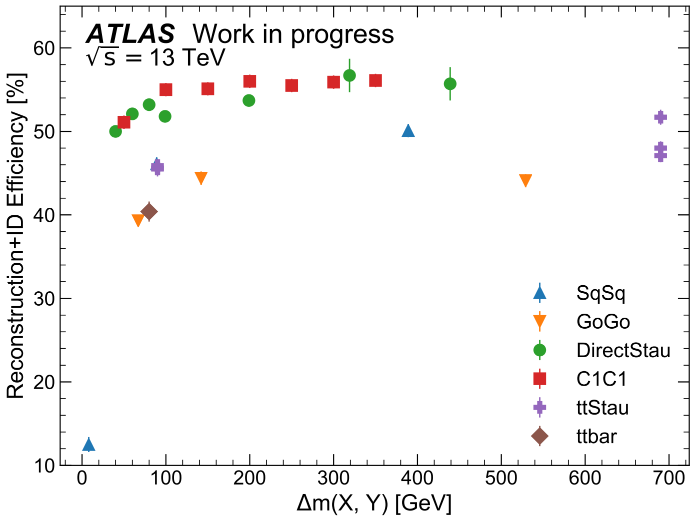

Figure 5.21: Overall reconstruction and ID efficiency on the vertical axis against the tau mass difference $\Delta m(\mathrm{X},\ \mathrm{Y})$ with X$\rightarrow$ τY for the available samples.

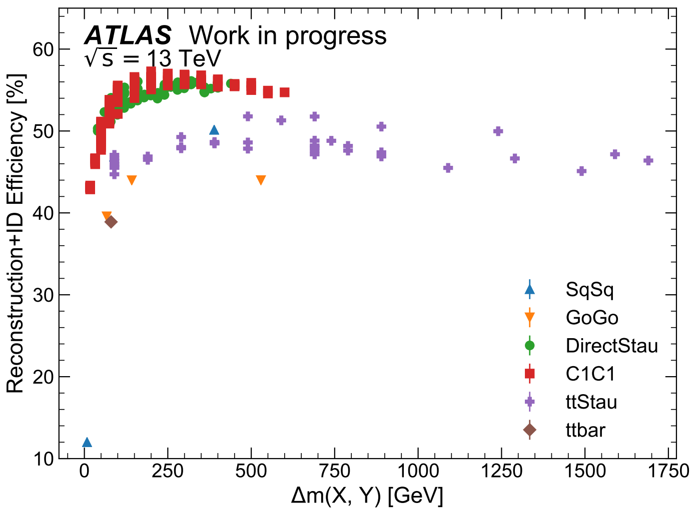

Figure 5.22: Overall reconstruction and ID efficiency on the vertical axis against the tau mass difference $\Delta m(\mathrm{X},\ \mathrm{Y})$ with X$\rightarrow$ τY on the horizontal axis for the PHYS samples.

In the case of the direct stau and C1C1 process samples, one can see the rapid increase in the efficiency until a certain mass difference where a plateau is reached and a subsequent slow decline in the efficiency at even higher $\Delta m(\mathrm{X},\ \mathrm{Y})$. This matches the observation made in figure 5.21 for the previously available samples.
However, one may notice that there are still efficiency differences among samples of the same $\Delta m(\mathrm{X},\ \mathrm{Y})$. These differences are due to varying masses of the initial produced particle m_1, i.e. the stau in the direct stau case and the lightest chargino in the C1C1 case. This influence of m_1 is shown in figure 5.23a where one can see that a higher initial particle mass coincides with higher efficiencies. In the direct stau case the behaviour is actually quite similar to the behaviour in the tau mass difference plot. In the C1C1 case, a structure of horizontal lines with a slight positive slope unfolds, each line corresponding to a different $\Delta m(\mathrm{X},\ \mathrm{Y})$.
The SqSq, GoGo, ttStau and ttbar model points open up the possibility for further investigation of the influence of the jet mass difference. Figure 5.23b shows the model points and their corresponding overall reconstruction and ID efficiency in dependence of both $\Delta m(\mathrm{X},\ \mathrm{Y})$

and the jet mass difference.
First, looking at the ttStau samples, one can see that Δm_{jet} only has a significant influence if it is very low as there, the efficiencies are increasing significantly. Also, it seems that the efficiencies peak at intermediate values of Δm(X, Y), declining slightly for both very low and very high Δm(X, Y). This seems to be in agreement with the behaviour of the direct stau and C1C1 process samples.
Then, looking at the SqSq, GoGo and ttbar samples, one is not able to make out the influence of Δm_{jet} as samples of the same tau mass difference are not available. One can, however, investigate the assumed influence of the number of jets in the decay chain. The SqSq process model points seem to be in agreement with the ttStau model points in the same region[8] which is consistent with the fact that both the SqSq and the ttStau process involve two jets. The GoGo and ttbar process samples appear to have the lowest efficiencies when compared to samples of other processes with the same Δm_{jet} and Δm(X, Y). This would be consistent with the number of jets in these processes, as GoGo involves four and ttbar involves four in most cases since the W boson decays predominantly into quarks[9]. The relatively small initial particle mass of the ttbar process might be responsible for the efficiency being lower than in the GoGo sample with a similar tau and jet mass difference.

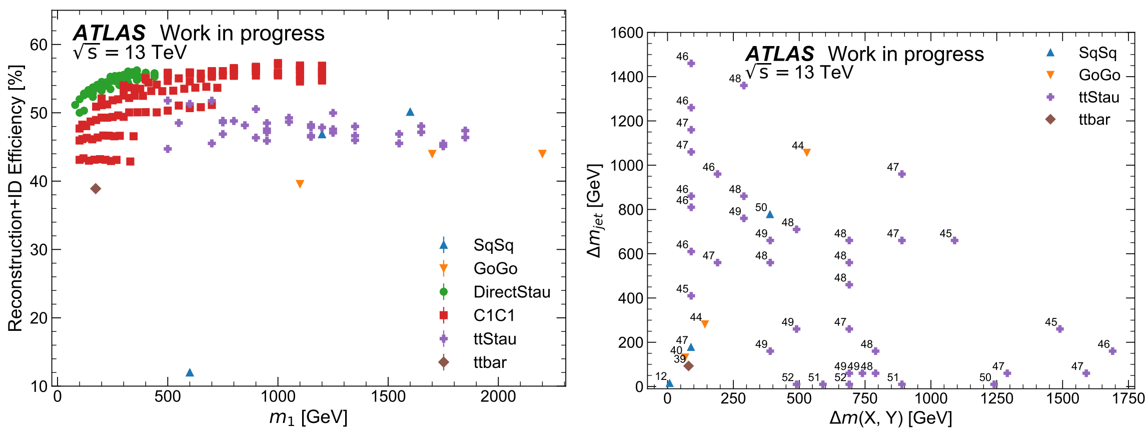

(a) (b)

Figure 5.23: On the left (a): Overall reconstruction and ID efficiency on the vertical axis against the mass of the initially produced particle m_1 on the horizontal axis for the PHYS samples. On the right (b): jet mass difference Δm_{jet} against Δm(X, Y) with X$\rightarrow \tau$Y for the PHYS samples. The reconstruction and ID efficiency in % of each model point is given as well, next to each marker. Due to space issues, the efficiencies are rounded to whole percentage points. The absolute uncertainty on the shown values is generally $< 0.6\%$.

5.4.3 Resolving the Sample Dependence

The sample dependence of the reconstruction and ID efficiency has been defined and it has been established how this phenomenon manifests itself across the sample spectrum available in this study. As this dependence on process and mass configuration is problematic both from a physical and a pragmatic point of view, one should aim to resolve this dependence.
The physical perspective might be helpful in this endeavour. It should be possible to reduce

[8] The DSID 378447 sample is of course not comparable to any other sample as it is the only sample with a tau mass difference this low.

[9] As at least one W has to decay leptonically for the event to contain a tau, around 65% of events containing taus will involve four jets and 35% will involve two.

the dependencies of the reconstruction and ID efficiency to properties of the tau or relations of the tau to other final state objects at generator level. A selection of such properties, i.e. tau p_{T}, η and prongness, was already used in the original smearing and in the efficiency maps previously calculated. However, these variables obviously were not able to completely resolve the sample dependency. Hence, more observables have to be at play here, and the patterns observed before when looking at the influence of certain properties of the model points on the efficiencies might help finding out which.

As quite some variables are possible candidates as influential parameters for the reconstruction and ID efficiency and the statistics per sample is quite limited, plotting efficiency maps will not be feasible. Trying different combinations of bins in many different observables to reach a completely sample-independent parametrisation with the available sample statistics turned out to be fruitless.

Instead, a different approach was chosen: classification with machine learning algorithms. An in-depth explanation of this alternative way to resolve the sample dependence will be given in the next chapter.

Chapter 6

Parametrisation of the Reconstruction and ID Efficiency

Up to now, improvements of the tau efficiency functions have been shown that result in a well performing truth smearing for tau leptons of a limited set of samples. It has been established that the sample dependence of the reconstruction and ID efficiency prohibits sufficiently accurate efficiency functions over a wider range of processes and mass configurations with the currently used parametrisation in tau p_{T}, η and prongness.
The conclusion was that a new parametrisation employing a more diverse set of observables is necessary to resolve the sample dependence. In this chapter, machine learning algorithms are used to find this parametrisation and to develop a sufficiently sample independent tau efficiency function for future tau truth smearing implementations.

6.1 Boosted Decision Trees

The machine learning method of choice in this study will be Boosted Decision Trees (BDTs). These are usually either used as regressors or as classifiers, where the latter will be important here. A short overview of the functionality of BDT classifiers and their usage in this study will be given in the following.

6.1.1 Theory

Decision Trees
To define a BDT, one has to define what a decision tree is first. A decision tree is a multivariate classification method, i.e. a method which makes use of a set of p input variables $\mathbf{x} = (x_1, ..., x_p)$ of an object to assign one out of K classes (e.g. 0,1,2,...,$K-1$) to this object. In the following, the case $K = 2$ is assumed.
In the end, the classification will be done by partitioning the feature variable space into different regions which are each assigned a certain class. If the observables $\mathbf{x}_i$ of an object i lie in a certain region, it will be assigned the corresponding class. The goal of the decision tree is now to find the best possible partition of the feature space to get an accurate classification of objects where the class is unknown. In order to achieve this, the decision tree is trained with some data, where both the features $\mathbf{x}_i$ and the class y_i of each object i is known [92].
A simple example of this procedure is shown in figure 6.1, where a set of two feature variables, X_1 and X_2, is considered. The partition of the feature space is acquired by recursively

splitting the space into two regions, i.e. first, a cut at $X_1 \leq t_1$ separates two regions and then each of these regions is further divided by a cut on one of the feature variables. This process is repeated for each new region until some stopping rule is applied which is referred to as the maximum depth of the tree. This partitioning can be visualised by a tree-like structure (see figure 6.1a) where at each node, a new cut is introduced to split up the feature space further — hence the name decision tree. An exemplary final partition is shown in figure 6.1b, where each region R_i now corresponds to the class that most of the training data objects belonged to in this region.

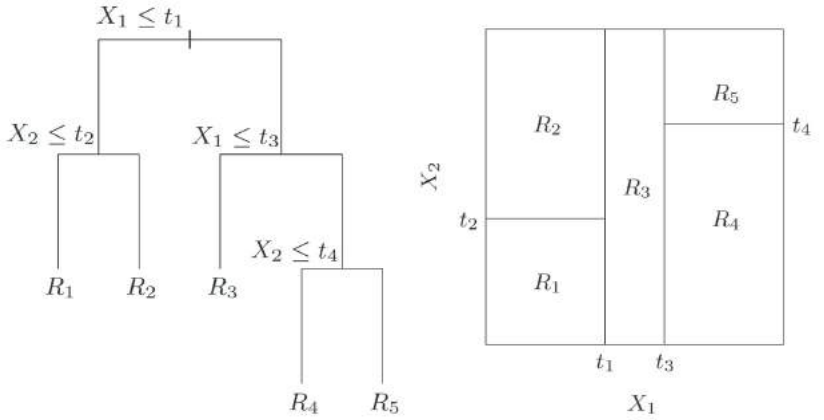

(a) (b)

Figure 6.1: An exemplary decision tree (a) corresponding to the partition of a two dimensional feature space (b). From [92].

Boosting

One single decision tree is usually a rather weak classifier. To improve the classification performance and its robustness, an ensemble of trees is used instead. The single trees are sequentially fit to the training data and for a classification of unknown data, a majority vote among the ensemble determines the final output. While this ensemble already performs better than a single tree [93], a further improvement can still be achieved by reweighting (boosting) the objects of the training data after each single decision tree fit. A BDT is such an ensemble of decision trees, where a boosting algorithm is used in each step, i.e. the training data is reweighted after each tree fit.

One very common implementation of this boosting is the Adaptive Boost (AdaBoost) algorithm: at each boosting step m, a single decision tree $h_m(\mathbf{x})$[1] is fitted to the training observations $(\mathbf{x}_i, y_i)$, $i = 1, ..., N$ where each object i is weighted with w_i^m. In the first step, the weights are set to $w_i^1 = \frac{1}{N}$. Then the misclassification/error rate err_m of this tree is calculated as the sum of weights of misclassified observations divided by the sum of weights of all observations[2]. This rate is then used to calculate the tree weight α_m of the decision tree as [92]

$$\alpha_m = \ln\left(\frac{1 - \mathrm{err}_m}{\mathrm{err}_m}\right), \tag{6.1}$$

with which only the misclassified training objects are reweighted for the next step:

$$w_i^{m+1} = \begin{cases} w_i^m & \text{if } i \text{ correctly classified} \\ w_i^m \cdot e^{\alpha_1} & \text{if } i \text{ misclassified} \end{cases} \tag{6.2}$$

[1]When $\mathbf{x}$ is in some region R_j of the feature space, $h_m(\mathbf{x})$ returns the class of higher probability (as evaluated from the training of the individual tree) in the region R_j.

[2]The error rate will satisfy $\mathrm{err}_m leq 0.5$ as an error rate of 0.5 corresponds to random guessing and a decision tree is specifically designed to have a better performance.

In the next step $m+1$, the next decision tree is fitted to the reweighted training objects. This process is repeated for a predefined number of steps/trees M. The classification of an object with the AdaBoost algorithm is evaluated through a weighted average of all trees [94]

$$y_{\text{predict}}(\mathbf{x}) = \frac{1}{M} \cdot \sum_{m=1}^{M} \alpha_m h_m(\mathbf{x}) \tag{6.3}$$

The advantages of AdaBoost are quite obvious: as α_m increases for a decreasing misclassification rate, decision trees of a high performance have a bigger impact and the training observations are reweighted in each step so that successive trees increasingly focus on misclassified objects.
However, the performance of the AdaBoost algorithm has been observed to degrade for data with a noisy setting, i.e. a large amount of outliers [92]. To define more robust techniques, the notion of loss functions has to be introduced.

Loss Functions
A loss function expresses the agreement between the decision tree prediction for the class $y_{\text{predict}}(\mathbf{x}_i)$ of a training object i and its actual class y_i. A boosting algorithm should aim to minimise such a loss function in each step to gradually increase the performance, i.e. the decision tree of step m, $h_m(\mathbf{x})$, is calculated as [95]

$$h_m(\mathbf{x}) = \arg\min_h \sum_{i=1}^{N} L(y_i, F_m(\mathbf{x}_i)), \tag{6.4}$$

where $L(y_i, F_m(\mathbf{x}_i))$ is the loss function and $F_m(\mathbf{x}) = F_{m-1}(\mathbf{x}) + h_m(\mathbf{x})$ is the sum over the previous decision trees. F_0 is defined as the constant value that minimises the loss function in the very first step.
An effective way of solving equation (6.4) is motivated by an taylor approximation of the loss function in F_m around F_{m-1}. The minimisation is then achieved by fitting the tree $h_m(\mathbf{x}_i)$ to the negative gradients g_i of the loss function [95], i.e.:

$$g_i = \left[\frac{\partial L(y_i, F(\mathbf{x}_i))}{\partial F(\mathbf{x}_i)}\right]_{F=F_{m-1}} \tag{6.5}$$

This method of minimising the loss is called gradient boosting. The final prediction of the BDT for an object with feature values $\mathbf{x}_i$ is then $y_{\text{predict}}(\mathbf{x}_i) = F_M(\mathbf{x}_i)$, where M is again the predefined number of trees. This prediction is further used to calculate the predicted probability of an object to belong to class 1, i.e. $p(y = 1|\mathbf{x})$[3]. The exact calculation depends on the loss function, however.

Interestingly, the AdaBoost algorithm can be retrieved from gradient boosting by employing an exponential loss function of the form:

$$L(y, F(\mathbf{x})) = e^{-yF(\mathbf{x})} \tag{6.6}$$

However, an algorithm less sensitive to noise can be achieved by using a binomial log-likelihood loss function, i.e.

$$L(y, F(\mathbf{x})) = \ln\left(1 + e^{-2yF(\mathbf{x})}\right), \tag{6.7}$$

which is the standard loss function of the gradient boosting algorithm used in this study. For the binomial log-likelihood loss, one can calculate the predicted class probabilities as follows:

$$p(y = 1|\mathbf{x}) = \sigma(y_{\text{predict}}(\mathbf{x})) = \frac{1}{1 + e^{-y_{\text{predict}}(\mathbf{x})}} \tag{6.8}$$

[3]The probability of the same object to belong to class 0 is obviously $p(y = 0|\mathbf{x}) = 1 - p(y = 1|\mathbf{x})$, as there are only two possible classes.

Here, $\sigma(x)$ describes the sigmoid function. This predicted probability will be the desired output of the BDTs in this study.

6.1.2 Application

First Settings
Now that the functionality of BDT classifiers for two possible classes have been explained, their usage in this thesis shall be discussed. Here, the goal of the BDTs will be to predict reconstruction and ID efficiencies based on a certain set of feature variables of truth-level tau leptons. Specifically, the BDT will predict the probability that a single truth-level tau will be reconstructed into a medium ID reconstruction-level tau. When averaging these probabilities over a certain set of taus, one could then talk about an efficiency. However, efficiency and probability will often be used in the same sense in the following. Therefore, the objects that the BDT will classify are truth-level taus and the two possible classes are

- truth-level tau not matched to a medium reconstruction-level tau ($y = 0$) and
- truth-level tau matched to a medium reconstruction-level tau ($y = 1$).

Hence, $p(y = 1|\mathbf{x})$ is the predicted reconstruction and ID efficiency/probability of a single truth-level tau with input variables $\mathbf{x}$. The taus of all available samples are combined into one file and then randomly split into a training sample to fit the BDT model and a test sample to check its performance. Around 75% of the taus enter the training and 25% the test sample. In this work, a classifier from the 'scikit-learn' software package based on a gradient boosting algorithm with binomial log-likelihood loss function is used [96]. A classifier based on the AdaBoost algorithm has been tested as well, but it resulted in worse results. This can be seen in the calibration plots in figure 6.2, where the actual reconstruction probability of the taus is shown depending on what probability the BDT algorithm predicted. Since the true reconstruction and ID probabilities for single truth-level taus cannot be calculated (they would either be 1 or 0), the predicted probabilities are separated into bins in which a true reconstruction and ID efficiency for the corresponding taus can be calculated. As can be seen, the AdaBoost algorithm shows a very bad calibration, i.e. it is not able to correctly predict probabilities smaller or greater than 0.5. The gradient boosting algorithm shows a good calibration, however.

Tuning
Furthermore, the BDT algorithms have multiple *hyperparameters* that can be tuned to ensure an optimal performance. In this study, three different parameters are varied:

- The number of trees M
- The maximum depth of the individual trees
- The learning rate ν

While the number of trees and the maximum depth have already been mentioned during the explanation of the functionality of BDTs, the learning rate needs further discussion. The learning rate ν scales the contribution of each tree in the following way [95]:

$$F_m(\mathbf{x}) = F_{m-1}(\mathbf{x}) + \nu h_m(\mathbf{x}) \tag{6.9}$$

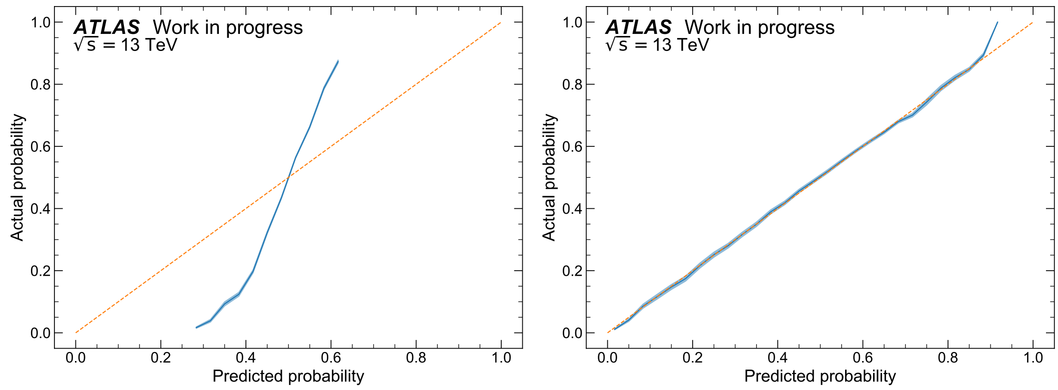

(a) AdaBoost

(b) Gradient Boosting

Figure 6.2: Calibration plots for an AdaBoost classifier (a) and a gradient boosting classifier (b) for the same input variables and BDT parameters. The horizontal axis is separated into 30 bins of the predicted probability and the vertical axis shows the corresponding actual probability of the taus in each bin. The actual probability is calculated as the true reconstruction and ID efficiency of the taus with a predicted probability inside a certain bin. The statistical uncertainty on the actual probability in a certain bin is shown by the light blue fringes of the curve.

It strongly interacts with the number of trees such that a smaller learning rate will require a larger number of trees to keep the training performance steady. For better performances on test samples, a small learning rate $\nu \leq 0.1$ is recommended [95] and therefore, a correspondingly high M. The maximum depth, like the number of trees, can also be used to increase the performance of the BDT algorithm.

Overtraining

There is a caveat to optimising the hyperparameters, though. When one uses too extreme values, e.g. a very high M without sufficiently low ν, one has to deal with a phenomenon called overtraining. Overtraining means that a BDT model is fitted not just to the actual, physical pattern necessary for the classification, but also to statistical fluctuations within the training sample. As these fluctuations are different in the training and the test sample, overtraining will reduce the performance in the test sample. One should aim to only train the BDT on physical patterns and avoid overtraining so that it will achieve similar results for any sample corresponding to the same physics.

Receiver Operating Characteristic Curves

One way to measure the performance of the BDT on some data is the receiver operating characteristic (ROC) curve. The ROC curve plots the false negative rate (FNR), i.e. the rate of class-0 objects being falsely classified as class-1, against the true positive rate (TPR), i.e. the rate of class-1 objects being correctly classified as class-1, for a decreasing classification threshold on the $p(y = 1|\mathbf{x})$ of the objects. Therefore, for well performing BDTs, the ROC curve would first go to high TPRs as the BDT correctly predicts high values of $p(y = 1|\mathbf{x})$ for the class-1 objects and only for low classification thresholds the curve would start going to high FNRs as the BDT correctly predicts low values of $p(y = 1|\mathbf{x})$ for class-0 objects. In figure 6.3a, a ROC curve of a BDT with a perfect performance is shown and in figure 6.3b, a ROC curve of a BDT with a significantly lower performance is shown. To measure the performance of the BDT quantitatively from the ROC curve, one can calculate the area under the curve (AUC), i.e. the area between the ROC curve and the horizontal axis. A perfect ROC curve would have an AUC of 1, the ROC curve of a BDT corresponding to random guessing (e.g.

giving every object $p(y = 1|\mathbf{x}) = 0.5$) would have an AUC of 0.5.

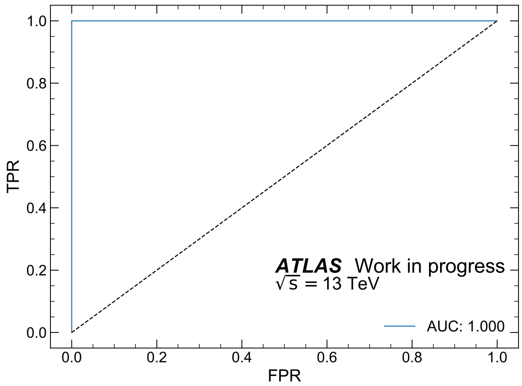

(a) AdaBoost

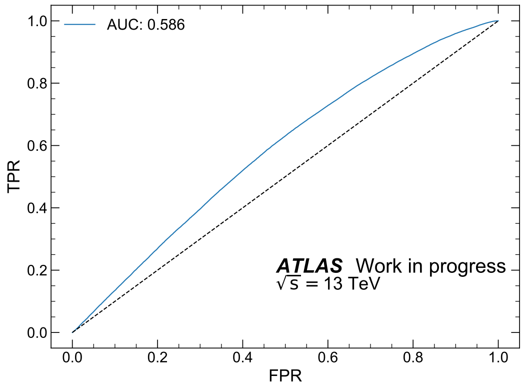

(b) Gradient Boosting

Figure 6.3: ROC curves for a BDT which classifies every object correctly (a) and a BDT with a significantly worse performance. The corresponding AUC is given in the legend.

As ROC curves give a measure of the performance of a BDT on some dataset, they can be used to spot overtraining by comparing the ROC curves of a certain BDT applied on both the training and a test sample. In figure 6.4, an example of an overtrained BDT is shown, clearly indicated by a significantly better ROC curve for the training than the test sample. This BDT was overtrained by using a very high $M = 3000$, a ν close to 1 and a rather high maximum tree depth of 8.

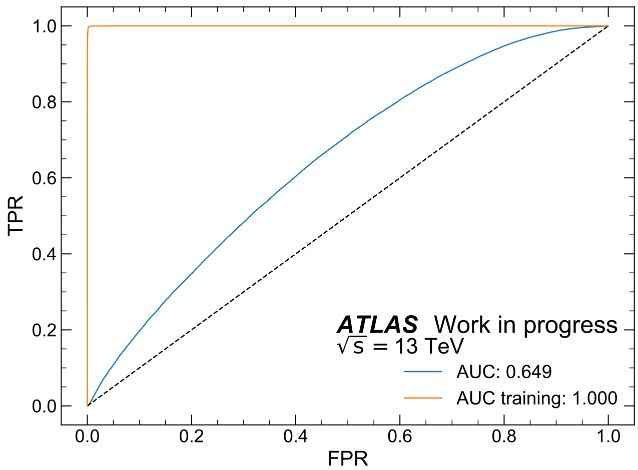

Figure 6.4: ROC curves for the BDT prediction for its training and a test sample with the BDT being overtrained.

6.2 Feature Optimisation

With the BDT set up to predict tau reconstruction and ID efficiencies and with the key BDT specific hyperparameters for optimisation defined, one can focus on the first goal set for this chapter: finding a better parametrisation for the reconstruction and ID efficiency. To achieve this goal, it will be determined which observables are needed in order to get predicted reconstruction and ID efficiencies from a BDT in good agreement with the true calculated efficiencies. Hence, a range of variables motivated by the observations in section 5.4 are used as input features for the BDT and then, a reduction of this range to the core observables needed for a good performance is done.

6.2.1 Input Variables

As has already been mentioned in section 5.4, there are two kinds of observables that can influence the tau reconstruction and ID efficiency from a physical point of view: properties of the truth tau itself and its relation to other final state objects that might affect the detector response to the truth-level tau. Both types of observables will be used as initial feature variables of the trained BDTs.
Objects used to define these variables obviously have to be at generator-level to be a possible input in a tau efficiency function in the truth smearing. Hence, the objects will not always be explicitly labelled as truth-level in the following. If a reconstruction-level object is mentioned, it will be explicitly labelled as reconstruction-level.

Tau Properties
In the efficiency maps shown in the previous chapter, the reconstruction and ID efficiency has already been parametrised in the truth tau properties p_T, $|\eta|$ and prongness. Apart from these, three more tau-specific observables were used, making a total of six tau properties as input for the BDTs:

- Truth tau p_T: In the development of the new SqSq and direct stau smearing, it has already been pointed out that the efficiencies depend on the tau p_T as the efficiencies were decreasing for higher p_T. Also, since the mass difference $\Delta m(\mathrm{X},\ \mathrm{Y})$ determines how much energy the tau has at its disposal, the tau p_T might be one factor contributing to the sample dependency seen in this mass difference.

- Truth tau $|\eta|$: Similar to the tau p_T, a dependency of the efficiency on this variable has already been established in the previous chapter. Higher $|\eta|$ seemed to correspond to lower efficiencies. Boosted event topologies as well as the more difficult reconstruction of forward objects might lie at the heart of this dependence.

- Truth tau prongness: As for tau p_T and $|\eta|$, a higher number of charged tau decay products corresponded to lower efficiencies.

- Truth tau neutral products: Since the number of charged tau decay products plays a role in the reconstruction of the tau, one might also expect the number of neutral tau decay products to be of importance.

- Truth tau ϕ: Another additional tau property is the azimuthal angle ϕ of the tau. Due to the cylindrical symmetry of the detector, one might not necessarily expect a dependence of the efficiency on this observable. As correlations with other variables might make ϕ important against expectations, it is included in the initial set of features.

- Truth tau Q: Similar to ϕ, it is not expected that the charge Q of the tau has an influence on the reconstruction and ID efficiency. Again, to make sure this expectation holds, this observable is included.

Other Objects

From a physical perspective, not only the properties of the tau itself, but also other final state objects of the respective process might influence the tau reconstruction and ID efficiency. Especially jets should affect the efficiency as the sample dependence on the jet mass difference and the number of jets in the decay chain suggests. Therefore, the following observables are included in the features of the BDTs:

- min(dR(truth tau, truth tau-jet)): This observable is defined as the angular distance ΔR between the truth tau and the nearest jet. This nearest jet can be assumed to be the jet caused by the decay of the tau itself, therefore this nearest jet will be called the 'tau-jet' in the following. As the definition of truth jets allows for the inclusion of objects not stemming from the tau decay into the tau-jet as well as for the exclusion of eventual tau decay products — both of which would change the direction of the tau-jet barycentre — the variable min(dR(truth tau, truth tau-jet)) is not necessarily zero.
  This observable therefore measures, how much the barycentre of the tau-jet is displaced from the true (visible) tau direction through a not entirely correct clustering of objects to form the tau-jet. High values in this variable indicate either contamination of the tau decay cone with other objects or a very wide tau decay cone. In both cases, one would expect a lower reconstruction and ID efficiency.
- min(dR(truth tau, truth jet)): This observable is defined very similar to min(dR(truth tau, truth tau-jet)). However, instead of the distance to the nearest jet (i.e. the tau-jet), the ΔR to the nearest jet that is not originating from a tau decay is taken. This distinction is possible due to the ConeTruthLabelID of the jets which determines the particle initiating the jet, i.e. light, c- or b-quarks or a tau lepton, by matching the respective initiating truth particle to the jet.
  Hence, while min(dR(truth tau, truth tau-jet)) measures the angular distance of the tau and its own tau-jet, min(dR(truth tau, truth jet)) measures the ΔR of the tau and the nearest non-tau jet. Rather low values of this observable might indicate overlapping of the hadron shower cones of the non-tau jet and the tau decay jet. Even though overlap removal is not used in this work, this might have consequences for the reconstruction and ID efficiency through contamination of the tau jet.
- min2(dR(tau, jet)): This observable is an alternative attempt to measure the distance of the tau to the nearest non-tau jet without relying on the ConeTruthLabelID. In this case, the ΔR between the tau and its second nearest jet is taken. As it is assumed that the nearest jet is the tau-jet itself, the second nearest jet would be the nearest non-tau jet — when neglecting the case of another tau lepton being nearby.
- Nearest jet p_{T}: The nearest jet p_{T}, i.e. the p_{T} of the tau's nearest non-tau jet, is an observable that might have a direct connection to the jet mass difference pattern of the sample dependence. To investigate this possible connection, this variable is used in the initial BDT feature space as well.
- Tau-jet p_{T}: The tau-jet p_{T} is the p_{T} of the tau's nearest jet, i.e. its tau-jet. This observable should be very similar to the truth tau p_{T}, but effects with an influence on the reconstruction might be hidden in the correlation between these two variables.
- Leading jet p_{T}: The leading jet of an event, i.e. the jet of highest momentum, does not necessarily influence the tau reconstruction directly. However, the leading jet might be radiated off back-to-back to the SUSY/ttbar process as ISR, hence boosting the whole event topology. This could in turn influence properties of the tau itself or its distance to other decay products. Therefore, the leading jet p_{T} could be important through correlations with other observables.

- N_{jet}: This observable gives the number of truth jets in the same event as the tau lepton. Since the sample dependence shows a pattern regarding the expected jets in a certain process's decay chain, this variable might be relevant to the reconstruction and ID efficiency. One would also expect that a high N_{jet} increases the probability of a tau-jet being contaminated with the constituents of other jets, thus influencing the reconstruction and ID efficiency.
- N_{τ}: This observable gives the number of truth taus in the same event as the covered tau lepton (counting the covered tau itself as well). Similar to N_{jet}, this observable might increase the probability of contamination in the tau-jet.
- N_e: N_e is the number of truth electrons in the same event as the tau lepton. A high number of electrons might again increase the probability of contamination of the tau-jet and therefore trigger the discrimination algorithms against electron misidentification. However, as the only electrons in the studied processes come from leptonically decaying tau leptons (and W bosons in the ttbar process), very few taus will 'share' an event with more than one electron. Hence, it is not expected that electrons have a great influence on the tau reconstruction and ID efficiency.
- N_{μ}: N_{μ}, i.e. the number of truth muons in the same event as the tau, is considered as well. However, as the misidentification of muons is not of concern in the tau reconstruction and muons are not very abundant in the studied processes, this variable is not expected to be very influential.

Correlations
It should have become clear that a few of the presented variables are correlated. This can be seen in figure 6.5, where the correlation coefficient of any pairing of the presented observables is shown[4]. Very high correlations between two variables indicates that one of them is redundant while a certain degree of correlation can be beneficial for the BDT's performance. From the correlation matrix, one can deduce that some of the variables might be redundant due to their correlations.
Apart from redundancies through correlations with other variables, one should also aim to eliminate those observables that are only of small benefit for the BDT's performance. In the end, one would want to have a reduced set of core variables which parametrise the reconstruction and ID efficiency best.

6.2.2 Measure of Success

In order to find this set of core observables, one has to measure how successful the BDT is in predicting the reconstruction and ID efficiencies with a certain set of input features. The set should be as small as possible, but result in successful efficiency predictions.
First, however, a BDT will be trained using all of the previously mentioned variables as features. This way, one gets a first estimate of the prediction power of BDT algorithms when it comes to the tau reconstruction and ID efficiency. The hyperparameters for this BDT are: $M = 1000$, $\nu = 0.04$ and 3 as maximum depth of the trees.

[4]The correlation of two variables, e.g. v_1 and v_2, describes how much one of the variables depends on the other. A correlation coefficient of 1 would mean that when v_1 increases, v_2 has to increase at the same rate and a correlation coefficient of -1 means that when v_1 increases, v_2 has to decrease at the same rate. Independent variables have a correlation coefficient equalling 0.

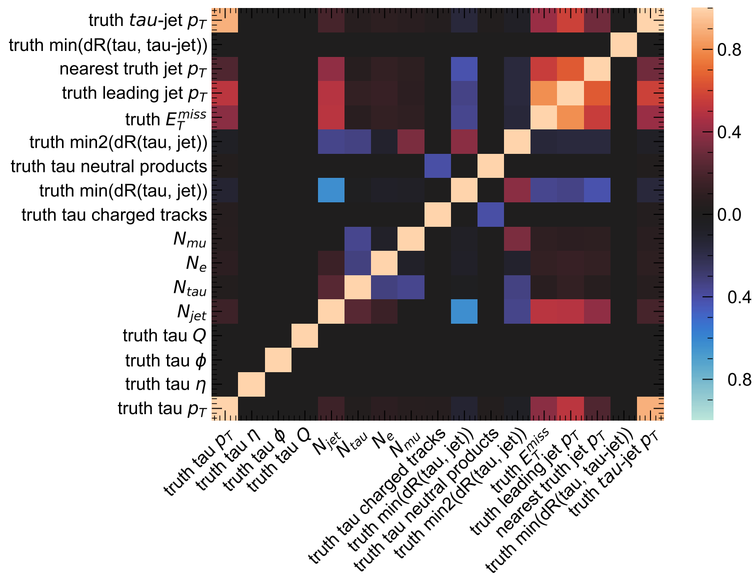

Figure 6.5: Correlation matrix of all considered input variables for the BDTs. The value of the correlation coefficient is indicated by the colour, the z-axis translates the colour scheme to the coefficients.

AUC

One way to estimate the performance of a BDT has already been mentioned: the AUC of the ROC curve. The hyperparameters of the BDT using all variables have been chosen such that overtraining is avoided, as can be seen in figure 6.6. The AUC of this BDT is around 0.73 for both the training and the test sample. From this value, one can deduce that the BDT is not perfectly predicting the reconstruction and ID probabilities of the taus. However, it is not really possible to see from this value if the predictions are sufficiently accurate.

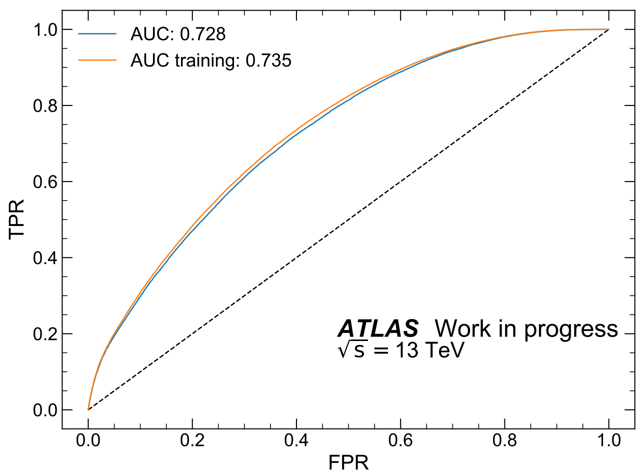

Figure 6.6: ROC curves for the BDT prediction for the training and a test sample. The BDT was trained using all variables described in 6.2.1 and the hyperparameters were adjusted in order to avoid overtraining.

Calibration

Another indicator of the performance of the BDT is the calibration curve. This curve showed the accuracy of the prediction in different regions of the predicted probability $p(y = 1|\mathbf{x})$ of the tau. Hence, the calibration curve shows how well the BDT performs in parameter space regions where the reconstruction and ID efficiency is either very high or very low. Apart from that, this curve does not quantitatively state how accurate the predictions are and is therefore not a suitable measure of successful prediction as well. The calibration of the BDT with all variables as features can be seen in figure 6.7, showing that the predicted probabilities agree reasonably well with the actual efficiencies up until quite high $p(y=1|\mathbf{x})$.

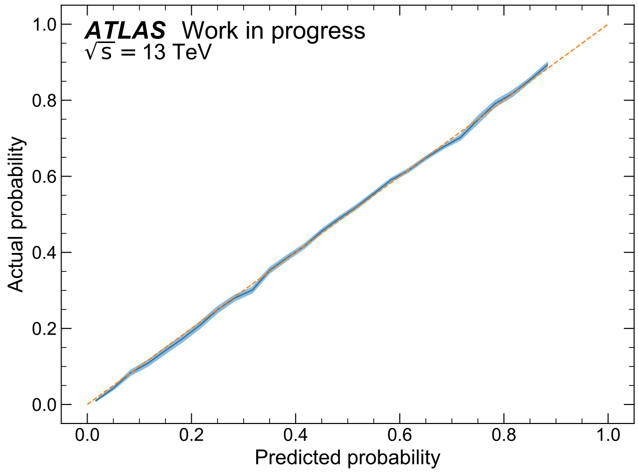

Figure 6.7: Calibration curve of the BDT when applied on the test sample in 30 bins. The BDT was trained using all variables described in 6.2.1.

Mean Squared Error

As the AUC and the calibration cannot give a meaningful conclusion on how well the predicted and the true reconstruction and ID efficiencies agree, another measure of this agreement is proposed: the sample-specific mean squared error (MSE).

The sample-specific MSE is defined for a certain binning in p_{T} and $|\eta|$ as:

$$\mathrm{MSE} = \left\langle \frac{(\varepsilon_n^{pred} - \varepsilon_n^{actual})^2}{(\sigma_n^{actual})^2} \right\rangle_{n\in\mathrm{bins}} \tag{6.10}$$

Here, ε_n^{pred} is the predicted and ε_n^{actual} the actual, calculated reconstruction and ID efficiency and σ_n^{actual} the statistical error on the calculated efficiency, all defined in the bin n. $\langle ... \rangle_{n\in\mathrm{bins}}$ indicates that the mean of all bins n is taken. In the following, the same binning is used for all calculations of the sample-specific MSE:

$$p_{\mathrm{T}}\ [\mathrm{GeV}] \in [20,30],\ ]30,40],\ ]40,80],\ ]80,120],\ ]120,200],\ ]200,350],\ ]350,2000] \tag{6.11a}$$
$$|\eta| \in\ ]0,0.5],\ ]0.5,1],\ ]1,1.5],\ ]1.5,2],\ ]2,2.5] \tag{6.11b}$$

The binning is chosen to be this fine in order to check that the predicted efficiencies model the tau p_{T} and $|\eta|$ distributions well enough. Since in most simplified model analyses, these two variables are the key tau properties[5] used to define the signal regions, the predicted efficiencies should not only ensure the same abundance of smeared truth-level and reconstruction-level taus but also a similar p_{T} and $|\eta|$ distribution.

This sample-specific MSE can now be used to define what is meant by 'successful prediction'. The MSE gives the squared differences of prediction and truth with respect to the efficiencies, weighted by the squared statistical error. Therefore, an MSE of around 1 would mean

[5] Tau ϕ is used quite often as well, but it will turn out that this variable is not relevant for the reconstruction and ID efficiency.

that the predicted efficiencies differ from the actual efficiencies at the order of the statistical uncertainty. For the time being, this will be the condition for a prediction to be sufficiently accurate.
The sample-specific MSE is shown in figure 6.8 for the available samples where the predicted efficiencies are given by the BDT trained on all variables. As can be seen, most of the samples' MSEs and the average are well below 1, indicating that this BDT yields a sufficient performance. The hyperparameters given before were actually derived by optimising the MSE distribution and avoiding overtraining. However, some samples have a MSE above one: DSID 378448, i.e. the GoGo sample with the lowest Δm(X, Y) and the two direct stau samples 396104 and 397017. For the GoGo sample the reason of the relatively bad performance might lie in its uniqueness, since only a few SqSq and GoGo samples are available and only two of them have a rather compressed mass constellation. Therefore, the training of the BDT might not have been able to fully embrace the physical patterns relevant for the reconstruction and ID efficiency in these samples. In the case of the direct stau samples, there appears to be no obvious reason for the MSE being bigger than one.

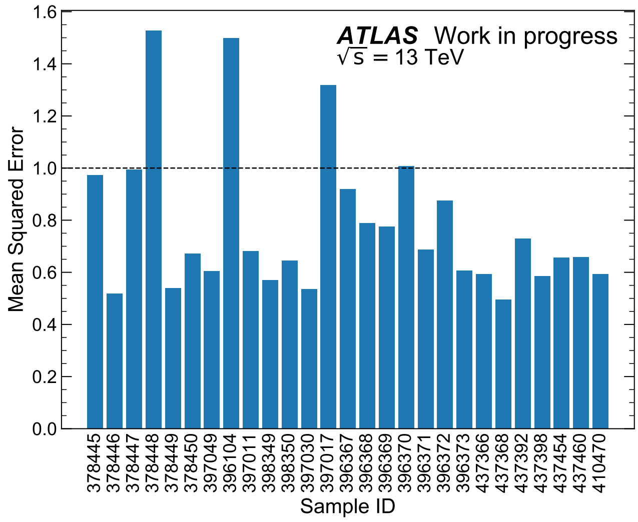

Figure 6.8: Sample-specific MSEs for the available samples. The BDT trained with all variables was used to calculate the predicted efficiencies.

Now that a meaningful measure for the success of the prediction has been established, the reduction of the current set of variables to a more compact set of core variables can be accomplished.

6.2.3 Final Set of Variables

Feature Importances

To get a first idea which of the aforementioned variables are needed for a parametrisation of the reconstruction and ID efficiency, one can look at the feature importances. The feature importances give the relative importance of each feature variable and the importances of all features sum up to 1. To calculate these, the gini/impurity importance is employed. This measure gives the sum over the discriminatory power of all tree nodes that involve a cut on the respective variable, averaged over all trees [97]. Therefore, the observables obtaining the highest feature importances in the BDT that was trained with all variables are natural candidates for the reduced set of core variables. In figure 6.9, the feature importances for all variables are shown. In this plot, seven variables stand out that seem to be crucial variables

for the prediction. These are: Truth tau p_{T}, $|\eta|$, prongness and the number of neutral products of the tau decay as well as min(dR(truth tau, truth tau-jet)), min(dR(truth tau, truth jet)) and the truth tau-jet p_{T}. Hence, the three variables already used for the efficiency maps and four new ones.
At this point however, it should be pointed out that the gini importance is not a perfect ranking of the used features. Variables that have a high number of possible outcomes, i.e. especially continuous variables, are preferred and tend to get higher importances. Therefore, variables like N_τ would be underestimated. Hence, in addition to the initial scouting using the feature importances, many different BDTs with different combinations of variables as input features were trained and the MSE distributions compared.

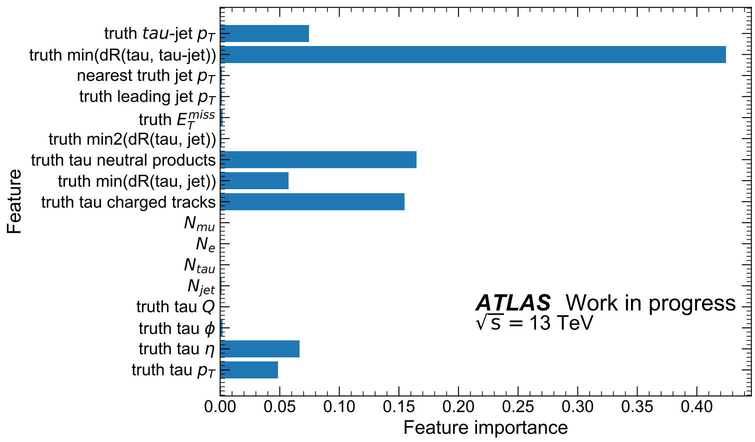

Figure 6.9: Feature importances calculated with the gini impurity for all variables in the training of the BDT that was trained with every observable.

The best performing, final set of variables was actually in good agreement with the set preferred by the feature importances, consisting of the following six variables:

- Truth tau p_{T}
- Truth tau $|\eta|$
- Truth tau prongness
- Truth tau neutral products
- min(dR(truth tau, truth tau-jet))
- min(dR(truth tau, truth jet))

The p_{T} of the tau-jet did not end up in the final set as its correlation to the truth tau p_{T} was so high that it turned out to be redundant. Now, this final set of variables will be put under further scrutiny to figure out how they influence the reconstruction and ID efficiency and how they are able to resolve the samples dependence.

Tau p_{T}
The fact that the reconstruction and ID efficiency is somewhat dependent on the tau p_{T} has already been seen in the efficiency maps of the previous chapter. In figure 6.10a, the efficiency is shown in different regions of the truth tau p_{T} for the SqSq and GoGo samples. It shows that the tau reconstruction and ID efficiency peaks at intermediate p_{T} of around 50 GeV –

100 GeV, but decreases both to higher and lower p_{T}. This behaviour can be seen for the other processes as well (see appendix B.1). The sample dependence is still quite obvious as samples of lower Δm(X, Y) and GoGo samples have lower efficiencies across the p_{T} spectrum.
Nevertheless, the tau p_{T} is contributing to resolving the sample dependence, as can be seen from the truth tau p_{T} distributions of the SqSq and GoGo samples in figure 6.10b. Samples of higher mass difference tend to have broader p_{T} distributions. This is again true for samples of different processes as well (see appendix B.1). This can be explained by the fact that a bigger Δm(X, Y) results in a higher amount of energy that the tau can potentially gain from the decay of the particle X. Hence, its momentum can reach higher values and the p_{T} distribution is broader.
In combination with the efficiency pattern for different tau p_{T} in figure 6.10a, it can be deduced that samples with a very compressed or very broad mass configuration will achieve lower efficiencies because of their p_{T} distribution. This is exactly the sample dependence which has been seen for samples of different Δm(X, Y).
In conclusion, the tau p_{T} being in the final set of variables makes sense not only because it is important to model the p_{T} distribution well in the smearing, but also because it helps resolving the sample dependence.

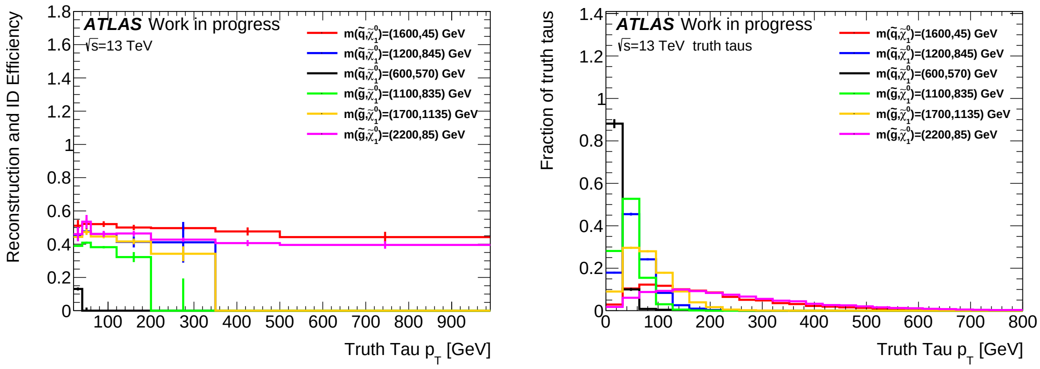

(a) SqSq/GoGo

(b) SqSq/GoGo

Figure 6.10: Left (a): Reconstruction and ID efficiencies calculated in different regions of p_{T} for the SqSq and GoGo samples. Right (b): p_{T} distribution for the SqSq and GoGo samples. The samples are labelled according to their mass configuration.

Tau $|\eta|$

The best examples for the influence of tau $|\eta|$ on the reconstruction and ID efficiency are the direct stau samples. The efficiencies in different regions of $|\eta|$ can be seen in figure 6.11a. It shows a small drop in the efficiency at $|\eta| \approx 1.4$ which is the approximate location of the crack region. After this drop, the efficiencies generally stay at a lower level than at small $|\eta|$. The same behaviour is observed for the other processes as well (see appendix B.1). The sample dependence is not as obvious as in the SqSq/GoGo case before, since the sample dependence is not as prominent in the direct stau process samples — even in figure 5.21.
When looking at the tau $|\eta|$ distribution of the direct stau samples in figure 6.11b, it becomes clear why this variable is needed to resolve the sample dependence as well. The plot shows that samples with a higher initially produced particle mass have $|\eta|$ distributions peaked at low values (e.g. the yellow sample) while a smaller initial mass results in a broader distribution (e.g. the magenta sample). A similar behaviour is also seen for other processes (see appendix B.1). However, at very high masses of the initially produced particle, the effect is no longer as prominent. This is illustrated by the $|\eta|$ distributions of the SqSq and GoGo samples in figure 6.11c as these have quite high initial masses. The reason for this dependence on the initial

mass lies in the pp collision itself. In order to produce particles of higher masses, the partons colliding need to possess an increasingly similar fraction of the proton momentum. If the momentum fractions of the partons were asymmetric, one of the partons would need to have a very high fraction, which is unlikely compared to the case of similar fractions. Therefore, higher initial masses demand a higher symmetry in the parton momenta which results in the process being less boosted in the z-direction. This, in turn, results in lower pseudorapidities of the participating particles, hence the more peaked $|\eta|$ distribution for high initial masses. Combined with the dependence of the reconstruction and ID efficiency on $|\eta|$, samples with a smaller initial mass should have lower efficiencies. This aspect of the sample dependence has been initially observed in figure 5.23a.

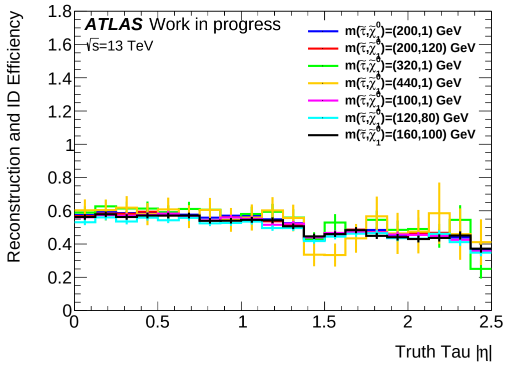

(a) Direct Stau

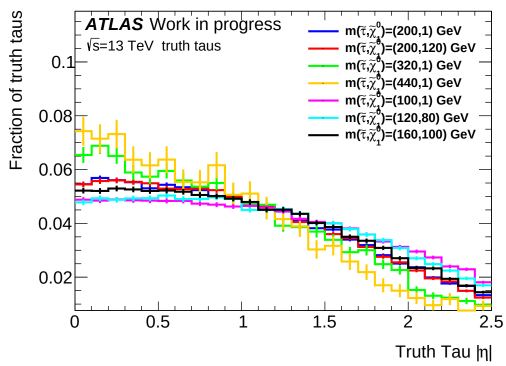

(b) Direct Stau

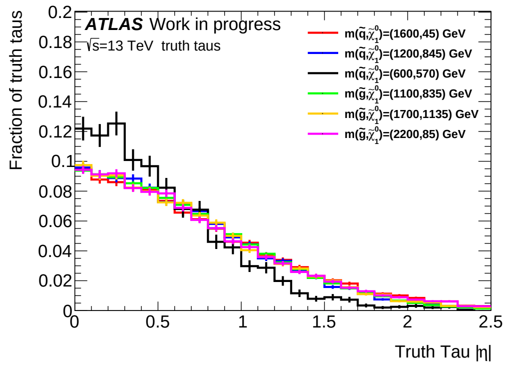

(c) SqSq/GoGo

Figure 6.11: Upper left (a): Reconstruction and ID efficiencies calculated in different regions of $|\eta|$ for the direct stau samples. Upper right (b): $|\eta|$ distribution for the direct stau samples. Below (c): $|\eta|$ distribution for the SqSq and GoGo samples. The samples are labelled according to their mass configuration.

Tau Prongness

Prongness is quite obviously influencing the tau reconstruction and ID efficiencies, as could be seen in the efficiency maps of the last chapter. There and in figure 6.12a one can see that 1-prong taus have a higher probability to be reconstructed and pass the ID criteria than 3-prong taus. This is true for any process, not just the SqSq and GoGo process shown in this plot (see appendix B.1). An obvious reason for this is the fact that the target ID efficiencies defined in table 4.3 are significantly lower for 3-prong taus.

Furthermore, the tau prongness actually depends on the sample's mass splitting, as can be seen in figure 6.12b for the SqSq and GoGo samples. A lower $\Delta m(\mathrm{X}, \mathrm{Y})$ tends to increase the fraction of 3-prong tau leptons. The reason for this is not trivial as the prongness of truth taus should only depend on the decay mode which is naturally not sample dependent. However, as the visible p_{T} of the truth taus is used, a higher fraction of 1-prong taus is cut away when setting lower limits on the p_{T}. Since the visible p_{T} neglects the tau neutrinos and these get an increasing fraction of the tau momentum in the decay for a smaller amount of hadronic decay products, 1-prong taus are more abundant in the lower tail of the p_{T} distribution than 3-prong taus. In the samples with a smaller mass splitting, a higher fraction of taus have a $p_{\mathrm{T}} < 20$ GeV, i.e. below the selection cut stated in the object definition, and therefore more 1-prong taus will be cut away than 3-prong taus, resulting in a relatively high fraction of 3-prong taus.

Combining these two aspects, samples with a smaller Δm(X, Y) will have lower efficiencies due to their higher proportion of 3-prong taus. Hence, the tau prongness is another variable contributing to resolving the Δm(X, Y) sample dependency.

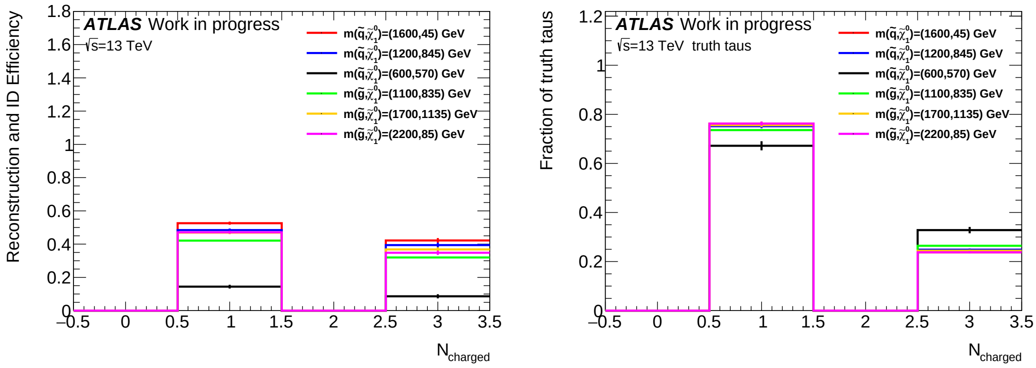

(a) SqSq/GoGo (b) SqSq/GoGo

Figure 6.12: Left (a): Reconstruction and ID efficiencies calculated for 1-prong and 3-prong taus for the SqSq and GoGo samples. Right (b): Fractions of the 1-prong and 3-prong taus for the SqSq and GoGo samples. The samples are labelled according to their mass configuration and $\mathrm{N}_{\mathrm{charged}}$ describes the number of charged tracks, hence the prongness.

Neutral Products of the Tau Decay

The number of neutral tau decay products is a new variable which has not been employed in the previous tau efficiency functions. However, as can be seen in figure 6.13a for the C1C1 samples, the reconstruction and ID efficiency depends quite clearly on the number of neutral hadrons in the tau decay. For the C1C1 samples, the plot shows that a higher multiplicity of neutral hadrons results in lower efficiencies. This can be observed in the other processes as well (see appendix B.1). The reason for this lies in the ID requirements in the reconstructed taus. Since tau decay modes with more neutral decay products have wider showers resembling jets originating from quarks or gluons, the ID algorithm is more likely to reject taus with these decay modes [68].

Also, the distribution of the neutral product multiplicity is sample dependent which can be seen in figure 6.13b for the C1C1 samples. The plot shows that samples with a smaller mass splitting tend to have more taus undergoing a decay with a high neutral hadron multiplicity. Again, this effect is seen in any of the available processes (see appendix B.1). The reason for this is the same as for the sample dependence in the prongness distribution: the lower cut on the visible tau p_{T} removes taus that decay in a small number of hadrons with a higher proportion. As this effect increases for a tau p_{T} distribution more skewed to low values, as it is the case for compressed samples, one expects to see a higher fraction of decay modes with a high multiplicity - both for charged and neutral hadrons. Hence the sample dependence in

truth tau charged and neutral decay product multiplicity.
With the sample dependent distribution in mind, one can deduce that samples with a lower Δm(X, Y) will achieve smaller reconstruction and ID efficiencies. Therefore, the number of neutral tau decay products is another key to resolving the sample dependence discussed in the previous chapter.

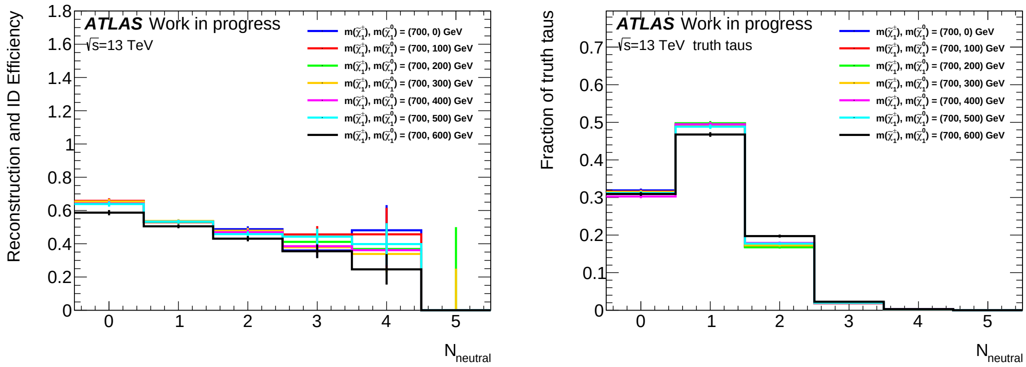

(a) C1C1

(b) C1C1

Figure 6.13: Left (a): Reconstruction and ID efficiencies calculated for different multiplicities of the neutral products of the tau decay for the C1C1 samples. Right (b): Distribution of the neutral tau decay products for the C1C1 samples. The samples are labelled according to their mass configuration.

Tau to Tau-Jet Distance

Another variable, that is new to the parametrisation of the reconstruction and ID efficiency, is the min(dR(truth tau, truth tau-jet)). It has already been motivated that one expects the efficiency to be lower for higher values of this distance variable. In figure 6.14a, this behaviour can be observed for the ttStau and ttbar samples. A steep drop in the efficiency with the efficiency going to essentially zero at min(dR(truth tau, truth tau-jet)) > 0.2 can be seen for every sample. This efficiency dependence is seen across the available processes (see appendix B.1).
The min(dR(truth tau, truth tau-jet)) distribution in the ttStau and ttbar samples is shown in figure 6.14b. As for the previous observables, a sample dependence can be detected. Samples of a smaller mass splitting appear to have a broader distribution in min(dR(truth tau, truth tau-jet)) while samples with a high Δm(X, Y) have a prominent peak at very small values. Apart from that, samples with a higher initially produced particle mass appear to be slightly more peaked compared to samples with the same mass splitting but lower initial mass (see e.g. the magenta, green and blue sample). One exception from this observation is the red sample which is more peaked although its initial mass is smaller. The red sample could be an indicator that the min(dR(truth tau, truth tau-jet)) distribution is affected by a small jet mass difference as well. One additional effect can be see when looking at the SqSq and GoGo distributions in figure 6.14c. GoGo samples, although having a slightly higher mass splitting than a corresponding SqSq counterpart (e.g. the red and the magenta sample), tend to have a broader distribution. Most[6] of these patterns can be observed in the other processes as well (see appendix B.1).
As more peaked distributions will result in higher efficiencies as the discussion of figure 6.14a showed, the min(dR(truth tau, truth tau-jet)) observable seems to be a key observable in resolving every pattern in the sample dependence observed in section 5.4. This includes the

[6]Since in the available samples, only one sample has a very low jet mass difference, this pattern is obviously not observable in the available samples of the other processes.

dependence of the efficiency on Δm(X, Y), the initial mass, the jet mass difference for very low values and the number of jets in the decay chain. Therefore, it is only logical that this observable achieves such a high feature importance in figure 6.9.

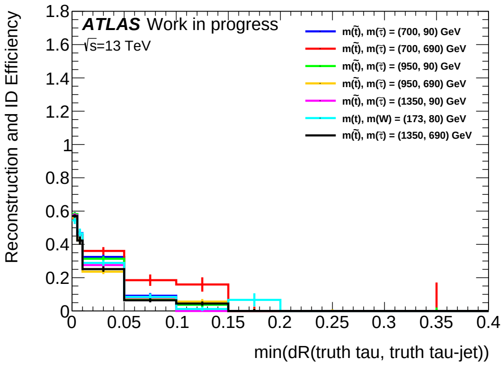

(a) ttStau/ttbar

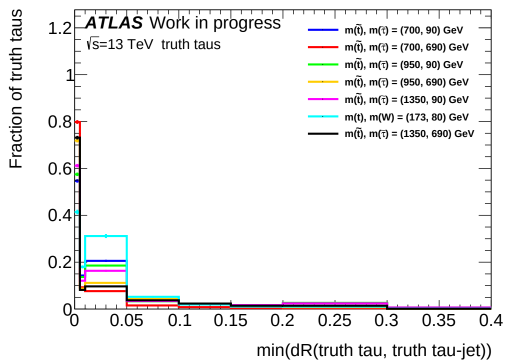

(b) ttStau/ttbar

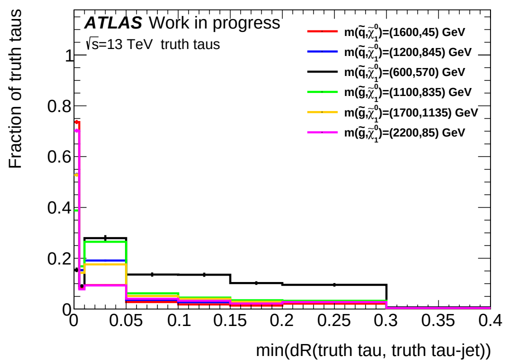

(c) SqSq/GoGo

Figure 6.14: Upper left (a): Reconstruction and ID efficiencies calculated in different regions of min(dR(truth tau, truth tau-jet)) for the ttStau and ttbar samples. Upper right (b): min(dR(truth tau, truth tau-jet)) distribution for the ttStau and ttbar samples. Below (c): min(dR(truth tau, truth tau-jet)) distribution for the SqSq and GoGo samples. The samples are labelled according to their mass configuration.

Tau to Jet Distance

The min(dR(truth tau, truth jet)) variable has a rather complex influence on the reconstruction and ID efficiency compared to the rest of the variables. Figure 6.15a shows the observable's influence on the efficiency in the ttStau and ttbar samples. One can see that there is a gap in the efficiency between 0.2 and 0.4 and that the nearer the value of the distance is to this gap, the lower the efficiency. For min(dR(truth tau, truth jet)) < 0.2, however, there is a distinction: the red sample, which has a very small jet mass difference, achieves significantly higher efficiencies than the other ttStau and ttbar samples. A higher efficiency in this region can be seen for the C1C1 samples in figure 6.15c as well. From these plots, one can deduce that the efficiency for min(dR(truth tau, truth jet)) < 0.2 is only significantly higher than zero if the process has no jets in the SUSY decay chain or if the jet mass difference is very small. This pattern is observed in the SqSq/GoGo processes (see figure 6.15e) and the direct stau process (see appendix B.1) as well. It does make sense that the efficiency drops when approaching min(dR(truth tau, truth jet)) $= 0.4$ from higher values as a smaller distance between tau and jet increases the probability of contamination. What does not make sense on the first glance is to see that the efficiencies are non-zero for min(dR(truth tau, truth jet)) < 0.4 as it suggests that some truth taus have such a small distance to a non-tau jet. Since the truth jets are defined with a distance parameter of $\Delta R = 0.4$ (see section 4.2), different jets should have a minimum distance of 0.4.

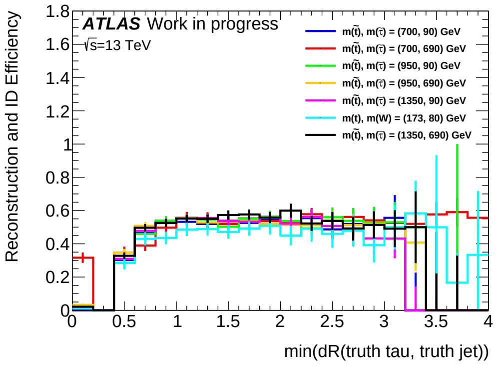

(a) ttStau/ttbar

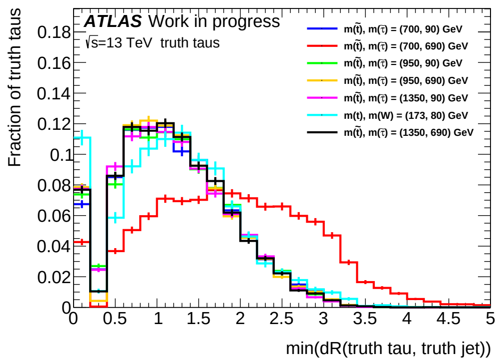

(b) ttStau/ttbar

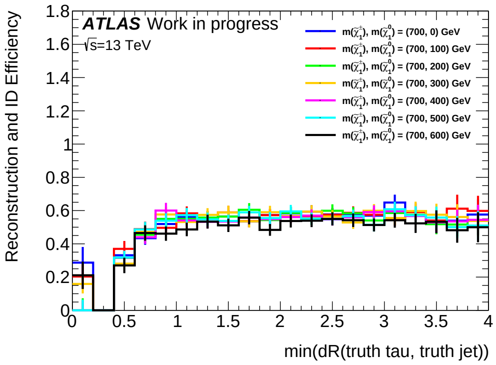

(c) C1C1

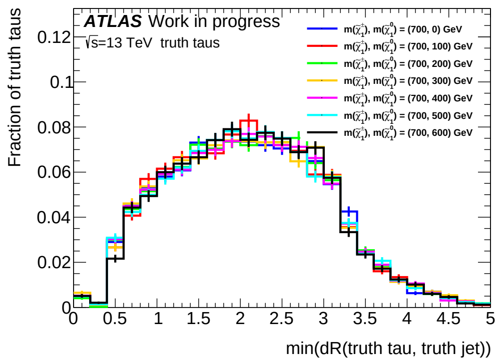

(d) C1C1

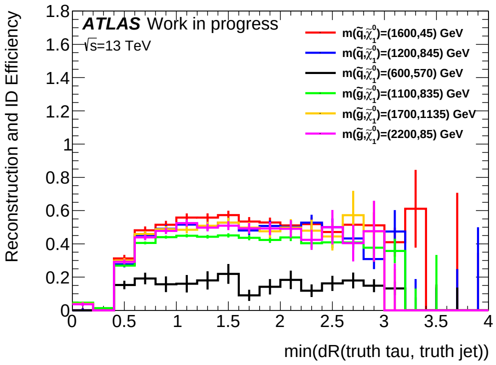

(e) SqSq/GoGo

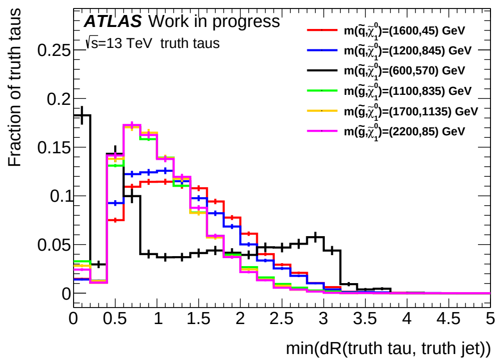

(f) SqSq/GoGo

Figure 6.15: On the left: Reconstruction and ID efficiencies calculated in different regions of min(dR(truth tau, truth jet)) for the ttStau and ttbar (a), the C1C1 (c) and the SqSq/GoGo (e) samples. On the right: min(dR(truth tau, truth jet)) distribution for the ttStau and ttbar (b), the C1C1 (d) and the SqSq/GoGo (f) samples. The samples are labelled according to their mass configuration.

Scrutinizing the min(dR(truth tau, truth jet)) distributions of the taus will help resolving this contradiction. As one can see in figure 6.15b for the ttStau/ttbar samples, indeed a non-vanishing fraction of taus can be found at distances below 0.4. It appears that the distribution is broader for very small jet mass differences and that the ttbar process has a large fraction of taus with distances to jets below 0.2. In figure 6.15d, one can see that samples of the C1C1 process have a min(dR(truth tau, truth jet)) distribution independent of the mass configuration. The SqSq samples in figure 6.15f show a very similar behaviour to the ttStau samples while the distribution for the GoGo samples is skewed towards lower values in comparison. The most compressed SqSq sample has a very large fraction of taus in the min(dR(truth tau, truth jet)) < 0.4 region.

One can conclude that the min(dR(truth tau, truth jet)) distribution is independent of the mass configuration if the process has no jets in its decay chain (i.e. C1C1, direct stau). Furthermore, the distribution is sensitive to very small values of the jet mass difference, to the Δm(X, Y) and to the jet multiplicity in the decay chain (GoGo and ttbar samples being more peaked at low values). For the min(dR(truth tau, truth jet)) distribution above 0.4, this makes sense, as less jets in the decay chain will reduce the probability of a jet being nearby the tau and a very small jet mass difference might make the quarks from the decay chain soft enough that they possibly won't be clustered as their own truth jet.

However, the explanation for values below 0.4 is more complicated. As has already been mentioned, a non-zero distribution for min(dR(truth tau, truth jet)) < 0.4 is not expected in the ideal case. Though, reminiscing how the variable was defined in section 6.2.1, three scenarios might explain the distribution below 0.4: the jet was falsely labelled a non-tau jet by the ConeTruthLabelID (scenario 1), the tau is not the initiator but instead just a constituent of the jet (scenario 2) or the tau is displaced from its own tau-jet (scenario 3).

An example for scenario 1 is the majority of taus in the peak of the red ttStau sample in figure 6.15b. When plotting the ConeTruthLabelID of the jets against the tau jet distance in figure 6.16a for this sample (DSID 473368), one can see that the majority of alleged non-tau jets, which are closer than 0.4 to the tau, are *b*-jets, probably from the top squark decay. However, it should not be possible for a non-tau jet to be this close to the tau. Hence, the ConeTruthLabelID falsely labelled a tau-jet as a *b*-jet, because the algorithm behind the ConeTruthLabelID prioritises *b*-quarks over tau leptons when looking for the origin of the jet. As a soft *b*-quark from the stop decay is likely to be near the tau and its tau-jet, some of the tau-jets are mislabelled by the algorithm to be a *b*-jet. Similar mislabellings happen in the other ttStau samples and the SqSq, GoGo and ttbar samples as well (some further plots can be found in the appendix B.2), explaining in part the peaks at low min(dR(truth tau, truth jet)) for processes with jets in the decay chain.

Scenario 2 will also contribute, but at a lower rate in most cases. As an example for this scenario, figure 6.16b shows again the ttStau sample of smallest jet mass difference. In this plot, one can see that a small fraction of taus in the min(dR(truth tau, truth jet)) < 0.2 region are not originating from the decay of the tau slepton but instead from some *c*-hadron. Most samples will have a quite small fraction of taus of this sort, but ttStau samples and samples that are more compressed and have jets in the decay chain are subject to scenario 2 at higher rates (see appendix B.2).

Scenario 3 describes taus which have a relatively high min(dR(truth tau, truth tau-jet)) and are therefore closer to a different, non-tau jet than their own tau-jet. In this scenario, the assumption made for the min(dR(truth tau, truth tau-jet)) variable, i.e. that the nearest jet is a tau-jet, would be false. However, since a a lot of contamination in the tau-jet is necessary to displace it from the truth-tau to this extent, this scenario will be quite rare as well.

Combining the discussions about the distribution and the dependencies of the reconstruction and ID efficiency, one can conclude that processes with a low number of jets in the decay chain and samples with a low jet mass difference will achieve higher efficiencies. This again resembles the observations in section 5.4. Very compressed samples with jets in the decay chain will also experience lower efficiencies as the previously discussed scenario 2 happens more frequently in these cases. The discussed scenarios will almost always result in efficiencies close to zero as scenario 1 and 3 imply a high level of contamination and scenario 2 involves taus

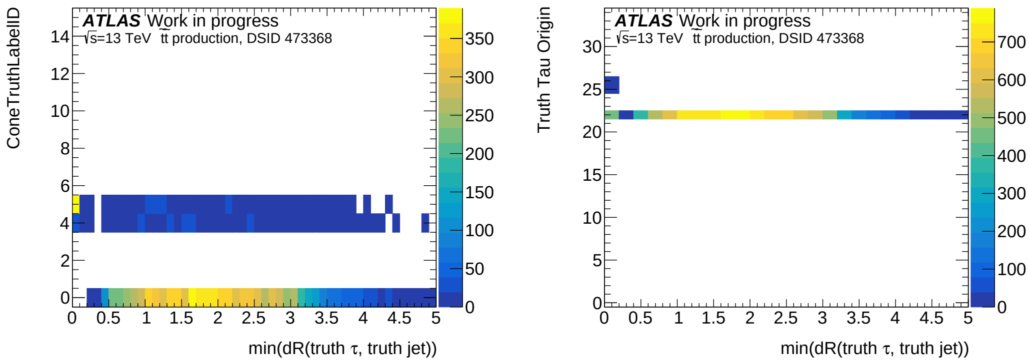

(a) DSID 473368

(b) DSID 473368

Figure 6.16: Left (a): Number of taus in dependence of min(dR(truth tau, truth jet)) and the ConeTruthLabelID of the nearest non-tau jet. The ConeTruthLabelID is 0 for jets from light quarks and gluons, 4 for c-jets and 5 for b-jets. Right (c): Number of taus in dependence of min(dR(truth tau, truth tau-jet)) and the origin of the truth tau. Origin refers to the particle X decaying into the tau and is 22 for SUSY particles, 25/26 for c-hadrons and 33 for b-hadrons. The taus belong to the ttStau sample with the very low jet mass difference (DSID 437368).

not originating from the desired process. In some cases, however, when the contaminating particles are very soft, as it is the case for a very low mass difference or jets not originating from the desired process (i.e. C1C1 and direct stau), scenario 1 is resulting in efficiencies significantly above zero (see figure 6.15a and 6.15c).

6.2.4 Final Feature BDT

With this reduced set of core variables, a new BDT is trained. The confusion matrix showing the correlations between the different variables is shown in figure 6.17. It can be seen that the variables are uncorrelated except for the prongness and number neutral tau decay products. This makes sense as high hadron multiplicities in the tau decay are rare therefore decay modes with a high prongness are more likely to have a low number of additional neutral hadrons and vice versa. However, this correlation does not lessen their influence in the training of the BDT, as can be seen in figure 6.18a, where the feature importances are shown. The most important variable appears to be the min(dR(truth tau, truth tau-jet)) observable again.
The hyperparameters were chosen to optimise the sample specific MSEs and to avoid overtraining. This was achieved with $M = 1000$ trees, a learning rate of $\nu = 0.05$ and a maximum tree depth of 3. The ROC curves of the BDT applied to the training and test sample is shown in figure 6.18b. From the calibration one can see that the BDT's predictions are in good agreement with the actual efficiencies over the whole interval from 0 to 1. How well the BDT performs in predicting efficiencies across different tau p_T and $|\eta|$ regions for different samples is shown in the MSE plot 6.18d. On average, the sample-specific MSE is well below 1, like for the previous BDT trained with the help of all variables. The samples having a MSE above one are the same as before plus the most compressed SqSq sample (DSID 378447). These samples appear to be consistently harder to predict.
To show that the predictions made by such a BDT are far more accurate than the original tau smearing functions, the sample-specific MSEs are calculated for this method as well. Instead of the BDT predicting the efficiency of each tau, the original tau efficiency function of the UpgradePerformanceFunctions is used for the individual 'prediction'. Then, the MSE is again

calculated using equation 6.10 with the same bins. The result can be seen in figure 6.19. It is quite obvious that the BDT method performs far better at predicting the tau reconstruction and ID efficiencies.

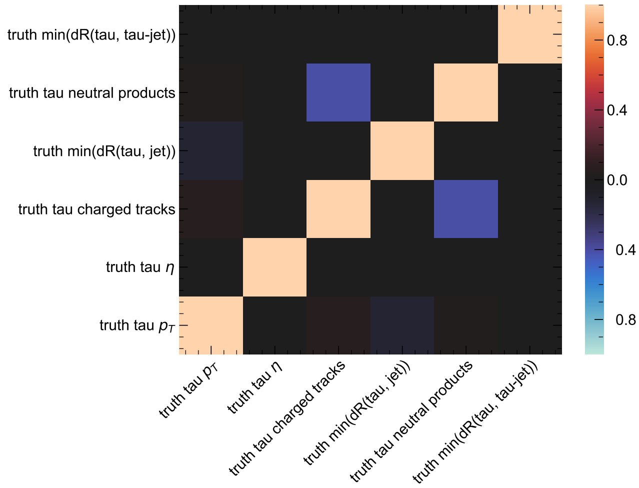

Figure 6.17: Correlation matrix of the final set of input variables for the BDT. The value of the correlation coefficient is indicated by the colour, the z-axis translates the colour scheme to the coefficients.

6.3 High Statistics BDT

With the previous results, the first goal of this chapter has been achieved: finding a parametrisation which has the potential of delivering sample independent reconstruction and ID efficiencies. The six final variables clearly have this potential as the correspondingly trained BDT was able to give sufficiently good predictions of the efficiencies for each of the available samples.

Now, the second goal should be dealt with: developing a sample independent implementation of a tau efficiency function. Until now, efficiency maps (with an $|\eta|$ interpolation in the original smearing) in three variables have been used as input for the tau efficiency functions. To achieve sample independence, the previous results of this study suggest that at least six variables are needed to parametrise the reconstruction and ID efficiency independently of the considered sample. However, developing efficiency maps in six dimensions is infeasible, hence a BDT could be used instead to get sample independent, accurate results out of this six dimensional feature space. This BDT would have to be trained on a wide range of different processes and mass configurations using the six suggested variables and could then be applied on any tau lepton to calculate its individual reconstruction and ID probability $p(y = 1|\mathbf{x})$. This probability would then be the output of this new tau efficiency function.

Using the high statistics PHYS samples of the six available processes, such BDTs will be developed for the classification of medium reconstruction-level taus and tight reconstruction-level taus in the following. They will be referred to as the *medium tau classifier* and the *tight tau classifier*. Since these BDTs will be used in a new sample independent truth smearing in SimpleAnalysis, it was necessary to use the XGBoost package [98] in order to save the models of the medium and tight tau classifier. However, the gradient boosting algorithm employed by this package is the same as was used with the BDTs previously presented.

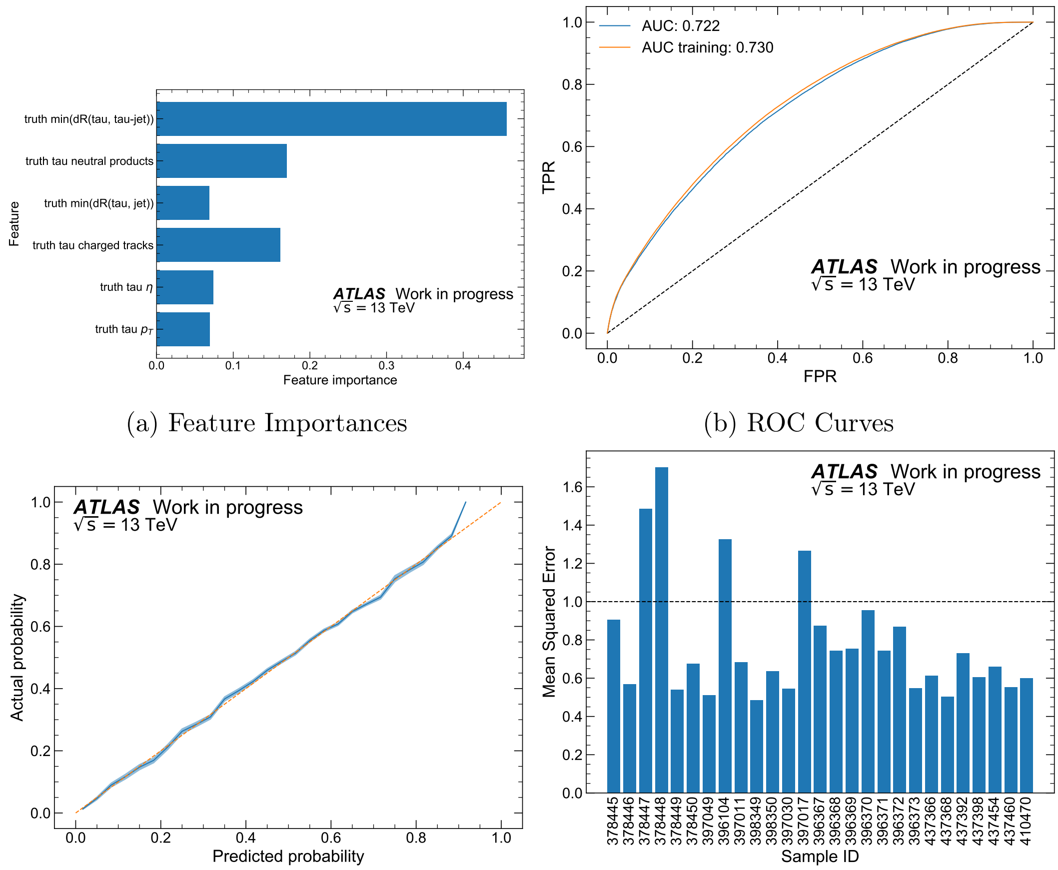

(a) Feature Importances

(b) ROC Curves

(c) Calibration

(d) Sample-Specific MSEs

Figure 6.18: Different characteristics of the BDT using the reduced set of input features: the feature importances (a), the ROC curves of the BDT applied to the training and test sample (b), the calibration curve of the BDT applied to the test sample in 30 bins (c) and the sample-specific MSEs (d).

6.3.1 Medium Tau Classifier

Similarly to the previously trained BDTs, this high statistics medium tau classifier can be used to calculate the reconstruction and ID probability $p(y = 1|\mathbf{x})$ of a truth-level tau, i.e. its probability of being matched to a medium reconstruction-level tau. However, this BDT will be using training and test samples derived from the whole set of truth taus in the PHYS samples presented in table 4.6. Again the training sample will contain a random subset with about 75% of the taus and the test sample will contain 25% of the taus. As can be seen in figure 6.20, the correlation matrix for the six final variables calculated with the taus from the PHYS samples shows the same correlations as in figure 6.17.

The medium tau classifier BDT was trained using the following values for the hyperparameters: $M = 2500$ trees, a learning rate of $\nu = 0.06$ and a maximum depth of 7. Increasing the maximum depth also changed the ranking of the feature importances to some extent, as can be seen in figure 6.21a. Now, the tau prongness and the number of neutral tau decay products are the most important variables while the distance between tau and tau-jet loses some importance[7]. A look at the ROC curves of training and test sample in figure 6.21b reveals that the

[7] The 'gain' method was used for the feature importance calculation in XGBoost. It is based on the gini importance, just as the feature importances used before.

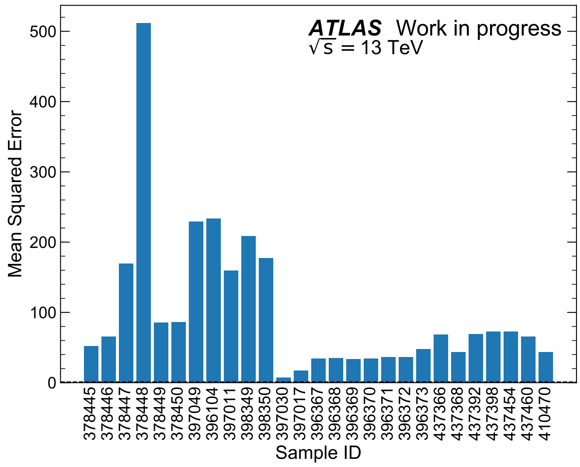

Figure 6.19: Sample-specific MSEs calculated using the tau efficiency functions from the UpgradePerformanceFunctions for the prediction of the efficiencies.

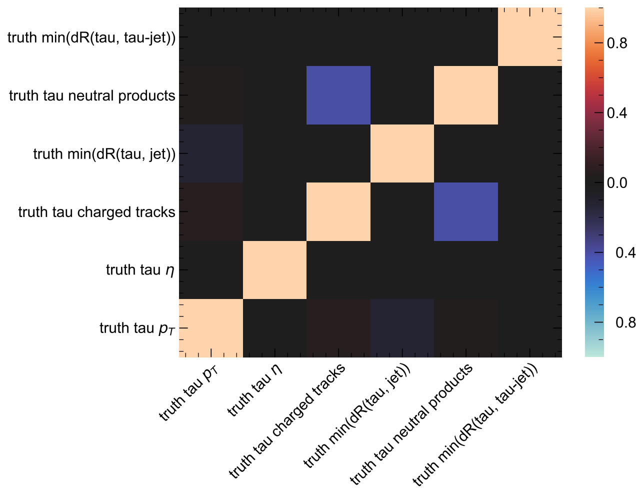

Figure 6.20: Correlation matrix of the final set of input variables, calculated with the truth taus of the PHYS samples.

hyperparameters were chosen such that overtraining is avoided. The calibration, now defined in 100 bins due to the high statistics, is shown in figure 6.21c and shows a good agreement of actual and predicted efficiencies across the binning of the predicted probability. The ROC curves, calibration and feature importances following from a choice of hyperparameters that induce overtraining and a choice of very weak hyperparameters is shown in the appendix B.3 to emphasise the influence of the hyperparameters on the BDT.
The sample-specific MSE of every available PHYS sample is shown in the figures 6.21d, 6.21e and 6.21f. The average MSE exceeds 1 slightly with 1.2 which is still sufficient, especially bearing in mind the performance of the original tau efficiency function in comparison (figure 6.19).

However, a few samples achieve quite high efficiencies above 4 or even close to 8. A reason for the bad performance in some of these samples might be the higher statistics. Due to a higher number of taus in the sample, the statistical uncertainty decreases, hence, for the same differences between predicted and actual efficiencies, the MSE would increase. This explanation is supported by the plot in figure 6.22 where the sample-specific MSE is plotted against the number of taus in the respective sample. Here, one can observe a more or less

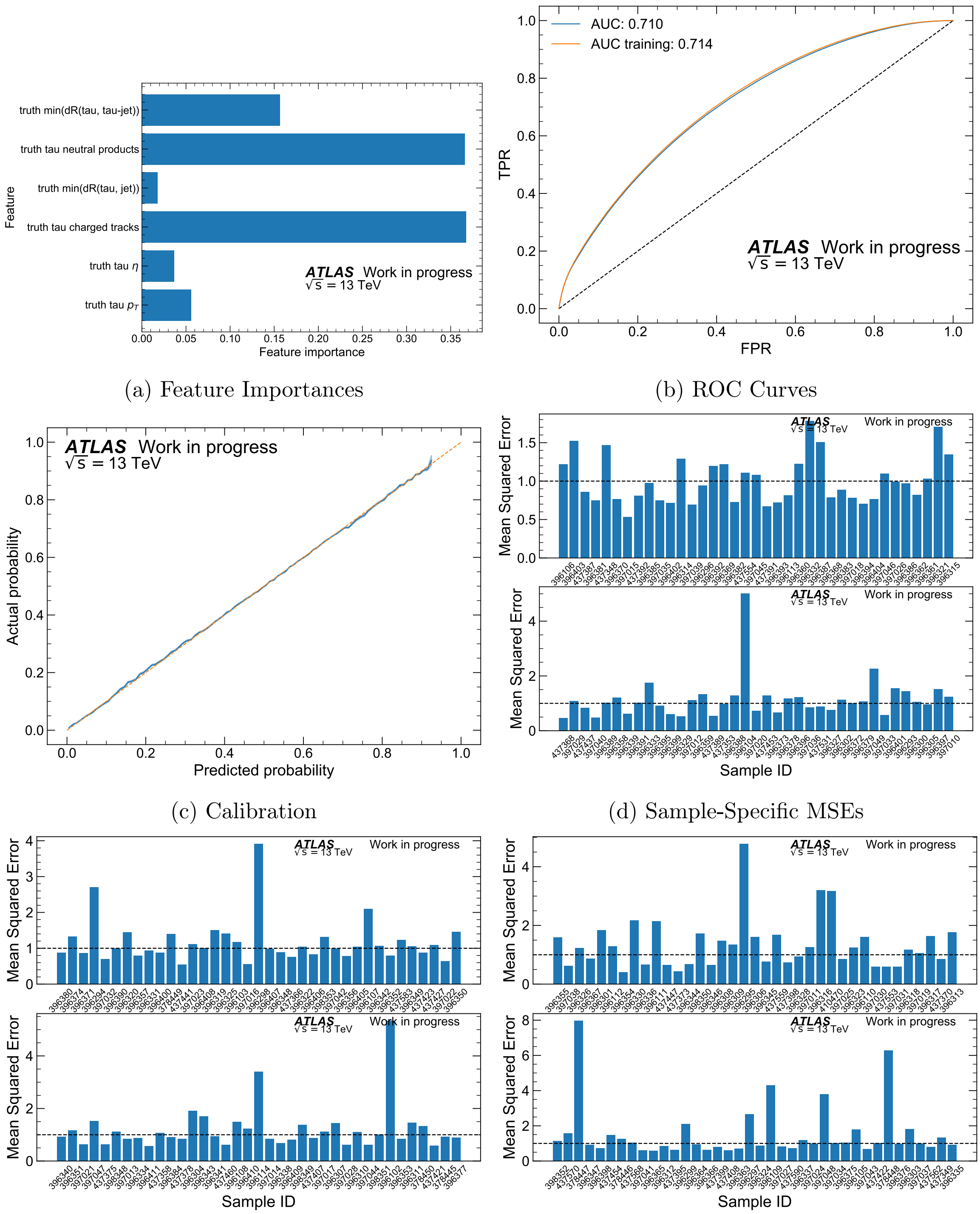

(a) Feature Importances (b) ROC Curves

(c) Calibration (d) Sample-Specific MSEs

(e) Sample-Specific MSEs (f) Sample-Specific MSEs

Figure 6.21: Different characteristics of the medium tau classifier BDT: the feature importances (a), the ROC curves of the BDT applied to the training and test sample (b), the calibration curve of the BDT applied to the test sample in 100 bins (c) and the sample-specific MSEs (d,e,f).

clear correlation of the MSE and the number of taus with two significant exceptions: the compressed SqSq sample 378447 and the compressed GoGo sample 378448. These appear to achieve relatively bad performances independently of their number of taus. The reason might be again, as has been mentioned already for the low statistics BDTs where these samples

achieved relatively bad results as well, their uniqueness. Especially the compressed SqSq sample has, as can be seen in figure 5.18, reconstruction and ID efficiencies as low as no other available sample.
However, one can argue that these results are still very much sufficient for a well performing truth smearing. Even the samples with a quite high sample-specific MSE only have an absolute difference of $\lesssim 4\%$ between predicted and actual efficiencies in the highest statistic bins used for the MSE calculation. At this point, it is worth mentioning the new direct stau smearing developed in section 5.3 again. There, significant differences in the efficiency maps of the different direct stau samples were observed (see figures 5.8 and 5.19). Even though the new tau efficiency function was based on only one of the samples (DSID 396104), the truth smearing yielded a good agreement for the other direct stau samples as well (see figures 5.14e and 5.14d). The same was observed for the new SqSq tau efficiency function which was based on only the DSID 378445 sample (see figures 5.11 and 5.14a). Only for a sample with an extreme difference in the efficiency maps, the truth smearing yielded a bad agreement (see figure 5.14b). Therefore, a difference of a few percentage points in the tau efficiency function does not necessarily spoil the performance of the truth smearing in general. Also, the truth smearing is not expected to be 100% accurate and the BDT method already yields far better results than the original tau efficiency functions for the processes in this study. The sample-specific MSEs calculated using the original medium ID tau efficiency function for all PHYS samples can be found in the appendix B.3.

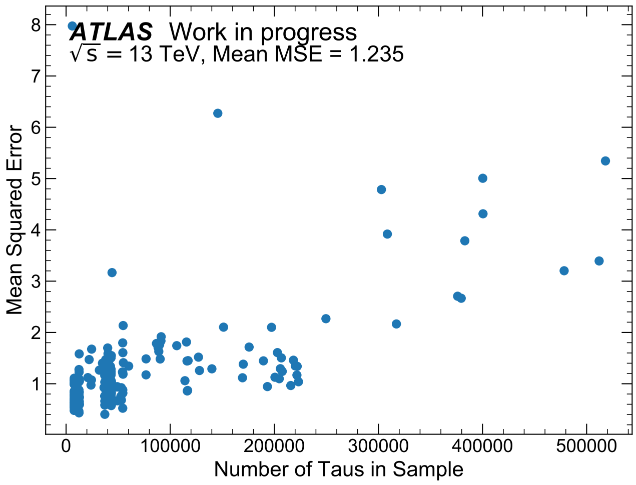

Figure 6.22: Sample-specific MSE for the medium tau classifier plotted against the number of taus in the respective sample.

6.3.2 Tight Tau Classifier

Until now, the reconstruction and ID efficiencies have exclusively been calculated using medium reconstruction-level taus. However, multiple analyses make use of tight reconstruction-level taus in the definition of their signal regions. One of these analyses is the direct stau analysis in the HadHad channel which will be used in the context of a pMSSM scan with the new classifiers later on. Therefore, it is necessary to develop a classifier BDT for the tight ID WP as well.

First, one has to calculate the reconstruction and ID efficiency with respect to tight taus. This is again done using the formula in equation (5.4). In this case, to determine if a truth-level tau is matched to a reconstruction-level tau, the condition $\Delta R(\text{truth tau, tight reco tau}) < 0.2$

is used. This way, one gets the reconstruction and ID efficiency for the tight ID WP. The calculated efficiencies for all PHYS samples is shown in figure 6.23. A very similar behaviour is observed as for the medium WP in figure 5.22, but at smaller efficiencies. Because of this and because the tight WP is merely involving stronger discrimination against non-tau jets and not some new criteria, one can expect that the reconstruction and ID efficiency can be parametrised with the same set of variables as in the medium WP case.

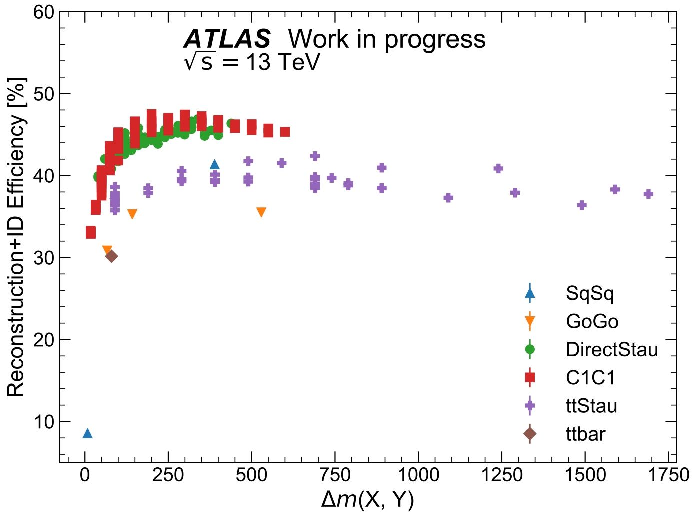

Figure 6.23: Overall reconstruction and ID efficiency for the tight ID WP on the vertical axis against the tau mass difference $\Delta m(\mathrm{X}, \mathrm{Y})$ with X$\rightarrow \tau$Y on the horizontal axis for the PHYS samples.

The tight tau classifier will be used to predict the probability of a truth-level tau being matched to a tight reconstruction-level tau $p(y = 1|\mathbf{x})$. These predicted efficiencies will then be compared to the actual reconstruction and ID efficiencies for the tight ID WP. The training and the test sample again consist of 75% and 25% of the whole set of truth taus in the PHYS samples, respectively. As motivated earlier, one can use the final set of six variables as input features for the tight reconstruction-level tau classification as well. Hence, see figure 6.20 for the already discussed correlations.
The tight tau classifier was trained using the same hyperparameters as the medium tau classifier: $M = 2500$ trees, a learning rate of $\nu = 0.06$ and 7 as the maximum depth. This choice avoided overtraining, as can be seen from the ROC curves of the BDT applied to training and test sample in figure 6.24b, while optimising the results with respect to the sample-specific MSEs. The calibration in 100 bins is presented in figure 6.24c where one can see that the BDT predictions align with the actual efficiencies up to high probability values, where the curve has a rather high uncertainty[8]. The feature importances are very similar to the importances in the medium tau classifier, as can be seen in figure 6.24a. The ROC curves, calibration and feature importances for a BDT with very weak hyperparameters and hyperparameters resulting in overtraining are shown in the appendix B.3 to show the influence of the these parameters on the BDT characteristics.
The sample-specific MSEs are shown in the figures 6.24d, 6.24e and 6.24f. It is clear that the performance of the tight tau classifier is worse than that of the medium tau classifier with an average sample-specific MSE of 1.7. Again, for the vast majority of samples, the BDT achieves MSEs below a value of 4.

[8]This is to be expected, since the reconstruction and ID efficiencies for a tight ID are in general quite low. Truth taus with a high probability should hence be rare.

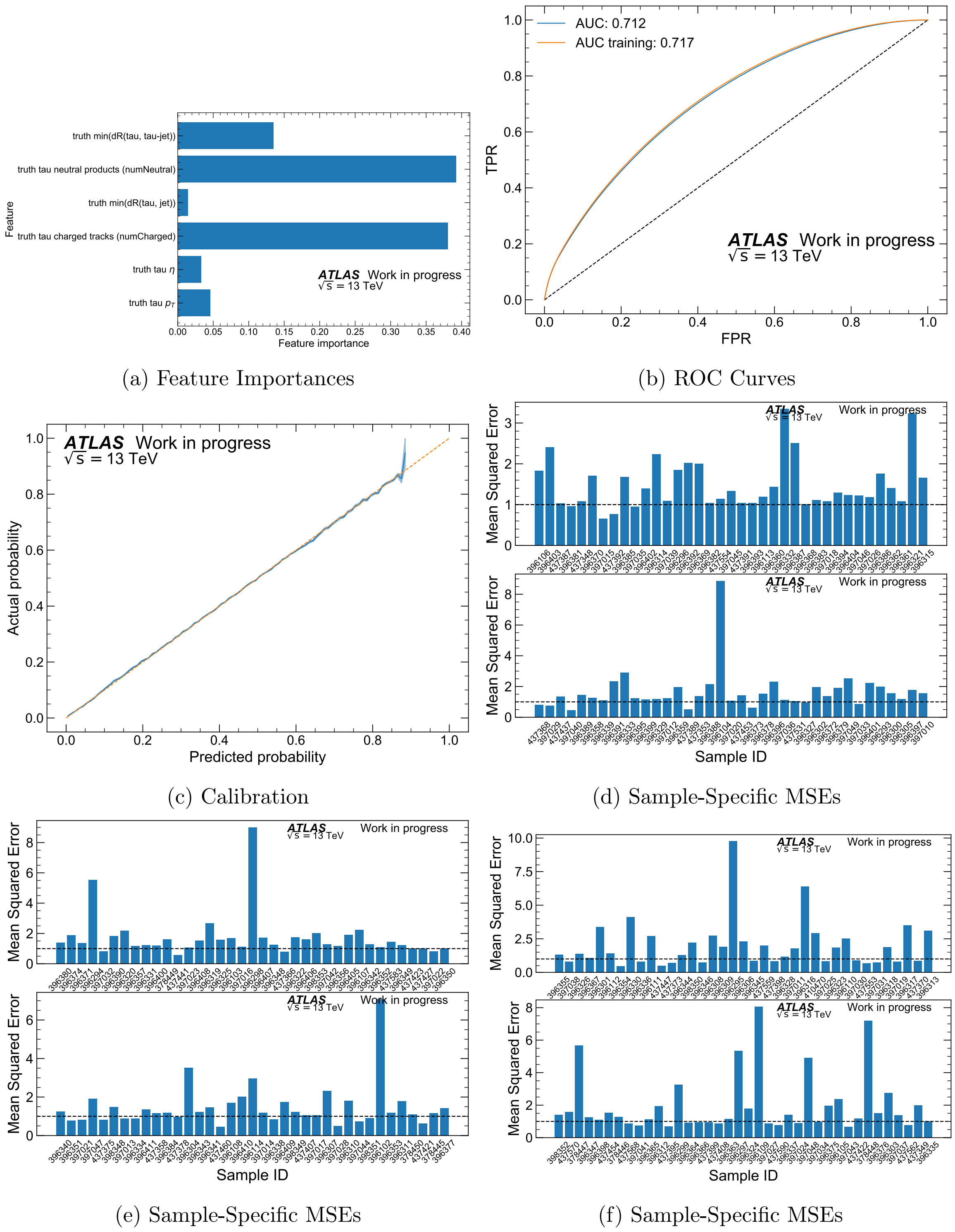

(a) Feature Importances

(b) ROC Curves

(c) Calibration

(d) Sample-Specific MSEs

(e) Sample-Specific MSEs

(f) Sample-Specific MSEs

Figure 6.24: Different characteristics of the tight tau classifier BDT: the feature importances (a), the ROC curves of the BDT applied to the training and test sample (b), the calibration curve of the BDT applied to the test sample in 100 bins (c) and the sample-specific MSEs (d,e,f).

However, some samples again exceed this margin, at a higher rate and by larger values than in the medium tau classifier case. In figure 6.25, the influence of the number of taus in a sample on its MSE is investigated again. It can be seen that also for the tight tau classifier, the samples with a very high MSE possess a high number of taus as well, with two exceptions.

These exceptions are once again the compressed SqSq and GoGo samples.
As before, one can make the case that the performance of this BDT is still very much sufficient for the implementation in a truth smearing. Absolute differences in the efficiencies of few percentage points might not have an impact that would significantly worsen the truth smearing's performance, as suggested before. In the case of the classification of tight reconstruction-level taus, 100% accuracy is not expected and the performance of the tight tau classifier again exceeds the performance of the original tau efficiency functions. This can be seen in the appendix B.3 where the sample-specific MSEs are shown for the predictions of the Upgrade-PerformanceFunctions tau efficiency function for a tight ID WP.

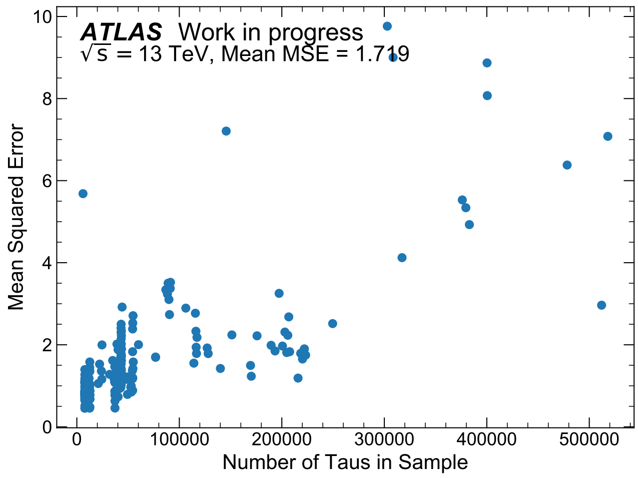

Figure 6.25: Sample-specific MSE for the tight tau classifier plotted against the number of taus in the respective sample.

Chapter 7

New Truth Smearing in the pMSSM Scan

Now that sufficiently well performing classifiers for the sample independent prediction of reconstruction and ID efficiencies have been developed, one can implement these in the setting of a pMSSM scan. In this chapter, the steps that were taken to conduct a test scan with a new smearing based on the classifiers are described. The scan will mostly follow the procedure presented in section 4.4.3. This pMSSM scan has the goal of investigating the sensitivity in the pMSSM parameter space of the direct stau analysis in the HadHad channel which has already been mentioned in section 4.4.2.
First, the generation of the pMSSM model points will be described. Then, the constraints and filters used to reduce the model points to the physically relevant ones are presented and the subsequent event generation for this reduced set of models. Finally, the smeared truth evaluation with the truth smearing involving the new tau classifiers will be discussed.

7.1 Model Generation

The first step of the pMSSM scan requires the generation of models in the pMSSM parameter space. A model will be defined as a set of random values for each of the 19 pMSSM parameters. The random values are sampled according to a flat distribution constrained to a predefined range. With these model parameters, the SUSY particle spectrum and the decay widths and BRs of the particles will be calculated.

7.1.1 Model Generation Software

The model generation is done using the Version1 of the pMSSM model generation framework by Jonas Würzinger [99], which consists of multiple programs. The generation of the random values for the 19 pMSSM parameters of each model is done by EasyScan_HEP v.1.0.0 [100]. The random values are then used as input for SoftSusy v.4.1.8 [101, 102] and SPheno v.4.0.4 [103, 104] as these two programs are responsible for the SUSY spectrum and decay width calculation. The mass of the SM higgs boson is calculated from the model parameters using FeynHiggs v.2.15.0 [105–112]. The dark matter relic density and the values of different electroweak and flavour observables are calculated with MicrOMEGAs v.5.2.4 [113] from the output of SPheno.
The two programs employed for the SUSY spectrum calculation have different roles in the

model generation process. SoftSusy is calculating the SUSY spectrum initially and is aborting the running of the other programs in the case that a model is unphysical due to e.g. some particles being tachyons. If the model appears to be physical and the other programs are run, the SUSY spectrum information provided by SPheno will be used for any following processing of the models. This is because SPheno provides more complete decay modes.

7.1.2 Settings

The scan ranges of the pMSSM parameters, which were used to constrain the flat distribution from which the random values were sampled, are shown in table 7.1.

pMSSM Parameter	Range
$\tan\beta$	1 - 60
μ	0 - 2000 GeV
M_1	-2000 - 2000 GeV
M_2	
A_t	-4000 - 4000 GeV
A_b	
A_τ	
$m_{\tilde{L}}$	0 - 1000 GeV
$m_{\tilde{\tau}_R}$	0 - 700 GeV
M_3	4000 GeV
M_A	
$m_{\tilde{Q}}$	
$m_{\tilde{t}_R}$	
$m_{\tilde{b}_R}$	
$m_{\tilde{q}}$	
$m_{\tilde{u}_R}$	
$m_{\tilde{d}_R}$	
$m_{\tilde{l}}$	
$m_{\tilde{e}_R}$	

Table 7.1: Scan ranges of the 19 pMSSM parameters employed in this study.

As this pMSSM scan will focus on the direct stau analysis, one is mostly interested in the parameters concerning electroweakinos and staus. Therefore, the parameters M_1 and M_2 will be varied between -2000 and 2000 GeV. The higgsino parameter μ is only allowed to take positive values up to 2000 GeV as negative values resulted in masses of the SM higgs boson not consistent with the measured value. Varying these three parameters along with $\tan\beta$ assures having a variety of electroweakino mixtures making up the neutralinos and charginos. The mass parameter of the left-handed stau and tau sneutrino, $m_{\tilde{L}}$, was allowed to take values up to 1000 GeV and the mass parameter of the right-handed stau $m_{\tilde{\tau}_R}$ values up to 700 GeV. An upper limit at 1000 GeV was chosen since above this value, the direct stau analysis will certainly not be sensitive (see figure 4.4). A lower value for the right-handed stau is chosen as the production of right-handed staus has a lower cross section [114] due to them being a weak isospin singlet. Therefore, the analysis will be sensitive up to a smaller mass for right-handed staus. Since the exact influence of the $\tan\beta$ and the trilinear couplings on the SUSY spectrum is unclear, these are varied over large ranges.

Every other parameter is fixed at a very high mass of 4 TeV as particles apart from electroweakinos and staus are not relevant to the direct stau process or similar processes involving tau sleptons.

With the aforementioned parameter ranges, 75000 models were generated. However, only 35951 of these models were physical and 31941 were successfully run by SPheno.

7.1.3 Model Spectrum

The 31941 models can now be used to take a closer look at the mass spectrum of the SUSY particles. In the figures 7.1a and 7.1b, one can see the mass distributions for the light and the heavy stau mass eigenstate, respectively. The influence of the different ranges for left- and right-handed stau masses can be inferred from both plots. the mass of the $\tilde{\tau}_1$ barely exceeds the maximum of $m_{\tilde{\tau}_R}$ and the mass distribution of the $\tilde{\tau}_2$ drops significantly at this value. The heavy stau mass in turn barely exceeds the maximum value of $m_{\tilde{L}}$. Models with very low stau masses below 100 GeV are extremely rare, this is probably due to these models being unphysical.
The mass distributions of the electroweakinos are shown in figure 7.1c. As was to be expected, the heavier electroweakino masses peak at the maximum (absolute) value of the range of the electroweakino pMSSM parameters M_1, M_2 and μ, while the lighter electroweakino masses peak at the minimum value.

From the mass distribution of the $\tilde{\chi}_1^0$ it becomes quite clear that it is not lighter than the light stau in every model, which would make a process similar to the direct stau process impossible. Figure 7.1d visualises how the physical models are distributed in the phase space of the light stau and lightest neutralino mass. Even though the $\tilde{\chi}_1^0$ mass extends to high values, it seems that still a major fraction of the models lie within the region where the direct stau process or similar processes are possible.

Another interesting aspect of the SUSY spectra is the LSP. From figure 7.1d, one could deduce that the lightest neutralino is not the LSP in every model, even though this was assumed in the simplified model of the direct stau analysis. Figure 7.2a shows which type of sparticles are the LSP in the various physical models. Apart from the lightest neutralino, a large fraction of models has a light stau, some models have the tau sneutrino and a very small fraction has the lightest chargino as LSP. Especially the stau or the chargino as LSP would be problematic. Since the SUSY LSP is seen as a DM candidate, these particles would contradict the observation that DM is electrically neutral. Models with such LSP types are therefore undesired.
Furthermore the pMSSM models should give a SM higgs mass consistent with the measured value in equation (2.1). As discussed in the theoretical introduction, the SUSY particle spectrum has an influence on this observable, hence not every pMSSM model will necessarily give the measured higgs mass. In figure 7.2b[1], it can be seen that a significant amount of models involve a higgs mass below the observed value. These models are therefore undesired as well.

[1]Since the SM higgs mass is calculated using FeynHiggs instead of SPheno, the number of models is somewhat higher as FeynHiggs results in an error for less models.

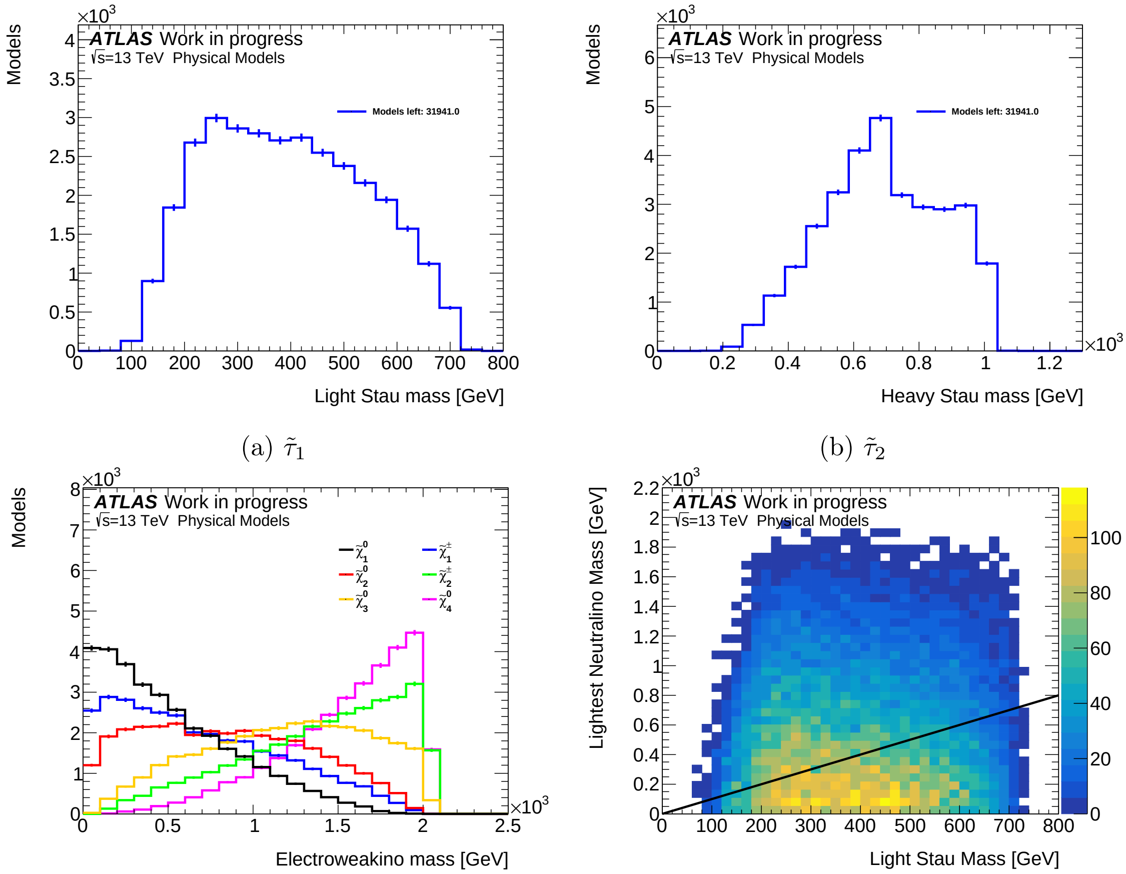

(a) $\tilde{\tau}_1$ (b) $\tilde{\tau}_2$

(c) $\tilde{\chi}_1^0$, $\tilde{\chi}_1^\pm$, $\tilde{\chi}_2^\pm$, $\tilde{\chi}_2^0$, $\tilde{\chi}_3^0$, $\tilde{\chi}_4^0$ (d) $\tilde{\tau}_1$ vs. $\tilde{\chi}_1^0$

Figure 7.1: Mass distributions of the light stau $\tilde{\tau}_1$ (a), the heavy stau $\tilde{\tau}_2$ and the electroweakino mass eigenstates (c). (d) plots the light stau mass against the lightest neutralino mass, the black line indicates equal masses for both sparticles.

7.2 Model Reduction

Two inconsistencies with current experimental evidence of the generated pMSSM models have already been pointed out. However, there are further potential discrepancies one has to consider. In order to address these, constraints and filters are used to get a selection of models which cannot be excluded in advance by recent experimental evidence. A discussion of the cross sections of processes within the models will bring a further reduction of the set of models.

7.2.1 Physics Constraints

As only models which are consistent with current SM precision measurements, DM (non-)observations and earlier particle collider searches should be analysed, a number of constraints are introduced. An overview of these constraints can be found in table 7.2.

Except for the chargino and the SM higgs mass (which are calculated by SPheno and FeynHiggs, respectively), every constrained observable in table 7.2 has been calculated using MicrOMEGAs.

Two collider constraints are employed in this study. First, the SM higgs mass calculated from the pMSSM models is allowed to be in the range of 120 GeV to 130 GeV, which is centred

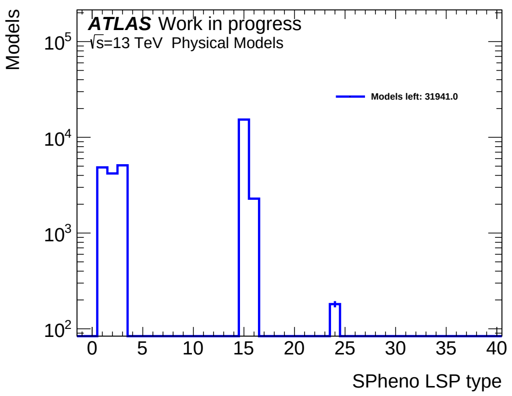

(a) LSP type

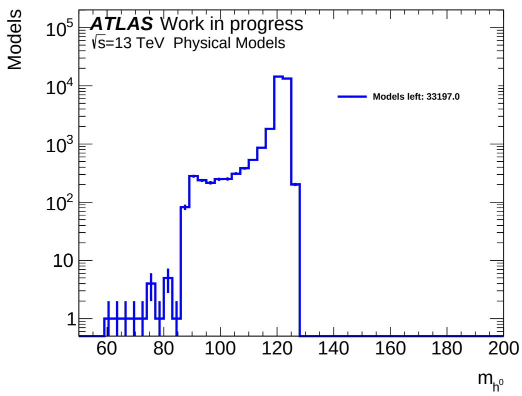

(b) m_{h^0}

Figure 7.2: Logarithmic plot of the LSP type of the physical models. The LSP type is encoded with the following numbers: 1, 2 and 3 correspond to lightest neutralinos with a dominant bino, wino and higgsino component, respectively. 15 corresponds to the light stau, 16 to the tau sneutrino and 24 to the lightest chargino.

Constrained Observable	Minimum value	Maximum value
m_{h^0}	120 GeV	130 GeV
$m_{\tilde{\chi}_1^\pm}$	103 GeV	-
$\Omega_c h^2$	0	0.1222
$\Delta\rho$	-0.0005	0.0017
$\Delta(g-2)_\mu$	$-1.77 \cdot 10^{-9}$	$4.48 \cdot 10^{-9}$
$\mathrm{BR}(b \to s\gamma)$	$2.69 \cdot 10^{-4}$	$3.87 \cdot 10^{-4}$
$\mathrm{BR}(B_s \to \mu^+\mu^-)$	$1.6 \cdot 10^{-9}$	$4.2 \cdot 10^{-9}$
$\mathrm{BR}(B^+ \to \tau^+\nu_\tau)$	$66 \cdot 10^{-6}$	$161 \cdot 10^{-6}$

Table 7.2: Constraints from collider experiments, the DM relic density and electroweak precision and flavour measurements. Inspired by [82].

around the measured value (see equation (2.1)) and includes a very generous estimate of the uncertainty in the FeynHiggs calculation. This constraint reduces the number of models to 25422 (see figure 7.2b). The second collider requirement, i.e. the lower limit on the lightest chargino mass, is based on the results from the predecessor of the LHC, the large electron positron collider (LEP) [115]. This limit constrains the set of models further to 23294 models (see figure 7.1c).

Additionally, the pMSSM models are required to be consistent with the measurement of the DM relic density shown in equation (2.17). The upper limit for the pMSSM models is taken to be the value measured by the Planck mission plus double its uncertainty, i.e. $\Omega_c h^2 < 0.1222$. This cut reduces the number of models to 18979. As mainly properties of the LSP are contributing to the calculated relic density of the pMSSM models, it is worth taking a closer look at the LSPs which get lost due to this requirement. In figure 7.3a, it can be seen that the cut will mainly discard models having a neutralino with a high bino mixture as LSP.

This can be explained with the coannihilation processes of neutralino LSPs with different gaugino/higgsino eigenstate mixtures. As there is only one bino eigenstate, the requirement of a low M_1 — to get a high bino component in the lightest neutralino — will only affect one mass eigenstate. This is different for winos, as the requirement of a low M_2 to get a wino-like $\tilde{\chi}_1^0$ will also result in a nearly mass-degenerate lightest chargino, since M_2 is the

mass parameter for one neutral and two charged gaugino eigenstates. This very small mass difference between $\tilde{\chi}_1^0$ and $\tilde{\chi}_1^\pm$ for models with a wino-like lightest neutralino LSP can be seen in figure 7.3b. In the higgsino case, a higgsino-like $\tilde{\chi}_1^0$ would result in the $\tilde{\chi}_1^\pm$ and the $\tilde{\chi}_2^0$ having also very similar masses due to there being 4 higgsino eigenstates. In figure 7.3c, this mass degeneracy becomes clear, as the maximum mass difference between any two of the three mass eigenstates $\tilde{\chi}_1^0$, $\tilde{\chi}_1^\pm$ and $\tilde{\chi}_2^0$ is shown to be very small for models with a higgsino-like lightest neutralino LSP. Since a mass degeneracy of two particles greatly increases the coannihilation cross section of these particles [116], wino- and higgsino-like lightest neutralinos will experience more frequent coannihilations with the other electroweakinos. A higher coannihilation frequency in turn reduces their relic density. Bino-like neutralino LSPs on the other hand depend on another particle like the stau to be mass degenerate in order to experience high coannihilation rates and reduce the relic density. Hence, one gets a broad relic density distribution for models with a bino-like neutralino LSPs.
Models with a stau or tau sneutrino LSP are affected as well by the $\Omega_c h^2$ cut, though at a far smaller rate. Hence, models with stau and chargino LSPs still persist after this constraint. This will be resolved with further filters later in the procedure.
Finally, five constraints motivated by electroweak and flavour precision measurements were taken into account. The ranges were taken from the pMSSM scan for the ATLAS run 1 [82]. $\Delta\rho$ describes the electroweak parameter which contains corrections to the Z boson coupling strength, the effective electroweak mixing angle and the W boson mass. $\Delta(g-2)_\mu$ is the supersymmetric contribution to the anomalous magnetic moment of the muon and the BRs come from important decays in B-physics. Actually, these five constraints did not further constrain the set of pMSSM models in this case. Therefore, these limits are not further discussed in the following.

7.2.2 Further Filters and Cross Sections

The 18979 models left after these physics constraints are then transferred to another framework, the pMSSM factory, which was designed to carry out the remaining steps of a pMSSM scan [117]. The calculation of cross sections in this framework is done using PROSPINO2 [118, 119].
At this point, the models are further filtered for long-lived and stable particles that are electrically/colour charged or not the LSP. At the time this study was conducted, this so-called 'LLVFilter' effectively discarded only the models which contained a stau-type LSP[2]. Figure 7.4a shows the LSP types of these remaining 7206 models. As can be seen, stau LSPs are not present anymore, but models with a chargino as LSP, though rare, are not completely filtered yet. This will be done in a later step. Furthermore, it is interesting to see that most of the models with a stau mass below the neutralino mass were filtered at this point (see figure 7.4b). The phase space corresponding to the expected sensitivity reach of the direct stau analysis is fortunately still well populated except for the region with $m_{\tilde{\chi}_1^0} < 100$ GeV. The models which are still present above the black mass diagonal in figure 7.4b have to be models with a tau sneutrino as LSP.
Then, for the remaining models, the cross sections of every SUSY production mode possible within each pMSSM model were calculated. These cross sections give rise to another filter, the 'PreFilter' which aims at discarding models where the cross section of a certain class of sparticle productions is so low or the produced sparticle masses are so high that a later analysis would not be sensitive anyway. In this test run, the set of models will be split into models where exclusively the production of sleptons is considered and models where the production

[2]This filter would normally target other sleptons, squarks and gluinos as well, but as these particles were assigned a high mass of 4 TeV, they were not bothered by this filter.

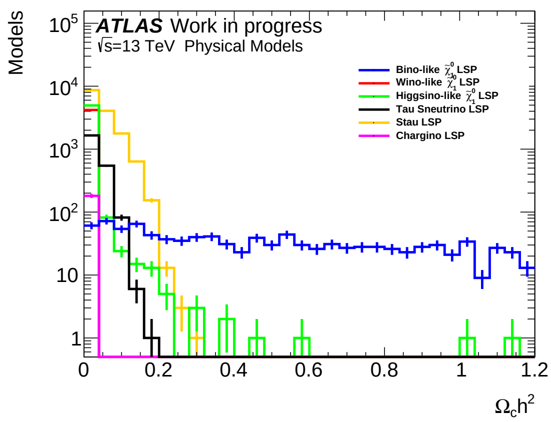

(a) $\Omega_c h^2$

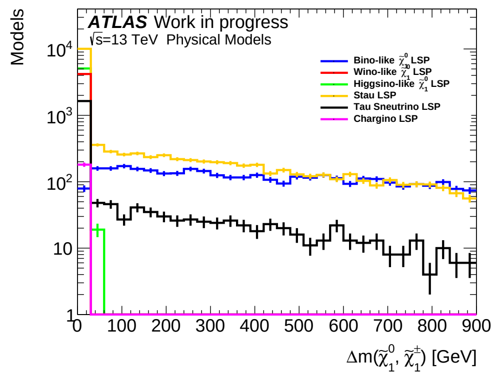

(b) $\Delta m(\tilde{\chi}_1^0, \tilde{\chi}_1^\pm)$

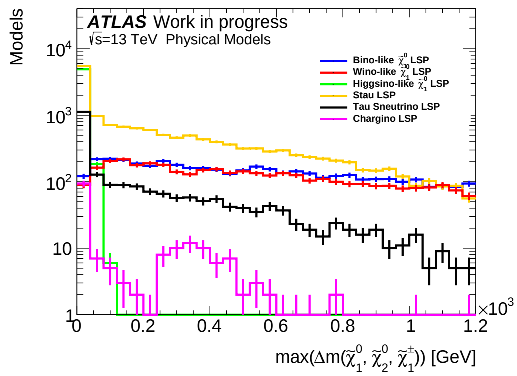

(c) $\max(\Delta m(\tilde{\chi}_1^0, \tilde{\chi}_1^\pm, \tilde{\chi}_2^0))$

Figure 7.3: Distributions of the DM relic density (a), of the mass difference between $\tilde{\chi}_1^0$ and $\tilde{\chi}_1^\pm$ (b) and of the maximum mass difference between either two of $\tilde{\chi}_1^0$, $\tilde{\chi}_1^\pm$ and $\tilde{\chi}_2^0$ (c) for the physical models. The distributions are separated into the different types of LSPs in the models.

of any electroweak sparticle, i.e. electroweakinos and sleptons, is considered. The reason for this will become clear when discussing the generation of events. Hence, the PreFilter was applied for both the production cross sections of all electroweak sparticle productions and just the slepton productions. In both cases, the filter discarded only 11 models, however.

7.3 Event Generation

After applying constraints and filtering the models and the calculation of the SUSY production cross sections, the next step in the pMSSM scan procedure is the event generation. In the pMSSM factory, truth-level information is generated using MadGraph v.2.6.1 and Pythia 8.230. In general, the number of events that will be generated scales with the cross section of the respective process, but the overall number of events generated per model is capped at 100000 to reduce time consumption. In the case of very low cross sections, a minimum number of events per model is set at 10000.

For most models, the production of electroweakinos will have in sum a far higher cross section than the production modes involving staus. This can be inferred from figure 7.5, which shows the cross sections of some production modes with either electroweakinos or stau/tau sneutrinos being produced. The plot shows that the chargino production alone has, at the same mass, a cross section up to an order of magnitude higher than any production mode

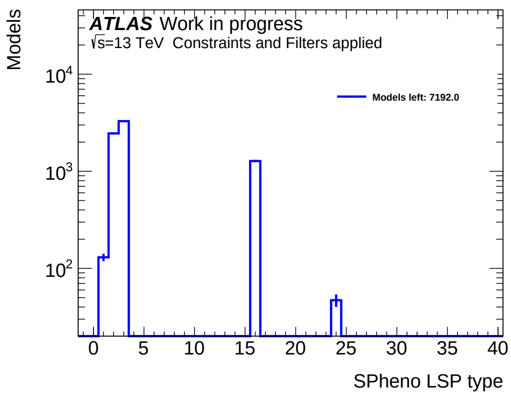

(a) LSP type, with constraints and filters

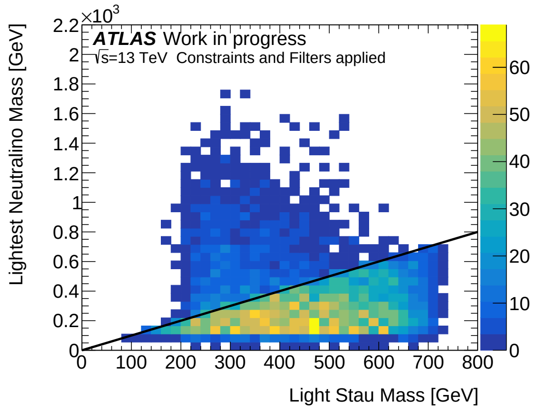

(b) $\tilde{\tau}_1$ vs. $\tilde{\chi}_1^0$ mass, with constraints and filters

Figure 7.4: Logarithmic plot of the LSP type (a) and the light stau against the lightest neutralino mass (b) for the models satisfying the constraints in table 7.2 and passing the LLVFilter. The LSP type is encoded with the following numbers: 1, 2 and 3 correspond to lightest neutralinos with a dominant bino, wino and higgsino component, respectively. 15 corresponds to the light stau, 16 to the tau sneutrino and 24 to the lightest chargino.

involving staus. Additionally, the masses of the lightest electroweakinos are smaller than the lightest stau mass in models with a lightest neutralino as LSP due to the degeneracy of light electroweakino masses for wino and higgsino $\tilde{\chi}_1^0$ (see figures 7.3b and 7.3c). Therefore, only a small fraction of the generated events will contain directly produced staus, especially for models with a $\tilde{\chi}_1^0$ as LSP. This would result in very low statistics for the processes which this study is focusing on. Therefore, the models were split in two sets, as has already been mentioned. For a fourth of the remaining models, i.e. 1816 models, events for all electroweak sparticle productions were generated. This set will be referred to as the EW set. For the rest, i.e. 5379 models, only events containing productions of sleptons were generated. This set will be referred to as the LL set. The LL set will provide higher model statistics for the later smeared truth evaluation while the EW set will provide insight in the influence of other electroweak production processes on the sensitivity of the direct stau analysis.

Concerning the LSP types in the remaining models, this test scan will keep models with a tau sneutrino. As the sneutrino is only weakly interacting, this sparticle is another DM candidate when it is the LSP. However, stable sneutrinos in the few GeV to several TeV mass range seem to be inconsistent with experiments investigating the scattering of heavy DM particles off nuclei [120]. As this is basically the mass range tau sneutrinos have in this scan, keeping these models in the scan might be debatable.
For models with a chargino as LSP, the event generation did not run successfully, therefore only models with either a neuralino or tau sneutrino LSP passed the event generation.
Due to the event generation being unsuccessful in some models (mostly chargino LSP models), 1798 models of the EW set and 5340 models of the LL set were left for the smeared truth evaluation.

As the EW set of models contains a rather small amount of models, the decision was made to produce more models for this set. To make this production more time efficient, models with $m_{\tilde{\chi}_1^\pm} < 300$ GeV were discarded, since these models would have high electroweakino production cross sections (see e.g. the $\tilde{\chi}_1^\pm\tilde{\chi}_1^\pm$-production in figure 7.5) and therefore require a high amount of produced events. Apart from this constraint, the same initial settings, physical constraints and filters were applied to these new models — called new EW set in the following

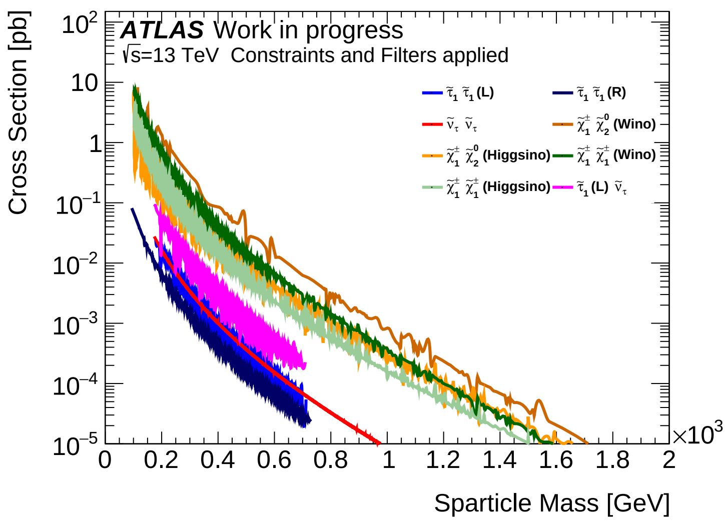

Figure 7.5: LO cross sections of chosen SUSY processes in dependence of the mass of the produced particles for the models passing the constraints and filters discussed in the previous sections. The electroweakino productions are separated according to their dominant gaugino eigenstate component and the stau productions are separated into the productions of left-handed (L) and right-handed (R) staus. For the $\tilde{\chi}_1^{\pm}\tilde{\chi}_2^0$-production, the smaller of the two masses is shown on the horizontal axis.

— as described in the previous sections. In the end, the new EW set contained 3052 models passing the requirements for the smeared truth evaluation step.

7.4 Smeared Truth Evaluation

The next step in the pMSSM scan procedure is the smeared truth evaluation using certain analyses. This is the point where the new truth smearing based on the previously developed tau classifiers will be implemented and the model exclusion will be evaluated using the direct stau analysis in the HadHad channel. For this work, this will be the last step, so the additional reconstruction-level evaluation for models with an uncertain exclusion will be skipped.

7.4.1 Tau Classification

Like in the studies in chapter 5, the original truth smearing in the pMSSM scan is done using the implementation of the UpgradePerformanceFunctions in SimpleAnalysis. Instead of employing a tau efficiency function which returns fixed (or slightly $|\eta|$ dependent) efficiency values for truth taus in different bins of p_{T}, $|\eta|$ and prongness, the previously developed tau classifier BDTs are implemented for the scan in this thesis. The medium/tight tau classifiers predict for each truth tau its probability of being reconstructed and of it passing the medium/tight ID WP.
Since the BDTs are not trained on taus with a $p_{\mathrm{T}} < 20$ GeV, the pre-smear cuts are left in place in SimpleAnalysis. Hence the replacement of the tau efficiency functions for medium and tight taus through the corresponding tau classifier BDTs are the only changes to the SimpleAnalysis truth smearing. It was determined in chapter 5 that overestimated recon-

struction and ID efficiencies are the main issue with the UpgradePerformanceFunctions tau truth smearing and in chapter 6 it was shown that the tau classifier BDTs greatly improve the efficiency prediction. Therefore, the described changes to the pMSSM scan tau truth smearing should result in a more accurate smeared truth evaluation for analyses based on tau leptons.
One caveat was discovered at a late stage of this work, however. The min(dR(truth tau, truth jet)) variable, used in the development of the medium and tight tau classifiers, employed the ConeTruthLabelID to determine non-tau jets. However, the labelling of jets in SimpleAnalysis is done with the ‘HadronConeExclTruthLabelID’. This label is employing a different algorithm to determine if a jet originated from a tau lepton, b, c or light quark. Therefore, the min(dR(truth tau, truth jet)) variable, when calculated in SimpleAnalysis, follows a different distribution. These differences were investigated for the available SqSq, GoGo and direct stau samples (see figure 7.6). As the plots show, the distribution of the tau to jet distance shows mainly disparities for values below 0.2, i.e. the region where the majority of jets were mislabelled. It seems that the HadronConeExclTruthLabelID is responsible for less mislabellings of jets. Therefore, it is advised that future implementations of such a variable describing the distance between a truth tau and a non-tau truth jet should define non-tau jets using this label instead of the ConeTruthLabelID. Unfortunately, this disparity was discovered too late to be respected in this particular study. But as the min(dR(truth tau, truth jet)) observable is the least important variable in the BDT training (see figure 6.21a and 6.24a) and the disparities are minor for most samples (and even if they are more significant, they can mostly be found in the first bin, see figure 7.6b), this difference in the jet labelling should not have a significant impact on the performance of the truth smearing.

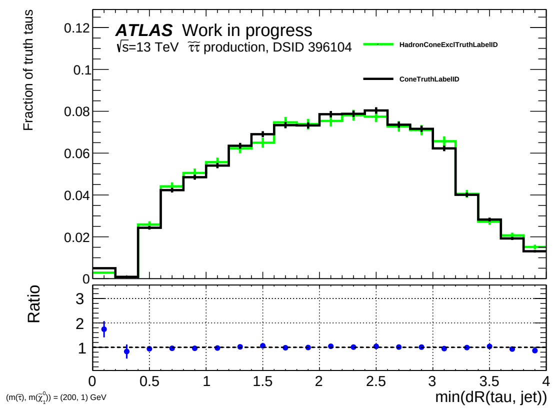

(a) DSID 396104

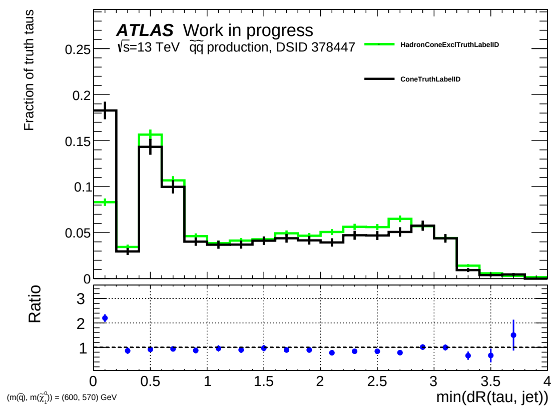

(b) DSID 378447

Figure 7.6: min(dR(truth tau, truth jet)) distribution of a direct stau sample (a) and the compressed SqSq sample (b). The observable was calculated with non-tau jets labelled by either the HadronConeExclTruthLabelID (green line) or the ConeTruthLabelID (balck line). The ratio of the two differently derived distributions is shown below.

7.4.2 Model Exclusion

Steps

In order to finally decide if a certain model can be excluded with the employed analysis, three steps are done in the pMSSM factory framework:

- Calculate Acceptance: First, the number of generated events which pass the selection criteria — which are applied on the smeared truth-level objects — of a SR of the considered analysis, N_{MC}^{acc}, is calculated using SimpleAnalysis. The acceptance $\mathcal{A}$ in a SR is now calculated as

$$\mathcal{A} = \frac{N_{MC}^{acc}}{N_{MC}}, \tag{7.1}$$

where N_{MC} is the total number of events that was generated for the considered model.

- Calculate Yields: From the acceptance of a certain model in a certain SR, one can then calculate the number of signal event yields N_{exp}, which pass the SR selection criteria, that one would expect to see at the ATLAS detector assuming an integrated luminosity L:

$$N_{exp} = \mathcal{A} \cdot \sigma_i \cdot L, \quad \text{i = EW, LL} \tag{7.2}$$

  Here, σ_i denotes the summed cross section of all considered SUSY processes in either the EW or LL model set.

- Calculate CL_s: Finally, the decision of whether to exclude a certain pMSSM model is made by calculating the corresponding CL_s value and excluding models with $CL_s < 0.05$, as described in section 4.4.1. This calculation is done using pyhf [121, 122] in the pMSSM factory framework. When an analysis defines more than one SR, it is possible to calculate a combined CL_s by using every SR as a bin in equation (4.3) (multi-bin) or to calculate the CL_s for every single SR (single-bin).

Direct Stau Analysis

As has been repeated throughout this chapter, the goal of the pMSSM scan of this thesis is to investigate the exclusion of models with the HadHad channel direct stau analysis [24]. This analysis defines two SRs: 'SR-lowMass' and 'SR-highMass'. Both SRs do not accept events containing light leptons, b-jets and more than two medium tau leptons. While SR-lowMass requires exactly two tight tau leptons with opposite electric charge and with $p_{\mathrm{T}} > 95$ (60) GeV for the leading (subleading) tau and intermediate $E_{\mathrm{T}}^{\mathrm{miss}}$ values, SR-highMass requires exactly two medium taus with opposite electric charge with at least one of them being a tight tau lepton and with $p_{\mathrm{T}} > 50$ (40) GeV for the leading (subleading) tau and high $E_{\mathrm{T}}^{\mathrm{miss}}$ values. Further requirements which aim to distinguish signal from background will not be discussed in this thesis. Instead, a detailed overview of the selection criteria of these two SRs can be found in section 5 of [24].

The selection criteria involving both tight and medium tau leptons explains the need for both a tight and medium tau classifier in the truth smearing. As in the original analysis, a luminosity of 139 fb^{-1} was used to calculate the expected number of signal yields in the SRs.

For the CL_s calculation, the full likelihood information of the background-only fit of [24] for the combination of both SRs was used. Therefore, both SRs and the two CRs of the most dominant background processes of the analysis were included in the likelihood and the correlations between the uncertainties of the event yields of different processes were considered. However, it was not possible to consider potential signal contamination in the CRs, i.e. the existence of signal events from SUSY processes in the CRs.

EwkTwoTau Analysis

Since the EW and the new EW set of pMSSM models include electroweakino production processes as well, another analysis was considered for this set of pMSSM models. This analysis is referred to as the EwkTwoTau analysis and it focuses on the direct production of charginos and neutralinos with tau leptons in the decay chain, i.e. the C1C1 process introduced in section 2.3 and the $\tilde{\chi}_1^{\pm}\tilde{\chi}_2^0$-production process (C1N2) visualised in figure 7.7 [25]. The simplified model this analysis was originally based on assumes a pure bino lightest neutralino LSP and

pure wino $\tilde{\chi}_1^\pm$ and $\tilde{\chi}_2^0$ which are mass degenerate[3]. The lightest stau is assumed to be purely left-handed and mass degenerate to the tau sneutrino [25].
The EwkTwoTau analysis defines two SRs of the same name as the previously explained analysis: a SR-lowMass and a SR-highMass. Here, the SR-lowMass requires at least two medium tau leptons with opposite electric charge, $p_T > 50$ (40) GeV for the leading (subleading) tau and $E_T^{\text{miss}} > 150$ GeV. The SR-highMass on the other hand requires at least one medium and one tight tau lepton with opposite electric charge and either $p_T > 80$ (40) GeV for the leading (subleading) tau and $E_T^{\text{miss}} > 150$ GeV or $p_T > 95$ (65) GeV for the leading (subleading) tau and $E_T^{\text{miss}} > 110$ GeV. Additional requirements of these SRs will not be discussed in this thesis, instead, a detailed overview can be found in section 5 of [25]. For the yield calculation step, a luminosity of 139 fb^{-1} was assumed to ensure comparability with the direct stau analysis evaluation of the EW and new EW set models.
For the EwkTwoTau analysis, the likelihood information of the background-only fit and therefore of the different background processes and CRs was not available. Instead, a CL_s-value has been calculated for both of the SRs separately using the number of background events and their uncertainty given in table 9 of [25] entering the likelihood function as fixed values. The number of observed events, i.e. the real data, was taken from this table as well. For every model, the SR which yields a lower CL_s is used to determine if the model is excluded. Since the EwkTwoTau analysis was originally working with 36.1 fb^{-1}, the number of background and data yields and the background uncertainties had to be scaled up so that they would correspond to a luminosity of 139 fb^{-1}.

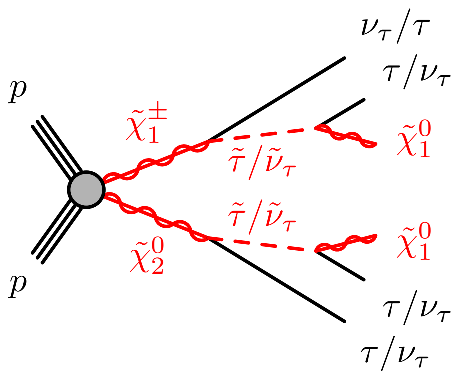

Figure 7.7: Tree-level feynman diagram of the C1N2 process.

This concludes the steps which were taken in order to conduct the pMSSM scan of this thesis. The results of the smeared truth evaluation, i.e. a comparison of the model exclusion in the pMSSM scan and the original simplified model analyses, will be presented in the next chapter in section 8.3.

[3]To be exact, the analysis defines two different models, one for the C1C1 process, where just the pure wino $\tilde{\chi}_1^\pm$ is considered apart from the $\tilde{\chi}_1^0$ and $\tilde{\tau}_1/\tilde{\nu}_\tau$ and the one for the C1N2 process, where the pure wino $\tilde{\chi}_2^0$ is considered as well.

Chapter 8

Results

In the previous chapters of this thesis, ways to improve the performance of the truth smearing that is currently in use have been presented. The presented improvement strategies included the recalculation of the reconstruction and ID efficiency which yielded a better smearing performance for a limited range of SUSY models (chapter 5) as well as using a BDT with a newly developed parametrisation of this efficiency in order to achieve a sample independent improvement (chapter 6). In this chapter, the results of applying these newly developed methods in previously discussed use cases are presented.
First, an estimate of the sensitivity in the SqSq grid (see section 4.4.4) will be shown, which was derived with the new tau truth smearing for samples of the SqSq process (see section 5.3.2). Then, the results of producing high statistics smeared truth-level samples for the direct stau LepHad analysis (see section 4.4.4), where a new smearing for taus, electrons and muons for direct stau samples was implemented, will be discussed shortly. Finally, the results of the pMSSM scan, which employs the newly developed tau classifier BDTs (see section 6.3) and has been described in detail in chapter 7, will be presented.

8.1 Sensitivity in the Squark-Squark Grid

In order to estimate the sensitivity of the GoGo analysis [23] in the SqSq grid, this grid needs to be generated first. This has been achieved by using the simplified model described in section 2.3 for the SqSq process, varying the squark and neutralino mass and producing 30000 generator-level events for each of these models. For this grid, squark masses between 600 GeV and 1600 GeV and neutralino masses between 45 GeV and 745 GeV were considered and the truth-level information was generated using MadGraph v.2.6.2 and Pythia 8.235. As one was mainly interested in the sensitivity limits, not every model in the mentioned ranges is investigated, but rather models being near those limits.
Here, the sensitivity of a GoGo analysis SR to a certain SqSq model is determined by calculating the significance Z of finding n events in the SR while assuming the background-only hypothesis ('Discovery'). The number of events n in the SR can be split into signal events s from the SqSq process and background events b from relevant SM processes in that region, i.e. $n = s + b$. A SR is said to be sensitive to a certain model if $Z > 1.64$, i.e. if the background-only hypothesis can be rejected at 95 % CL. In this thesis, Z is calculated using

the formula which is recommended for significance estimation at ATLAS [123][1]:

$$Z = \begin{cases} +\sqrt{2\left(n\ln\left[\frac{n(b+\sigma_b^2)}{b^2+n\sigma_b^2}\right] - \frac{b^2}{\sigma_b^2}\ln\left[1+\frac{\sigma_b^2(n-b)}{b(b+\sigma_b^2)}\right]\right)} & n \geq b \\ -\sqrt{2\left(n\ln\left[\frac{n(b+\sigma_b^2)}{b^2+n\sigma_b^2}\right] - \frac{b^2}{\sigma_b^2}\ln\left[1+\frac{\sigma_b^2(n-b)}{b(b+\sigma_b^2)}\right]\right)} & n < b \end{cases} \tag{8.1}$$

In this formula, σ_b denotes the uncertainty on the predicted number of background events b. The values of b and σ_b in the different SRs of the GoGo analysis were taken from table 10 and 11 in [23]. As the GoGo analysis was originally conducted using a luminosity $L = 36.1$ fb^{-1} and the sensitivity estimates in this thesis are calculated assuming a luminosity $L = 139$ fb^{-1}, b and σ_b were multiplied by the corresponding scaling factor. In order to get the number of signal yields s in the SRs, SimpleAnalysis is employed. First, the truth-level objects from the generated events were smeared using the new smearing for the SqSq process (see section 5.3.2). On these, the selection criteria of the SRs are applied to get the acceptance $\mathcal{A}$ (see equation (7.1)) with which s can be calculated:

$$s = \mathcal{A} \cdot \frac{4}{10} \cdot \sigma_{\tilde{q}\tilde{q}}(m_{\tilde{q}}) \cdot L \tag{8.2}$$

Here, $\sigma_{\tilde{q}\tilde{q}}(m_{\tilde{q}})$ is the cross section of the SqSq process for a simplified SqSq model with a certain squark mass $m_{\tilde{q}}$. The used cross sections $\sigma_{\tilde{q}\tilde{q}}(m_{\tilde{q}})$ for the SqSq process are given in [125] at NNLO. However, a factor of $\frac{4}{10}$ had to be added to the calculation as these $\sigma_{\tilde{q}\tilde{q}}(m_{\tilde{q}})$ assume ten squarks with degenerate masses while the simplified model of the considered SqSq process only assumes four (see section 2.3).
Now that the estimation of the sensitivity for a certain SqSq model in a certain SR has been explained, a short description of the SRs, which are defined in the GoGo analysis, will be presented. A more complete description can be found in section 5 of [23]. For the GoGo process described in section 2.3, the GoGo analysis defines four single-bin SR:

- 1τ Compressed: This SR requires exactly one tau lepton and at least two jets. The p_{T} of the tau is constrained between 20 GeV and 45 GeV, which favours more compressed scenarios. Additionally, $E_{\mathrm{T}}^{\mathrm{miss}} > 400$ GeV is required, which favours models with high neutralino masses.

- 1τ Medium-mass: This SR, like the other 1τ SR, requires exactly one tau lepton and at least two jets. In contrast to the compressed SR, a lower limit is set for the tau p_{T} at 45 GeV and the p_{T} of the tau plus the p_{T} of all jets have to sum up to at least 1 TeV. These requirements favour less compressed scenarios and relatively high squark masses. Furthermore, a cut on $E_{\mathrm{T}}^{\mathrm{miss}} > 400$ GeV is set.

- 2τ Compressed: This SR requires at least two tau leptons and at least two jets. The transverse momenta of the taus are not directly constrained, however the sum of all tau and jet p_{T} is required to be below 1.1 TeV, favouring rather small squark masses. Also, a cut on $E_{\mathrm{T}}^{\mathrm{miss}} > 180$ GeV is applied, which allows for models with lower neutralino masses than in the case of the 1τ SRs.

- 2τ High-mass: As the previous 2τ SR, this SR needs at least two tau leptons and jets. However, here the sum of all tau and jet p_{T} has to be above 1.1 TeV, favouring high squark masses. The same $E_{\mathrm{T}}^{\mathrm{miss}}$ cut is applied as in the 2τ Compressed SR.

These SRs were used to evaluate the sensitivity for the produced SqSq models. In figure 8.1, the produced SqSq models are shown in the $m_{\tilde{q}}$-$m_{\tilde{\chi}_1^0}$-space. The plot also shows the value of

[1] This formula also corresponds to equation (25) of [124].

Z which was calculated with the SR that yielded the highest sensitivity. The corresponding SR is indicated by the colour of the model points.
From figure 8.1, it can be seen that at least one SR of the GoGo analysis is sensitive to the SqSq process up to squark masses of about 1500 GeV and neutralino masses of around 500 GeV – 600 GeV. However, one has to keep in mind that the new smearing for the SqSq process yielded a significantly worse performance for very compressed mass configurations. Therefore, one can assume that the significances calculated for models near the $m_{\tilde{q}} = m_{\tilde{\chi}_1^0}$ diagonal might be somewhat overestimated. This is due to the fact that the new smearing for the SqSq process overestimated the tau efficiency for compressed mass configurations and would therefore overestimate the number of tau leptons passing the SR selection criteria. Nevertheless, it is clear that employing the GoGo analysis to constrain the parameter space of the SqSq simplified model appears to be promising.

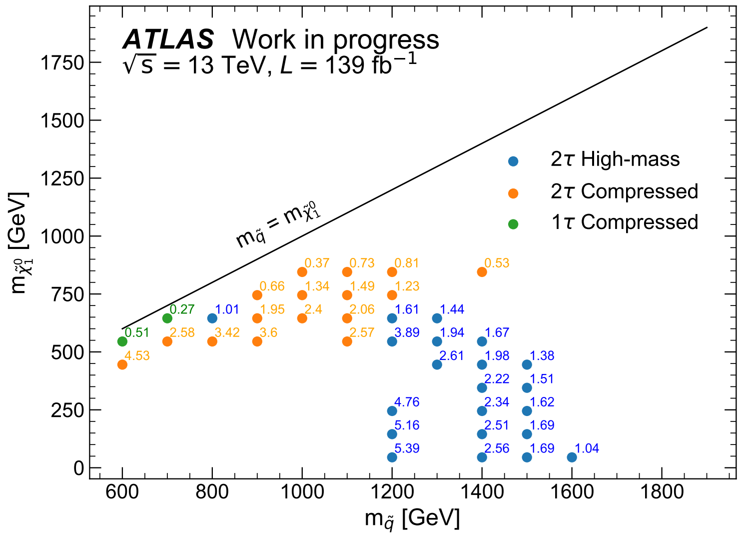

Figure 8.1: Values of the sensitivity for the produced simplified models in the SqSq grid. The SR which yielded the highest sensitivity is indicated by the colour of the model marker.

8.2 Truth Smeared Direct Stau Samples

Another example where the application of truth smearing appeared to be of use was the direct stau analysis in the LepHad channel. As described in section 4.4.4, a sample with high statistics is needed that can be used for a BDT selection procedure. Hence, a direct stau process sample with high statistics, i.e. a million events, was produced at generator-level. The simplified model described in section 2.3 for the direct stau process was employed with a stau mass of 120 GeV and a neutralino mass of 40 GeV. Then, the new truth smearing for the direct stau process, including the improved tau, electron and muon efficiency functions (see section 5.3), was used to smear the truth-level objects for this high statistics sample. This sample was then used in the direct stau analysis in the LepHad channel, as can be seen in detail in section 9.5 of [85].
Unfortunately, the smeared truth sample was not able to help improve the results of that analysis. The main reasons appear to be the fact that the analysis used reconstruction-level variables, which could not be provided using smeared generator-level information, and that the BDT training with a single sample, i.e. just one model, yields worse results compared to using a variety of samples [85].

8.3 Direct Stau Analysis in the pMSSM Scan

In chapter 7, a pMSSM scan has been described which focused on the part of the pMSSM parameter space which allows for an abundant production of tau sleptons and SUSY processes with similar topologies. Now, it will be investigated how the sensitivity of the direct stau analysis in the HadHad channel for the generated pMSSM models differs from its sensitivity for the direct stau simplified models. As has already been mentioned, the pMSSM models were separated into the EW and new EW set for which events containing slepton and electroweakino production were generated and the LL set for which only slepton production was considered in the generated events (see section 7.3). For the EW and new EW set, the EwkTwoTau analysis was employed as well.

Direct Stau Analysis
First, the results of the smeared truth evaluation of the pMSSM models using the direct stau analysis will be analysed. In figures 8.2a and 8.2b, one can see the exclusion rate, i.e. the rate with which pMSSM models are excluded in a certain region of the parameter space, binned in the lightest stau and neutralino mass for both the LL and the EW set of models. Additionally, the figure shows the exclusion limits that the analysis placed on the parameter space of the used simplified models. Obviously, these plots show some interesting phenomena.
A quite obvious feature is the existence of pMSSM models above the $m_{\tilde{\tau}} = m_{\tilde{\chi}_1^0}$ diagonal. This is a consequence of keeping pMSSM models with a tau sneutrino LSP which allow for lightest neutralinos with higher masses than the stau as they are not required to be the LSP. Hence, models above the diagonal have a $\tilde{\nu}_\tau$ LSP and models below the diagonal have a $\tilde{\chi}_1^0$ LSP. This can be seen directly in figures 8.2c and 8.2d, which show the exclusion rates binned in the lightest stau and neutralino mass again, but this time without the pMSSM models that had a tau sneutrino as LSP. Another phenomenon that can be seen immediately is the low abundance of pMSSM models in the low-$m_{\tilde{\chi}_1^0}$ region. This can be explained by the fact that models with a bino-like $\tilde{\chi}_1^0$ LSP were in large parts discarded by the DM relic density constraint, hence the remaining low-mass lightest neutralinos are predominantly wino- and higgsino-like. Such neutralino compositions would imply a lightest chargino with a very similar mass (see figures 7.3b and 7.3c). As the lightest chargino mass is required to be above 103 GeV, one would therefore expect models with $m_{\tilde{\chi}_1^0} < 103$ GeV to be very rare. Unfortunately, the lack of models at small lightest neutralino masses makes a comparison between a large part of the exclusion limit for simplified models[2] and the exclusion rates for pMSSM models difficult. However, for $m_{\tilde{\chi}_1^0} > 100$ GeV, a comparison is possible.
In this 'upper' part of the exclusion limit, one can see that pMSSM models of the LL set (figure 8.2a) are excluded at rates up to 50 % as well. This means that the direct stau analysis is able to exclude more general pMSSM models for these stau and neutralino masses as well. But, it also means that there is still a range of pMSSM models with these masses that were out of reach for this analysis even though the corresponding simplified models could be excluded.
In the LL set plot, another phenomenon catches the eye. Obviously, the analysis was able to exclude pMSSM models with stau masses significantly exceeding the exclusion limit contour. This is best explained by the fact that in contrast to the simplified model analysis, this study considered not only the direct production of staus but also the direct production of tau sneutrinos and the associated production of a stau and a tau sneutrino. From figure 7.5, it is evident that these processes significantly increase the cross section of processes with event topologies that the direct stau analysis is sensitive to[3]. A higher cross section in turn results

[2]Note that the direct stau simplified model assumed a bino-like neutralino LSP, see section 2.3.

[3]A produced tau sneutrino could decay into a chargino and a tau, since the chargino will have a similarly small mass as the neutralino LSP. This would — apart form the chargino to neutralino decay — give the same

in a higher potential signal strength and therefore results in potentially lower CL_s values and higher exclusion rates.

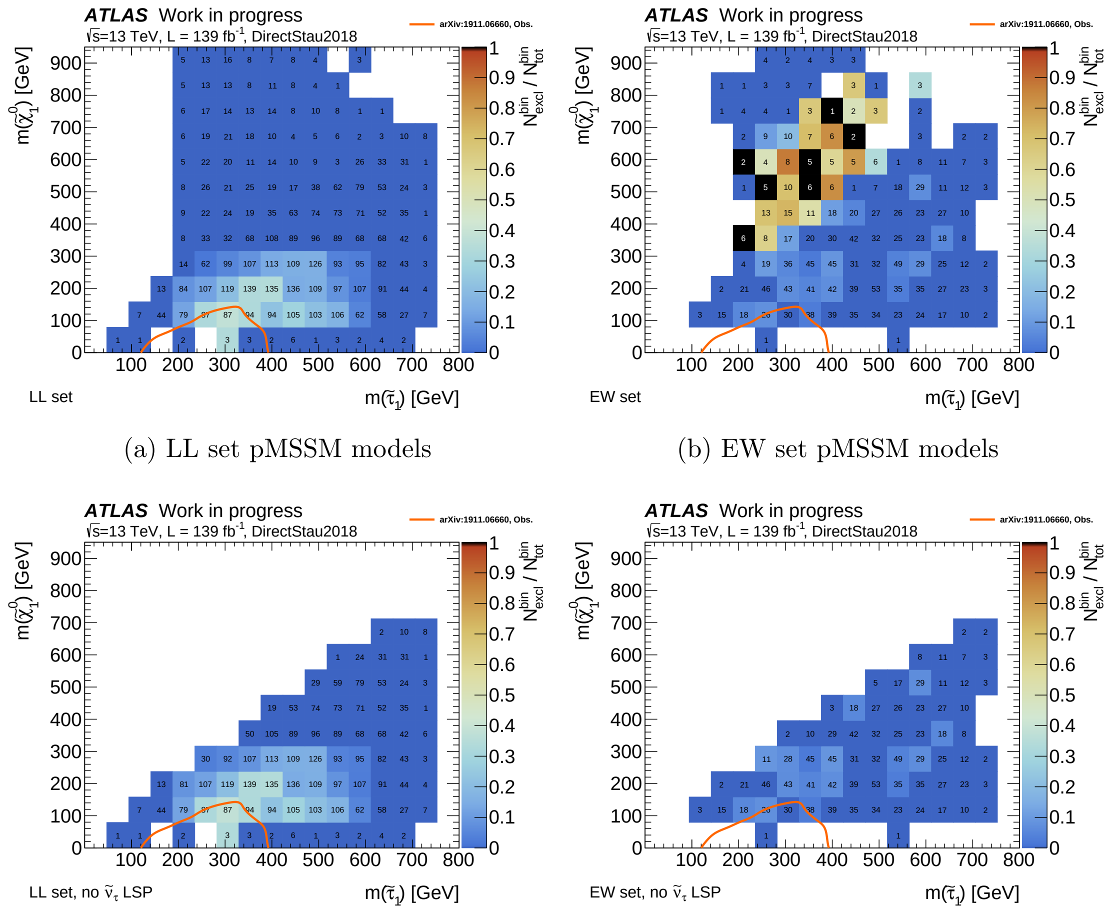

(a) LL set pMSSM models (b) EW set pMSSM models

(c) LL set pMSSM models, no $\tilde{\nu}_\tau$ LSP (d) EW set pMSSM models, no $\tilde{\nu}_\tau$ LSP

Figure 8.2: Exclusion rate $\mathrm{N}_{\mathrm{excl}}^{\mathrm{bin}}/\mathrm{N}_{\mathrm{tot}}^{\mathrm{bin}}$ for the pMSSM models, i.e. the number of excluded models $\mathrm{N}_{\mathrm{excl}}^{\mathrm{bin}}$ divided by the total amount of models $\mathrm{N}_{\mathrm{tot}}^{\mathrm{bin}}$ in a certain bin, binned in the $\tilde{\tau}_1$ mass and $\tilde{\chi}_1^0$ mass for the LL (a) and EW (b) set. Below, the same plots are shown without models containing a tau sneutrino as LSP for the LL (c) and the EW (d) set. The direct stau analysis was employed to determine if a model can be excluded and the orange line shows the exclusion limit this analysis derived by considering simplified models [24]. The colour of a bin indicates the pMSSM model exclusion rate in this bin while the number shows the total amount of models $\mathrm{N}_{\mathrm{tot}}^{\mathrm{bin}}$ in the bin.

Changing the focus to figure 8.2b, the plot of the exclusion rates for the EW set models looks quite different. On the one hand, the exclusion rates near the simplified model exclusion limit are significantly lower than in the LL set case. Probably, this can be explained by the low proportion of stau and tau sneutrino production mode events among the EW set events as the cross sections of electroweakino production modes are up to a magnitude higher. As the selection criteria of the SRs only accept a small percentage of the produced events, it can be assumed that for many EW models, the statistics of stau/tau sneutrino production modes is insufficient to derive the acceptance correctly. This would predominantly result in an underestimation of the acceptance and therefore the expected signal strength which in turn reduces the sensitivity and exclusion rate.

signature as the usual stau decay in the direct stau process.

While for the LL set, nothing interesting could be seen in the region above the $m_{\tilde{\tau}} = m_{\tilde{\chi}_1^0}$ diagonal, the EW set models show a high exclusion rate in this region. From the fact that these high exclusion rates for EW set models are only seen above the diagonal and from figure 8.2d, one can deduce that this behaviour only applies to models with a tau sneutrino LSP. Since this phenomenon was not observed for the LL set, it is quite clear that electroweakinos decaying to tau sneutrinos (or staus) make for this increased sensitivity. As such processes would produce similar signatures as the original direct stau process, it appears logical that the direct stau process is sensitive to these pMSSM models.

However, especially in the high exclusion region above the diagonal, the EW set contains only a very small number of models. Because of the small amount of EW set models, the new EW set was generated. However, the additional cut $m_{\tilde{\chi}_1^\pm} > 300$ GeV on these models makes a comparison with the EW set in the $m_{\tilde{\tau}_1}$–$m_{\tilde{\chi}_1^0}$ plane impossible. Therefore, the exclusion rates of the EW and the new EW set are shown binned in $m_{\tilde{\tau}_1}$ and the smaller of the two masses $m_{\tilde{\chi}_1^\pm}$ and $m_{\tilde{\chi}_2^0}$ in figure 8.3 since the additional cut is clearly visible in this depiction. Note that most of the models lie on the diagonal as most models have a wino- or higgsino-like neutralino LSP.

As the region of moderate exclusion rates near the simplified model exclusion limits in figure 8.2b is below a neutralino mass of 300 GeV, it will not be possible to see a sufficient amount of new EW set models in this region since most of the low neutralino mass models have a wino- or higgsino-like neutralino and therefore the chargino mass cut will constrain the neutralino mass as well. This can be seen immediately in figure 8.3b.

The second phenomenon seen in figure 8.2b on the other hand, i.e. the region with high exclusion rates due to tau sneutrino LSPs, can now be observed with higher model statistics. From figure 8.3a, it can be seen that these tau sneutrino LSP models with high exclusion rates lie at relatively high $\tilde{\chi}_1^\pm/\tilde{\chi}_2^0$ masses and approximately on the diagonal in the $m_{\tilde{\chi}_1^\pm}/m_{\tilde{\chi}_2^0}$–$m_{\tilde{\chi}_1^0}$ plane. Figure 8.3b confirms this behaviour for the new EW model set. It even seems that this region of high exclusion rate is even more wide-spread than the EW set plot suggested.

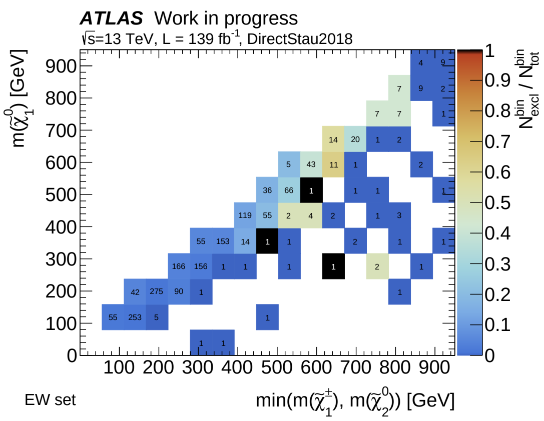

(a) EW set pMSSM models

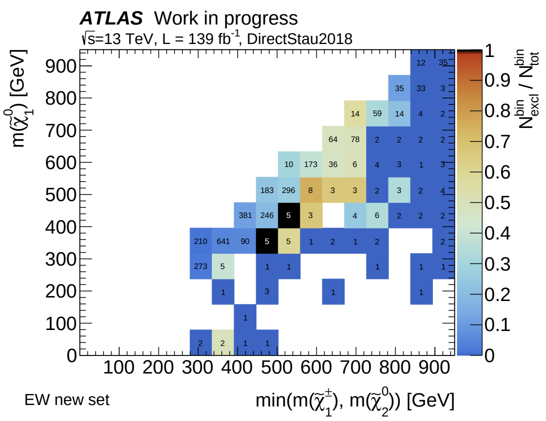

(b) New EW set pMSSM models

Figure 8.3: Exclusion rate of pMSSM models binned in the minimal value of the $\tilde{\chi}_1^\pm$ and $\tilde{\chi}_2^0$ mass on the horizontal axis and the $\tilde{\chi}_1^0$ mass on the vertical axis for the EW (a) and new EW (b) set. The direct stau analysis was employed to determine if a model can be excluded.

EwkTwoTau Analysis

Now, the results of using the EwkTwoTau analysis for the smeared truth evaluation of the pMSSM models of the EW and new EW set will be presented. In figures 8.4a and 8.4b, the exclusion rates binned in the minimum of the $\tilde{\chi}_1^\pm$ and $\tilde{\chi}_2^0$ masses and the $\tilde{\chi}_1^0$ mass is shown for the EW and new EW set. In these plots, the EwkTwoTau analysis was employed to

determine if a model could be excluded and the orange line shows the exclusion limit this analysis derived for the simplified models. Since the vast majority of the generated models lie on the diagonal in this plane and the simplified model exclusion limit is located exclusively in the region below it[4], a comparison of the exclusion limit and the pMSSM model exclusion rates is not possible in a statistically relevant fashion. Even for the new EW set, the pMSSM models are not abundant enough in the region below the diagonal. At low $\tilde{\chi}_1^0$ masses, where the exclusion limit comes near the diagonal, one can observe merely small, non-zero exclusion rates in figure 8.4a. These are probably due to additional production modes being considered in the pMSSM model samples.
However, a similar phenomenon as in the direct stau analysis case can be observed for lightest neutralino masses above the exclusion limit. Here, high exclusion rates, in some bins exceeding 50 %, can be observed. As these models vanish when looking at the same plots without pMSSM models containing a tau sneutrino LSP (figures 8.4c and 8.4d), it can be deduced that the high exclusion rates in this region primarily stem from models with a tau sneutrino LSP.

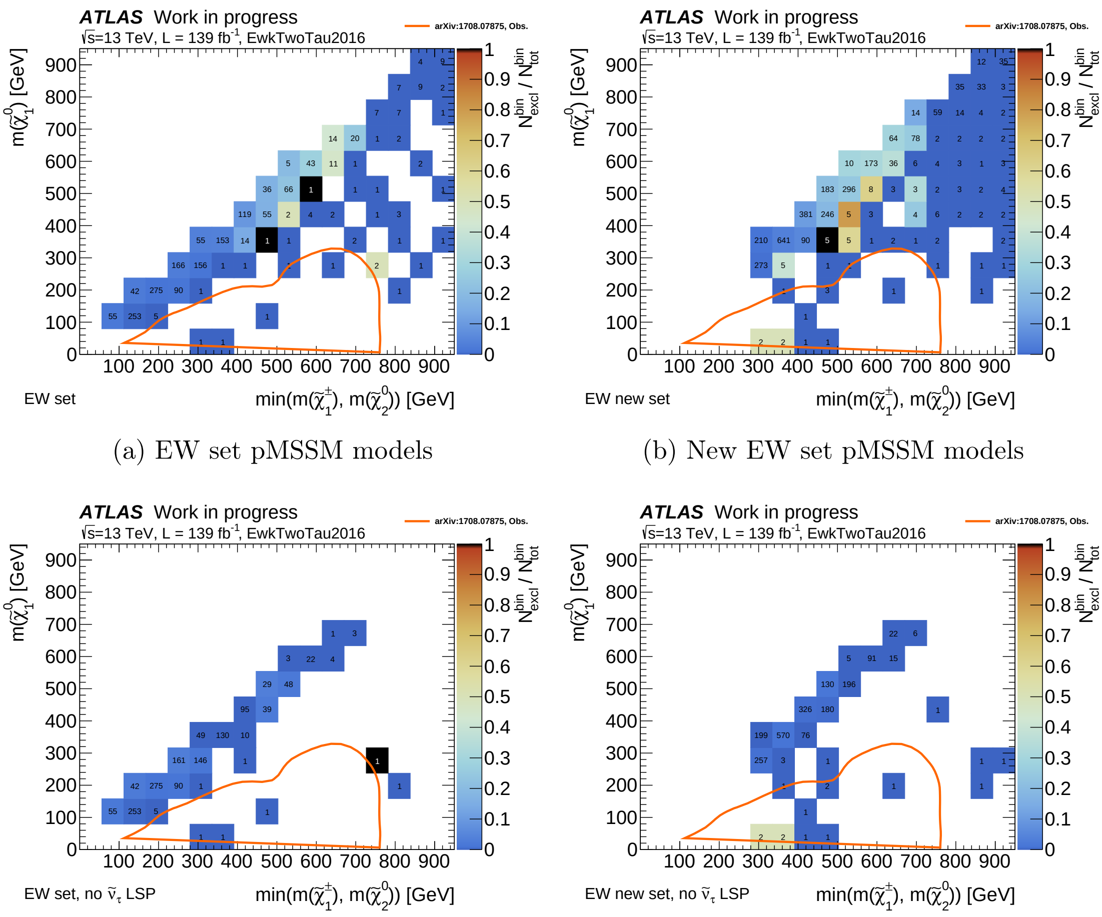

(a) EW set pMSSM models

(b) New EW set pMSSM models

(c) EW set pMSSM models, no $\tilde{\nu}_\tau$ LSP

(d) New EW set pMSSM models, no $\tilde{\nu}_\tau$ LSP

Figure 8.4: Exclusion rate of pMSSM models binned in the minimal value of the $\tilde{\chi}_1^\pm$ and $\tilde{\chi}_2^0$ mass on the horizontal axis and the $\tilde{\chi}_1^0$ mass on the vertical axis for the EW (a) and new EW (b) set. Below, the same plots are shown without models containing a tau sneutrino as LSP for the EW (c) and the new EW (d) set. The EwkTwoTau analysis was employed to determine if a model can be excluded and the orange line shows the exclusion limit this analysis derived by considering simplified models [25].

[4]Note that the simplified models used in this analysis assumed a pure bino neutralino LSP, like in the direct stau analysis.

It is interesting to see that for both analyses, high exclusion rates are observed well outside the simplified model exclusion limits on the stau and electroweakino masses. The corresponding excluded models seem to be exclusively models that contain a tau sneutrino LSP. One can therefore deduce that the investigated analyses are, apart from the mass ranges excluded for the simplified models, sensitive to electroweakino production modes if the considered model has a tau sneutrino as LSP.

This similarity between the two analyses can also be seen in figure 8.5, where the exclusion rates for the new EW set are shown in the $m_{\tilde{\nu}_\tau}$–$\min(m_{\tilde{\chi}_1^\pm}, m_{\tilde{\chi}_2^0})$ plane. In figure 8.5a, the direct stau analysis is employed and in figure 8.5b, the EwkTwoTau analysis. These plots show that the exclusion rate is quite high for both analyses in the region directly below the $m_{\tilde{\nu}_\tau} = \min(m_{\tilde{\chi}_1^\pm}, m_{\tilde{\chi}_2^0})$ diagonal. This region only contains models with a tau sneutrino LSP, as can be deduced from figures 8.5c and 8.5d which show the same plots, but without models having the $\tilde{\nu}_\tau$ as LSP. Therefore, the direct stau analysis and the EwkTwoTau analysis are sensitive to nearly the same region in the $m_{\tilde{\nu}_\tau}$-$\min(m_{\tilde{\chi}_1^\pm}, m_{\tilde{\chi}_2^0})$ plane, with the sensitive region of the direct stau analysis being somewhat larger.

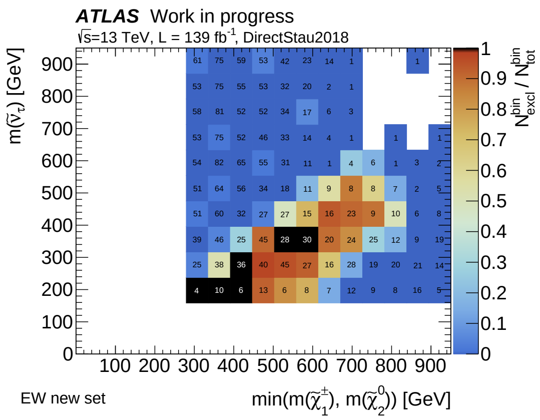

(a) Direct Stau Analysis

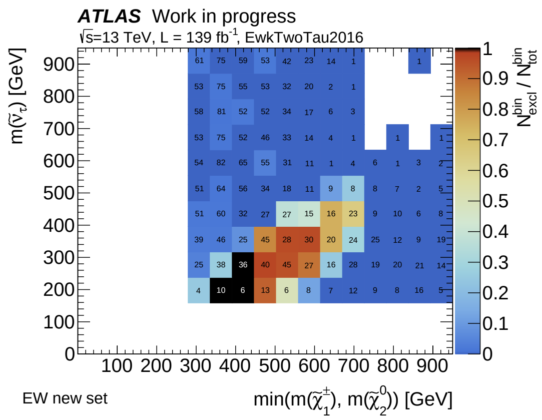

(b) EwkTwoTau Analysis

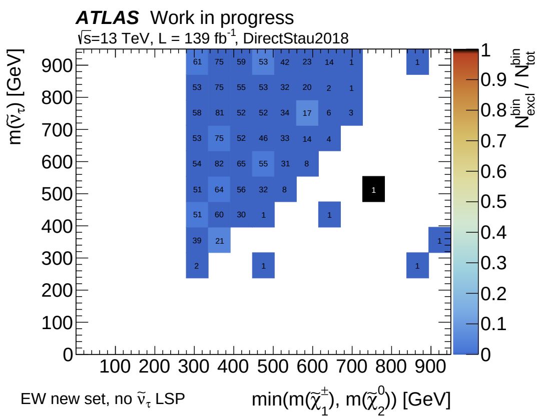

(c) Direct Stau Analysis, no $\tilde{\nu}_\tau$ LSP models

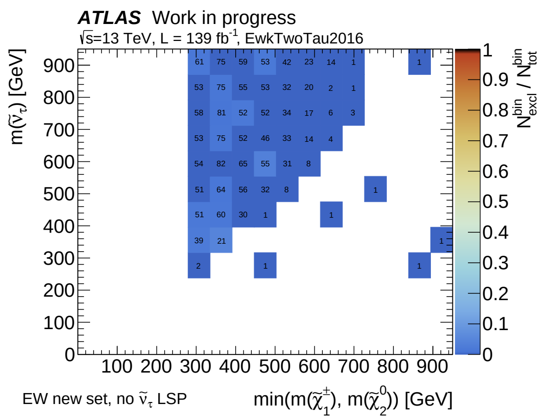

(d) EwkTwoTau Analysis, no $\tilde{\nu}_\tau$ LSP models

Figure 8.5: Exclusion rate of pMSSM models binned in the minimal value of the $\tilde{\chi}_1^\pm$ and $\tilde{\chi}_2^0$ mass on the horizontal axis and the $\tilde{\nu}_\tau$ mass on the vertical axis for the new EW set. The direct stau analysis (a) and the EwkTwoTau analysis (b) were employed to determine if a model can be excluded. Below, the models with the $\tilde{\nu}_\tau$ as LSP were neglected, but again, the direct stau analysis (c) and the EwkTwoTau analysis (d) were used.

Chapter 9

Conclusion and Outlook

The search for SUSY is one of the great endeavours of the ATLAS experiment at the LHC. As SUSY encompasses a vast spectrum of different models, searches usually employ only a simplified model which constrains the SUSY parameter space to just two parameters of interest. In most cases, such a simplified model allows for only one SUSY process to be of relevance which can then be analysed in detail and searched for. An approach which accounts for a broader spectrum of SUSY phenomena is a scan of the pMSSM, a supersymmetric extension of the Standard Model which is constrained to 19 parameters. This thesis studied a method that is a crucial part of the pMSSM scan procedure and has many use cases in searches for simplified models: truth smearing.
Truth smearing describes a technique that aims to reduce the amount of computational resources needed for the simulation of data. This simulation usually consists of two steps: first, the event generation, where physical objects and their properties are produced assuming a centre of mass energy of 13 TeV (truth-level) and secondly, the ATLAS detector simulation and reconstruction, where the detector response to the truth-level objects is simulated and the physical objects are reconstructed from the detector response (reconstruction-level). In order to reduce the needed resources, truth smearing introduces smearing functions that are applied to truth-level objects and replace the second part of the simulation chain. Since the pMSSM scan considers a huge amount of models and since for each of these, simulated data is needed for the analysis, the standard procedure in the pMSSM scan is already employing truth smearing instead of the detector simulation in order to save computational resources. For simplified model searches the usage of truth smearing can be beneficial as well, e.g. for the production of samples with high statistics or preliminary studies which explore the sensitivity reach of a reinterpreted analysis. In order to ensure that the results of studies employing truth smearing are reliable, the smeared truth-level objects have to resemble the corresponding reconstruction-level objects as much as possible.
Therefore, in the beginning of this thesis, the performance of the smearing functions that are currently in use was tested for tau leptons. This test yielded a bad agreement between smeared truth-level and reconstruction-level tau leptons in the final state of the squark pair production and the direct stau production process. From that test, it was also obvious that the main reason of this insufficient performance was the overestimation of the reconstruction and identification (ID) efficiency for these processes. This efficiency determines the fraction of truth-level tau leptons that will be reconstructed and pass the ID criteria. Consequently, the main focus of this thesis was to improve the efficiency functions in the truth smearing for tau leptons.

The first approach to this task was the sample specific recalculation of the reconstruction and ID efficiencies. Here, sample refers to a certain mass configuration in a certain SUSY

or SM process. Two new truth smearings were developed for tau leptons of the squark pair (SqSq) and stau pair (direct stau) production processes by implementing the recalculated efficiencies of a sample of the respective process in the efficiency function of the truth smearing. These new truth smearings showed a significantly improved agreement between smeared truth-level and reconstruction-level tau leptons. However, it was found that the performance of these truth smearings deteriorated when applied to samples with a very different mass configuration than that of the sample used for the efficiency recalculation.
The truth smearing for objects of the direct stau process was further improved by implementing recalculated reconstruction and ID efficiencies for electrons and muons. The efficiencies were recalculated for the same sample as in the tau lepton case. This improvement for light leptons was necessary as the original truth smearing did not consider the influence of impact parameter cuts on the reconstruction and ID efficiency, which again leads to an overestimation.
The new truth smearings were then employed in studies related to simplified model searches. Namely, the newly developed smearing for objects of the direct stau process was used to generate a high statistics sample of this process assuming a stau mass of 120 GeV and a neutralino mass of 40 GeV. This sample was then used in the direct stau analysis in the LepHad channel [85]. Furthermore, the new truth smearing for objects of the SqSq process was employed to estimate the sensitivity reach in the parameter space of the corresponding simplified model with a reinterpreted analysis. This analysis [23] was originally used to search for the gluino pair production process with tau leptons in the final state (GoGo), but due to the similarities between the GoGo and SqSq process, such a reinterpretation was deemed possible. Indeed, this sensitivity estimation using smeared truth-level data showed that the GoGo analysis is sensitive to the SqSq simplified models up to squark masses of around 1.5 TeV and neutralino masses of around 500 GeV – 600 GeV, assuming an integrated luminosity of $L = 139\ \text{fb}^{-1}$. Since the recalculation of efficiencies for the new smearing or the SqSq process was carried out using a sample with a high mass difference between squark and neutralino, the sensitivity estimates for samples with a very compressed mass configuration should be considered carefully.

The calculation of reconstruction and ID efficiencies of the tau leptons revealed an unforeseen problem: the efficiencies were sample dependent. This also appeared to be the reason for the worsening performance of the new truth smearings when they were used for samples with a very different mass configuration. From a physical perspective, it is not logical that the reconstruction and ID efficiency depends on the mass configuration of the considered SUSY process. Instead, the efficiency should only depend on properties of the tau lepton itself. The fact that one expects a different tau reconstruction and ID efficiency for tau leptons with different properties was already incorporated in the original and new truth smearings. Namely, a binning in the transverse momentum p_{T}, the pseudorapidity $|\eta|$ and the prongness (the number of charged decay products of the tau) was employed. However, even though these observables were considered when calculating the efficiency, the sample dependence persisted. Therefore, additional observables were needed to achieve a sample independent parametrisation of the tau lepton reconstruction and ID efficiencies. Since a binning in more than three observables wouldn't be feasible with the available statistics, Boosted Decision Trees (BDTs) were employed to find and implement this new parametrisation. These were trained with a large set of samples from the SqSq process, the GoGo process, the direct stau process, the chargino pair production process with tau leptons in the final state (C1C1), the top squark pair production process with tau leptons in the final state (ttStau) and the top quark pair production (ttbar) process. It was found that the optimal parametrisation, i.e. the best input features for the BDT, consisted of the tau p_{T}, the tau $|\eta|$, the tau prongness, the number of neutral tau decay products, min(dR(truth tau, truth jet)) (minimal distance between the tau and a non-tau jet) and min(dR(truth tau, truth tau-jet)) (minimal distance between the

tau and its own tau-jet). The BDTs could then be used to predict the reconstruction and ID efficiency of an arbitrary tau lepton based on these six observables. By measuring the mean squared error of the predicted efficiencies with respect to the actual efficiencies in a tau p_{T} and $|\eta|$ binning for each sample, it was found that this approach of determining the efficiencies yielded a far better agreement than the original tau efficiency functions across the considered samples. Also, this efficiency prediction appeared to be sufficiently sample independent.
Hence, this work suggests that the complex dependencies of the reconstruction and ID efficiency of tau leptons can best be incorporated in a truth smearing by employing a BDT or machine learning methods in general. Furthermore, this thesis shows that the original three variables, which were used to parametrise the efficiencies in a bin-like manner, are insufficient. Instead, this thesis proposes an expanded set of observables that appear to sufficiently reflect the dependencies of the tau reconstruction and ID efficiency. However, future implementations should revise the min(dR(truth tau, truth jet)) variable, since it seems that a more accurate labelling of non-tau jets than used in this thesis is available. Also, it was seen that the predictions were less accurate for samples which were quite unique among the training samples, e.g. the SqSq process samples as only three of these were available. Therefore, it is suggested that the training should employ a set of samples that is as diverse as possible with respect to different processes and mass configurations.

In the final part of this thesis, a pMSSM scan was conducted with the newly developed BDTs implemented as efficiency functions in the truth smearing. This scan targeted a subspace of the pMSSM parameter space where the analysis targeting the direct stau process [24] was expected to be sensitive, i.e. rather light stau masses were assumed and other sleptons and squarks were neglected by giving them a mass of 4 TeV. The pMSSM models generated in this scan were required to be in agreement with the measured SM higgs mass, the dark matter relic density measured by the Planck mission and the lower limit on the chargino mass by LEP. Furthermore, charged lightest supersymmetric particles (LSPs) were prohibited in the models. Therefore, the remaining pMSSM models had either the lightest neutralino or the tau sneutrino as LSP, where the lightest neutralino LSP was mainly wino- or higgsino-like due to the relic density constraint.
At last, it was studied to which of the remaining pMSSM models either the direct stau analysis or the analysis targeting the C1C1 process [25] are sensitive, i.e. which pMSSM models these analyses can exclude. In this study, four important phenomena were observed: first, the stau/neutralino/chargino mass combinations that the analyses originally excluded using simplified models with a bino-like neutralino LSP were extremely rare among the remaining models due to the relic density and chargino mass constraint. Secondly, when only considering slepton-slepton production processes, the direct stau analysis appeared to be sensitive to stau masses exceeding the simplified model exclusion limit. This is due to the pMSSM models allowing additional production processes like the associated production of a stau and a tau sneutrino. These additional processes increased the cross section of final states with the desired signature of the analysis. Thirdly, when one does also consider the production of electroweakino pairs, the previously described sensitivity dropped heavily. It is suggested that this is due to low event statistics in the produced pMSSM model samples. Finally, it was found that both analyses are quite sensitive to pMSSM models that have a tau sneutrino as LSP.
The last observation, suggesting that the considered analyses are sensitive to tau sneutrino LSP models, is possibly the most interesting one. However, the tau sneutrino is disfavoured as an LSP candidate since it contradicts the results of some experiments [120]. Hence, it might be worth investigating the exact conditions under which a tau sneutrino LSP can be excluded to see if there are still possible pMSSM models with such a LSP as of now. For these models, the results of this pMSSM scan would be very important.

Bibliography

[1] G. Aad et al., ATLAS Collaboration, "Observation of a new particle in the search for the Standard Model Higgs boson with the ATLAS detector at the LHC", Phys. Lett. **B716**, 1–29 (2012), arXiv:1207.7214 [hep-ex].

[2] S. Chatrchyan et al., CMS Collaboration, "Observation of a new boson at a mass of 125 GeV with the CMS experiment at the LHC", Phys. Lett. **B716**, 30–61 (2012), arXiv:1207.7235 [hep-ex].

[3] P. Zyla et al., Particle Data Group, "Review of Particle Physics", PTEP **2020**, 083C01 (2020), https://pdg.lbl.gov/2020/tables/rpp2020-sum-gauge-higgs-bosons.pdf.

[4] P. Zyla et al., Particle Data Group, "Review of Particle Physics", PTEP **2020**, 083C01 (2020), https://pdg.lbl.gov/2020/tables/rpp2020-sum-leptons.pdf.

[5] P. Zyla et al., Particle Data Group, "Review of Particle Physics", PTEP **2020**, 083C01 (2020), https://pdg.lbl.gov/2020/tables/rpp2020-sum-quarks.pdf.

[6] M. D. Schwartz, *Quantum Field Theory and the Standard Model* (Cambridge University Press, 2013).

[7] D. H. Perkins, *Introduction to High Energy Physics*, 4th edition (Cambridge University Press, 2000).

[8] J. P. Ellis, "TikZ-Feynman: Feynman diagrams with TikZ.", Computer Physics Communications **210**, 103–123 (2017), arXiv:1601.05437.

[9] E. Noether, "Invariant variation problems", Transport Theory and Statistical Physics **1**, 186–207 (1971).

[10] A. Salam and J. Ward, "Electromagnetic and weak interactions", Physics Letters **13**, 168–171 (1964), https://www.sciencedirect.com/science/article/pii/0031916364907115.

[11] S. Weinberg, "A Model of Leptons", Phys. Rev. Lett. **19**, 1264–1266 (1967), https://link.aps.org/doi/10.1103/PhysRevLett.19.1264.

[12] C. S. Wu, E. Ambler, R. W. Hayward, D. D. Hoppes, and R. P. Hudson, "Experimental Test of Parity Conservation in Beta Decay", Phys. Rev. **105**, 1413–1415 (1957), https://link.aps.org/doi/10.1103/PhysRev.105.1413.

[13] A. Bettini, *Introduction to Elementary Particle Physics* (Cambridge University Press, 2008).

[14] A. Djouadi, "The anatomy of electroweak symmetry breaking", Physics Reports **457**, 1–216 (2008), http://dx.doi.org/10.1016/j.physrep.2007.10.004.

[15] S. P. Martin, "A SUPERSYMMETRY PRIMER", Advanced Series on Directions in High Energy Physics, 1–98 (1998), http://dx.doi.org/10.1142/9789812839657_0001.

[16] A. de Gouvêa, D. Hernández, and T. M. P. Tait, "Criteria for natural hierarchies", Physical Review D **89**, 10.1103/physrevd.89.115005 (2014), http://dx.doi.org/10.1103/PhysRevD.89.115005.

[17] F. Zwicky, "Die Rotverschiebung von extragalaktischen Nebeln", Helvetica Physica Acta **Band 6, Heft II** (1933), http://doi.org/10.5169/seals-110267.

[18] N. Aghanim et al., Planck Collaboration, "Planck 2018 results", Astronomy & Astrophysics **641**, A6 (2020), http://dx.doi.org/10.1051/0004-6361/201833910.

[19] K. Garrett and G. Duda, "Dark Matter: A Primer", Adv. Astron. **2011**, 968283 (2011), arXiv:1006.2483 [hep-ph].

[20] P. Zyla et al., Particle Data Group, "Review of Particle Physics", PTEP **2020**, 083C01 (2020), https://pdg.lbl.gov/2020/tables/rpp2020-sum-baryons.pdf.

[21] P. Zyla et al., Particle Data Group, "Review of Particle Physics", PTEP **2020**, 083C01 (2020), https://pdg.lbl.gov/2020/reviews/rpp2020-rev-susy-1-theory.pdf.

[22] A. Djouadi et al., MSSM Working Group, "The Minimal supersymmetric standard model: Group summary report", in GDR (Groupement De Recherche) - Supersymetrie (Dec. 1998), arXiv:hep-ph/9901246.

[23] M. Aaboud et al., ATLAS Collaboration, "Search for squarks and gluinos in final states with hadronically decaying τ-leptons, jets, and missing transverse momentum using pp collisions at $\sqrt{s} = 13$ TeV with the ATLAS detector", Phys. Rev. D **99**, 012009 (2019), https://link.aps.org/doi/10.1103/PhysRevD.99.012009.

[24] G. Aad et al., ATLAS Collaboration, "Search for direct stau production in events with two hadronic τ-leptons in $\sqrt{s} = 13$ TeV pp collisions with the ATLAS detector", Phys. Rev. D **101**, 032009 (2020), https://link.aps.org/doi/10.1103/PhysRevD.101.032009.

[25] M. Aaboud et al., "Search for the direct production of charginos and neutralinos in final states with tau leptons in $\sqrt{s} = 13$ TeV pp collisions with the ATLAS detector", The European Physical Journal C **78**, 10.1140/epjc/s10052-018-5583-9 (2018), http://dx.doi.org/10.1140/epjc/s10052-018-5583-9.

[26] M. Aaboud et al., ATLAS Collaboration, "Search for top squarks decaying to tau sleptons in pp collisions at $\sqrt{s} = 13$ TeV with the ATLAS detector", Phys. Rev. D **98**, 032008 (2018), https://link.aps.org/doi/10.1103/PhysRevD.98.032008.

[27] ATLAS Collaboration, *Search for new phenomena in pp collisions in final states with tau leptons, b-jets, and missing transverse momentum with the ATLAS detector*, technical report ATLAS-CONF-2021-008 (CERN, Geneva, 2021), https://cds.cern.ch/record/2759282.

[28] J.-L. Caron, "CERN Accelerator Complex (operating and approved projets).. Chaine des accelerateurs du CERN (en fonctionnement et avec les projets aprouves).", https://cds.cern.ch/record/841493, AC Collection. Legacy of AC. Pictures from 1992 to 2002., 1991.

[29] Education, Communications and Outreach Group, *CERN-Brochure-2017-002-Eng*, 2017, http://cds.cern.ch/record/2255762/files/CERN-Brochure-2017-002-Eng.pdf.

[30] The ATLAS Experiment, *Detector & Technology*, 2021, https://atlas.cern/discover/detector (Accessed: 03/26/2021).

[31] W. Herr and B. Muratori, *Concept of luminosity*, CERN Document Server, 2006, http://cds.cern.ch/record/941318.

[32] ATLAS Collaboration, "The ATLAS Experiment at the CERN Large Hadron Collider", Journal of Instrumentation **3**, S08003 (2008), http://stacks.iop.org/1748-0221/3/i=08/a=S08003.

[33] M. Lamprecht, "Studien zu Effizienz und Akzeptanz des ATLAS-Myontriggers mit simulierten Messdaten", Diplomarbeit (Ludwig-Maximilians-Universität München, 2007).

[34] ATLAS Collaboration, *ATLAS inner detector: Technical Design Report, 1*, Technical design report. ATLAS (CERN, Geneva, 1997), https://cds.cern.ch/record/331063.

[35] J. Pequenao and P. Schaffner, "An computer generated image representing how ATLAS detects particles", 2013, https://cds.cern.ch/record/1505342.

[36] A. R. M. and, "The Run-2 ATLAS Trigger System", Journal of Physics: Conference Series **762**, 012003 (2016), https://doi.org/10.1088/1742-6596/762/1/012003.

[37] T. Sjöstrand, "Monte Carlo Tools", (2009), arXiv:0911.5286 [hep-ph].

[38] B. Andersson, G. Gustafson, G. Ingelman, and T. Sjostrand, "Parton Fragmentation and String Dynamics", Phys. Rept. **97**, 31–145 (1983).

[39] B. R. Webber, "A QCD Model for Jet Fragmentation Including Soft Gluon Interference", Nucl. Phys. B **238**, 492–528 (1984).

[40] G. Aad et al., ATLAS Collaboration, "The ATLAS Simulation Infrastructure", The European Physical Journal C **70**, 823–874 (2010), http://dx.doi.org/10.1140/epjc/s10052-010-1429-9.

[41] D. Schaile, "Advanced Particle Physics", Lecture Notes, Ludwigs-Maximilians-Universität München (2020), http://www-static.etp.physik.uni-muenchen.de/EM2/vorlesung.html.

[42] S Agostinelli et al., GEANT4 Collaboration, "GEANT4 – a simulation toolkikt", Nucl. Instrum. Methods Phys. Res., A **506**, 250–303. 54 p (2002), https://cds.cern.ch/record/602040.

[43] M. H. Seymour and M. Marx, "Monte Carlo Event Generators", (2013), arXiv:1304.6677 [hep-ph].

[44] A. Buckley, J. Butterworth, S. Gieseke, D. Grellscheid, S. Höche, H. Hoeth, F. Krauss, L. Lönnblad, E. Nurse, P. Richardson, et al., "General-purpose event generators for LHC physics", Physics Reports **504**, 145–233 (2011), http://dx.doi.org/10.1016/j.physrep.2011.03.005.

[45] J. Alwall, R. Frederix, S. Frixione, V. Hirschi, F. Maltoni, O. Mattelaer, H.-S. Shao, T. Stelzer, P. Torrielli, and M. Zaro, "The automated computation of tree-level and next-to-leading order differential cross sections, and their matching to parton shower simulations", Journal of High Energy Physics **2014**, 10.1007/jhep07(2014)079 (2014), http://dx.doi.org/10.1007/JHEP07(2014)079.

[46] S. Frixione, G. Ridolfi, and P. Nason, "A positive-weight next-to-leading-order Monte Carlo for heavy flavour hadroproduction", Journal of High Energy Physics **2007**, 126–126 (2007), http://dx.doi.org/10.1088/1126-6708/2007/09/126.

[47] P. Nason, "A New Method for Combining NLO QCD with Shower Monte Carlo Algorithms", Journal of High Energy Physics **2004**, 040–040 (2004), http://dx.doi.org/10.1088/1126-6708/2004/11/040.

[48] S. Frixione, P. Nason, and C. Oleari, "Matching NLO QCD computations with parton shower simulations: the POWHEG method", Journal of High Energy Physics **2007**, 070–070 (2007), http://dx.doi.org/10.1088/1126-6708/2007/11/070.

[49] S. Alioli, P. Nason, C. Oleari, and E. Re, "A general framework for implementing NLO calculations in shower Monte Carlo programs: the POWHEG BOX", Journal of High Energy Physics **2010**, 10.1007/jhep06(2010)043 (2010), http://dx.doi.org/10.1007/JHEP06(2010)043.

[50] T. Sjostrand, S. Mrenna, and P. Z. Skands, "A Brief Introduction to PYTHIA 8.1", Comput. Phys. Commun. **178**, 852–867 (2008), arXiv:arXiv:hep-ph/0710.3820 [hep-ph].

[51] B. Maier, "Search for the associated production of a single top quark and a Higgs boson in the H to bbbar decay channel at 8 and 13 TeV with the CMS experiment", PhD thesis (KIT, Karlsruhe, EKP, 2016), http://inspirehep.net/record/1647443/files/EKP-2016-00010.pdf.

[52] ATLAS Collaboration, *ATLAS Pythia 8 tunes to 7 TeV data*, technical report ATL-PHYS-PUB-2014-021 (CERN, Geneva, 2014), https://cds.cern.ch/record/1966419.

[53] R. D. Ball et al., NNPDF Collaboration, "Parton distributions with LHC data", Nuclear Physics B **867**, 244–289 (2013), http://dx.doi.org/10.1016/j.nuclphysb.2012.10.003.

[54] L. Lönnblad, "Correcting the Colour-Dipole Cascade Model with Fixed Order Matrix Elements", Journal of High Energy Physics **2002**, 046–046 (2002), http://dx.doi.org/10.1088/1126-6708/2002/05/046.

[55] L. Lönnblad and S. Prestel, "Matching tree-level matrix elements with interleaved showers", Journal of High Energy Physics **2012**, 10.1007/jhep03(2012)019 (2012), http://dx.doi.org/10.1007/JHEP03(2012)019.

[56] P. Artoisenet, R. Frederix, O. Mattelaer, and R. Rietkerk, "Automatic spin-entangled decays of heavy resonances in Monte Carlo simulations", Journal of High Energy Physics **2013**, 10.1007/jhep03(2013)015 (2013), http://dx.doi.org/10.1007/JHEP03(2013)015.

[57] R. D. Ball et al., NNPDF Collaboration, "Parton distributions for the LHC run II", Journal of High Energy Physics **2015**, 10.1007/jhep04(2015)040 (2015), http://dx.doi.org/10.1007/JHEP04(2015)040.

[58] M Beckingham, M Duehrssen, E Schmidt, M Shapiro, M Venturi, J Virzi, I Vivarelli, M Werner, S Yamamoto, and T Yamanaka, ATLAS Collaboration, *The simulation principle and performance of the ATLAS fast calorimeter simulation FastCaloSim*, technical report ATL-PHYS-PUB-2010-013 (CERN, Geneva, 2010), https://cds.cern.ch/record/1300517.

[59] ATLAS Collaboration, *Vertex Reconstruction Performance of the ATLAS Detector at* $\sqrt{s}$ *= 13 TeV*, technical report ATL-PHYS-PUB-2015-026 (CERN, Geneva, 2015), https://cds.cern.ch/record/2037717.

[60] G. Aad et al., ATLAS Collaboration, "Electron and photon performance measurements with the ATLAS detector using the 2015–2017 LHC proton-proton collision data", Journal of Instrumentation **14**, P12006–P12006 (2019), http://dx.doi.org/10.1088/1748-0221/14/12/P12006.

[61] G. Aad et al., ATLAS Collaboration, "Muon reconstruction performance of the ATLAS detector in proton–proton collision data at $\sqrt{s}$=13 TeV", The European Physical Journal C **76**, 10.1140/epjc/s10052-016-4120-y (2016), http://dx.doi.org/10.1140/epjc/s10052-016-4120-y.

[62] G. Aad et al., ATLAS Collaboration, "Topological cell clustering in the ATLAS calorimeters and its performance in LHC Run 1", The European Physical Journal C **77**, 10.1140/epjc/s10052-017-5004-5 (2017), http://dx.doi.org/10.1140/epjc/s10052-017-5004-5.

[63] M. Cacciari, G. P. Salam, and G. Soyez, "The anti-ktjet clustering algorithm", Journal of High Energy Physics **2008**, 063–063 (2008), http://dx.doi.org/10.1088/1126-6708/2008/04/063.

[64] M. Aaboud et al., ATLAS Collaboration, "Jet energy scale measurements and their systematic uncertainties in proton-proton collisions at $\sqrt{s} = 13$ with the ATLAS detector", Physical Review D **96**, 10.1103/physrevd.96.072002 (2017), http://dx.doi.org/10.1103/PhysRevD.96.072002.

[65] ATLAS Collaboration, *Tagging and suppression of pileup jets with the ATLAS detector*, technical report ATLAS-CONF-2014-018 (CERN, Geneva, 2014), https://cds.cern.ch/record/1700870.

[66] ATLAS Collaboration, *E_T^{miss} performance in the ATLAS detector using 2015-2016 LHC p-p collisions*, technical report ATLAS-CONF-2018-023 (CERN, Geneva, 2018), https://cds.cern.ch/record/2625233.

[67] M. Aaboud et al., ATLAS Collaboration, "Jet reconstruction and performance using particle flow with the ATLAS Detector", The European Physical Journal C **77**, 10.1140/epjc/s10052-017-5031-2 (2017), http://dx.doi.org/10.1140/epjc/s10052-017-5031-2.

[68] G. Aad et al., ATLAS Collaboration, "Reconstruction of hadronic decay products of tau leptons with the ATLAS experiment", The European Physical Journal C **76**, 10.1140/epjc/s10052-016-4110-0 (2016), http://dx.doi.org/10.1140/epjc/s10052-016-4110-0.

[69] G. Aad et al., ATLAS Collaboration, "Identification and energy calibration of hadronically decaying tau leptons with the ATLAS experiment in pp collisions at $\sqrt{s} = 8$ TeV", The European Physical Journal C **75**, 10.1140/epjc/s10052-015-3500-z (2015), http://dx.doi.org/10.1140/epjc/s10052-015-3500-z.

[70] ATLAS Collaboration, *Measurement of the tau lepton reconstruction and identification performance in the ATLAS experiment using pp collisions at $\sqrt{s} = 13$ TeV*, technical report ATLAS-CONF-2017-029 (CERN, Geneva, 2017), https://cds.cern.ch/record/2261772.

[71] G. Aad et al., ATLAS Collaboration, "Reconstruction of hadronic decay products of tau leptons with the ATLAS experiment", The European Physical Journal C **76**, 10.1140/epjc/s10052-016-4110-0 (2016), http://dx.doi.org/10.1140/epjc/s10052-016-4110-0.

[72] ATLAS Collaboration, *Identification of hadronic tau lepton decays using neural networks in the ATLAS experiment*, technical report ATL-PHYS-PUB-2019-033 (CERN, Geneva, 2019), https://cds.cern.ch/record/2688062.

[73] ATLAS Collaboration, *Proposal for truth particle observable definitions in physics measurements*, technical report ATL-PHYS-PUB-2015-013 (CERN, Geneva, 2015), https://cds.cern.ch/record/2022743.

[74] J. Catmore, ATLAS Collaboration, *TruthDAOD*, 2020, https://twiki.cern.ch/twiki/bin/viewauth/AtlasProtected/TruthDAOD (Accessed: 04/02/2021).

[75] J. Nielsen, ATLAS Collaboration, *UpgradePerformanceFunctions*, 2021, https://twiki.cern.ch/twiki/bin/view/AtlasProtected/UpgradePerformanceFunctions (Accessed: 04/02/2021).

[76] G. Cowan, *Statistics for Searches at the LHC*, 2013, arXiv:`1307.2487 [hep-ex]`.

[77] A. L. Read, "Presentation of search results: theCLstechnique", Journal of Physics G: Nuclear and Particle Physics **28**, 2693–2704 (2002), `https://doi.org/10.1088/0954-3899/28/10/313`.

[78] G. Cowan, K. Cranmer, E. Gross, and O. Vitells, "Asymptotic formulae for likelihood-based tests of new physics", The European Physical Journal C **71**, `10.1140/epjc/s10052-011-1554-0` (2011), `http://dx.doi.org/10.1140/epjc/s10052-011-1554-0`.

[79] M. Baak, G. J. Besjes, D. Côté, A. Koutsman, J. Lorenz, and D. Short, "HistFitter software framework for statistical data analysis", The European Physical Journal C **75**, `10.1140/epjc/s10052-015-3327-7` (2015), `http://dx.doi.org/10.1140/epjc/s10052-015-3327-7`.

[80] G. S. Lukas Heinrich Matthew Feickert, *pyhf documentation*, 2018, `https://scikit-hep.org/pyhf/index.html` (Accessed: 05/24/2021).

[81] D. Alves et al., "Simplified models for LHC new physics searches", Journal of Physics G: Nuclear and Particle Physics **39**, 105005 (2012), `http://dx.doi.org/10.1088/0954-3899/39/10/105005`.

[82] G. Aad et al., ATLAS Collaboration, "Summary of the ATLAS experiment's sensitivity to supersymmetry after LHC Run 1 — interpreted in the phenomenological MSSM", Journal of High Energy Physics **2015**, `10.1007/jhep10(2015)134` (2015), `http://dx.doi.org/10.1007/JHEP10(2015)134`.

[83] B. Petersen and F. Ruehr, *pMSSM Status*, `https://indico.cern.ch/event/906943/contributions/3816591/attachments/2025703/3388662/pMSSMStatus.pdf`, CERN, 2020.

[84] G. Aad et al., ATLAS Collaboration, "Search for squarks and gluinos with the ATLAS detector in final states with jets and missing transverse momentum using $\sqrt{s} = 8$ TeV proton-proton collision data", Journal of High Energy Physics **2014**, `10.1007/jhep09(2014)176` (2014), `http://dx.doi.org/10.1007/JHEP09(2014)176`.

[85] A. Bertolini, "Search for Direct Production of Tau Sleptons with One Leptonically and One Hadronically Decaying Tau Lepton in Run-2 Data Taken with the ATLAS Detector", Master Thesis (Ludwig-Maximilians-Universität München, 2020).

[86] ATLAS SUSY Working group, *Simplified ATLAS SUSY analysis framework*, `https://simpleanalysis.docs.cern.ch/` (Accessed: 04/18/2021).

[87] *XAMPPstau*, `https://gitlab.cern.ch/atlas-mpp-xampp/XAMPPstau` (Accessed: 04/18/2021).

[88] C. W. Fabjan and F Gianotti, "Calorimetry for Particle Physics", Rev. Mod. Phys. **75**, 1243–1286. 96 p (2003), `https://cds.cern.ch/record/692252`.

[89] A. Salvucci, "Measurement of muon momentum resolution of the ATLAS detector", EPJ Web of Conferences **28**, 12039 (2012), `http://dx.doi.org/10.1051/epjconf/20122812039`.

[90] A. Mann, ATLAS Collaboration, *LHC SUSY Cross Section Working Group*, 2021, `https://twiki.cern.ch/twiki/bin/view/LHCPhysics/SUSYCrossSections` (Accessed: 05/26/2021).

[91] F. Palm, "Stop-Stau Models in the phenomenological MSSM", Private Communication (Ludwig-Maximilians-Universität München, 2019).

[92] T. Hastie, R. Tibshirani, J. Friedman, and J. Franklin, "The Elements of Statistical Learning: Data Mining, Inference, and Prediction", Math. Intell. **27**, 83–85 (2004).

[93] C. Böser, S. Fink, and S. Röcker, *Introduction to Boosted Decision Trees*, https://indico.scc.kit.edu/event/48/contributions/3410/attachments/1690/2312/BDT_KSETA_Freudenstadt.pdf, KIT, 2014.

[94] A. Hoecker, P. Speckmayer, J. Stelzer, J. Therhaag, E. von Toerne, and H. Voss, "TMVA: Toolkit for Multivariate Data Analysis", PoS **ACAT**, 040 (2007), arXiv:physics/0703039.

[95] scikit-learn developers, *scikit-learn User Guide*, https://scikit-learn.org/stable/user_guide.html (Accessed: 04/18/2021).

[96] F. Pedregosa, G. Varoquaux, A. Gramfort, V. Michel, B. Thirion, O. Grisel, M. Blondel, P. Prettenhofer, R. Weiss, V. Dubourg, J. Vanderplas, A. Passos, D. Cournapeau, M. Brucher, M. Perrot, and E. Duchesnay, "Scikit-learn: Machine Learning in Python", Journal of Machine Learning Research **12**, 2825–2830 (2011).

[97] S. Nembrini, I. König, and M. Wright, "The revival of the Gini Importance?", Bioinformatics (Oxford, England) **34**, 10.1093/bioinformatics/bty373 (2018).

[98] T. Chen and C. Guestrin, "XGBoost: A Scalable Tree Boosting System", in Proceedings of the 22nd ACM SIGKDD International Conference on Knowledge Discovery and Data Mining, KDD '16 (2016), pages 785–794, http://doi.acm.org/10.1145/2939672.2939785.

[99] J. Würzinger, *pMSSM*, https://gitlab.cern.ch/jwuerzin/pMSSM (Accessed: 04/25/2021).

[100] J. Cao, L. Shang, J. M. Yang, and Y. Zhang, *EasyScan_HEP*, https://easyscanhep.hepforge.org/ (Accessed: 04/25/2021).

[101] B. Allanach, "SOFTSUSY: A program for calculating supersymmetric spectra", Computer Physics Communications **143**, 305–331 (2002), http://dx.doi.org/10.1016/S0010-4655(01)00460-X.

[102] B. Allanach and T. Cridge, "The calculation of sparticle and Higgs decays in the minimal and next-to-minimal supersymmetric standard models: SOFTSUSY4.0", Computer Physics Communications **220**, 417–502 (2017), http://dx.doi.org/10.1016/j.cpc.2017.07.021.

[103] W. Porod, "SPheno, a program for calculating supersymmetric spectra, SUSY particle decays and SUSY particle production at e+ e- colliders", Comput. Phys. Commun. **153**, 275–315 (2003), arXiv:hep-ph/0301101.

[104] W. Porod and F. Staub, "SPheno 3.1: extensions including flavour, CP-phases and models beyond the MSSM", Computer Physics Communications **183**, 2458–2469 (2012), http://dx.doi.org/10.1016/j.cpc.2012.05.021.

[105] H. Bahl, T. Hahn, S. Heinemeyer, W. Hollik, S. Paßehr, H. Rzehak, and G. Weiglein, "Precision calculations in the MSSM Higgs-boson sector with FeynHiggs 2.14", (2019), arXiv:1811.09073 [hep-ph].

[106] H. Bahl, S. Heinemeyer, W. Hollik, and G. Weiglein, "Reconciling EFT and hybrid calculations of the light MSSM Higgs-boson mass", The European Physical Journal C **78**, 10.1140/epjc/s10052-018-5544-3 (2018), http://dx.doi.org/10.1140/epjc/s10052-018-5544-3.

[107] H. Bahl and W. Hollik, "Precise prediction for the light MSSM Higgs-boson mass combining effective field theory and fixed-order calculations", The European Physical Journal C **76**, 10.1140/epjc/s10052-016-4354-8 (2016), http://dx.doi.org/10.1140/epjc/s10052-016-4354-8.

[108] T. Hahn, S. Heinemeyer, W. Hollik, H. Rzehak, and G. Weiglein, “High-Precision Predictions for the LightCP-Even Higgs Boson Mass of the Minimal Supersymmetric Standard Model”, Physical Review Letters **112**, 10.1103/physrevlett.112.141801 (2014), http://dx.doi.org/10.1103/PhysRevLett.112.141801.

[109] M. Frank, T. Hahn, S. Heinemeyer, W. Hollik, H. Rzehak, and G. Weiglein, “The Higgs boson masses and mixings of the complex MSSM in the Feynman-diagrammatic approach”, Journal of High Energy Physics **2007**, 047–047 (2007), http://dx.doi.org/10.1088/1126-6708/2007/02/047.

[110] G. Degrassi, S. Heinemeyer, W. Hollik, P. Slavich, and G. Weiglein, “Towards high-precision predictions for the MSSM Higgs sector”, The European Physical Journal C **28**, 133–143 (2003), http://dx.doi.org/10.1140/epjc/s2003-01152-2.

[111] S. Heinemeyer, W. Hollik, and G. Weiglein, “The masses of the neutral $\mathcal{CP}$-even Higgs bosons in the MSSM: Accurate analysis at the two-loop level”, The European Physical Journal C **9**, 343–366 (1999), http://dx.doi.org/10.1007/s100529900006.

[112] S. Heinemeyer, W. Hollik, and G. Weiglein, “FeynHiggs: a program for the calculation of the masses of the neutral-even Higgs bosons in the MSSM”, Computer Physics Communications **124**, 76–89 (2000), http://dx.doi.org/10.1016/S0010-4655(99)00364-1.

[113] G. Bélanger, F. Boudjema, A. Pukhov, and A. Semenov, “micrOMEGAs: Version 1.3”, Computer Physics Communications **174**, 577–604 (2006), http://dx.doi.org/10.1016/j.cpc.2005.12.005.

[114] ATLAS Collaboration, *Prospect for a search for direct stau production in events with at least two hadronic taus and missing transverse momentum at theHigh Luminosity LHC with the ATLAS Detector*, technical report, All figures including auxiliary figures are available at https://atlas.web.cern.ch/Atlas/GROUPS/PHYSICS/PUBNOTES/ATL-PHYS-PUB-2016-021 (CERN, Geneva, 2016), https://cds.cern.ch/record/2220805.

[115] The LEP SUSY Working Group and the ALEPH, DELPHI, L3 and OPAL experiments, *note LEPSUSYWG/01-03.1*, http://lepsusy.web.cern.ch/lepsusy/ (Accessed: 04/27/2021).

[116] K. Griest and D. Seckel, “Three exceptions in the calculation of relic abundances”, Phys. Rev. D **43**, 3191–3203 (1991).

[117] A. S. W. group, *pMSSMFactory*, https://gitlab.cern.ch:8443/atlas-phys-susy-wg/summaries/pmssm/pMSSMFactory (Accessed: 04/28/2021).

[118] W. Beenakker, R. Hopker, and M. Spira, “PROSPINO: A Program for the production of supersymmetric particles in next-to-leading order QCD”, (1996), arXiv:hep-ph/9611232.

[119] T. Plehn, *Prospino2*, https://www.thphys.uni-heidelberg.de/~plehn/index.php?show=prospino (Accessed: 04/28/2021).

[120] J. Ellis and K. A. Olive, “Supersymmetric Dark Matter Candidates”, (2010), arXiv:1001.3651 [astro-ph.CO].

[121] L. Heinrich, M. Feickert, and G. Stark, “pyhf: v0.6.1”, version 0.6.1, 10.5281/zenodo.1169739, https://github.com/scikit-hep/pyhf/releases/tag/v0.6.1.

[122] L. Heinrich, M. Feickert, G. Stark, and K. Cranmer, “pyhf: pure-Python implementation of HistFactory statistical models”, Journal of Open Source Software **6**, 2823 (2021), https://doi.org/10.21105/joss.02823.

[123] W. Buttinger and M. Lefebvre, *Formulae for Estimating Significance*, technical report (CERN, Geneva, 2018), https://cds.cern.ch/record/2643488.

[124] R. D. Cousins, J. T. Linnemann, and J. Tucker, "Evaluation of three methods for calculating statistical significance when incorporating a systematic uncertainty into a test of the background-only hypothesis for a Poisson process", Nuclear Instruments and Methods in Physics Research Section A: Accelerators, Spectrometers, Detectors and Associated Equipment **595**, 480–501 (2008), https://www.sciencedirect.com/science/article/pii/S0168900208010255.

[125] A. Mann, ATLAS Collaboration, *Squark-antisquark production cross sections*, 2019, https://twiki.cern.ch/twiki/bin/view/LHCPhysics/SUSYCrossSections13TeVsquarkantisquark (Accessed: 05/31/2021).

Appendix A

Additional Figures to Chapter 5

A.1 Comparison plots of truth-level and reconstruction-level leptons

A.1.1 Tau Leptons

Figure A.1 shows the tau p_{T} distribution of the smeared truth-level (of both the original and the new direct stau smearing) and reconstruction-level taus for the remaining available direct stau samples. Again, the agreement between the new smearing and the reconstruction-level taus is generally good except for the missing fake taus.

A.1.2 Electrons and Muons

Figure A.2 shows the electron and muon p_{T} distribution of the smeared truth-level (of both the original and the new direct stau smearing) and reconstruction-level electrons/muons for the remaining direct stau process samples. Like in the case of the already shown electron p_{T} distribution of the sample with DSID 398349, the distributions of the samples 397011 and 397049 show that the new smearing slightly underestimates the electron reconstruction and ID efficiency for these samples. Since all of these samples have a more compressed mass configuration than the DSID 396104 sample that was used for implementing the recalculated efficiencies, this could hint at a sample dependence as in the case of tau leptons.

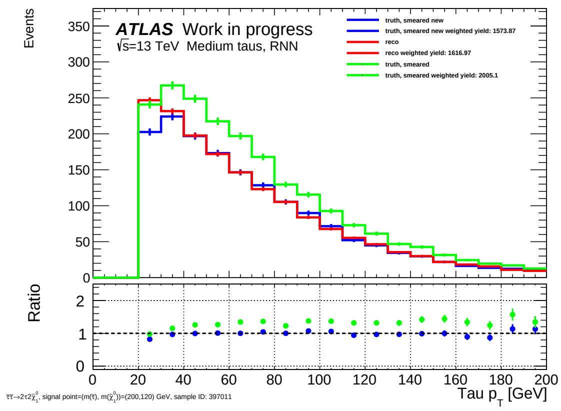

(a) 397011

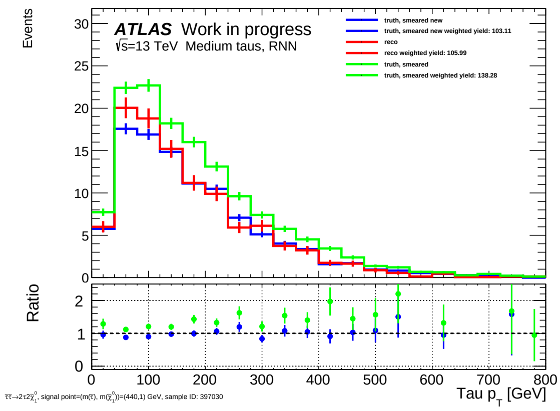

(b) 397030

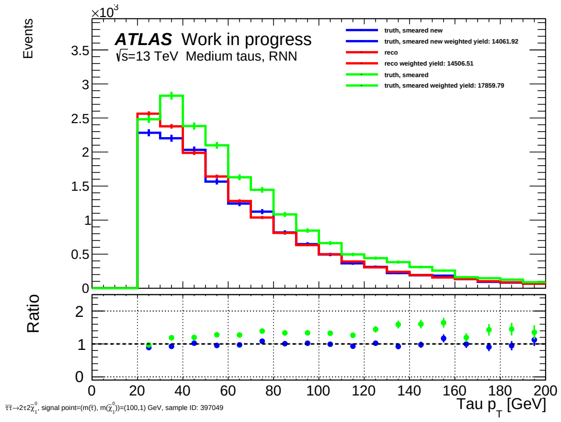

(c) 397049

Figure A.1: The tau p_{T} distribution of the remaining direct stau samples with DSID 397011 (a), 397030 (b) and 397049 (c) for the new smeared, original smeared truth-level and reconstruction-level taus.

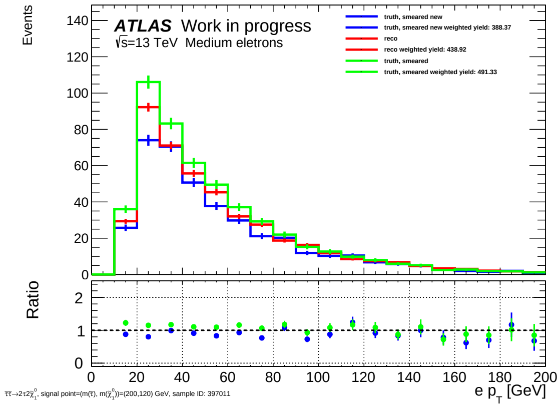

(a) electron p_{T}, DSID 397011

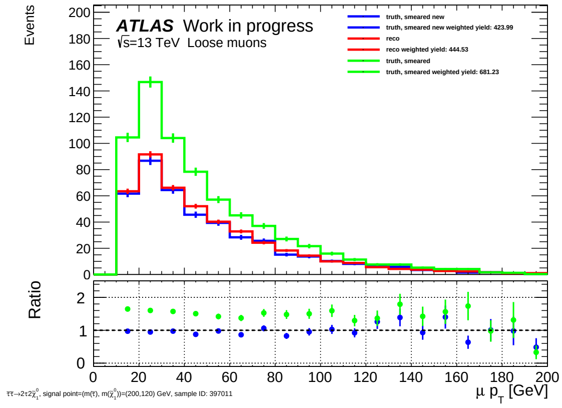

(b) muon p_{T}, DSID 397011

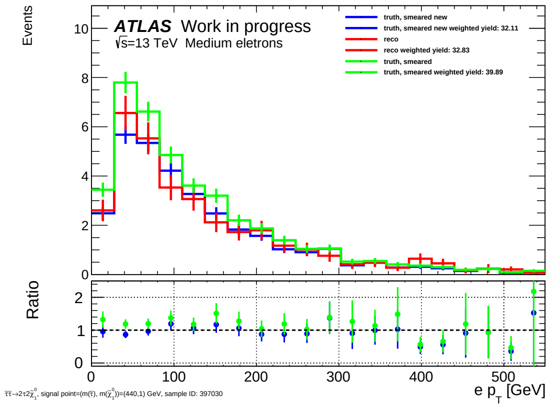

(c) electron p_{T}, DSID 397030

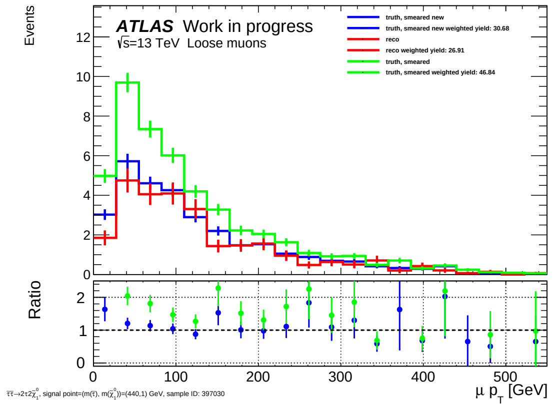

(d) muon p_{T}, DSID 397030

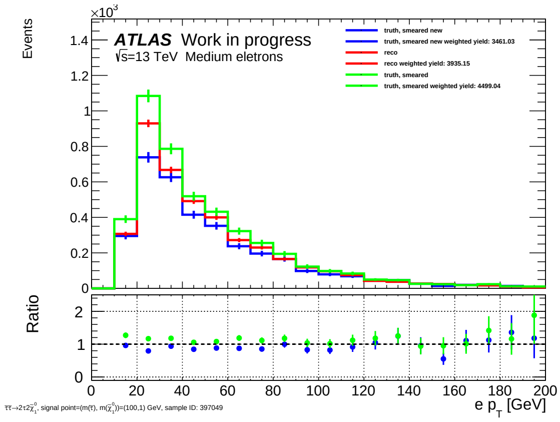

(e) electron p_{T}, DSID 397049

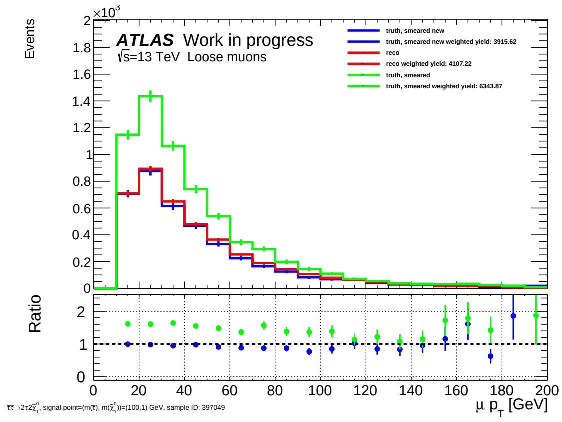

(f) muon p_{T}, DSID 397049

Figure A.2: Electron (a) and muon (b) p_{T} distribution for the new smeared and original smeared truth-level as well as the reconstruction-level electrons/muons for the direct stau sample with DSID 397011. Below, the electron (c) and muon (d) p_{T} distributions for the direct stau sample with DSID 397030 and the electron (e) and muon (f) p_{T} distributions for the direct stau sample with DSID 397049 can be found.

A.2 Lepton reconstruction and ID efficiency maps

A.2.1 Tau Leptons

The following figures (figure A.3 to figure A.9) show the tau reconstruction and ID efficiency mapped in the variables tau p_{T}, tau $|\eta|$ and tau prongness of the remaining available samples (see table 4.5 and 4.4). These maps show similar patterns of sample dependence with respect to the mass configuration and the process of the sample as were deduced from figure 5.21 in the discussion in section 5.4. For example, samples with high mass differences generally show higher efficiencies across the maps compared to more compressed samples of the same process. Also, the ttStau sample with the very low jet mass difference (437368) shows significantly higher efficiencies than the other ttStau samples. And finally, process-wise, the GoGo samples and the ttbar sample exhibit the lowest efficiencies while the C1C1 and direct stau samples are among the samples with the highest efficiencies. This again confirms the statement that the three variables which were used in the original parametrisation are not able to resolve the sample dependence in the tau reconstruction and ID efficiency.

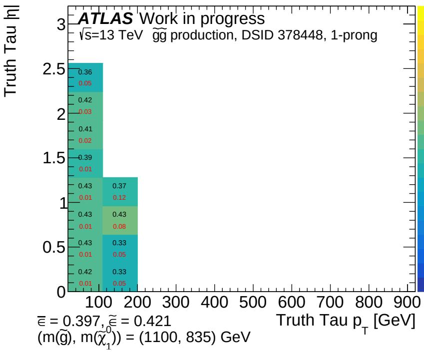

(a) DSID 378448, 1-prong

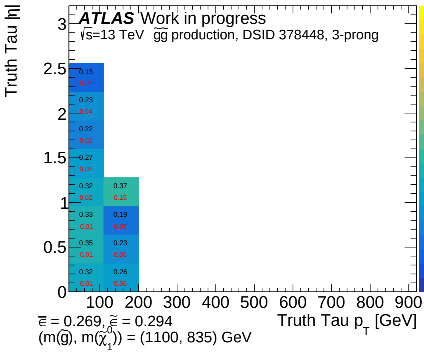

(b) DSID 378448, 3-prong

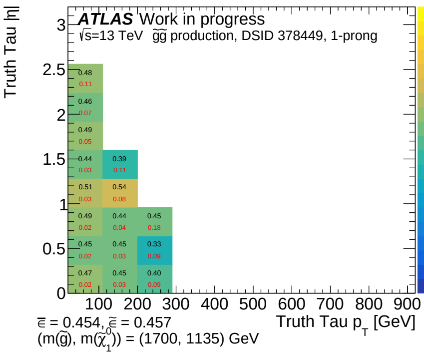

(c) DSID 378449, 1-prong

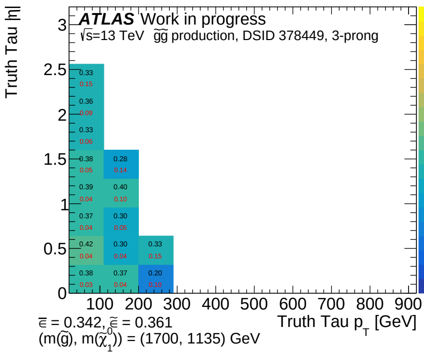

(d) DSID 378449, 3-prong

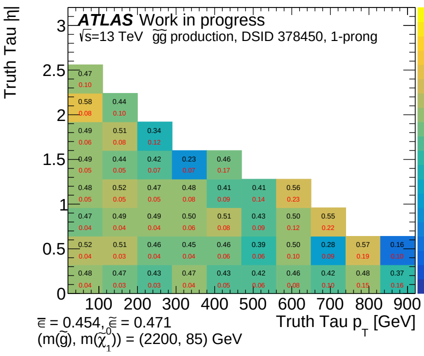

(e) DSID 378450, 1-prong

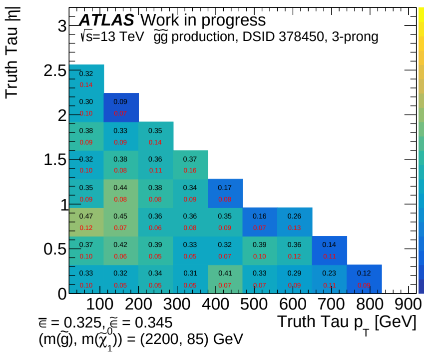

(f) DSID 378450, 3-prong

Figure A.3: Tau reconstruction and ID efficiency maps in tau p_{T} and $|\eta|$ for 1-prong and 3-prong tau leptons of the GoGo samples with DSID 378448 ((a) and (b)), 378449 ((c) and (d)) and 378450 ((e) and (f)).

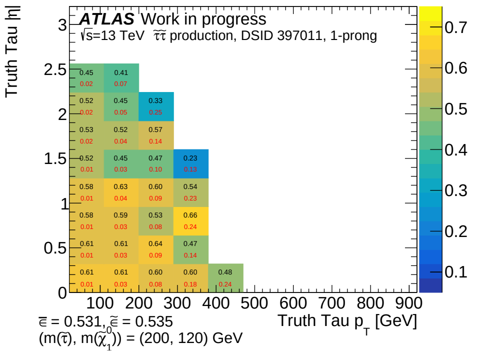

(a) DSID 397011, 1-prong

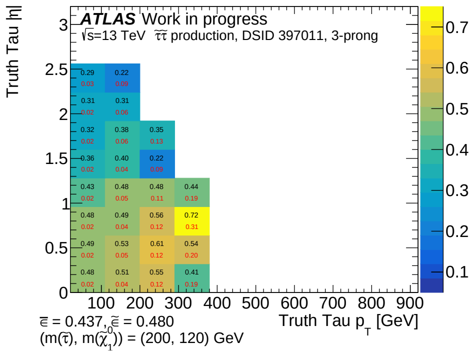

(b) DSID 397011, 3-prong

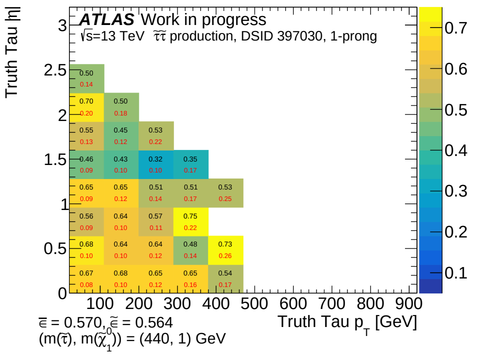

(c) DSID 397030, 1-prong

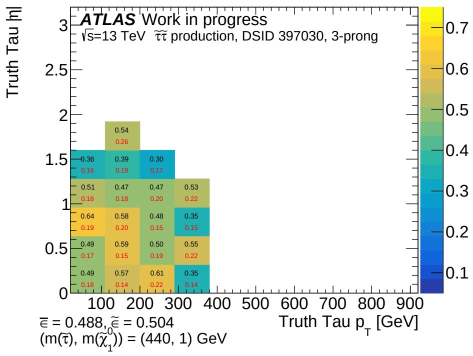

(d) DSID 397030, 3-prong

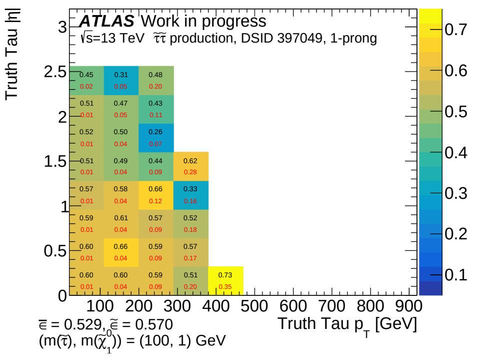

(e) DSID 397049, 1-prong

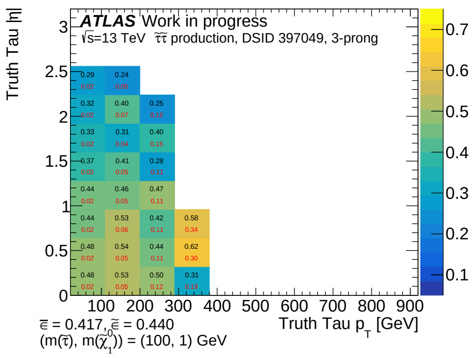

(f) DSID 397049, 3-prong

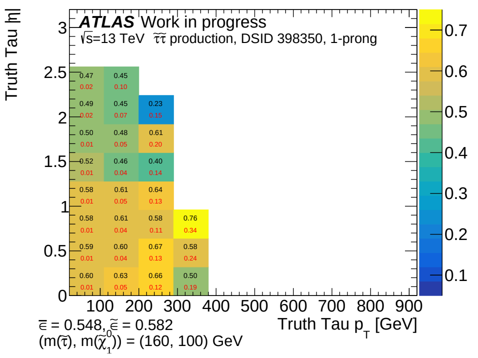

(g) DSID 398350, 1-prong

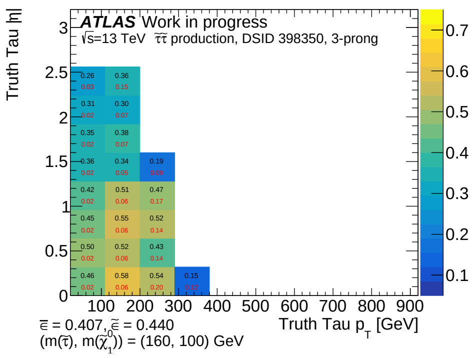

(h) DSID 398350, 3-prong

Figure A.4: Tau reconstruction and ID efficiency maps in tau p_{T} and $|\eta|$ for 1-prong and 3-prong tau leptons of the remaining direct stau samples with DSID 397011 ((a) and (b)), 397030 ((c) and (d)), 397049 ((e) and (f)) and 398350 ((g) and (h)).

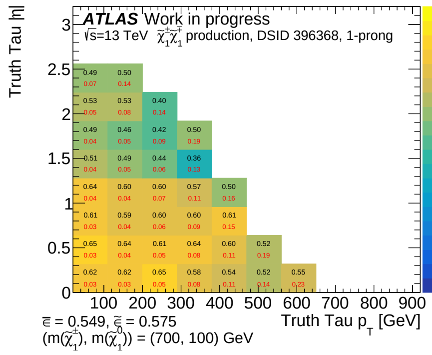

(a) DSID 396368, 1-prong

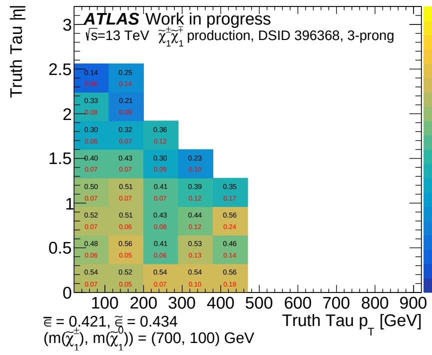

(b) DSID 396368, 3-prong

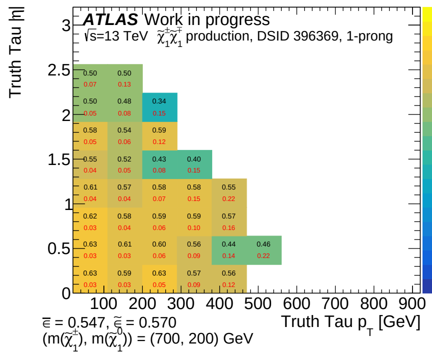

(c) DSID 396369, 1-prong

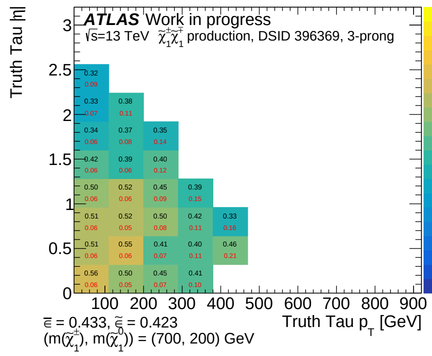

(d) DSID 396369, 3-prong

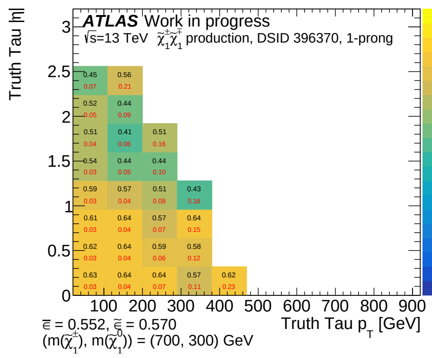

(e) DSID 396370, 1-prong

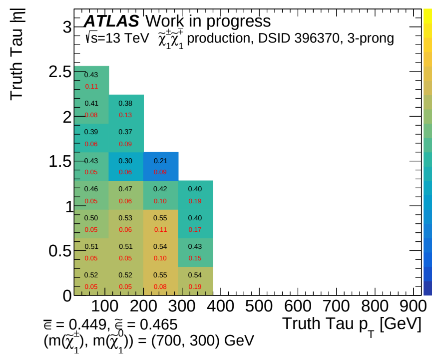

(f) DSID 396370, 3-prong

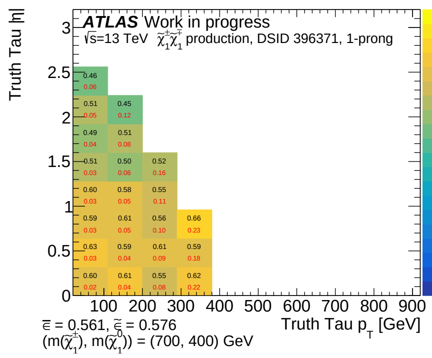

(g) DSID 396371, 1-prong

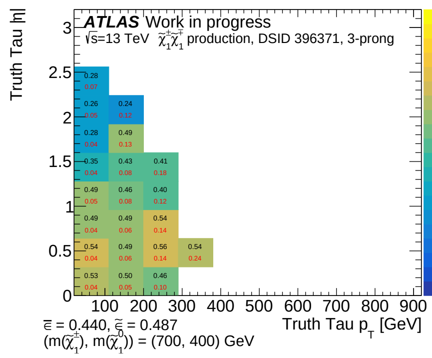

(h) DSID 396371, 3-prong

Figure A.5: First set of tau reconstruction and ID efficiency maps in tau p_{T} and $|\eta|$ for 1-prong and 3-prong tau leptons of the remaining C1C1 samples with DSID 396368 ((a) and (b)), 396369 ((c) and (d)), 396370 ((e) and (f)) and 396371 ((g) and (h)).

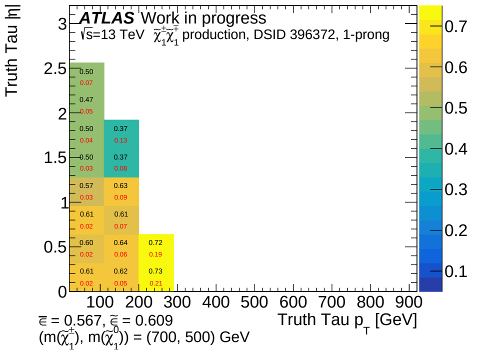

(a) DSID 396372, 1-prong

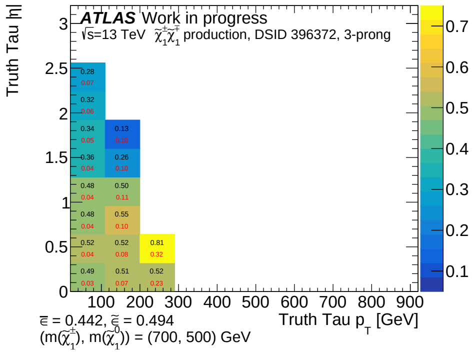

(b) DSID 396372, 3-prong

Figure A.6: Second set of tau reconstruction and ID efficiency maps in tau p_{T} and $|\eta|$ for 1-prong and 3-prong tau leptons of the remaining C1C1 samples with DSID 396372 ((a) and (b)).

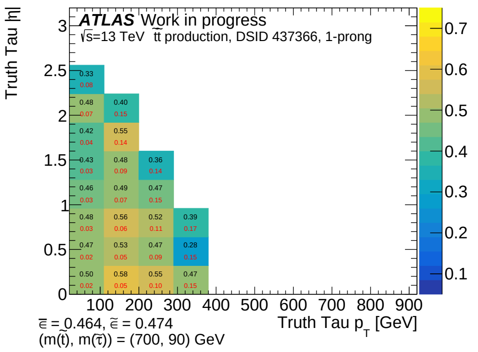

(a) DSID 437366, 1-prong

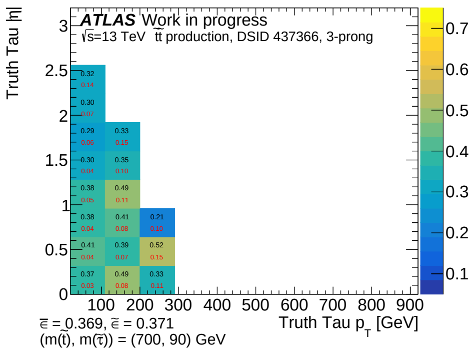

(b) DSID 437366, 3-prong

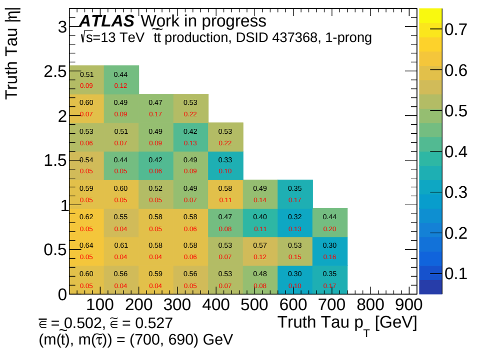

(c) DSID 437368, 1-prong

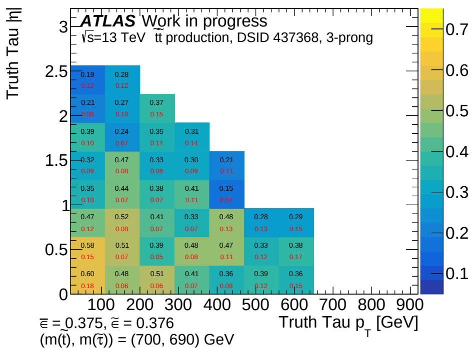

(d) DSID 437368, 3-prong

Figure A.7: First set of tau reconstruction and ID efficiency maps in tau p_{T} and $|\eta|$ for 1-prong and 3-prong tau leptons of the ttStau samples with DSID 437366 ((a) and (b)) and 437368 ((c) and (d)).

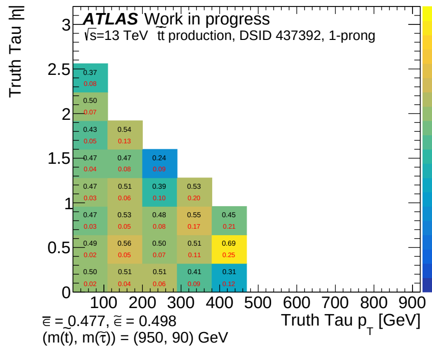

(a) DSID 437392, 1-prong

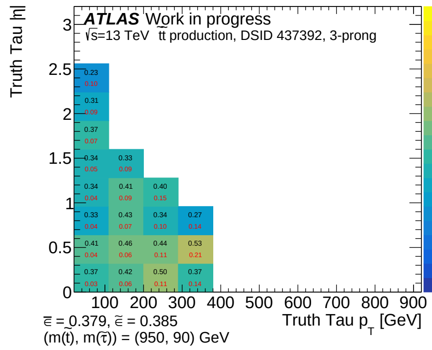

(b) DSID 437392, 3-prong

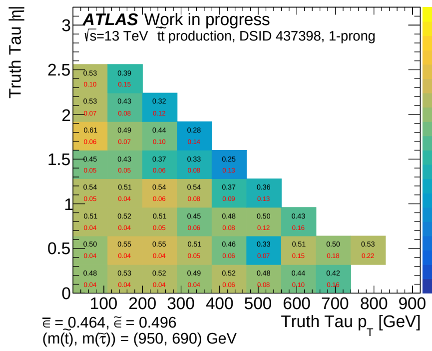

(c) DSID 437398, 1-prong

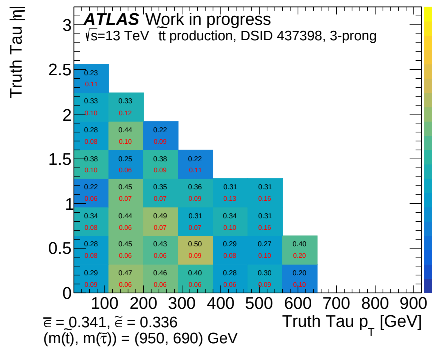

(d) DSID 437398, 3-prong

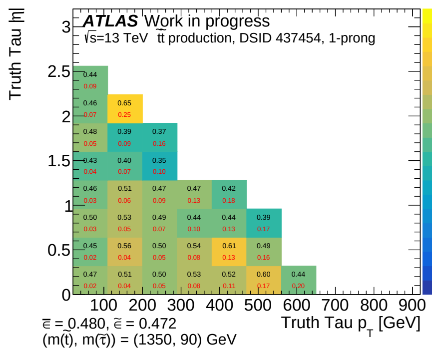

(e) DSID 437454, 1-prong

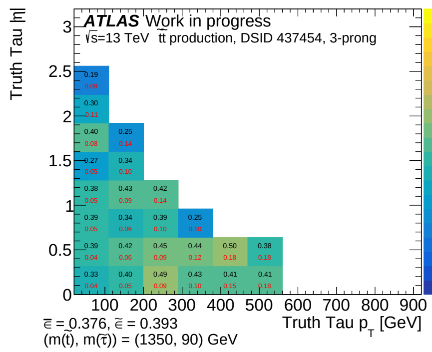

(f) DSID 437454, 3-prong

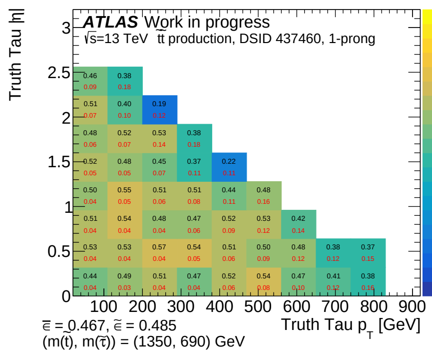

(g) DSID 437460, 1-prong

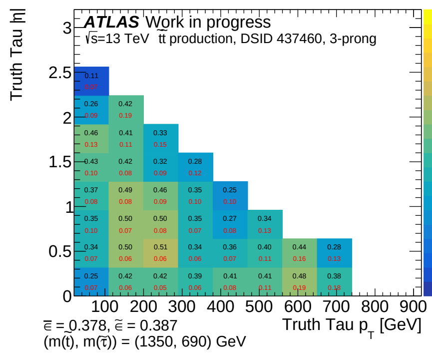

(h) DSID 437460, 3-prong

Figure A.8: Second set of tau reconstruction and ID efficiency maps in tau p_{T} and $|\eta|$ for 1-prong and 3-prong tau leptons of the ttStau samples with DSID 437392 ((a) and (b)), 437398 ((c) and (d)), 437454 ((e) and (f)) and 437460 ((g) and (h)).

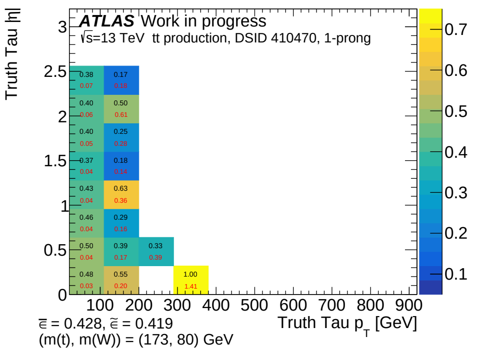

(a) DSID 410470, 1-prong

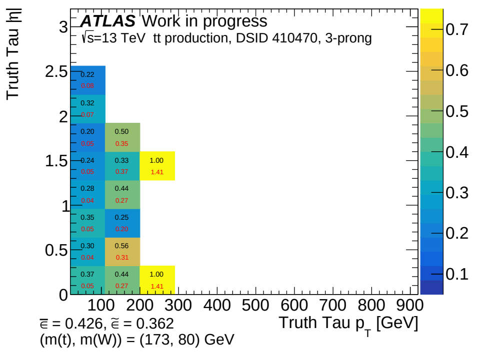

(b) DSID 410470, 3-prong

Figure A.9: Tau reconstruction and ID efficiency maps in tau p_{T} and $|\eta|$ for 1-prong and 3-prong tau leptons of the ttbar sample with DSID 410470 ((a) and (b))).

A.2.2 Electrons and Muons

In figures A.10 and A.11, one can see the electron and muon reconstruction and ID efficiency mapped in electron/muon p_{T} and $|\eta|$ of the remaining direct stau samples (see section 5.3.3 for the original discussion). Bearing in mind that the comparisons of smeared truth-level and reconstruction-level electrons suggest that the new direct stau smearing underestimates the electron reconstruction and ID efficiency for more compressed samples, one can see the reason for this observation from these efficiency maps. They show that samples with a smaller mass difference of stau and neutralino exhibit higher efficiencies across the used binning. This, in turn, leads to the underestimation as the new smearing is based on the sample with DSID 396104 which has a relatively high mass difference.
Even though in the comparisons of smeared truth-level and reconstruction-level muons, no significant worsening of the smearing for more compressed samples was observed, such a sample dependence can be seen in the muon efficiency maps. As in the case of electrons, it seems that a smaller mass difference of stau and neutralino results in generally higher efficiencies.
Hence, the observed sample dependence of the electron and muon reconstruction and ID efficiency exhibits the opposite behaviour as in the tau lepton case. For tau leptons, the efficiency was observed to increase for higher mass differences. However, as this thesis focused on the truth smearing of tau leptons, the possible sample dependence of the electron and muon efficiencies was not further investigated.

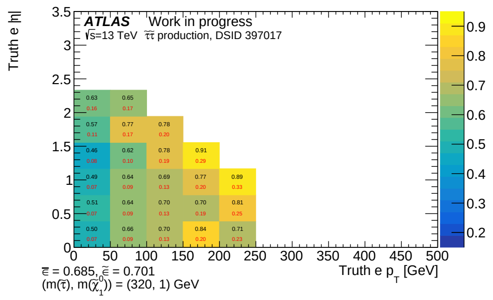

(a) DSID 397017, electron efficiency map

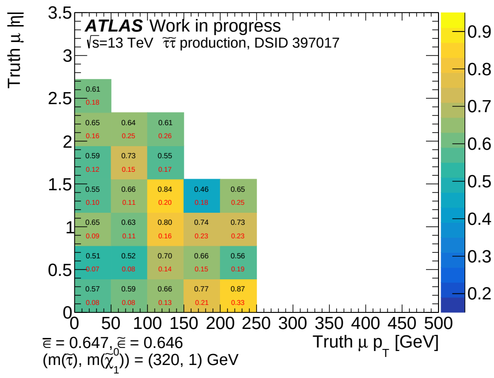

(b) DSID 397017, muon efficiency map

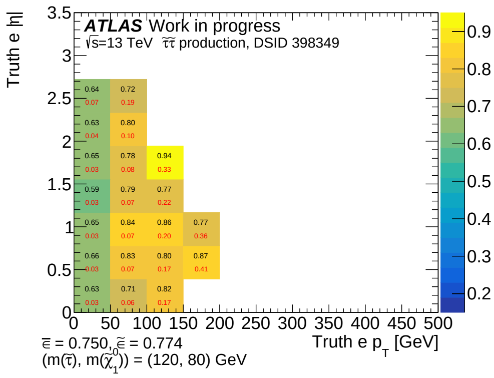

(c) DSID 398349, electron efficiency map

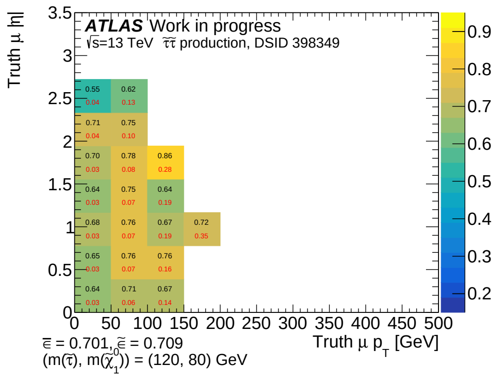

(d) DSID 398349, muon efficiency map

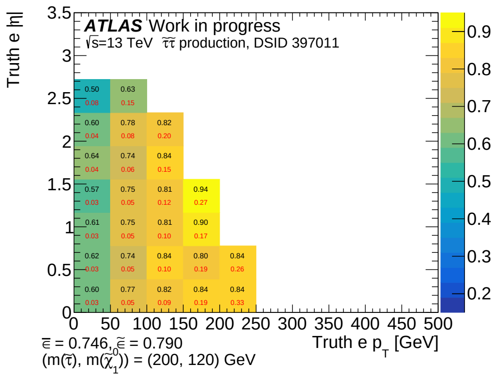

(e) DSID 397011, electron efficiency map

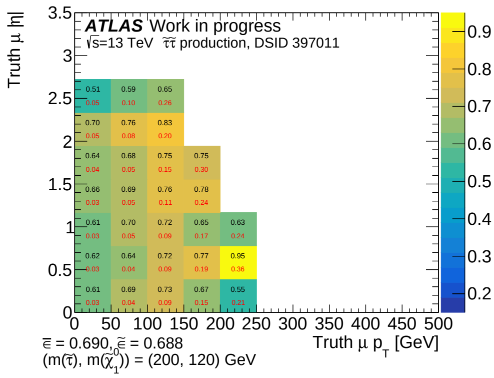

(f) DSID 397011, muon efficiency map

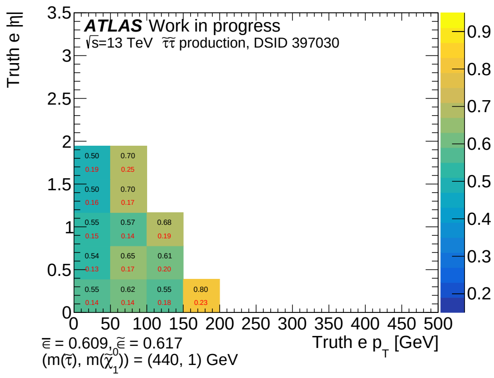

(g) DSID 397030, electron efficiency map

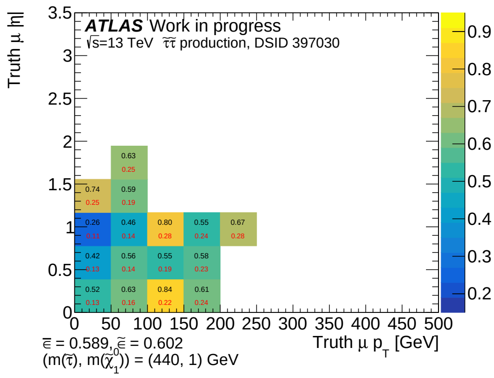

(h) DSID 397030, muon efficiency map

Figure A.10: First set of electron and muon reconstruction and ID efficiency maps in electron/muon p_{T} and $|\eta|$ of the direct stau samples with DSID 397017 ((a) and (b)), 398349 ((c) and (d)), 397011 ((e) and (f)) and 397030 ((g) and (h)).

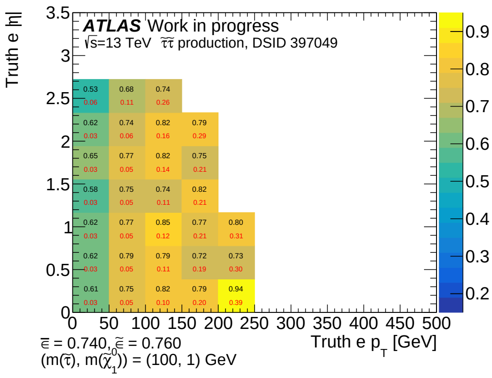

(a) DSID 397049, electron efficiency map

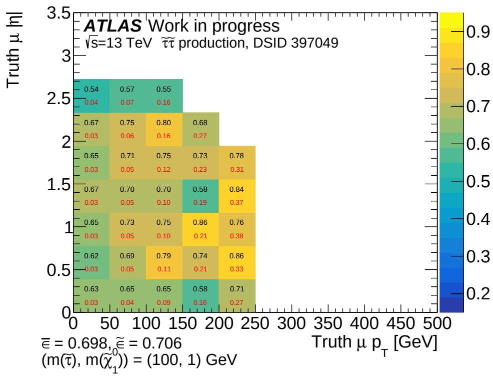

(b) DSID 397049, muon efficiency map

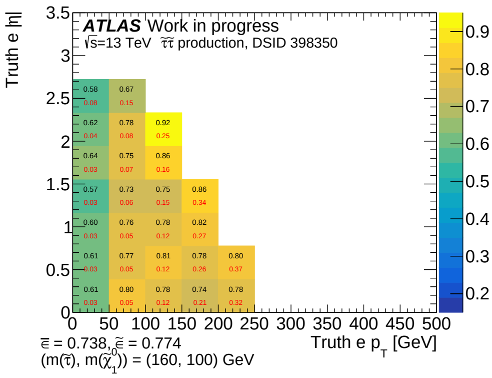

(c) DSID 398350, electron efficiency map

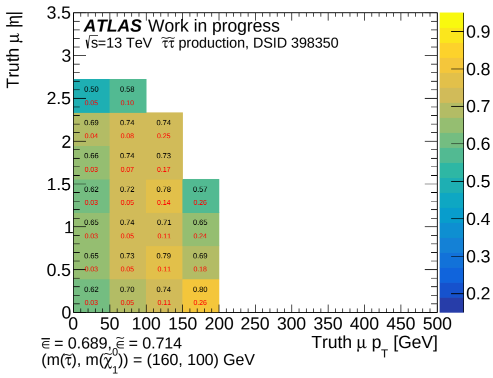

(d) DSID 398350, muon efficiency map

Figure A.11: Second set of electron and muon reconstruction and ID efficiency maps in electron/muon p_T and $|\eta|$ of the direct stau samples with DSID 397049 ((a) and (b)) and 398350 ((c) and (d)).

Appendix B

Additional Figures to Chapter 6

B.1 Distributions of the final input features

In section 6.2.3, important features in the tau reconstruction and ID efficiency distribution and the tau lepton distribution in the final feature variables were discussed. The distributions for the process samples not previously shown are presented in the following for the respective observable.

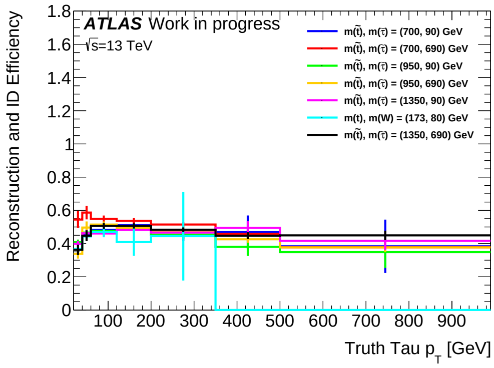

(a) ttStau/ttbar

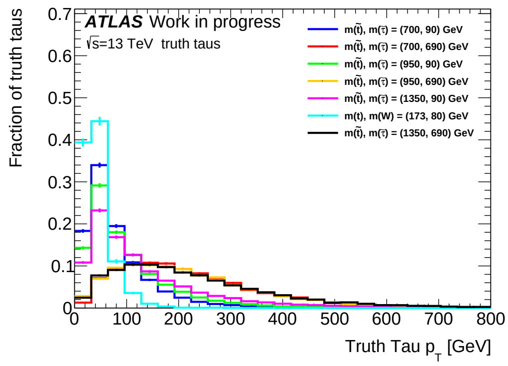

(b) ttStau/ttbar

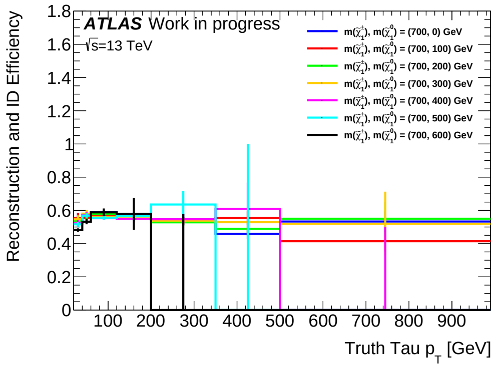

(c) C1C1

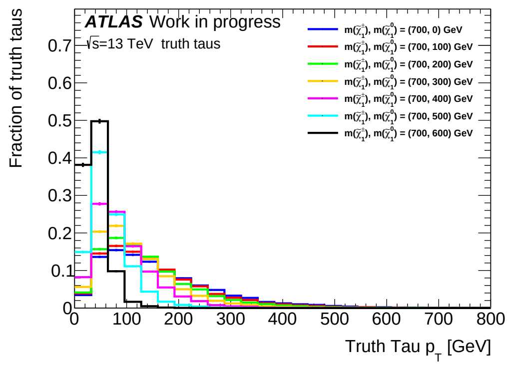

(d) C1C1

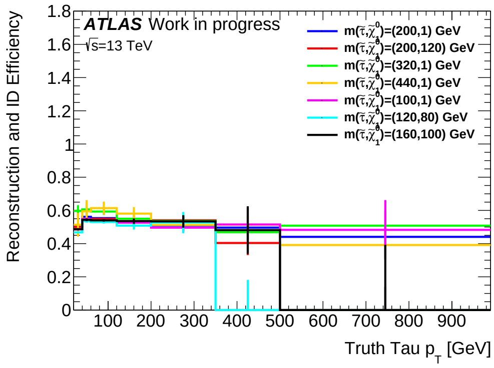

(e) Direct Stau

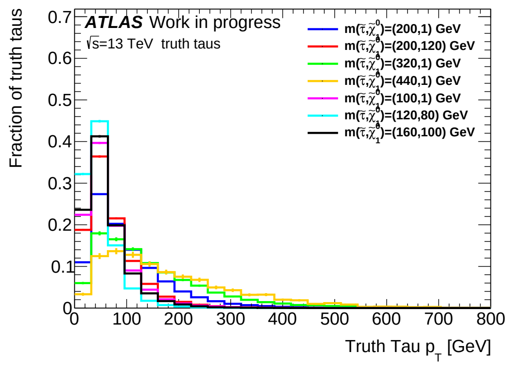

(f) Direct Stau

Figure B.1: On the left: Reconstruction and ID efficiencies calculated in different regions of the tau p_T for the ttStau and ttbar (a), the C1C1 (c) and the direct stau (e) samples. On the right: tau p_T distribution for the ttStau and ttbar (b), the C1C1 (d) and the direct stau (f) samples. The samples are labelled according to their mass configuration.

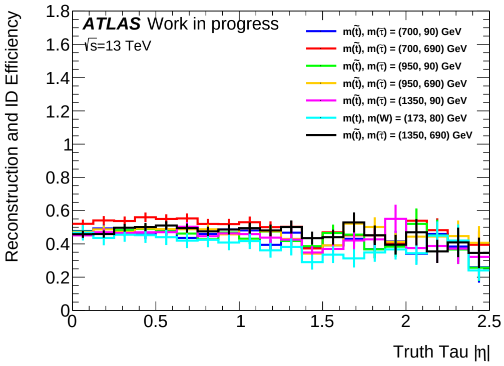

(a) ttStau/ttbar

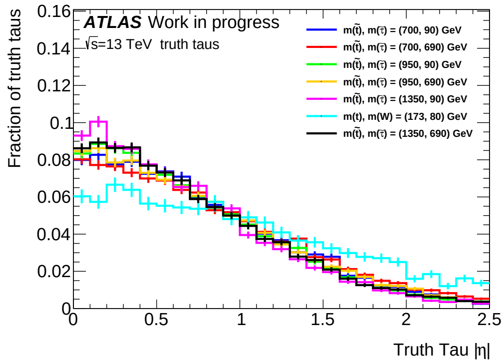

(b) ttStau/ttbar

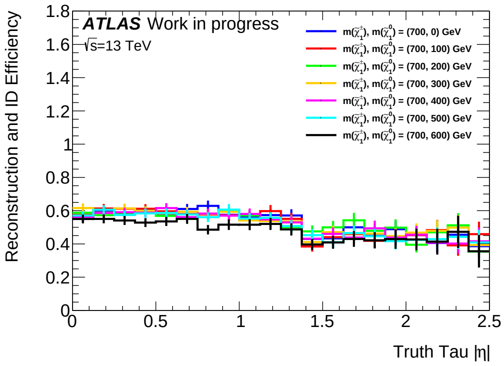

(c) C1C1

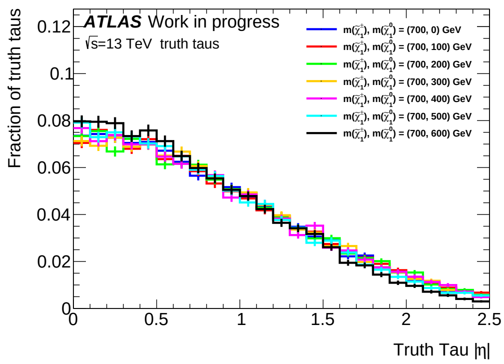

(d) C1C1

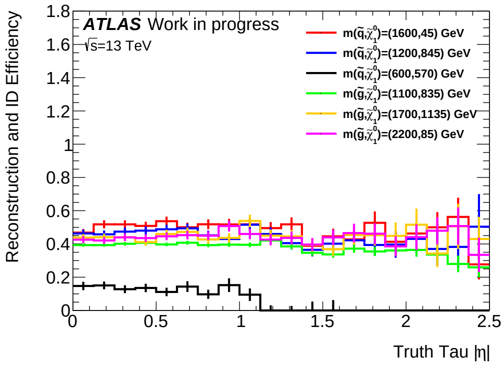

(e) SqSq/GoGo

Figure B.2: On the left: Reconstruction and ID efficiencies calculated in different regions of the tau $|\eta|$ for the ttStau and ttbar (a), the C1C1 (c) and the SqSq/GoGo (e) samples. On the right: tau $|\eta|$ distribution for the ttStau and ttbar (b) and the C1C1 (d) samples. The samples are labelled according to their mass configuration.

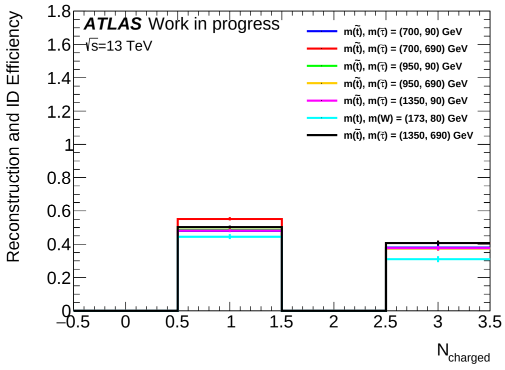

(a) ttStau/ttbar

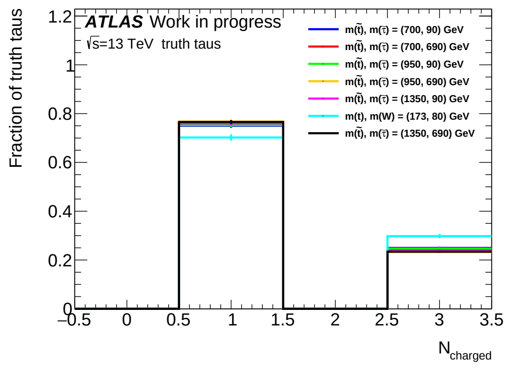

(b) ttStau/ttbar

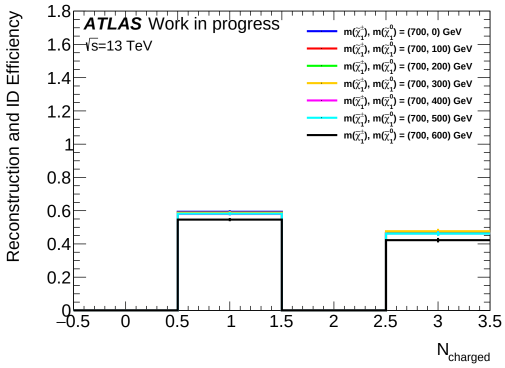

(c) C1C1

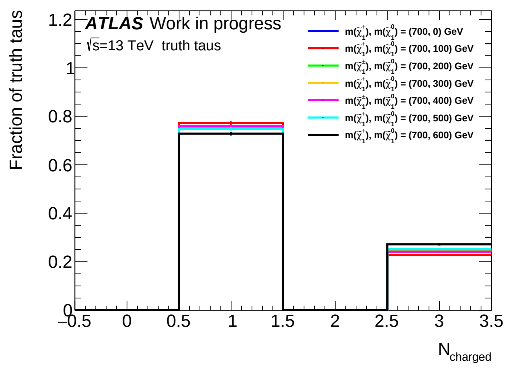

(d) C1C1

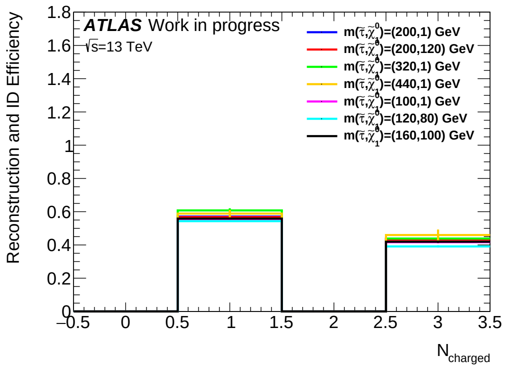

(e) Direct Stau

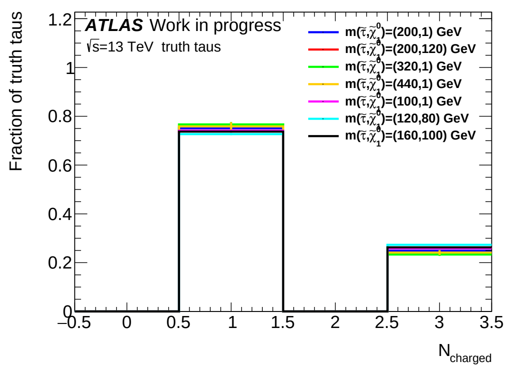

(f) Direct Stau

Figure B.3: On the left: Reconstruction and ID efficiencies calculated for 1-prong and 3-prong taus for the ttStau and ttbar (a), the C1C1 (c) and the direct stau (e) samples. On the right: Fractions of the 1-prong and 3-prong taus for the ttStau and ttbar (b), the C1C1 (d) and the direct stau (f) samples. The samples are labelled according to their mass configuration.

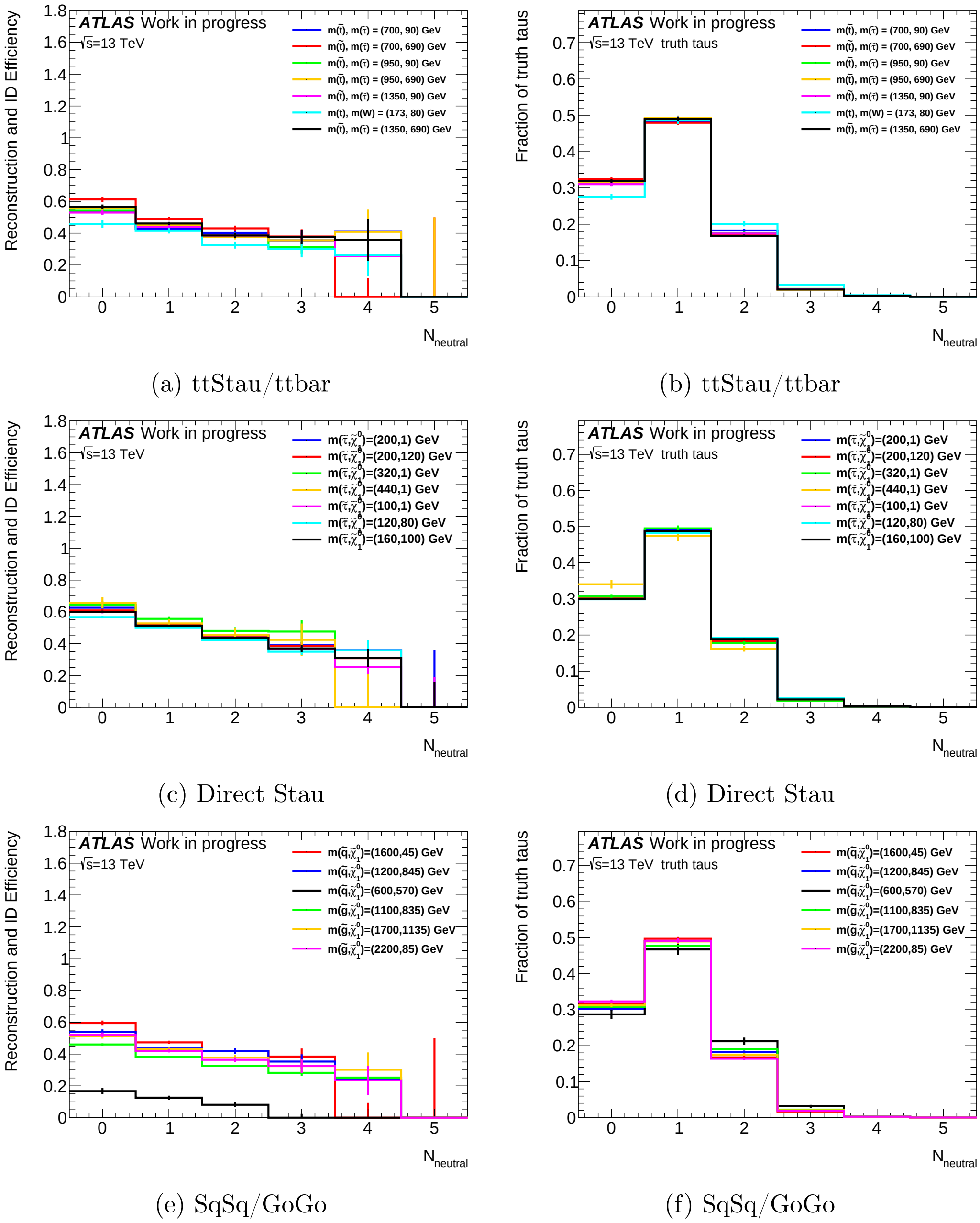

(a) ttStau/ttbar (b) ttStau/ttbar

(c) Direct Stau (d) Direct Stau

(e) SqSq/GoGo (f) SqSq/GoGo

Figure B.4: On the left: Reconstruction and ID efficiencies calculated for different multiplicities of the neutral products of the tau decay for the ttStau and ttbar (a), the direct stau (c) and the SqSq/GoGo (e) samples. On the right: Distribution of the neutral tau decay products for the ttStau and ttbar (b), the direct stau (d) and the SqSq/GoGo (f) samples. The samples are labelled according to their mass configuration.

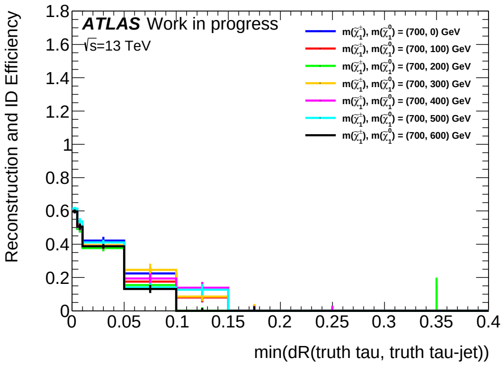

(a) C1C1

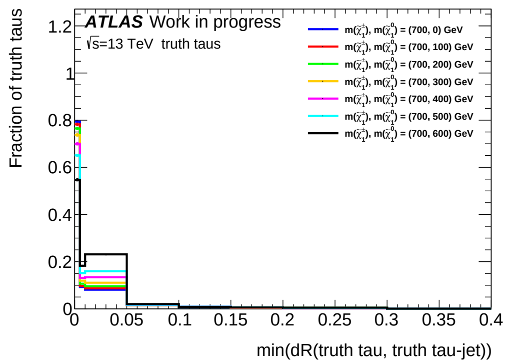

(b) C1C1

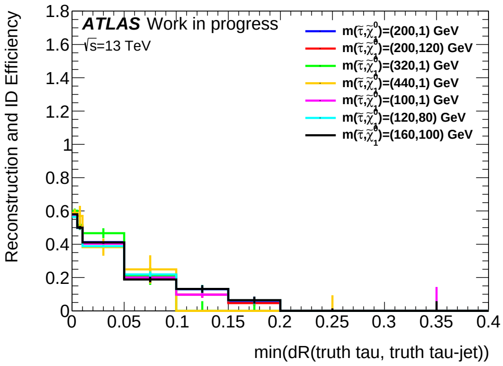

(c) Direct Stau

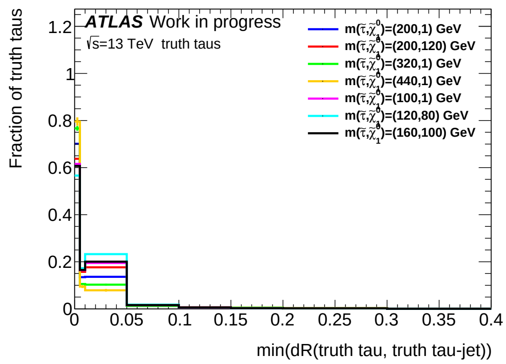

(d) Direct Stau

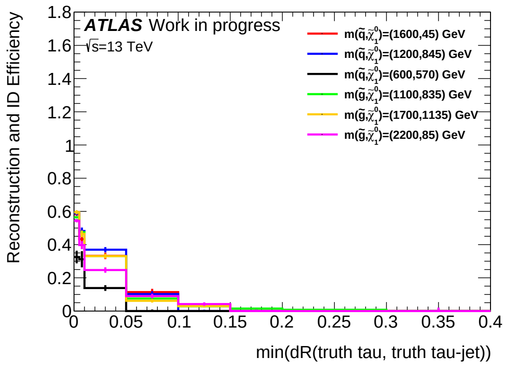

(e) SqSq/GoGo

Figure B.5: On the left: Reconstruction and ID efficiencies calculated in different regions of min(dR(truth tau, truth tau-jet)) for the C1C1 (a), the direct stau (c) and the SqSq/GoGo (e) samples. On the right: min(dR(truth tau, truth tau-jet)) distribution for the C1C1 (b) and the direct stau (d) samples. The samples are labelled according to their mass configuration.

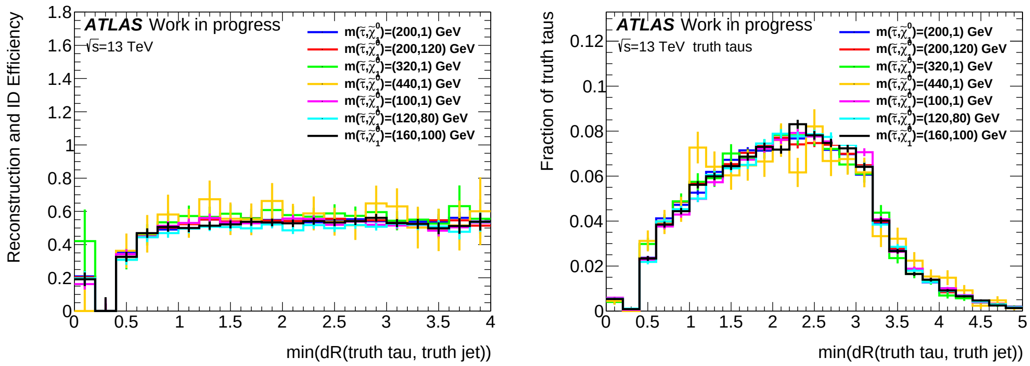

(a) Direct Stau (b) Direct Stau

Figure B.6: On the left: Reconstruction and ID efficiencies calculated in different regions of min(dR(truth tau, truth jet)) for the direct stau (a) samples. On the right: min(dR(truth tau, truth jet)) distribution for the direct stau (b) samples. The samples are labelled according to their mass configuration.

B.2 Tau-to-jet distance plots

As has been discussed in section 6.2.3, looking at plots which show the min(dR(truth tau, truth jet)) variable against the ConeTruthLabelID or the tau origin reveal more information about the taus in the region where the distance is below 0.4. In figure B.7, these plots are shown for further ttStau samples and the ttbar sample and in figure B.8, they are shown for selected SqSq/GoGo samples.
As expected from the decay chain of the ttStau and ttbar process, the nearest non-tau jets with respect to the truth-level tau are b-jets in the majority of cases. For the SqSq and GoGo process, on the other hand, the nearest jets are mainly originating from light quarks (or gluons) which also fits the decay chain of these processes. One exception to this is the most compressed SqSq sample with DSID 378447, as for this sample, a significantly higher amount of b- and c-jets can be seen for distances below 0.4. This is an indicator of either a mislabeling in the ConeTruthLabelID (scenario 1) or the taus not originating from a SUSY decay (scenario 2).
Actually, from figure B.8d, one can see that over half of the taus with a tau-to-jet distance below 0.4 come from scenario 2. For the ttStau samples (except for DSID 437368, the one shown in section 6.2.3) and especially the ttbar sample, scenario 2 is seen to make up a significant fraction of the taus with min(dR(truth tau, truth jet)) < 0.4 as well.

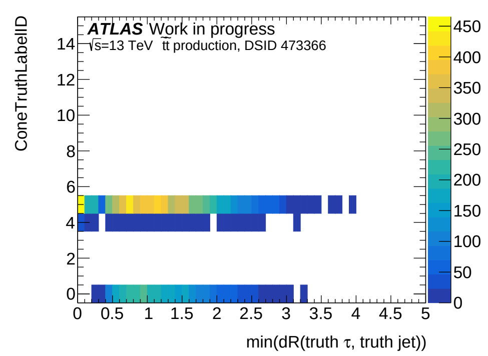

(a) DSID 437366

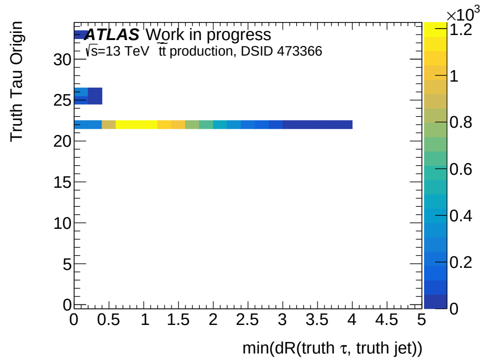

(b) DSID 437366

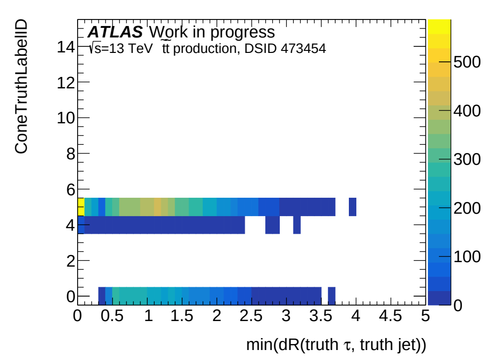

(c) DSID 437454

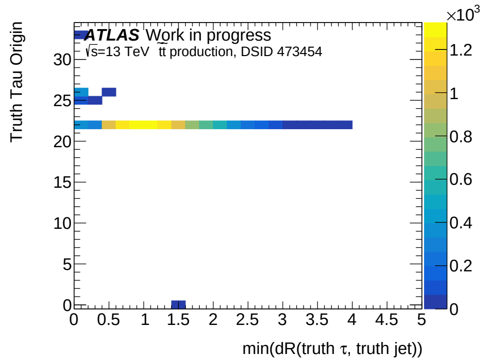

(d) DSID 437454

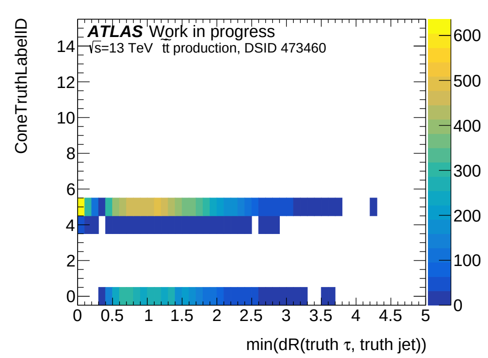

(e) DSID 437460

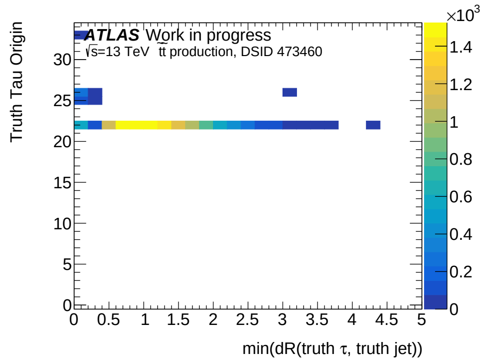

(f) DSID 437460

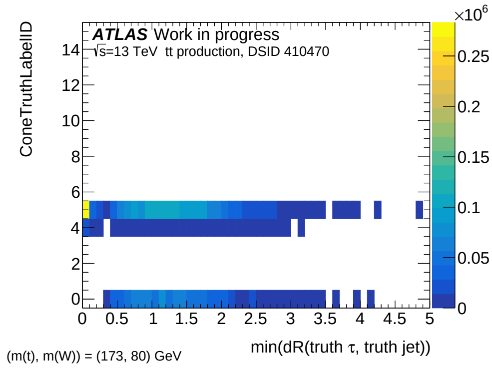

(g) DSID 410470

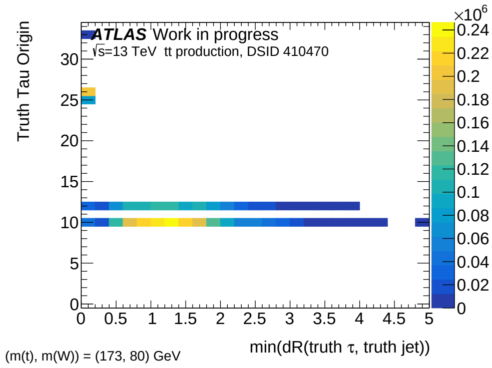

(h) DSID 410470

Figure B.7: On the left: Number of taus in dependence of min(dR(truth tau, truth jet)) and the ConeTruthLabelID of the nearest non-tau jet for further ttStau/ttbar samples with the DSID 437366 (a), 437454 (c), 437460 (e) and 410470 (g). The ConeTruthLabelID is 0 for jets from light quarks and gluons, 4 for c-jets and 5 for b-jets. On the right: Number of taus in dependence of min(dR(truth tau, truth tau-jet)) and the origin of the truth tau for further ttStau/ttbar samples with the DSID 437366 (b), 437454 (d), 437460 (f) and 410470 (h). Origin refers to the particle decaying into the tau and is 22 for SUSY particles, 25/26 for c-hadrons and 33 for b-hadrons (10/12 stand for isolated/background taus from W decays).

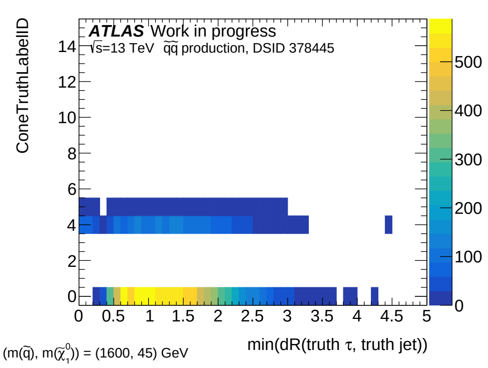

(a) DSID 378445

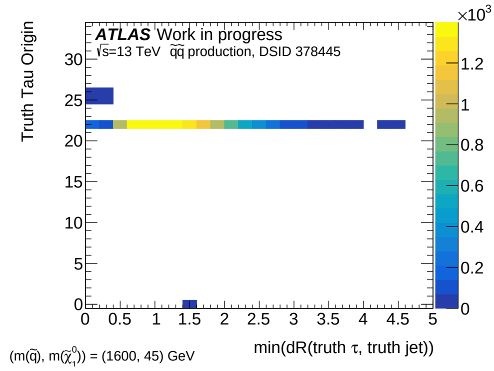

(b) DSID 378445

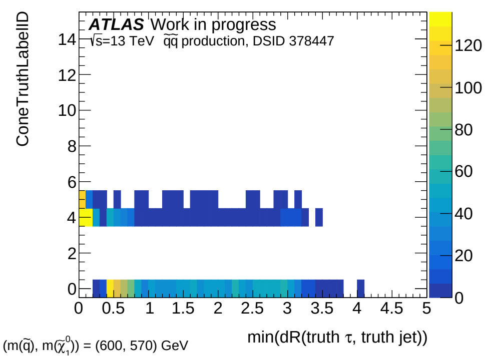

(c) DSID 378447

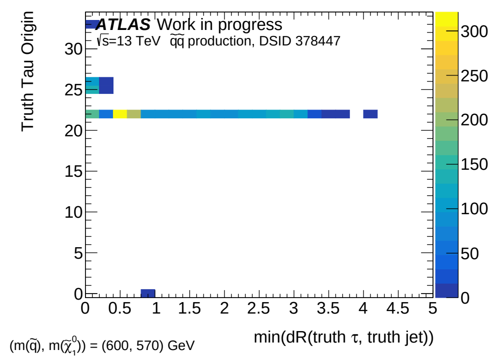

(d) DSID 378447

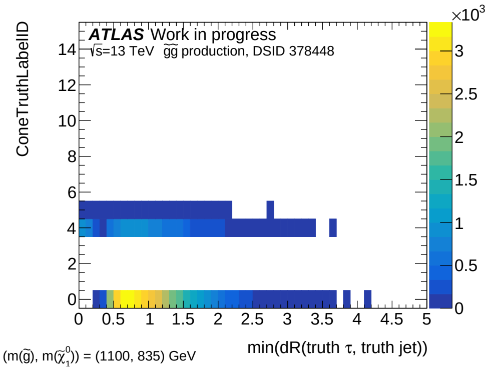

(e) DSID 378448

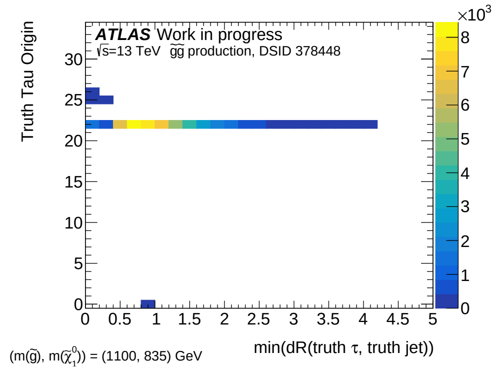

(f) DSID 378448

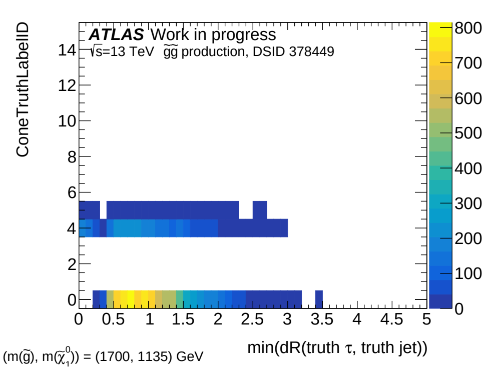

(g) DSID 378449

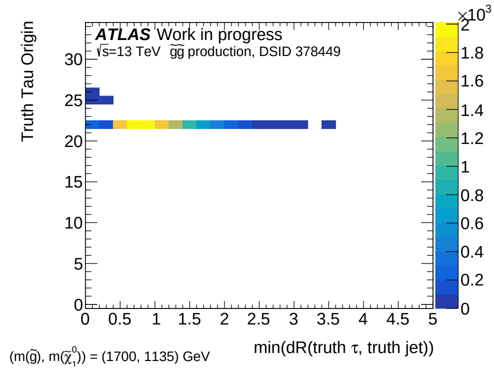

(h) DSID 378449

Figure B.8: On the left: Number of taus in dependence of min(dR(truth tau, truth jet)) and the ConeTruthLabelID of the nearest non-tau jet for the SqSq/GoGo samples with the DSID 378445 (a), 378447 (c), 378448 (e) and 378449 (g). On the right: Number of taus in dependence of min(dR(truth tau, truth tau-jet)) and the origin of the truth tau for the SqSq/GoGo samples with the DSID 378445 (b), 378447 (d), 378448 (f) and 378449 (h).

B.3 Figures regarding the tau classifiers

In order to highlight the influence of the hyperparameters on the medium and tight tau classifier, different BDT properties were also determined for versions of these classifiers with very weak hyperparameters (undertraining) and with hyperparameters inducing overtraining. For both classifiers, undertraining was achieved with $M = 100$ trees, a learning rate of $\nu = 0.01$ and a maximum depth of 2 and overtraining was achieved with $M = 3500$ trees, a learning rate of $\nu = 0.9$ and a maximum depth of 8.
Figure B.9 shows the feature importances, the ROC curves, the calibration and the sample-specific MSEs against the number of taus in the respective sample for the undertrained medium tau classifier. The same plots can be found in figure B.10 for the overtrained medium tau classifier and in figures B.11 and B.12 for the undertrained and overtrained tight tau classifier, respectively. It can be seen that the undertraining has a huge negative impact on the MSEs and the calibration. Also, the least important features loose their feature importance completely, while the more important ones gain in turn. The overtraining has only a small impact on the MSEs (slightly negative for the medium tau classifier, slightly positive for the tight tau classifier), but the calibration is worse and the ROC curves show the overtraining quite clearly. The overtraining does not alter the feature importance ranking.
Additionally, the sample-specific MSEs calculated using the medium and tight tau efficiency functions of the UpgradePerformanceFunctions for the available PHYS samples are presented in figures B.13 and B.14, respectively.

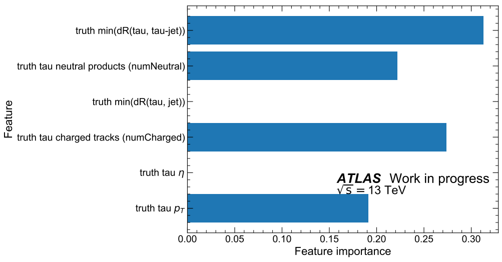

(a) Feature Importances

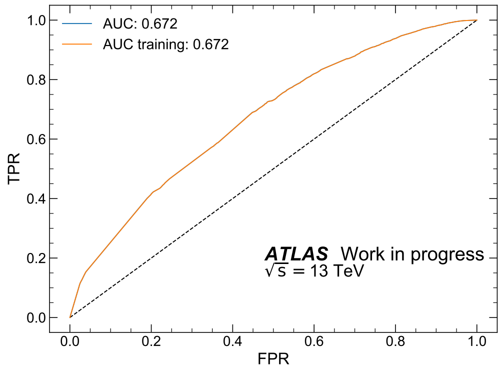

(b) ROC Curves

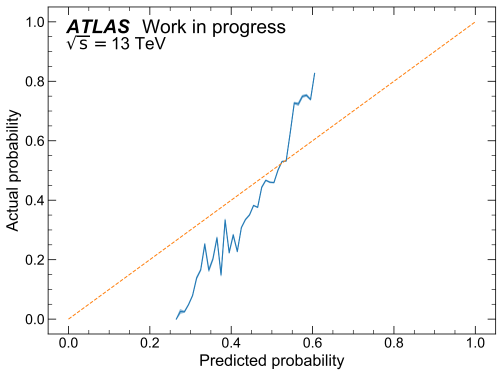

(c) Calibration

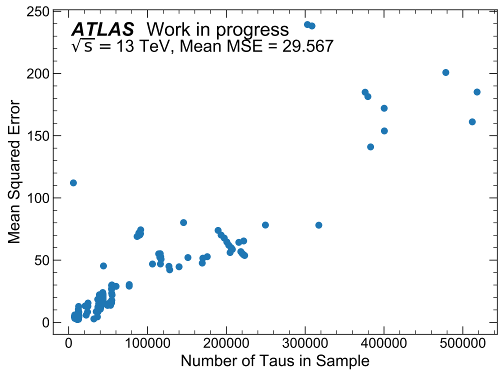

(d) Sample-Specific MSEs vs N_τ^{sample}

Figure B.9: Different characteristics of the medium tau classifier BDT with weak hyperparameters: the feature importances (a), the ROC curves of the BDT applied to the training and test sample (b), the calibration curve of the BDT applied to the test sample in 100 bins (c) and the sample-specific MSEs against the number of taus in the respective sample (d).

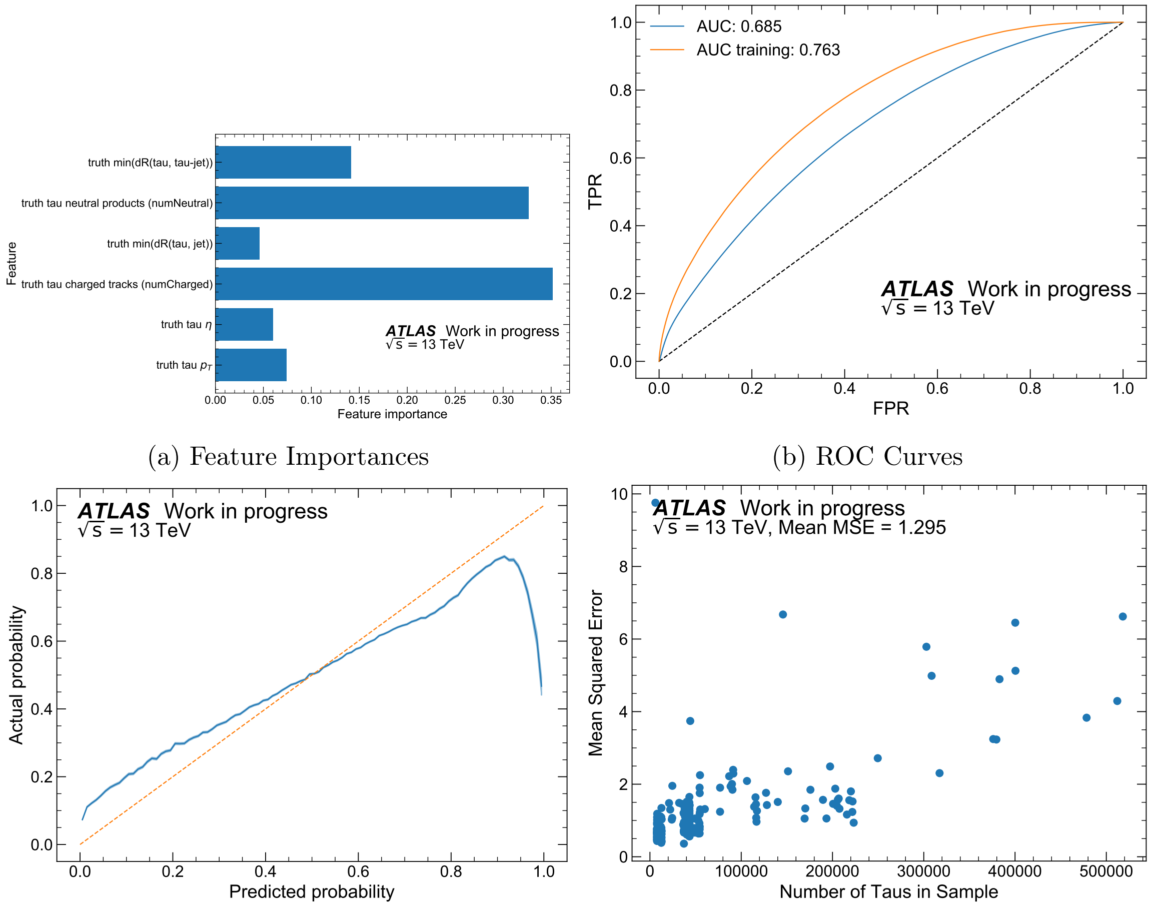

(a) Feature Importances

(b) ROC Curves

(c) Calibration

(d) Sample-Specific MSEs vs N_τ^{sample}

Figure B.10: Different characteristics of the medium tau classifier BDT with weak hyperparameters: the feature importances (a), the ROC curves of the BDT applied to the training and test sample (b), the calibration curve of the BDT applied to the test sample in 100 bins (c) and the sample-specific MSEs against the number of taus in the respective sample (d).

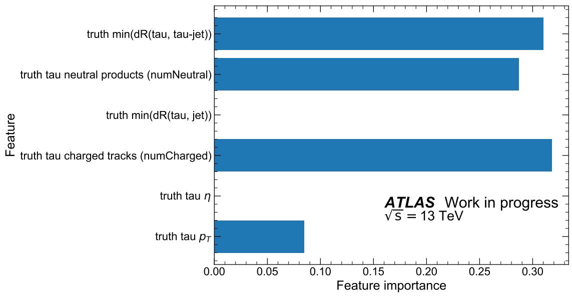

(a) Feature Importances

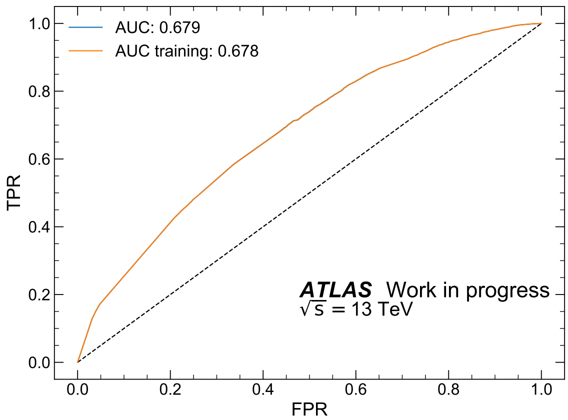

(b) ROC Curves

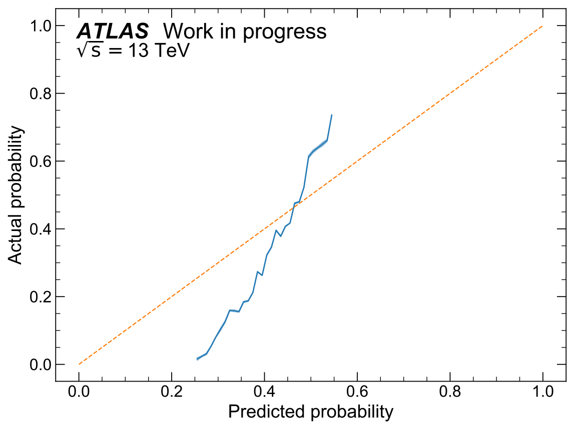

(c) Calibration

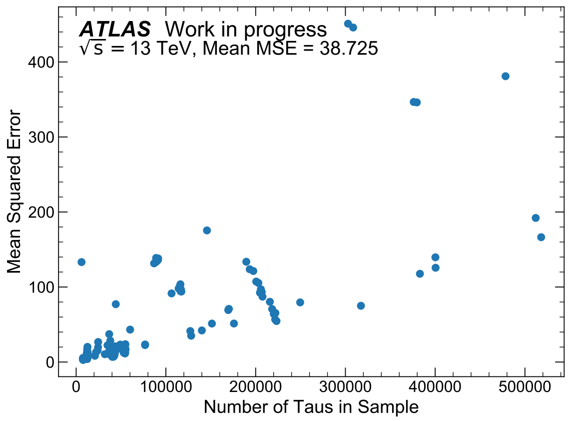

(d) Sample-Specific MSEs vs N_τ^{sample}

Figure B.11: Different characteristics of the tight tau classifier BDT with weak hyperparameters: the feature importances (a), the ROC curves of the BDT applied to the training and test sample (b), the calibration curve of the BDT applied to the test sample in 100 bins (c) and the sample-specific MSEs against the number of taus in the respective sample (d).

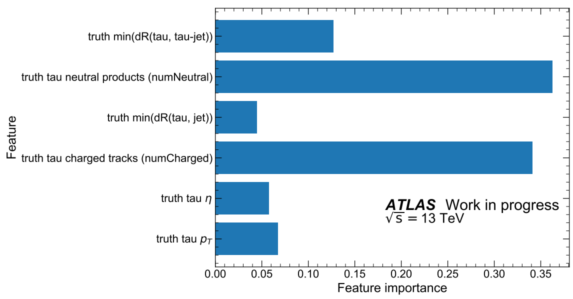

(a) Feature Importances

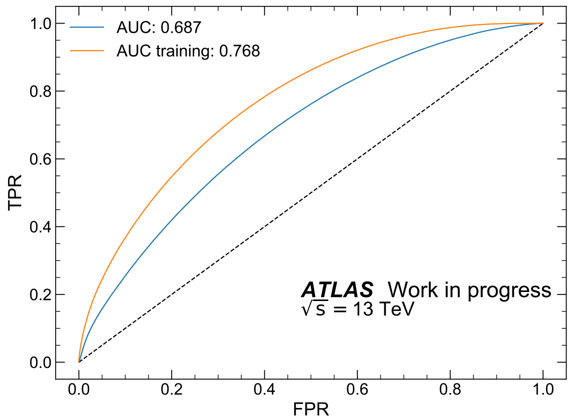

(b) ROC Curves

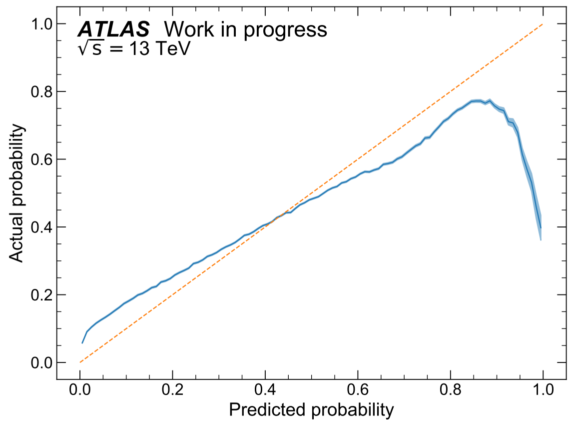

(c) Calibration

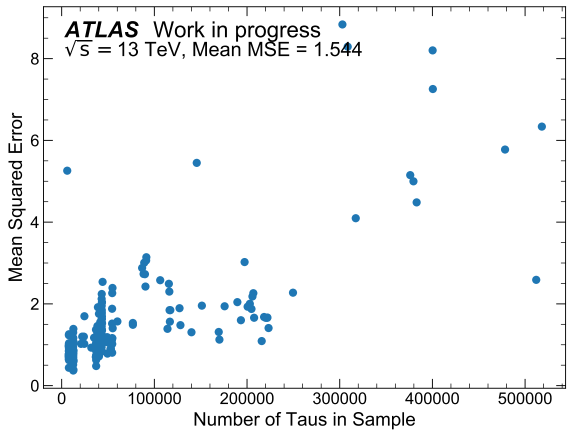

(d) Sample-Specific MSEs vs N_τ^{sample}

Figure B.12: Different characteristics of the tight tau classifier BDT with weak hyperparameters: the feature importances (a), the ROC curves of the BDT applied to the training and test sample (b), the calibration curve of the BDT applied to the test sample in 100 bins (c) and the sample-specific MSEs against the number of taus in the respective sample (d).

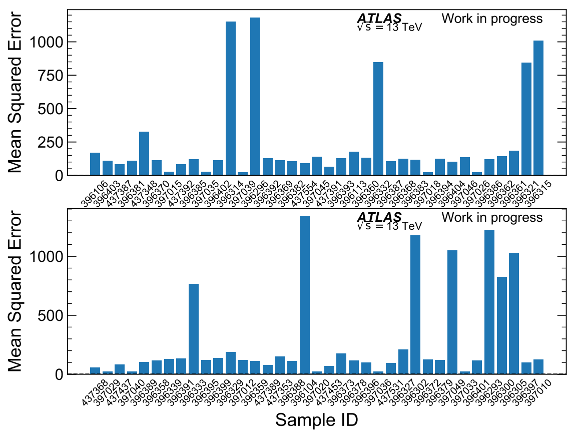

(a)

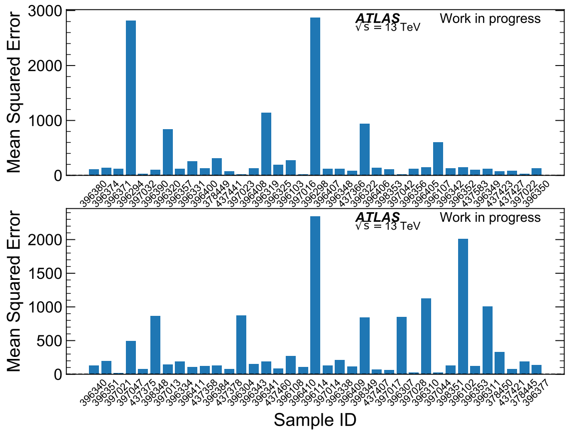

(b)

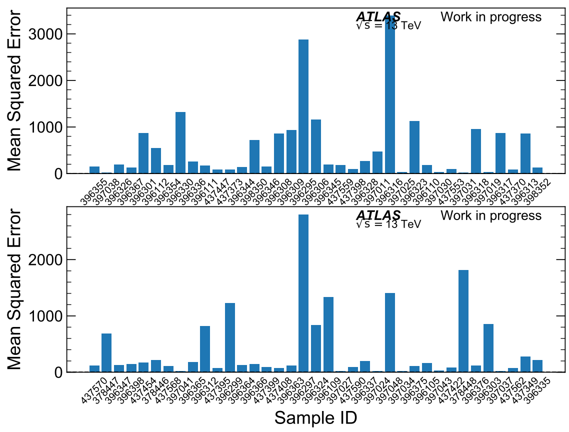

(c)

Figure B.13: Sample-specific MSEs calculated using the medium tau efficiency functions from the UpgradePerformanceFunctions for the prediction of the efficiencies.

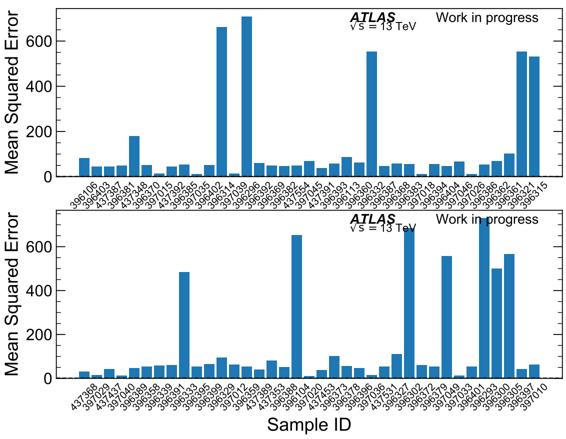

(a)

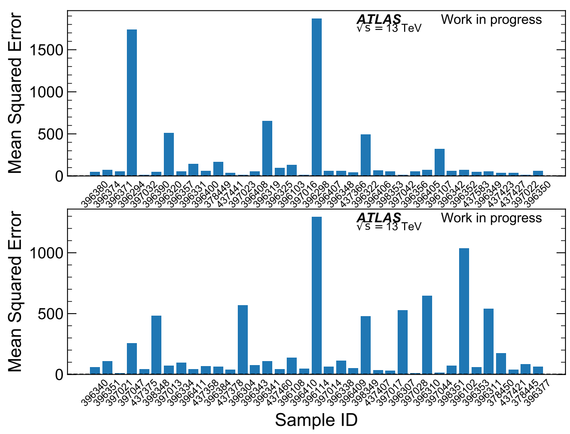

(b)

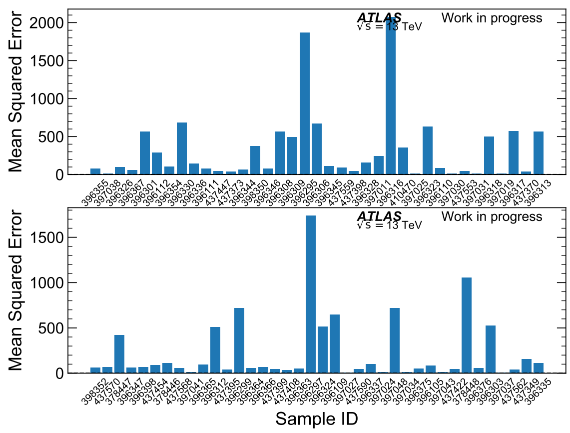

(c)

Figure B.14: Sample-specific MSEs calculated using the tight tau efficiency functions from the UpgradePerformanceFunctions for the prediction of the efficiencies.

Selbständigkeitserklärung

Hiermit erkläre ich, die vorliegende Arbeit mit dem Titel

Development of an Improved Parametrisation of the ATLAS Detector Performance for Tau Leptons and their Application in Studies of Supersymmetric Models within the pMSSM

selbständig verfasst zu haben und keine anderen als die in der Arbeit angegebenen Quellen und Hilfsmittel benutzt zu haben.

Daniel Buchin

München, den 09. Juni 2021